Mechanics of Fatigue Damage In Titanium-Graphite Hybrid Laminates

by

Dennis Arthur Burianek

S.B., Massachusetts Institute of Technology
(1996)
S.M., Massachusetts Institute of Technology
(1998)

Submitted to the Department of Aeronautics and Astronautics
in partial fulfillment of the requirements for the degree of

Doctor of Philosophy in Aeronautics and Astronautics

at the

MASSACHUSETTS INSTITUTE OF TECHNOLOGY

June 2001

Author ....
Department of Aeronautics and Astronautics
March 19, 2001

Certified by ....
S. Mark Spearing
Esther and Harold E. Edgerton Associate Professor of Aeronautics and Astronautics
Thesis Supervisor

Certified by ....
Antonios Giannakopoulos
Research Scientist, Department of Materials Science and Engineering

Certified by ....
Paul Lagace
Professor of Aeronautics and Astronautics and Engineering Systems

Certified by ....
Subra Suresh
R.P. Simmons Professor of Materials Science and Engineering

Accepted by ....
Wallace Vander Velde, Professor of Aeronautics and Astronautics, Emeritus
Chairman, Department Committee on Graduate Students

Mechanics of Fatigue Damage In Titanium-Graphite Hybrid Laminates

by

Dennis Arthur Burianek

Submitted to the Department of Aeronautics and Astronautics
on March 19, 2001, in partial fulfillment of the
requirements for the degree of
Doctor of Philosophy in Aeronautics and Astronautics

Abstract

Titanium-graphite hybrid laminates are being developed for high-temperature aerospace applications. Experimental observations have indicated that cracks in the titanium facesheets initiate at free edges as well as in areas of high stress concentration, such as holes and notches and that a delaminated region between the facesheet and the intact plies develops and propagates in the wake of the facesheet crack. This thesis experimentally and analytically evaluates the facesheet crack and delamination growth behavior of TiGr laminates. The delamination growth behavior is studied by isolating delamination growth using TiGr specimens with facesheet seams. The growth rate of delamination from facesheet seams is related via a power law to the applied strain energy release rate. It is shown that elevated temperatures significantly increase the growth rate of facesheet delamination. The facesheet crack growth behavior in TiGr laminates was measured experimentally and compared to model predictions. It is shown that the crack growth rate in TiGr facesheets is significantly lower for TiGr laminates as compared to monolithic titanium. After an initial decrease in crack growth rate, the crack propagates at a constant rate while the crack growth rate for monolithic titanium increases as the crack extends. A three-dimensional finite element model was implemented that captured the experimental crack growth trends without any additional tuning parameters. A global, bridged-crack model was not accurate in predicting the facesheet crack growth behavior of TiGr laminates. The bridged-crack model failed because it did not capture the details of the bridging stresses and delamination in the vicinity of the crack tip. In contrast to the delamination growth from facesheet seams, it was shown that elevated temperatures did not significantly affect the growth rate of the titanium facesheet crack. Future efforts to model composite damage growth using global modeling approach must validate the model to ensure that all of the necessary parameters are captured.

Thesis Supervisor: S. Mark Spearing
Title: Esther and Harold E. Edgerton Associate Professor of Aeronautics and Astronautics

Acknowledgments

It has been a long road to get all the way through MIT, but my journey is finally ending. I would not have made it this far without the help of a number of people that have helped me academically and personally over the past eight and a half years. First and foremost, I have to thank my advisor Mark Spearing who hired me to work on TiGr five years ago and along the way taught me numerous things about composites and the research process. Without his guidance, this project would never have come about.

I would also like to thank my committee members, Prof. Paul Lagace, Prof. Subra Suresh, and Dr. Antonios Giannakopoulos. In particular, Antonios has worked with me over the past year teaching me all about modeling and fracture mechanics. The TELAC faculty, Carlos, Hugh, and Prof. Dugundji have been helpful in supporting my research.

With any experimental program, especially involving fatigue, the lab work isn't possible without an extensive support staff. John Kane and I started in TELAC at about the same time and he was a great help in the lab. A team of UROP's has worked with me over the years conducting the long and tedious fatigue experiments: Todd, Barbara, David, and Michelle put in long hours and I am very thankful for all of their efforts. Dick Perdichizzi and Don Weiner in the Aero/Astro shops have always been willing to help with machining and ideas. Ping Lee, my personal ATM machine, always made sure that I got paid on time and had money for purchases. The graduate students in TELAC have also been of great help in the lab and in the office. Brian, Lauren, Tom, Kaustubh, Chris, Mike ("Pole position, baby!"), Jose, Torrey, Randal, Catherine, Seth, DJ, Barbara, Ariela, Kevin, Sahoo, Gordon, Mark, and Pong.

I also couldn't have made it through MIT without my friends, especially the Aero/Astro study group, Malinda (& Jean), Corinne (& Mike), and Brian (& Judy), my freshman roomates Shawn and Luis plus everyone else who has helped me get through MIT with my sanity in tact.

The last group of people I would like to acknowledge is my family who has continuously supported me during my time at MIT. Mom, Dad, Joe, Jennifer, Mike, Connie, Theresa, Elizabeth, Katherine, Jonathan and the Minard family: Thank you all, I wouldn't be here

without you.

Lastly, I have to acknowledge the one person who has made this journey worth it. My wife Sarah has unfailingly supported me in my quest for a PhD. She endured long evenings without complaint alone while I toiled away at the office and was always there to lift me up after a rough day. Since I met her 4 years ago, my life hasn't been the same and I wouldn't change one minute of the time we have spent together.

Forward

This work was performed in the Technology Laboratory for Advanced Composites (TELAC) of the Department of Aeronautics and Astronautics at the Massachusetts Institute of Technology. Funding for this project was provided under NSF Career Award #CMS-9702399. Additional funding was provided by The Boeing Company under P.O. #JV9429.

Contents

List of Figures

List of Tables

Chapter 1

Introduction

Titanium-graphite hybrid laminates (TiGr) are being developed to satisfy the requirements for future high temperature aerospace applications [1]. Hybrid laminates such as TiGr, sometimes called fiber metal laminates (FML), are made of polymer matrix composite (PMC) plies interspersed with metal foil plies. The two materials are assembled by curing the PMC plies and metal foils to form a composite laminate. A schematic of a TiGr laminate is shown in Figure 1-1.

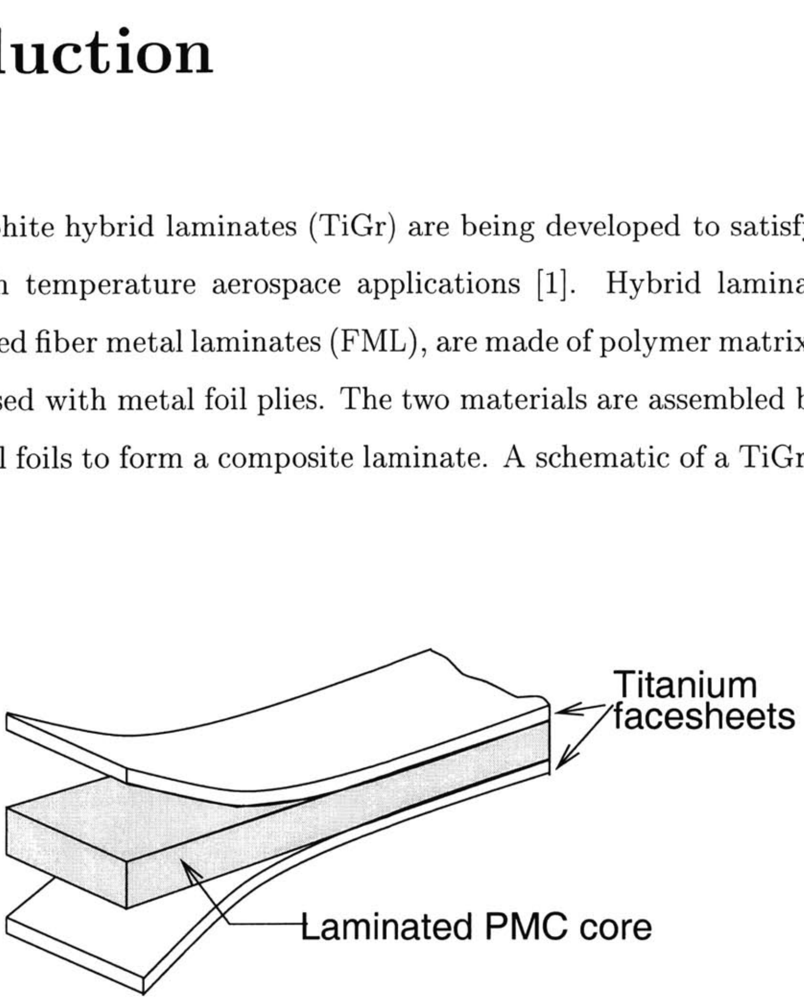

Figure 1-1: Schematic of TiGr laminate

The benefits of hybrid laminates arise from the ability to tailor the materials so that the attractive aspects of the two component materials are utilized whereas their weaknesses are avoided. The titanium protects the PMC core from environmental and temperature-dependent effects such as oxidation and moisture ingress, except along exposed edges, as well as potentially providing improved impact resistance and bearing properties [2]. The composite core has higher strength and stiffness to weight ratios than the monolithic titanium and is presumed to be less sensitive to fatigue effects. The combination of the two materials as a hybrid composite could potentially outperform either of the two constituent materials in elevated temperature structural applications where fatigue resistance and durability are key requirements.

Composite materials, and TiGr in particular, typically exhibit complex damage states as a result of fatigue loading [3]. Often, different damage modes interact with one another and combine to cause structural failure. It is important to identify and model the critical damage modes in TiGr laminates to determine the critical fatigue damage mechanisms. TiGr was developed specifically for elevated temperature (≈177° C), durability-critical structural applications. Therefore, it is important to understand not only the critical fatigue damage mechanisms, but also the effects of temperature on the formation and growth of the damage modes.

Currently, new materials, such as TiGr, undergo extensive experimental programs to verify their performance before they are certified for use in aircraft design. In order to reduce the cost of validating new materials, it has been proposed that analytic models may be substituted for some experiments as part of the validation process. For models to be effective, as well as to ensure the safety of the design, it is essential to develop an understanding of the different techniques that have been developed for modeling damage growth. The time and high cost of conducting fatigue experiments has led to a significant volume of research on the modeling of fatigue damage growth. By reducing the number of fatigue experiments, the cost of validating a new material can potentially be reduced significantly. In conjunction with this, methods for accelerated fatigue testing, using environmental accelerators such as temperature, may prove to be useful in further reducing the cost of material validation.

There are two principal objectives for this thesis. The first objective is to model the critical fatigue failure modes for TiGr laminates and to quantify the effects of temperature on the propagation of damage. The second objective is to evaluate the modeling techniques available to model fatigue damage growth in composites, as applied to the particular case of damage observed in TiGr laminates. The broader goal is to develop an understanding of the applicability and limitations of the modeling procedures and to identify areas where modeling will be most beneficial in future material development programs.

The particular critical failure mechanism that will be modeled in this thesis is the coupled growth of cracks in the titanium facesheets and delamination between the facesheet and the composite core that occurs in the wake of the crack. Propagation of these two damage modes results in a stiffness reduction in the laminate that will lead to catastrophic failure [3]. In order to model the coupled damage growth, the behavior of the individual damage modes, i.e. crack propagation in titanium and TiGr facesheet delamination, will be studied experimentally and analytically. At the end, the procedures used to develop the models for TiGr will be analyzed to determine their applicability to similar problems in composite laminates.

Chapter 2 provides an overview of previous composite fatigue research, including fatigue life modeling in composites, an overview of typical fatigue damage modes in composites and an overview of previous research efforts on hybrid laminates. In Chapter 3, the materials and the experimental techniques used in this thesis are described. Specific details of the individual experiments are included with the results of those experiments presented in subsequent chapters. Chapter 4 presents analysis and results on the study of facesheet delamination of TiGr laminates. The results from the facesheet delamination experiments and modeling are critical inputs into the modeling of facesheet cracks presented in Chapter 5. Two models are presented in Chapter 5, both of which attempt to calculate the effective stress intensity factor at the crack tip and hence, the crack growth rate. The first is a global two-dimensional bridged-crack model and the second is a three-dimensional finite element model using the virtual crack closure technique. Chapter 6 presents the experimental results from the facesheet crack growth experiments for three different laminates and compares the results to the models developed in Chapter 5. A discussion of the potential methods for applying the results from this research is presented in Chapter 7, including an extension of the modeling to predict the open hole fatigue behavior. The final chapter outlines the conclusions from the research and potential areas for future research.

Chapter 2

Background and Approach

Composite materials have brought new challenges to structural engineers, particularly in design against failure and for durability, because of the variety of damage modes that can occur. A number of modeling techniques have been proposed to predict the fatigue failure modes and life of composite laminates and these have achieved varying degrees of success. The goal of this chapter is to present an overview of the previous research that has been performed on the observation and modeling of fatigue damage in composite materials. The first section discusses methodologies that have been proposed to model fatigue life of composite laminates. The second section discusses the modeling of specific damage modes typically observed in composite laminates. Particular attention is focused on those damage modes, such as delamination, that have been identified as key failure mechanisms for hybrid laminates. The third section outlines the research performed on hybrid laminates and the benefits and concerns of designing with hybrid laminates. These topics provide a foundation for the research described in this thesis on the modeling of damage in TiGr laminates. The final section outlines the approach taken in this thesis for modeling coupled damage growth in TiGr laminates.

2.1 Fatigue Life Modeling in Composites

The inability to model and to predict accurately the fatigue life of composite laminates is one of the major drawbacks for widespread application of composites in primary aircraft structures. The complexity of the multiple, interacting damage modes that occur at various length-scales during fatigue loading conditions makes it difficult to capture all aspects of the failure process in a single model. It is even more difficult to relate the damage mechanisms to the residual life of the composite. The multiple lay-ups and materials that are available as design variables adds additional complexity to the problem. As a result of this overall complexity, a significant amount of expensive experimental work is currently necessary to validate composite materials for structural applications [4]. The development of accurate modeling techniques may provide a means of replacing some of these experiments and therefore reducing the cost of validating new materials and structures. This section discusses the different modeling philosophies that have been developed for fatigue life of composite materials in order to provide a framework for the damage models discussed subsequently in this thesis.

2.1.1 Phenomenological models

One class of fatigue life models for composites, often called phenomenological models, use either a strength-based failure criteria or a stiffness-based failure criteria. Phenomenological models typically characterize strength and/or life in terms of macroscopically observable properties, such as strength or stiffness [5]. The damage modes are identified via experiments. The effects of the critical damage mechanisms on either strength or stiffness are modeled and a failure criterion is applied to predict the life of the material.

One example of a phenomenological fatigue life model would be a Safe-Life Design using S-N curves and Goodman diagrams along with some form of damage accumulation model, such as Miner's Rule, similar to methods that have been used for metal structures. However, because the S-N behavior depends on many factors such as lay-up, geometry, and loading, large experimental programs are necessary to produce an S-N curve for every potential configuration. The large number of experiments necessary to build a database of S-N curves for every potential configuration makes such an approach very costly and time-consuming.

In order to avoid the high cost of generating numerous S-N curves, attempts have been made to identify the critical damage modes and to predict how they affect either the stiffness or strength. The key is how to relate the propagation of the various damage mechanisms to the laminate strength and/or stiffness degradation and then apply a suitable failure criterion. Two different phenomenological approaches are discussed in this section. The first, commonly known as Continuum Damage Mechanics uses a stiffness-based failure criterion. The second method, known as The Critical Element Method uses a strength-based failure criterion.

Continuum damage mechanics

Continuum damage mechanics (CDM) modeling [6, 7] assumes that individual damage modes, such as matrix cracking and debonding, can be identified and that their effect on the global behavior is characterized by a damage tensor. A combination of the damage tensors for the individual damage modes produces the global, "smeared" properties. This method relies on the accurate identification of the individual damage modes and the determination of a series of constants in defining the damage tensor [7]. The property most often used as the global damage metric is the stiffness of the laminate.

Stiffness or modulus degradation is a simple method that has been utilized as a basis to model fatigue life in composite materials [8-11]. It is relatively simple to evaluate the stiffness of a laminate non-destructively using strain gauges or an extensometer as opposed to residual strength-based failure theories that require destructive evaluation. In addition, two of the primary causes of stiffness degradation, transverse ply cracking and delamination, have been studied extensively and simple relationships have been developed linking the stiffness to the growth of damage [10]. The effects of the multiple damage modes are combined and implicitly included into the stiffness of the specimen as a single damage metric that contains the effects of all of the damage that is occurring.

A simple way of applying a stiffness degradation model [8, 10] is to define a damage variable, D, as follows:

$$D = 1 - \frac{E}{E_0} \tag{2.1}$$

where:

E = modulus of the material

E_0 = original, undamaged modulus

Failure is assumed to occur when D is equal to D_{cr}, some critical level of damage or critical stiffness when catastrophic failure occurs. Because the stiffness reduction of the laminate is related to the delamination growth, it can be related to the strain energy release rate and, hence, the applied stress, using a power law equation. This is convenient for calculating projected fatigue life. However, modeling of this type is largely based on experimental data. Changes in the laminate configuration require a recalibration of the model and identification of the damage modes. In addition, this type of model does not address the possibility of interaction between multiple damage modes or the effects of length scale.

The Critical Element Method

The Critical Element Method developed by Reifsnider, et al. [12-15] is based on identifying elements that are repeatable within a structure or volume of material and determining the stress and displacement fields within the element [7]. In addition, the damage patterns that arise in the element are also assumed to be repeatable within the structure. Critical elements are defined such that a failure of the element would indicate catastrophic failure of the structure. An example of a critical failure mechanism is fiber fracture. Sub-critical elements are those in which failure of the element causes a degradation in properties or a redistribution of stresses but does not directly cause catastrophic laminate failure. Fatigue loading of composites often leads to sub-critical failure modes such as delamination or transverse ply cracking. The evolution of the damage, in both critical and sub-critical elements, changes the stress state in the elements and eventually leads to failure.

The use of critical elements to model failure in composites relies on first accurately identifying the different damage modes and their effect on the life of the material and then defining a suitable element that captures all of the damage phenomena, but remains simple enough to analyze. The stress and displacement fields in the critical element must be accurately modeled in order to predict the failure. In fatigue loading, it is also necessary to be able to model the progression of damage at load levels lower than the critical load levels as well as to model the interaction of multiple damage modes propagating together.

The damage metric applied by Reifsnider et al. for determining fatigue life is the remaining strength [5, 12, 15-17]. The model relies on an assumption that fatigue cycling at different stress amplitudes will produce the same reduction in residual strength and, hence, the same damage state. For example, a structure is loaded at a stress amplitude of S_1 for N_1 cycles. The remaining life at a second stress amplitude, S_2, can be predicted by determining the number of cycles at S_2 necessary to reach the current residual strength due to the initial loading at S_1 and subtracting that from the total life for the second stress level. The difficulty with this method is that it requires a significant amount of experimental data in order to be able to determine the stress-life curves or an accurate model to predict the progression of damage during fatigue loading as well as final failure. It is, in effect, a generalized Miner's Rule method that attempts to capture the sequence effects that are often associated with multiple fatigue stress levels. It also assumes that the failure mechanisms are not dependent on the applied load or sequencing effects.

One of the benefits of the critical element method is that it has the potential to take into account the actual physical phenomena that determine the remaining strength. However, composite materials can be fabricated with many different lay-ups and configurations and the failure modes are usually not consistent from one configuration to another. The mechanics of failure observed in a laboratory on test coupons may not be relevant to the failure of a wing skin or fuselage panel because of different damage mechanisms and interaction between damage mechanisms that may exist at the different structural scales [4]. Small changes in processing and environment can also change the failure behavior of a material. This apparently prevents a unified theory that can be applied to all composite materials. Although the critical element method uses the micro-mechanical failure mechanisms in calculating the remaining strength, the damage is homogenized at a certain level and the actual mechanics of the growth and interaction of the various damage modes are not well represented.

2.1.2 Mechanism-based modeling

Composite modeling approaches have traditionally relied on empirical/phenomenological models that require a significant number of experiments for calibration. In addition, the experiments must be recalibrated when changes are made to the material configuration as the critical damage mechanism for one configuration may not be the same for another configuration. Length-scale is another important parameter. Failure mechanisms are often associated with a particular length-scale. For example, transverse ply cracking in composite laminates is strongly dependent on the thickness of the laminate [18, 19]. For this reason, results obtained from specimen-level experiments may not apply to structural level components.

Mechanism-based models attempt to define the failure modes in terms of the physical and/or chemical processes that contribute to the propagation of the failure mode. Recognizing that it may not always be possible to model the exact physics of the behavior, Ashby [20] states that: "...the aim [of mechanism-based models] is to establish a physical framework within which empirical descriptions of the behavior of some of the variables are embedded." The advantage of such models is that they can provide a predictive capability for the damage growth and can be applied to different material configurations without relying on empirical recalibration. However, it is likely that some experiments will always be necessary in the modeling process, both for identification of critical damage modes as well as validation of the models. One possibility for where analytic models can reduce the cost and time of material validation is during preliminary design studies. Often, critical choices (with high-cost implications) are made about material type and configuration during the early phases of a design. Models can be used during this phase to make relative comparisons between different material configurations. The use of mechanism-based models can also lead to procedures for accelerated testing of composites, which can reduce the number and length of high-cost environmental experiments.

An example of the procedures and processes for developing mechanism-based models is given in Reference [20]. Mechanism-based models have been applied to composites for damage that develops around notches [21-23]. The particular case of the development of fatigue damage around notches is discussed in Section 2.2.4.

Mechanism-based models have been successfully applied for individual damage modes growing within a composite laminate. An example is for metal matrix composites (MMC) modeling a matrix crack growing perpendicular to the fibers in a unidirectional SiC/Ti laminate [24, 25]. The method consists of a bridged-crack model to calculate the effective stress intensity factor at the crack tip along with the Paris' Law relationship for the monolithic matrix material to predict the crack growth. The bridging tractions were determined from the experimentally obtained properties of the matrix-fiber interface. Using the data from the individual mechanisms, i.e. the monolithic matrix fatigue behavior and the fiber/matrix interface behavior, an accurate prediction was made for the fatigue behavior of the composite.

A predictive model is the goal for fatigue life of composites, however it has to be built up from smaller components. The models for delamination growth coupled with a facesheet crack presented later in this work are similar in approach to the model developed for SiC/Ti composites. The properties of the individual damage modes are measured using independent experiments and then combined to form a model of multiple, interacting damage models.

2.1.3 Summary

The modeling approaches discussed each have strong and weak points. The critical element method has the potential to take into account the physical mechanisms causing failure, however the issue of multiple interacting damage modes is not adequately addressed. In addition, developing the remaining life curves used in the model requires extensive experimental programs. The CDM approach generally uses stiffness to model life, which is easy to monitor experimentally, but does not consider the growth and interaction of the individual damage modes.

Both of these model types seem to strive for a fully predictive model that can estimate life based on past observation of basic damage modes. However, experimental observation is an important component in modeling the fatigue life of composites. The seemingly infinite number of combinations of fiber and matrix choices combined with different lay-ups, ply-thicknesses, and loading conditions can produce numerous distinct damage sequences. The only way to capture the damage sequence accurately is to conduct experiments. Even then, the experimental results do not always lead to an accurate picture of the damage sequence. The experimental observations can be incorporated into mechanism-based models that are representative of the observed damage modes. A key step in developing a model is identifying the most efficient, in terms of both time and cost, experimental program that accurately captures the critical damage features.

Other issues such as specimen size and loading configuration may affect the predictions in the fatigue crack growth models discussed in this section. Often, the damage modes that dominate at the coupon level do not dominate at a structural level. Coupon level experiments and models are the easiest and most cost-effective to develop, but caution needs to be exercised when using the results for structural design. Potentially, the models discussed above can be applied in the material selection process to compare different materials and configurations. It is also important to note that the models discussed above have been demonstrated primarily for uniaxial loading conditions while actual in-service conditions are generally biaxial in nature. Therefore, the damage state is likely to be different than the uniaxial case.

2.2 Fatigue Damage and Modeling in Laminated Composites

One of the benefits of using composite materials in structural applications is the potential for a fatigue-resistant material because the fibers generally perform well under fatigue loading. However, due to the non-homogeneous, laminated nature of composite materials, a complex damage state also arises under fatigue loading. Examples of fatigue damage mechanisms include off-axis ply cracking, delamination between layers, splitting in the longitudinal direction, and fiber failure. While these damage modes do not always cause a reduction in residual strength, especially in laminates with plies predominately aligned with the load, they can affect the laminate stiffness and increase exposure to the environment. In the process of developing models for fatigue damage in TiGr laminates, many damage models were reviewed. This section outlines the key fatigue damage modes observed in composite laminates. Particular attention is focused on those damage modes, such as delamination and bridged-crack growth, that are important to the modeling conducted in this thesis. Summaries of the other damage modes are included for completeness with references to more detailed analyses.

2.2.1 Delamination

Delamination between plies is a critical damage mode for composite materials. Delamination can initiate for a variety of reasons including manufacturing flaws, impact damage, around structural details such as free edges or holes, fatigue loading, or combinations of these factors. As a result of delamination, failure may occur at stresses lower than the ultimate failure stress, the stiffness of the laminate may be reduced, and the fatigue life of the structure can be affected.

Modeling of composite delamination is typically based on either a fracture mechanics approach or a strength of materials approach. The fracture mechanics approach specifies that delamination will grow under monotonically increasing load when the sum of the internal strain energy and the applied work is greater than the energy required to create new fracture surfaces. The strength of materials approach specifies delamination propagation when the interlaminar stresses exceed the fracture strength of the material in the interply layer. Often it is a combination of interlaminar shear and normal stresses which lead to failure and a multi-axial failure criterion is applied. The goal of this section is to review the important aspects of delamination growth in order to provide a basis for the models developed for TiGr.

Fracture mechanics approach

The fracture mechanics approach for modeling delamination in composite materials is based on work by Griffith and Irwin for cracks growing in isotropic materials as referenced by Anderson [26]. The strain energy release rate, G, is the energy available for an increment of crack extension. It is defined as the derivative with respect to crack extension area, A, of the potential energy in the system, Π, where Π is the difference between the amount of work done, W, and the amount of stored strain energy, U, for a small area of crack extension, δA:

$$G = \frac{\delta(W - U)}{\delta A} \tag{2.2}$$

When the strain energy release rate (SERR) reaches some critical value, G_c, the crack will propagate. This type of analysis assumes that a flaw exists in the material and that exceeding the critical strain energy value will cause the flaw to extend. Irwin introduced the concept of the stress intensity factor, which describes the stresses and displacements in the area around a crack tip with a single variable. For a linear-elastic, isotropic material, the stress intensity factor, K, is related to the strain energy release rate via:

$$G = \frac{K^2}{E'} \tag{2.3}$$

where:

K = Stress intensity factor

E = Effective Young's Modulus ($E' = E$ for plane stress, $E' = \frac{E}{1-\nu^2}$ for plane strain)

The concept of the stress intensity factor is applied to fatigue via Paris' Law, which states that the crack growth rate is a power law function of the applied stress intensity factor (Equation 2.4) [27]. A strain energy release rate can be related to a crack growth rate for linear-elastic materials by inserting Equation 2.3 into Equation 2.4 and noting that $\Delta G = \frac{K_{max}^2 - K_{min}^2}{E'}$.

$$\frac{da}{dN} = A(\Delta K)^m \tag{2.4}$$

where:

$\frac{da}{dN}$ = crack growth rate

ΔK = applied stress intensity factor

A, m = material or laminate constants obtained experimentally

Early work utilizing fracture mechanics to model delamination growth in composites was conducted by O'Brien [28] for delamination growing from a free edge. Figure 2-1 shows a schematic of a specimen with an edge delamination. An analytical expression, Equation 2.5, was derived to evaluate the strain energy release rate for a laminate with edge delaminations.

$$G = \frac{\epsilon^2 t}{2}(E_{lam} - E^*) \tag{2.5}$$

where:

ϵ = applied strain

t = laminate thickness

E_{lam} = Young's Modulus of undamaged laminate

E^* = Young's Modulus of completely delaminated laminate

The value for E^* is calculated using the rule of mixtures for the case where the critical interfaces were completely delaminated. The Young's Modulus is calculated using Classical Laminated Plate Theory (CLPT). The strain energy release rate in Equation 2.5 represents the total strain energy release rate and has no dependence on the fracture mode.

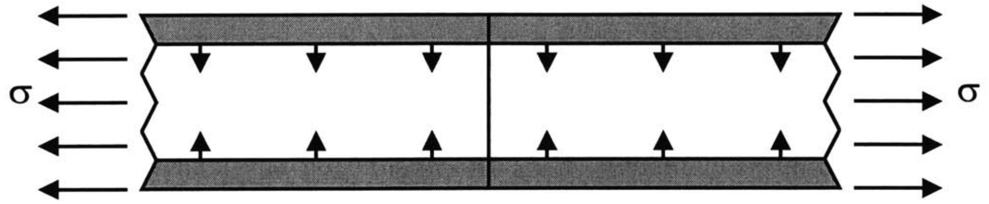

Figure 2-1: Schematic of edge delamination

O'Brien's procedure for calculating delamination growth relied on an accurate method for calculating the stresses at the free edges to determine the appropriate location for delamination onset. However, once the delamination extends beyond a certain length, generally on the order of the laminate thickness, the strain energy release rate becomes independent of the delamination length. This points out one of the weaknesses of a strain energy approach as compared to the strength of materials approach discussed below. There is not a robust way for predicting the location and initiation of delamination using the strain energy release rate. Application of the fracture mechanics approach assumes that the initiation phase of the delamination is short compared to the growth of the delamination to a critical size. If that is the case, then the strain energy release rate can be effectively applied for modeling the delamination behavior. Additional work was conducted describing the effects of matrix cracking on the propagation of edge delaminations [29].

The work was also extended to discuss the fatigue delamination growth rate which was characterized as a power law function of the applied strain energy release rate, similar to the Paris' Law function discussed above. The delamination growth rate was also found to have a linear relationship with the stiffness reduction rate in the laminate. Trethewey et al. [30] also showed that delamination growth obeys a power law function of the applied strain energy release rate.

A number of numerical methods have been formulated to calculate the strain energy release rate for delaminations. The Virtual Crack Closure Technique (VCCT) [31-34] uses a finite element model to calculate the stresses ahead of the crack tip and the displacements behind the crack tip to formulate the value of the strain energy release rate. One benefit of the VCCT and related methods is the ability to calculate the various modes of the strain energy release rate relatively easily for simple configurations. Yang and He [35] developed a finite element procedure to calculate efficiently both the interlaminar stresses and the strain energy release rate (using a modified crack closure technique).

Davidson [36] developed a crack tip element approach for determining the strain energy release rate in delaminated elements. By first considering the stress distribution derived using CLPT for an uncracked laminated and superimposing it with the resultant forces and moments that arise in a cracked laminate, the strain energy release rate can be determined. This procedure can be easily modified to include the effects of thermal residual stresses and moisture ingress in determining the strain energy release rate [37, 38].

Another method commonly used to calculate the strain energy release rate numerically is the J-integral [39, 40]. Finite element models are used to evaluate a closed surface integral around the crack tip:

$$J = G = \int_{\Gamma} \left(W\, dy - \sigma_{if} \frac{\delta u_i}{\delta x}\, ds \right) \tag{2.6}$$

where:

Γ = arbitrary surface around the crack tip

W = strain energy density

x = crack propagation direction

dy = increment of length normal to crack propagation direction

σ_{if} = stress vector

u = displacement vector

ds = increment of length along surface

For a linear elastic material, J is equivalent to the strain energy release rate, G. The J-integral determines the total strain energy release rate. In order to determine the mode-mixture of the crack growth, a decomposition method is necessary.

An extension of the J-integral method has been derived to calculate the strain energy release rate for steady-state delamination growth [41-44]. The "strip" method, or "cut and paste" method calculates the strain energy in a section of length, Δa, far ahead of the delamination front and far behind the delamination front using:

$$G = \frac{1}{2} \int (\vec{\sigma} \cdot \vec{\epsilon})\, dt \tag{2.7}$$

The difference between the two calculations is the amount of strain energy available to extend the crack. If the energy available is higher than the energy required to grow the crack, the crack will grow. This is equivalent to taking the uncracked strip and pasting it in the cracked region, thereby extending the crack by Δa as shown in Figure 2-2.

The strip method provides a relatively easy method for calculating the strain energy

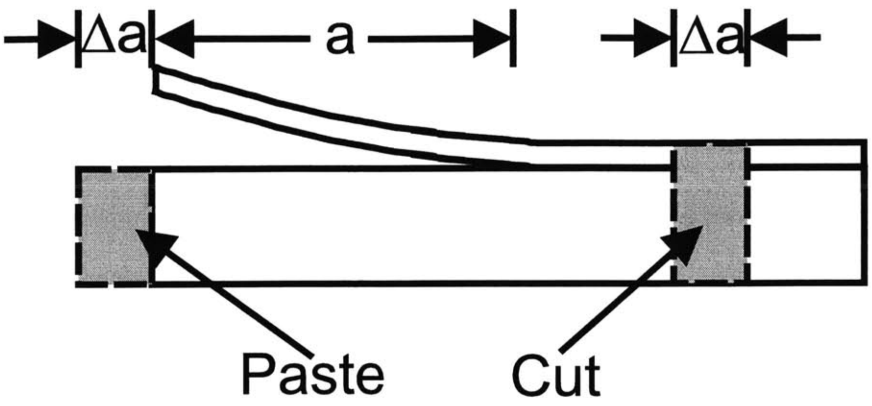

Figure 2-2: Schematic of the strip method

release rate for a specific configuration. However, it is limited to cases with simple delaminations that grow in a self-similar manner, such as the delamination growth from seams observed in TiGr laminates. In addition, it only provides the total strain energy release rate and not the mode mixture of the configuration.

A two-dimensional approximation for the strain energy release rate can be derived from the definition of G given in Equation 2.2 [26]. For the fixed displacement case, the work done by external forces, W, is zero, which gives,

$$G = -\left(\frac{dU}{dA}\right)_{\Delta} \tag{2.8}$$

and since,

$$U = \int_0^{\Delta} P d\Delta = \frac{P\Delta}{2} \tag{2.9}$$

G can be written as,

$$G = -\frac{\Delta}{2}\left(\frac{dP}{dA}\right)_{\Delta} \tag{2.10}$$

The compliance of the specimen is defined as:

$$C = \frac{\Delta}{P} \tag{2.11}$$

where:

Δ = displacement

P = applied load

Taking the derivative with respect to the Area, A, and inserting that expression into Equation 2.10, an analytic expression for G as a function of the rate of change of compliance with respect to A is:

$$G = \frac{P^2}{2}\left(\frac{dC}{dA}\right) \tag{2.12}$$

The compliance method described above is a simple method for calculating the strain energy release rate for delamination propagation. A simple quasi-3D finite element approach can be constructed using two layers of elements and systematically increasing the delamination length by releasing the delaminated nodes between the layers to obtain the compliance as a function of delamination area [45]. This can then be inserted into Equation 2.12 in order to calculate the strain energy release rate for that configuration. This type of model is easy to implement because it applies the global compliance and avoids a well-refined mesh around the crack tip. However, it can only be applied for self-similar delamination growth and does not account for thermal or other self-equilibrating stresses. In order to calculate the exact profile at each point along a delamination front or to determine the dependence on fracture mode-mixture, a full 3D model using a method such as the J-integral or VCCT calculation would be necessary.

The criterion for growth of delaminations using the strain energy release rate method is widely researched and many different approaches have been used to predict failure. The first assumes that a total strain energy release rate reaches a critical value with no dependence on fracture mode:

$$G_{total} \geq G_c \tag{2.13}$$

This technique was applied by O'Brien [28] and works best for cases where G_{Ic}=G_{IIc}. The second criterion specifies that the delamination propagates if one of the three components of strain energy release rate (mode I, mode II, or mode III) reaches the critical value associated with that mode:

$$\begin{aligned} G_I \geq G_{Ic} \quad & or \\ G_{II} \geq G_{IIc} \quad & or \\ G_{III} \geq G_{IIIc} & \end{aligned} \tag{2.14}$$

The third criterion specifies the interaction of the three modes:

$$\left(\frac{G_I}{G_{Ic}}\right)^m + \left(\frac{G_{II}}{G_{IIc}}\right)^n + \left(\frac{G_{III}}{G_{IIIc}}\right)^p = 1 \tag{2.15}$$

Many researchers have attempted to define a suitable mixed-mode failure criterion [46-48]. A summary of the research conducted on the interaction of damage modes can be found in [49]. Donaldson [48] compared different proposals for applying Equation 2.15 for interacting damage modes and found that no one method worked for all cases of mode-mixture and material types. Often empirical fits are conducted to find the value of the constants, m, n, and p in Equation 2.15 [47]. However empirically fit curves are not generally applicable to multiple materials and configurations. In addition, the use of a mixed-mode failure criterion assumes the ability to calculate the various modes of delamination. Methods such as the virtual crack closure technique have the ability to differentiate the modes and research has been conducted to analytically determine the mode-mixture for layered materials [50].

Strength of materials approach

The strength of materials approach for modeling delamination assumes that delamination will initiate when the interlaminar stresses exceed the strength of the interlaminar layer between the plies. An interlaminar stress field arises at material discontinuities such as a free edge, an open hole, or a bonded joint and other areas where a gradient in the in-plane stress field exists. Classical laminated plate theory (CLPT) does not account for interlaminar stresses.

Various techniques have been applied to determine the interlaminar stress state of a laminate near a free edge, including finite difference methods [51], finite element methods [35], and an analytical method known as the force-balance method [52]. A method for determining the interlaminar stresses around a hole has also been developed [53]. The force-balance method stems from the break down of CLPT at the free edge. A stress gradient must exist in order to achieve the zero-stress boundary condition at the free edge. The force-balance method applies the equilibrium equations for the forces and moments with the free edge boundary conditions applied to calculate the interlaminar stress state. The Quadratic Stress Criterion was developed by Brewer and Lagace [54] to predict the delamination initiation for graphite/epoxy laminates using stress fields derived using the force balance method or any other techniques. It can be applied to cope with the multi-axial stress state, and is somewhat analogous to Equation 2.15 in that it accounts for the directional components of the stress field independently. In order to apply the Quadratic Stress Criterion, the stress fields are averaged over some characteristic distance, which is determined experimentally [54].

Interlaminar stress calculation provides a simple way to predict the initiation of delamination. This is very useful for locating the critical interfaces and the primary location for delamination initiation. However, the strength of materials approach has not yielded a viable method for studying delamination growth. In order to develop a working model for a combination of damage modes growing together in fatigue, a fracture mechanics approach to delamination growth has been applied in this research.

2.2.2 Transverse ply cracks

Transverse ply cracking has been widely studied [55-60]. Transverse ply cracks do not generally cause final catastrophic failure of the laminate, however multiple cracks cause a reduction in the stiffness of the laminate and allow the external environment to degrade the laminate further. TPC's can also act as initiation points for other damage modes and act in conjunction with other damage modes such as delamination to degrade further the laminate properties [61, 62].

Since transverse ply cracks do not generally cause laminate failure, it is important to look at how they can interact with the rest of the laminate. One-dimensional shear lag models [55] have been applied in order to model the stress redistribution around the crack. Some characteristic distance away from the crack, the stress in the transverse ply builds up to a value that exceeds the strength of the material, and causes additional cracks to form and propagate. Models have been proposed to predict the stiffness reduction associated with the formation of multiple transverse ply cracks [59, 60, 63].

A model was developed by Nairn [58] to determine the strain energy release rate for tunneling cracks in off-axis plies. Nairn applies a variational approach to calculate the thermoelastic stress state in a cross-ply laminate with constrained layer cracks. The stress state is used to calculate the strain energy release rate due to the propagation of micro-cracks in the constrained layer. For the situation of a crack growing in the outer ply of a cross-ply laminate, (see Figure 2-3) the strain energy release rate is:

$$G = \left(\sigma_0^2 \frac{E_T^2}{E_0^2} + \frac{\Delta\alpha^2 T^2}{C_1^2} \right) t_1 C_3 \left[2\chi\left(\frac{\rho}{2}\right) - \chi(\rho) \right] \tag{2.16}$$

if $\frac{4q}{p^2} > 1$:

$$\begin{aligned} \chi(\rho) &= 2\alpha\beta\left(\alpha^2+\beta^2\right)\frac{\cosh 2\alpha\rho - \cos 2\beta\rho}{\beta\,\sinh 2\alpha\rho - \alpha\,\sin 2\beta\rho} \\ \alpha &= q^{\frac{1}{4}}\cos\frac{\theta}{2} \\ \beta &= q^{\frac{1}{4}}\sin\frac{\theta}{2} \\ \tan\theta &= \sqrt{\frac{4q}{p^2}-1} \end{aligned} \tag{2.17}$$

if $\frac{4q}{p^2} < 1$:

$$\begin{aligned} \chi(\rho) &= \alpha\beta\left(\beta^2-\alpha^2\right)\frac{\tanh\beta\rho\,\tanh\alpha\rho}{\beta\,\tanh\beta\rho - \alpha\,\tanh\alpha\rho} \\ \alpha &= \sqrt{\frac{-p}{2}+\sqrt{\frac{p^2}{4}-q}} \\ \beta &= \sqrt{\frac{-p}{2}-\sqrt{\frac{p^2}{4}-q}} \end{aligned} \tag{2.18}$$

where p and q are defined as:

$$p = \frac{C_2 - C_4}{C_3} \tag{2.19}$$

$$q = \frac{C_1}{C_3} \tag{2.20}$$

and the constants C_1, C_2, C_3, C_4 are:

$$C_1 = \frac{h\,E_0}{t_2\,E_A\,E_T} \tag{2.21a}$$

$$C_2 = \frac{\nu_A}{E_A}\left(\frac{2}{3}\lambda + 1\right) - \frac{\nu_T}{3E_T} \tag{2.21b}$$

$$C_3 = \frac{\lambda + 1}{60E_T}\left(3 + 12\lambda + 8\lambda^2\right) \tag{2.21c}$$

$$C_4 = \frac{1}{3}\left(\frac{1}{G_T} + \frac{1}{G_A}\right) \tag{2.21d}$$

$$\lambda = \frac{t_2}{t_1} \tag{2.21e}$$

where:

t_2, t_1, h = as defined in Figure 2-3

E_0 = Young's modulus of undamaged laminate

E_T,E_A = Young's modulus of cracked and uncracked layer, respectively

G_T,G_a = Shear modulus of cracked layer and uncracked layer, respectively

ν_T,ν_A = Poisson's ratio of cracked and uncracked layer, respectively

$\Delta\alpha$ = difference in coefficient of thermal expansion between cracked and uncracked layer

T = temperature change from stress-free state

Equation 2.16 exhibits a linear dependence on the thickness of the cracking play and has a strong dependence on both the applied stress and the thermal stresses. The dependence on the ply thickness is in agreement with the observation that thicker ply groups tend to crack more readily. The model captured the experimental results well for predicting the crack density as a function of applied stress for cross-ply composite laminates.

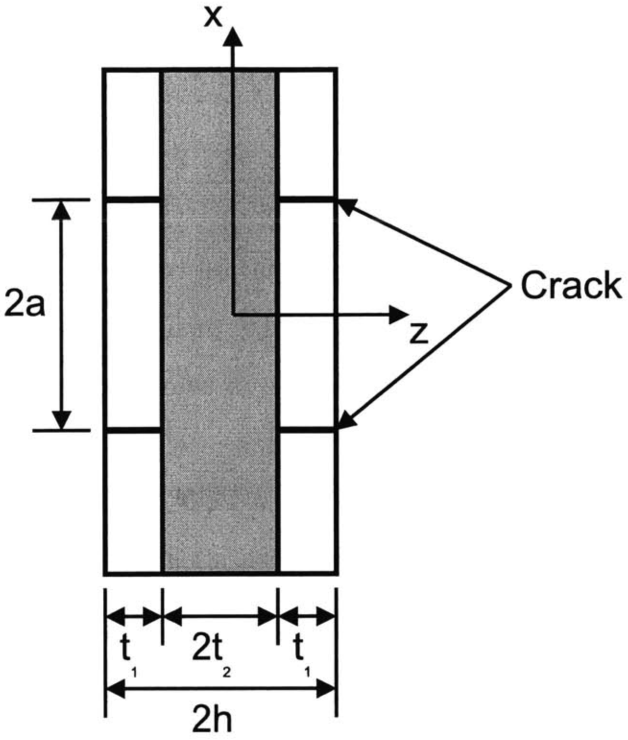

Figure 2-3: Schematic of configuration for transverse ply crack model

2.2.3 Fatigue fiber failure

Fiber failure under fatigue loading was not observed as a critical damage mode in the TiGr laminates studied in this thesis. However, a brief section on fatigue failure of fibers in composite laminates is included here for completeness.

Fiber failure under static loading is controlled by the distribution of defects along the fiber, and can be described statistically [64]. Under fatigue loading, fiber failure is still controlled by statistics, however other conditions can arise to contribute to fiber fracture. The presence of transverse ply cracks in adjacent plies has been shown to cause fiber failure in the load-bearing 0° plies [65, 66]. The accumulation of a significant number of fiber fractures leads to catastrophic laminate failure. However, it is possible for the same fiber to fracture in numerous locations because the stresses can redistribute around a fracture location. Fibers can also fail under compressive cyclic loading. Under compressive loading, the reduced laminate stiffness due to the accumulation of damage can lead to fiber buckling. Localized micro-buckling and kink-bands under compressive loading can lead to laminate failure. A review of previous research on micro-buckling, kinking and other compressive failure mechanisms can be found in [67].

2.2.4 Damage around notches

Notches are a prime location for the nucleation of both in-plane and out-of plane damage in composite materials. The damage modes include transverse ply cracking, longitudinal matrix splits, and delamination. Often, two or more damage modes interact to form a more complex damage state.

Longitudinal matrix splits generally form in 0° plies tangential to the hole or notch and run parallel to the loading direction in both static and fatigue loading configurations [21, 22, 68]. Splits can also form in slightly off-axis plies. The problem of a split forming in 15° plies at free edges in [40]. The splits often act to blunt out the effect of the notch and thereby reduce the stress intensity factor at the notch tip. This results in an increase in the residual tensile strength as the number of cycles, and therefore the split length, increases [69]. However, the splits also provide an initiation location for delamination and transverse ply cracks which act to reduce the laminate stiffness [70].

The key point to recognize for damage around notches is that the damage modes often interact with one another making modeling and prediction a difficult task. Kortschot et al. [71, 72] and Spearing et al. [22, 23] modeled the growth of the splits with an associated delamination after determining the damage mechanisms through experimental observation.

2.2.5 Modeling of bridged cracks

The phenomenon of crack-toughening can arise from a variety of physical characteristics such as plasticity, material non-uniformity, and unbroken fibers and/or particles in the wake of the crack tip. The global result of the toughening is a reduction in the effective stress intensity factor at the crack tip, which reduces the crack growth rate in the material. The toughening mechanism is typically modeled either as a bridging zone exerting a traction on the flanks of the crack behind the tip or as a damage zone ahead of the crack tip toughening the material ahead of the crack. Thouless [73] presents a discussion of the difference between the two methods and shows that both types of models produce the same results.

This discussion will focus mainly on the application of bridged crack models since that is most analogous to the facesheet crack growth behavior observed in TiGr. The effects of the damage mechanisms are lumped into a bridging traction that acts on the crack flanks behind the tip to close the crack. For linear elastic problems, modeling the effects of the damage as a bridging traction and applying superposition makes the calculation of the effective stress intensity amplitude, ΔK_{eff}, at the crack tip a tractable problem using superposition:

$$\Delta K_{eff} = \Delta K_{appl} + \Delta K_{br} \tag{2.22}$$

where:

ΔK_{appl} = applied stress intensity amplitude

ΔK_{br} = stress intensity amplitude due to bridging

Many resources, such as Tada [74], provide solutions for the stress intensity factors of various loading and specimen geometrics, from which the stress intensity due to the applied load, K_{appl}, and that due to the bridging, K_{br}, can be calculated.

An example of a bridging traction model was proposed by Dugdale (as described in [26]) for plastic zone modeling for an infinite metal plate with a through-thickness crack (also known as a strip yield model). The through-thickness crack of length $2a$ is assumed to have an unknown plastic zone size of length ρ at each crack tip (Figure 2-4).

The model assumes that the crack is artificially extended to the end of this region and a constant bridging traction with a magnitude equal to the yield stress, σ_y, was applied over the length, ρ. The size of the bridging zone can be calculated by assuming that the effective stress intensity factor at each crack tip of the artificial crack (length $2a + 2\rho$) is equal to zero, i.e.:

$$K_{appl} + K_{br} = 0 \tag{2.23}$$

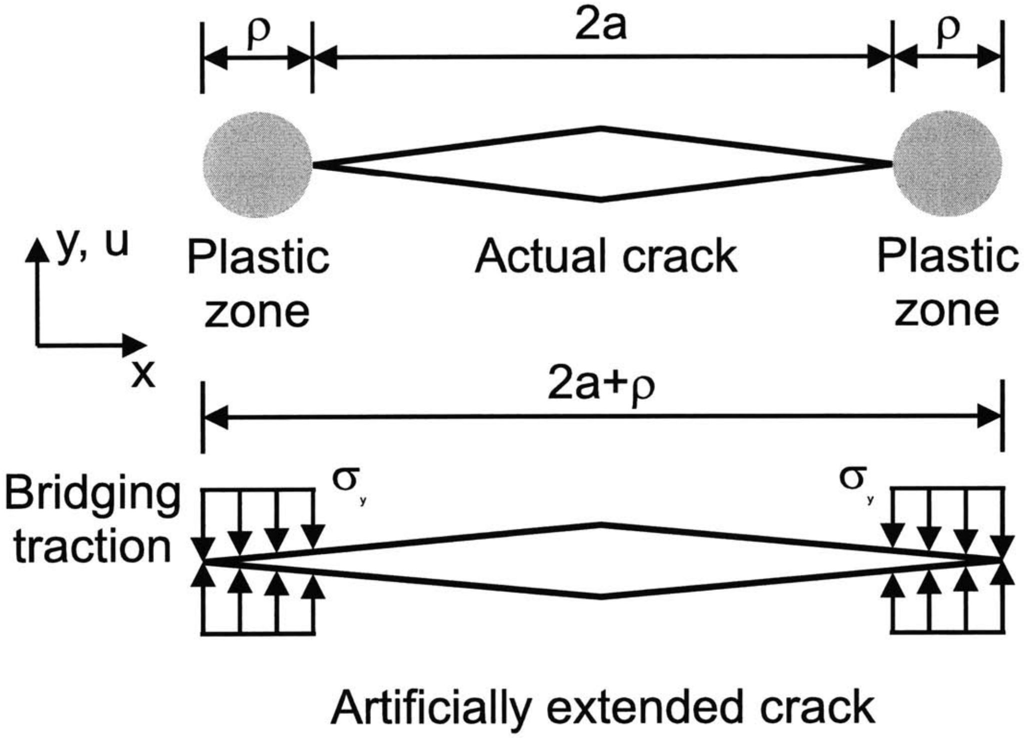

Figure 2-4: A schematic of an isotropic plate with a crack under uniaxial tension for the Dugdale plastic model

Using expressions from Tada [74] for the stress intensity factor due to the bridging and due to the applied load, a relationship for the bridging zone size can be written as:

$$\frac{a}{a+\rho} = cos\left(\frac{\pi\sigma}{2\sigma_y}\right) \tag{2.24}$$

Techniques for solving Equation 2.24 can be found in [26].

A Dugdale-type model can also be applied to cases with physical bridging mechanisms, such as TiGr, where intact plies and/or fibers continue to transfer load around the cracked region and shield the crack tip. In this type of model, the bridged portion of the crack is equivalent to the artificial crack in the Dugdale model. The bridging mechanism exerts a closing force on the crack front with a magnitude determined by the crack opening displacement and the bridging law. Three common types of bridging laws are shown in Figure 2-5, a constant bridging (similar to the Dugdale model), a linear-hardening law, and a linear-softening law. For the hardening and the softening behaviors, the crack opening, u, affects the bridging stress, σ. The hardening mechanism exerts a higher closing force further from the crack tip and the softening mechanism exerts a lower closing force further from the crack tip. Physically, the hardening behavior might be representative of linear-elastic springs or fibers bridging the crack faces. The softening mechanism is often used to describe a bridging mechanism controlled by frictional sliding and has been widely used in damage zone models for compressive failure of composites [75, 76].

As opposed to the Dugdale model, where the stress intensity factor at the artificial crack tip is assumed to be zero in order to calculate the yielding zone size (Equation 2.23), a bridged crack model assumes that the stress intensity factor at the crack tip, ΔK_{eff} is reduced due to the bridging:

$$K_{appl} + K_{br} = K_{eff} \tag{2.25}$$

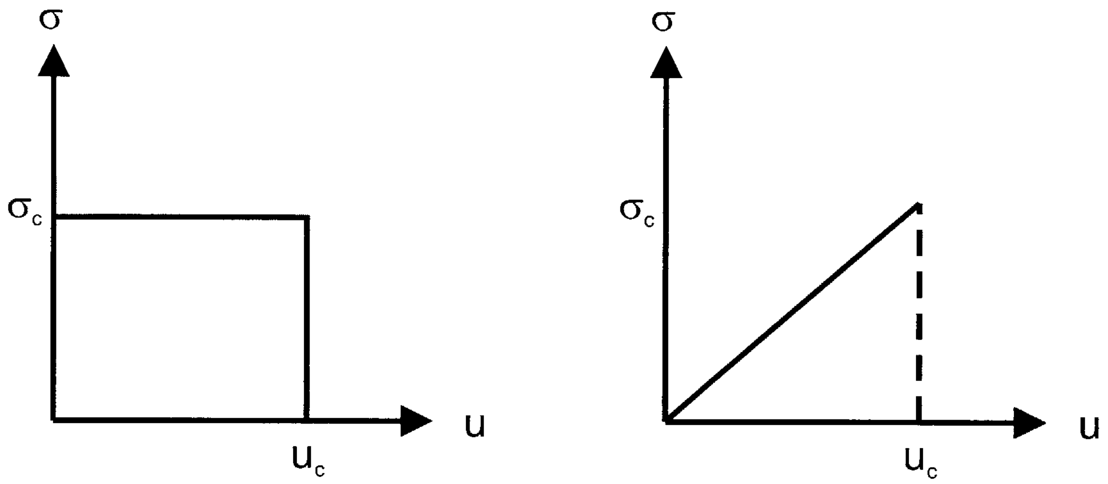

(a) Constant (b) Hardening

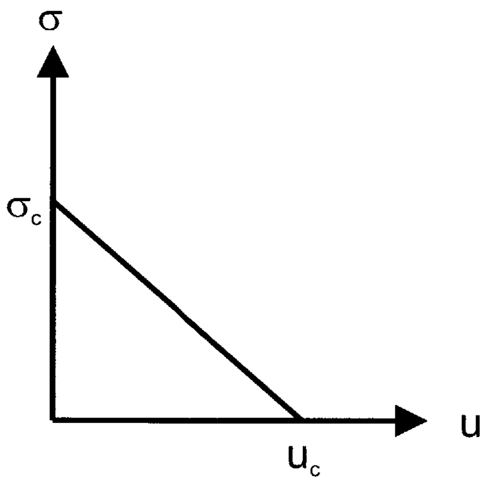

(c) Softening

Figure 2-5: Examples of bridging traction laws

Bridged-crack models have been successfully applied for matrix cracking in fiber reinforced ceramic matrix and metal matrix composites for static [77] and fatigue [24, 25, 78, 79] loading. For these materials, the matrix crack propagates perpendicularly to the fibers and leave intact fibers in their wake. The effective stress intensity factor is calculated from the applied load and the physical mechanisms of the bridging fibers. The effective stress intensity factor is input into the Paris' Law relationship for the monolithic matrix material to determine the crack growth rate. The models have been very successful at predicting the crack growth rate in the matrix.

2.3 Overview of Hybrid Laminates

Hybrid laminates combining metal and composite layers are a relatively new class of composite materials and were originally developed in the early 1980's at Delft University in The Netherlands. The original configuration, Aramid-Aluminum Laminates (ARALL), was developed to be a fatigue resistant material for aerospace applications. ARALL and the follow-on material Glass Fiber-Aluminum Reinforced Laminates (GLARE) are manufactured commercially by The Structural Laminates Company. In the early 1990's, The Boeing Company began developing TiGr to possess the same favorable fatigue properties as ARALL and GLARE as well as the high temperature capabilities necessary for future aerospace applications.

2.3.1 Fatigue of hybrid laminates

The application of ARALL in aerospace applications is mainly focused on areas such as the lower wing skin panels where its tension-dominated, fatigue resistant behavior can be most beneficial. ARALL laminates potentially provide 15-20% reduction in density as compared to aluminum and possess up to 60% higher tensile strength compared to Aluminum 2024 and 7075 with a comparable stiffness [80]. A prototype lower wing skin for the Fokker F-27 was tested successfully and provided a potential weight savings of 30% [81]. Fokker also tested an ARALL panel on the lower wing skin of the Fokker F-50 [2] and a redesigned cargo door on the C-17 military transport provided a 27% savings in weight over the original aluminum design.

Facesheet delamination has been studied for ARALL, GLARE, and Carbon fiber-reinforced laminates (CARALL) [82-84]. Experimental studies were conducted relating the facesheet crack growth rate to the applied strain energy release rate. Marissen [82] and Lin et. al [84] applied a Paris Law-type relationship to relate the strain energy release rate to the crack growth rate. Guo et al. [83] considered applied R-ratio effects and used a Walker-type equation to relate the strain energy release rate to the crack growth rate. Guo also developed a relationship between delamination size and compliance.

A major area of research on ARALL and GLARE laminates has been the study of the crack growth behavior in the aluminum plies. Cracks in the aluminum layers propagate while the underlying composite plies remain intact. The composite plies act as a bridging/shielding mechanism and reduce the effective stress intensity factor and hence, the crack growth rate of the aluminum plies. A schematic of the two damage modes is shown in Figure 2-6. It was found that the crack growth rate in the aluminum plies of ARALL-2 was up to three orders of magnitude lower than those in monolithic aluminum [85]. Other researchers have experimentally researched the crack growth rate in ARALL and GLARE laminates and demonstrated the superior fatigue properties over monolithic aluminum [86-89]. Absent from most of the discussions on facesheet crack growth rate in ARALL is the effect of the delamination on the crack growth rate and the shape of the delamination. In addition, since ARALL and GLARE were mainly intended for subsonic applications, the effect of temperature on the crack growth rate was not a factor in the above studies.

A number of researchers have proposed models for the crack growth behavior of hybrid laminates [89-92]. An empirical model by Toi [89] treats the crack growth in the aluminum ply as if it were growing in a homogeneous material and determines the crack growth rate as a function of the applied stress intensity amplitude, ΔK, for the configuration. An empirical knock-down factor, derived from the $\frac{da}{dN}$ vs. ΔK behavior of the aluminum, is applied to the apparent ΔK for the composite. The result is the relation between crack growth rate for the composite as a function of the applied cyclic strain energy release rate multiplied by the knock-down factor. While this model would be relatively easy for a design engineer to utilize,

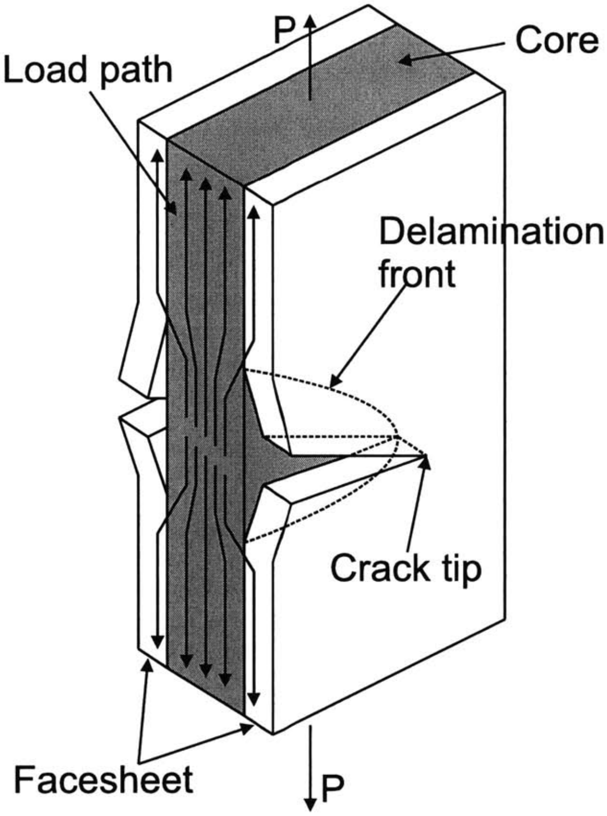

Figure 2-6: A schematic of facesheet crack and delamination in a fiber metal laminate

it relies on a significant amount of experimental data and calibration. A new knock-down factor would need to be determined for different material configurations. This method also assumes nothing about the role of delamination in the crack growth process.

The model by Marissen [90, 82] provides an analytical method for predicting facesheet crack growth in ARALL based on the damage characteristics of the constituent materials. Using the fatigue crack growth data for monolithic aluminum in the form of Equation 2.26 and the delamination growth data in the form of Equation 2.27 for the delamination of the aluminum ply from the composite, the author predicted the growth of the crack in the aluminum layer in center cracked tension specimens.

$$\frac{da}{dN} = A(\Delta K_{eff})^m \tag{2.26}$$

$$\frac{dD}{dN} = B(\Delta G)^n \tag{2.27}$$

where:

$\frac{da}{dN}$ = crack growth rate
$\frac{dD}{dN}$ = delamination growth rate
ΔK_{eff} = effective stress intensity factor
ΔG = strain energy release rate
A, B, m, n = material/laminate constants determined experimentally

The effective stress intensity amplitude, ΔK_{eff}, is the sum of the stress intensity amplitude due to the applied loading and the stress intensity amplitude due to the composite bridging effect (Equation 2.22). By assuming an elliptical delamination profile and calculating the bridging stress due to the delamination, an effective stress intensity factor, and hence a crack growth rate, can be calculated for the aluminum facesheets. An elliptical delamination profile results in a constant bridging stress along the crack front, which simplifies the calculations. However, Marissen's model makes no predictions regarding the delamination growth. The strain energy release rate for the delamination was calculated assuming a full width delamination and was not coupled with the crack growth. The prediction of the delamination growth rate and its extent is important for the calculation of stiffness reduction, which is one of the key failure modes for TiGr laminates as discussed below.

Recent work by Lin, Kao, et al. [84, 93-96] investigated a material similar to ARALL and GLARE composed of aluminum sheets bonded to a carbon-fiber composite core. The research consisted of experiments to observe the growth of cracks in the facesheets in single edge notch specimens to evaluate the effect of crack bridging due to the delamination. They utilized Marissen's model for ARALL facesheet crack growth to predict the delamination, including the assumption that the delamination profile was elliptical in order to simplify the calculations. However, in calculating the strain energy release rate for the delamination a constant, a rectangular shape was assumed as opposed to the full-width delamination assumed by Marissen.

Guo and Wu [91] developed a model similar to Marissen's using a linear delamination profile as opposed to the elliptical profile modeled by Marissen. Their experimental data showed a more linear profile and they integrated the bridging stress along the crack front in order to obtain the effective stress intensity factor at the crack tip. Guo and Wu also studied which factors affect the bridging stress distribution [97] and represented the effects of the damage mechanisms as an effective crack length [98]. Further work by Guo and Wu [99] recognized that the crack growth rate is constant for long cracks and they presented a phenomenological approach for determining an effective crack length for determining the crack tip stress intensity factor. The effective crack length was independent of the size and loading conditions on the specimen, however it was not independent of lay-up and it relies on experimental results to determine the effective crack length.

Both methods presented above for facesheet crack growth with delamination have their benefits. The assumption of an elliptical delamination front makes the model developed by Marissen computationally simple to implement, however if the delamination front is not elliptical, the model by Guo and Wu provides an analytic way to calculate the magnitude of the bridging stresses. Neither model was rigorous in the calculation of the strain energy release rate of the growing delamination. The exact shape of the delamination was not used in either model to calculate the strain energy release rate and no predictions were made on the growth behavior for the delamination. In addition, neither model included the effects of temperature on the damage growth behavior. Understanding the elevated temperature behavior of TiGr is essential if it is to be applied on projects such as the high speed civil transport.

2.3.2 Titanium-Graphite Laminates

Research on the first generation of fiber metal laminates, i.e. ARALL and GLARE, has provided insight into the factors affecting their potential uses for structural applications. In order to utilize the benefits of hybrid laminate for use in higher temperature structures, such as the proposed High Speed Civil Transport (HSCT), The Boeing Company developed TiGr.

In work similar to that done on ARALL and GLARE, Miller et al. determined that the crack growth rate in titanium facesheets was lower than that of monolithic titanium [100]. Their work also studied the bond quality and the effects of temperature on the performance of titanium graphite laminates. Additional research was conducted by Li and Johnson [1, 101, 102]. It was found that Ti-15-3-3-3 had better monolithic fatigue properties than Timetal-21S, but both performed similarly as part of a TiGr laminate. Multiple cracks formed in the titanium layers during the fatigue tests due to the bridging of the cracks by the composite fibers. When a crack formed, stress was transferred to the underlying fibers via interlaminar stresses. This bridging allowed multiple cracks to grow and propagate in the titanium layers.

Parametric studies were conducted by Johnson, et al. to study the effects of varying the laminate stacking sequence, fiber volume fraction, the choice of fiber type, and the percentage of titanium in the lay-up [87]. They concluded that one of the key points in designing a hybrid laminate is to ensure the PMC core has a higher modulus than the facesheets in order to take advantage of the superior strength and stiffness properties of the PMC. Otherwise, the drawbacks in using a complex material system such as a hybrid laminate may outweigh the benefits. They commented that parametric studies are useful, but more testing is needed.

The high temperature fatigue behavior was investigated for specimens containing open holes [3, 103]. The primary failure mechanisms for these experiments was a reduction in laminate stiffness. Figure 2-7 shows the reduction of stiffness as a function of cycles for multiple maximum stress levels, expressed as percentages of the open hole tension strength (OHT). The static open hole tension strength of the laminates was approximately 1000 MPa. The experiments were conducted at 177° C at an R-ratio of -0.2.

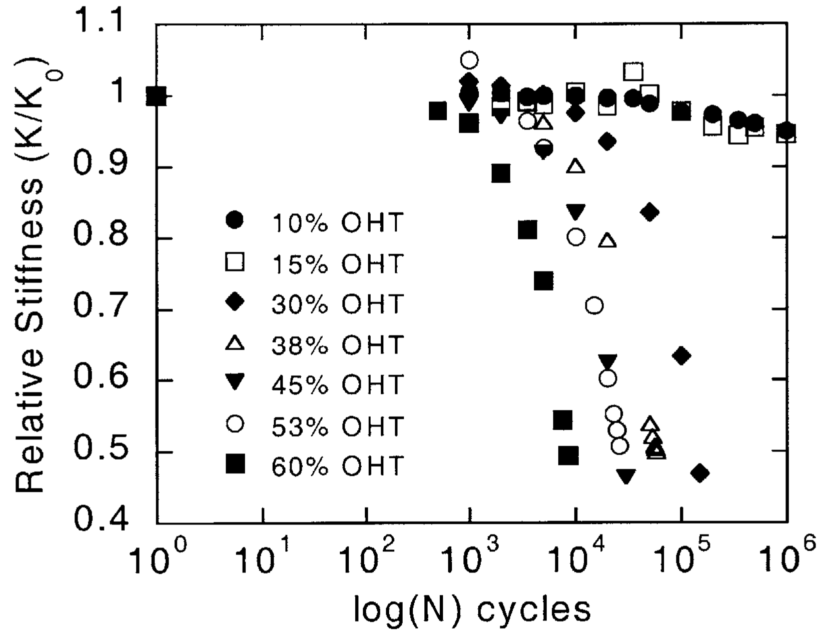

Figure 2-7: Stiffness reduction in a TiGr laminate with an open hole as a function of cycles for different maximum tensile stress levels [3]

Delamination was identified as the key damage mode for stiffness reduction during fatigue cycling. In addition, elevated temperatures increased the rate of stiffness reduction for TiGr laminates as shown in Figure 2-8. Delamination initiated in the wake of cracks in the titanium facesheets as well as at free edges. The combination of facesheet cracking and the delamination in the crack wake is an example of combined damage growth. This combination is important for two principal reasons. Firstly, the titanium facesheet cracks are visible externally and can be identified during inspections. Secondly, the delamination reduces the laminate stiffness. Stiffness reduction was identified as a potential damage metric, and is particularly important if there is any compressive component to the load cycle. The damage modeling in this thesis will focus on the coupled growth of these two damage modes at both room temperature and elevated temperatures.

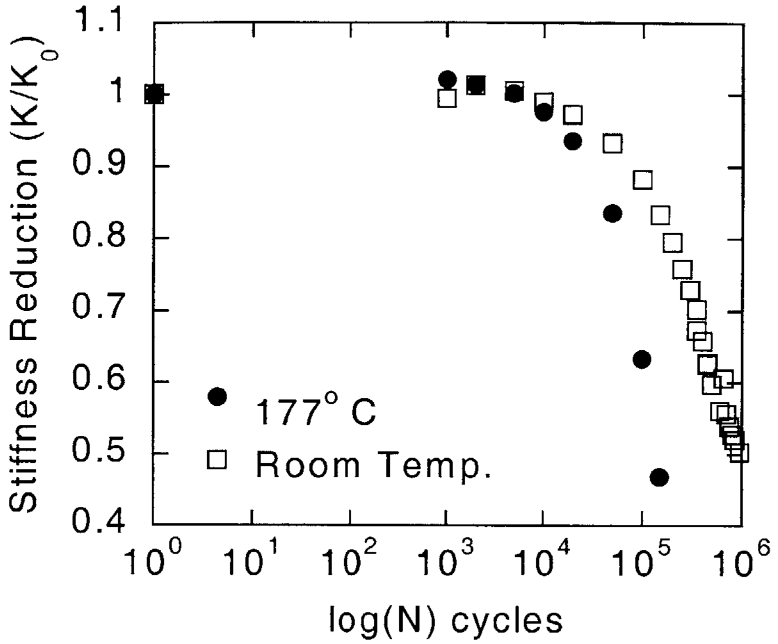

Figure 2-8: Dependence of stiffness reduction on temperature for open hole specimens, σ_{max}=302 MPa, R=-0.2 [3]

2.4 Summary

A vast amount of literature exists for modeling the fatigue life of composites and the many damage modes present in composite laminates. This chapter has attempted to provide an overview of the critical damage modes present in fatigue damage of TiGr laminates and how they have been modeled in non-hybrid composites. In addition, a summary of the previous work conducted on the TiGr predecessors, ARALL and GLARE, has been provided. Many of the damage characteristics observed in ARALL and GLARE are also evident in TiGr and models have been developed to describe the behavior. Based on the results in the literature, delamination does not seem to be a critical issue for ARALL and GLARE and the effects of different temperatures on the failure modes has not been investigated. Much of the work published on TiGr laminates thus far has been on evaluating the performance of the interface and evaluating the best choices for the constituent materials.

2.5 Thesis approach

The objectives of this thesis, as stated in Chapter 1, are to identify and model the critical damage modes in TiGr laminates and to evaluate the validity and potential applications for the modeling techniques. The focus of the modeling effort will be on the coupled damage growth of facesheet cracks and an associated delamination. An outline of the key steps in modeling the coupled damage growth are shown in Figure 2-9. The first step in modeling the coupled damage growth is to study the damage modes independently. Studies were conducted at Boeing on the crack growth behavior of monolithic titanium. The behavior of facesheet delamination growth is studied as part of this thesis and the results are presented in Chapter 4. The results of the studies on the two independent damage modes are inputs into the bridged-crack model presented in Chapter 5. The bridged-crack model is based on the previous research on hybrid laminates discussed herein. A three-dimensional finite element model is developed to evaluate the effectiveness of the bridged-crack model. The modeling results are validated with facesheet crack growth experiments and related to previous work via a stiffness degradation model. In conducting this research, the following questions are addressed:

- How well can a bridged-crack model be applied to predict the growth of the coupled facesheet crack and delamination growth in TiGr laminates?
- If the bridged-crack model is not effective at predicting the facesheet crack growth, what parameters prevent the model from effectively predicting the damage growth?
- For new continuous-fiber, laminated composite material systems, what damage modes and geometric parameters need to be considered when applying damage growth models?
- With regard to TiGr laminates, what controls the growth of key damage mechanisms?
- How can the lessons learned through this research be applied to structures designed with TiGr?

- Can the results from the model developed to predict fatigue damage growth in single edge notch specimens be applied to predict the stiffness reduction in TiGr laminates with open hole?

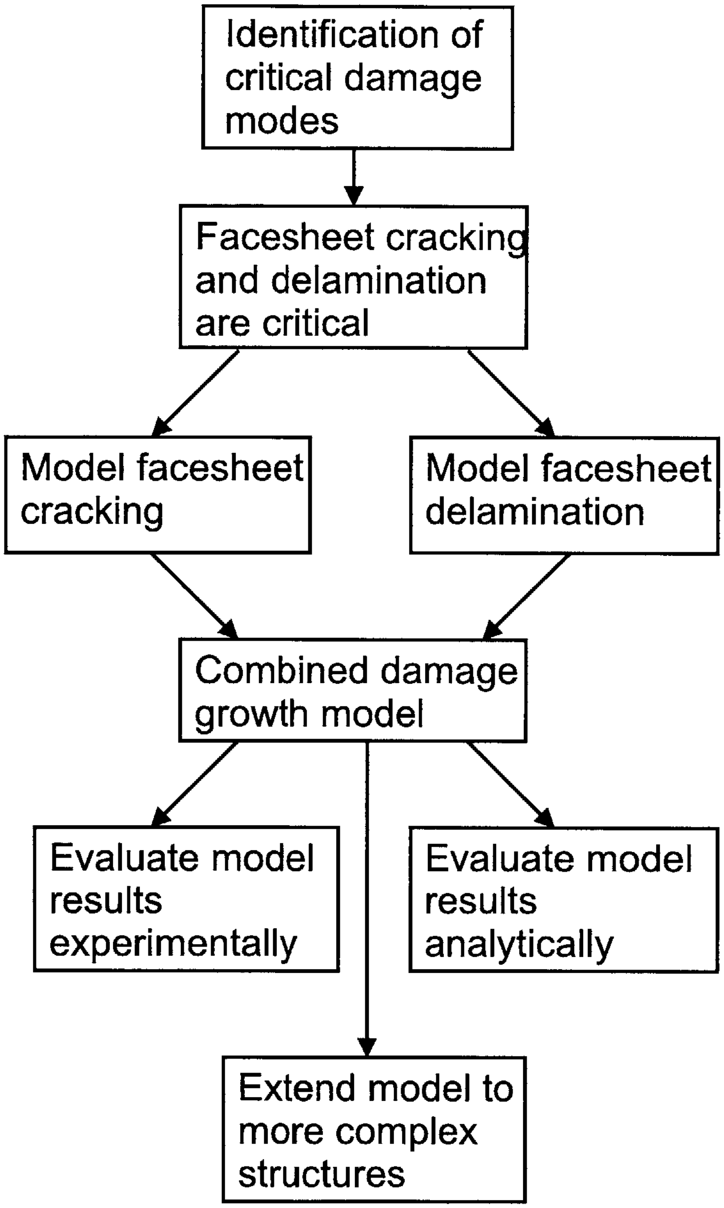

Figure 2-9: Outline of key steps in modeling the growth of the coupled damage modes

Chapter 3

Experimental Procedures

The goal of this chapter is to provide an overview of the material properties and configurations that will be studied. In addition, this chapter provides an overview of the experimental equipment and procedures that were generic to all of the experiments conducted for this research. A description of the specific procedures for the experiments are provided with the discussion of the experimental results in subsequent chapters.

3.1 Materials

3.1.1 Laminate characteristics

The TiGr specimens were manufactured by The Boeing Company in Seattle, WA. A majority of the specimens were provided having been cut to the appropriate dimensions for the experiments. The facesheets were made from 0.127 mm thick Titanium 15V-3Cr-3Al-3Sn (Ti 15-3) foil. Ti 15-3 is a metastable beta titanium alloy chosen for its low density and minimum processing and fabrication costs [104]. The polymer matrix composite (PMC) core consisted of an IM-7/PIXA-M cross-ply laminate with a ply thickness of 0.142 mm and a fiber volume fraction of approximately 0.6. IM-7 is an intermediate modulus graphite fiber. PIXA-M is a thermoplastic polyimide resin [105] with a very low fraction of volatile species. In most composite materials, volatiles can escape during the cure cycle, however, in TiGr laminates the impermeable titanium facesheets prevent this from occurring. If the vapor pressure of volatiles was too high, voids would result in the material.

The base laminate for the experiments was a high strength configuration with a lay-up of $[\text{Ti}/0/90/0_2]_s$, which is also referred to as TiGr 2-6-2. In addition to the base laminate, specimens with a lay-up of $[\text{Ti}/90/0/90_2]_s$ (TiGr 2-2-6) and $[\text{Ti}/0/90/\pm 30]_s$ (TiGr ±30) were also used during the experimental program. Material properties for the constituent materials and the two laminates listed above are shown in Table 3.1. The stress-free temperature used for determining the thermally-induced thermal stresses is approximately 260° C. The material properties for TiGr and the stress-free temperature were provided by Boeing based on proprietary experiments [106].

Table 3.1: Material properties

Material Property	Ti 15-3	IM-7/PIXA-M (Unidirectional)	TiGr 2-6-2	TiGr 2-2-6	TiGr ±30
E_1 (GPa)	107	162	118	58.5	86.9
E_2 (GPa)	112	6.9	58.5	118	59.6
G_{12} (GPa)	41.4	4.5	11.7	11.7	22.3
ν_{12}	0.33	0.35	0.162	0.081	0.315
thickness (mm)	0.127	0.142	1.39	1.39	1.39

The yield stress, σ_y for the titanium alloy is 1100 MPa. The coefficient of thermal expansion for the titanium alloy is $8.64\,\mu\epsilon/°\text{C}$. The coefficient of thermal expansion for the composite lamina is $0.9\,\mu\epsilon/°\text{C}$ in the longitudinal (fiber) direction and $4.5\,\mu\epsilon/°\text{C}$ in the transverse direction.

3.1.2 Specimen preparation

As stated previously, the specimens were manufactured by the Boeing Company. The specimens were cut to the required size using a water-jet cutter or a carbide cutting wheel. In some specimens, the cutting process left residual titanium covering the composite plies, and obscured the interface between the titanium and the outermost composite ply. When this occurred, the edge was lightly sanded with fine sandpaper (600 grit) so that the interface between the composite core and the titanium facesheet could be more easily observed using the Questar™ Microscope.

The notches in the facesheet crack growth specimens were introduced using a diamond-coated end mill 0.64 mm in diameter. The end mill was inserted into a variable speed Dremel™ tool. The Dremel™ was mounted in a milling machine with a digitally encoded platform. The cuts were made with the Dremel™ speed set to four. For through-thickness notches, the cut was made in two passes, using the digital encoder to ensure that the notch length was uniform for both cuts. For notches in the facesheet only, the table was raised until the top of the specimen barely touched the tip of the end mill. The tool was moved away from the specimen and the table was raised 0.127 mm, i.e. the facesheet thickness. The Dremel™ was then switched on and the cut only extended through the facesheet. For these specimens, a visual inspection of the specimen was conducted using a stereo microscope to verify that the notch did not extend into the composite core. A picture of the notch cutting set-up is shown in Figure 3-1.

In order to prevent the serrated grip faces from damaging the titanium, emory cloth inserts were attached to the gripped ends of the specimens before testing. The emory cloth inserts were cut slightly narrower than the specimen so that they did not interfere with the alignment guides on the hydraulic grips. For elevated temperature experiments, the thermocouple was attached to the specimen in the appropriate location using flash tape. A schematic of the prepared specimen is shown in Figure 3-2.

3.2 Mechanical Testing

The mechanical testing portion of this thesis was conducted in The Technology Laboratory for Advanced Composites (TELAC) at the Massachusetts Institute of Technology. The section describes the equipment utilized to perform the experiments and discusses the calibration and verification procedures where applicable.

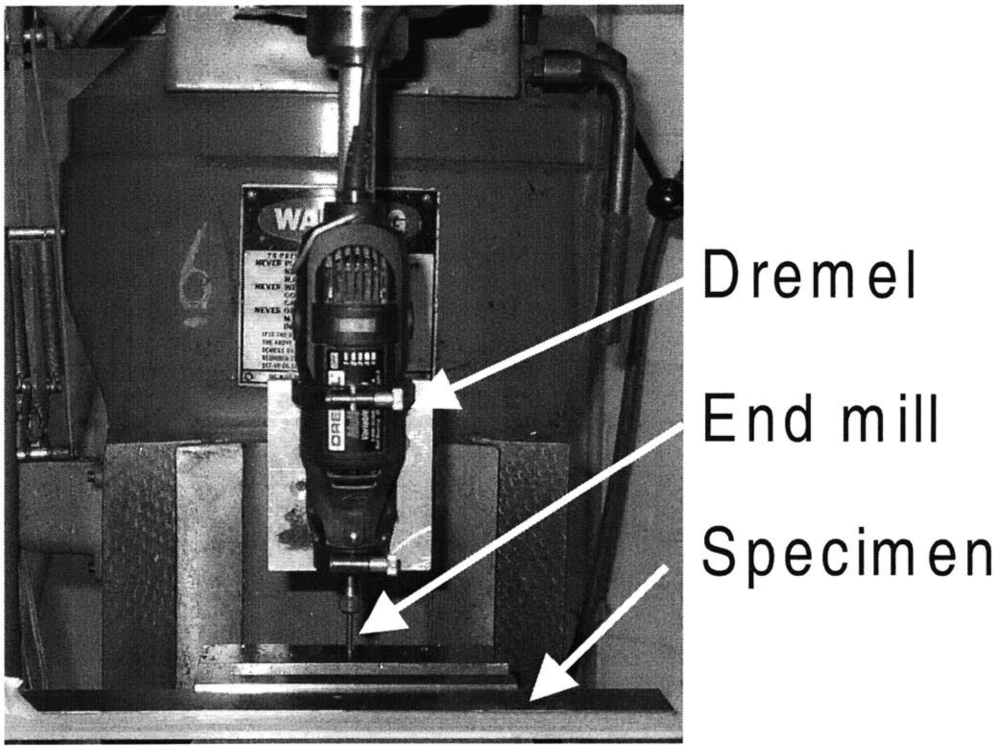

Figure 3-1: Set-up for cutting notches

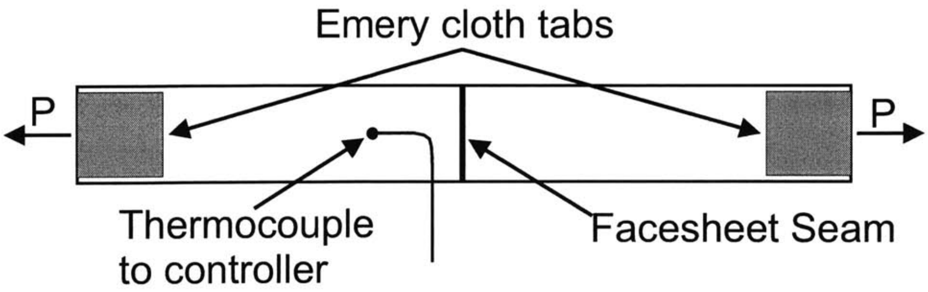

Figure 3-2: Specimen lay out

3.2.1 Load frame

The mechanical tests were conducted on an Instron 1332 servo-hydraulic load frame with a 222 kN capacity. The load frame was controlled using an Instron 8500+ digital controller. The load frame was equipped with water-cooled hydraulic grips to allow high temperature testing. A photograph of the Instron load frame and controller is shown in Figure 3-3.

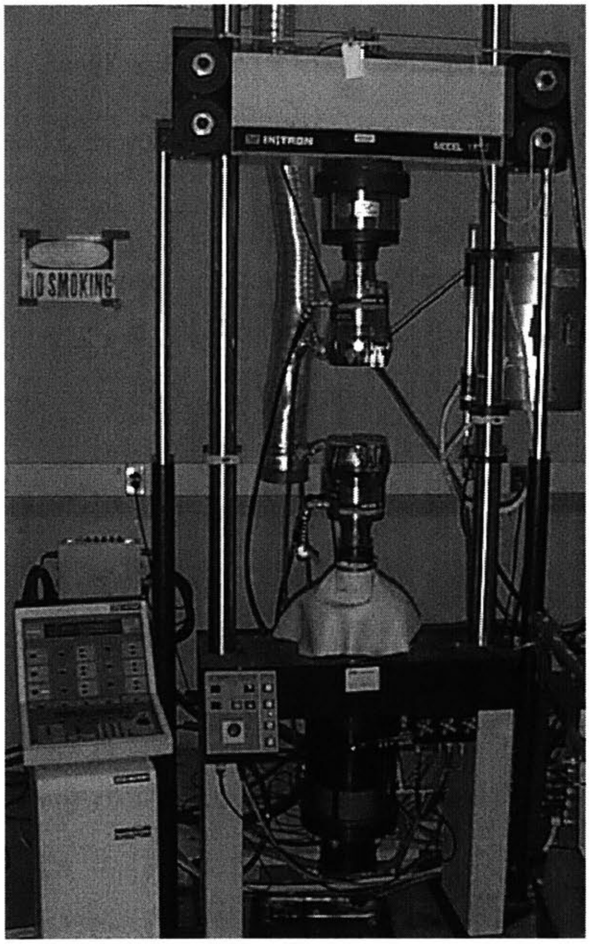

Figure 3-3: Instron 1332 load frame and controller

It was necessary to align the grips to ensure that the grip faces on the top and the bottom were parallel. In order to align the grips, the first step was to loosen the top and the bottom grip heads such that they were free to rotate. A steel bar was then inserted into the grips and was loaded in displacement control to a peak load greater than the maximum expected experimental load. For these experiments, this load was generally between 75 kN and 90 kN.

While holding at this load, the grip heads were tightened so that they could no longer rotate.

The alignment was verified using a TiGr sample with a strain gauge rosette in identical positions on the front and back facesheets. The specimen was loaded up to approximately 13 kN. The longitudinal stress vs. strain plots for the front and the back gauges were compared to determine if any bending or misalignment twist was present in the system. A strain parameter was defined as:

$$\frac{(\epsilon_{front} - \epsilon_{back})}{(\epsilon_{front} + \epsilon_{back})} * 100 \tag{3.1}$$

If the value of the strain parameter was greater than 5% for tensile experiments, the alignment procedure was repeated until the grip alignment was satisfactory. For most cases, the strain parameter at low loads varied significantly and would be larger than 5% This was attributed to noise in the system at low values of load and strain and was considered not to indicate misalignment.

Data collection was performed using a Macintosh computer with LabView™ software. The typical inputs from the load frame controller were load, displacement, and strain (from the extensometer or from strain gauges). The output range from the Instron controller was ±10 Volts. The signal was input into the computer via a National Instruments A/D conversion board and the conversion from voltage to the appropriate value was made using a script written in LabView™. The data was output as a text file that could be read into a spreadsheet.

3.2.2 Extensometer

A high temperature extensometer (Instron model # 2620-827) was used to monitor specimen stiffness during some experiments. The extensometer had a 50 mm gauge length and was centered over the seam/crack in the center of the specimen. In some cases, epoxy beads were placed on the surface of the specimen in order to locate the extensometer and prevent it from moving during the fatigue cycling. However, it was found that these epoxy beads were not necessary and later experiments did not include them. To record the stiffness during fatigue experiments, the load cycling was paused and the stiffness was measured using a half triangle wave from the midpoint value to the maximum value of the fatigue load cycle. Figure 3-4 shows the cycle used to measure the specimen stiffness.

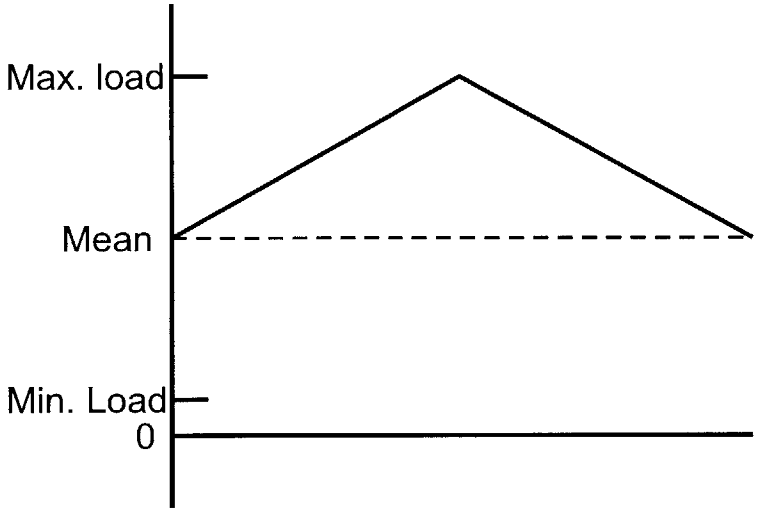

Figure 3-4: Triangle waveform used to measure specimen stiffness

3.2.3 Temperature cabinet

The temperature cabinet was based on a design by Fisher et al. [107]. The cabinet is constructed out of a sheet metal box and is insulated with structural board insulation. A schematic of the cabinet is shown in Figure 3-5. The cabinet was modified from the original design by adding three windows to one side of the box: a 102 mm x 25 mm window for viewing and one 51 mm x 13 m window on either side of the viewing window to provide a location for a light source. The windows allowed the specimen to be monitored from the outside without opening the box using a Questar™ long working-distance microscope. In some cases, it was difficult to obtain an accurate measurement through the windows and it was necessary to open the oven.

A photograph of the cabinet set-up installed on the load frame is shown in Figure 3-6. The cabinet was heated using a 1000W heat gun. The temperature in the cabinet was

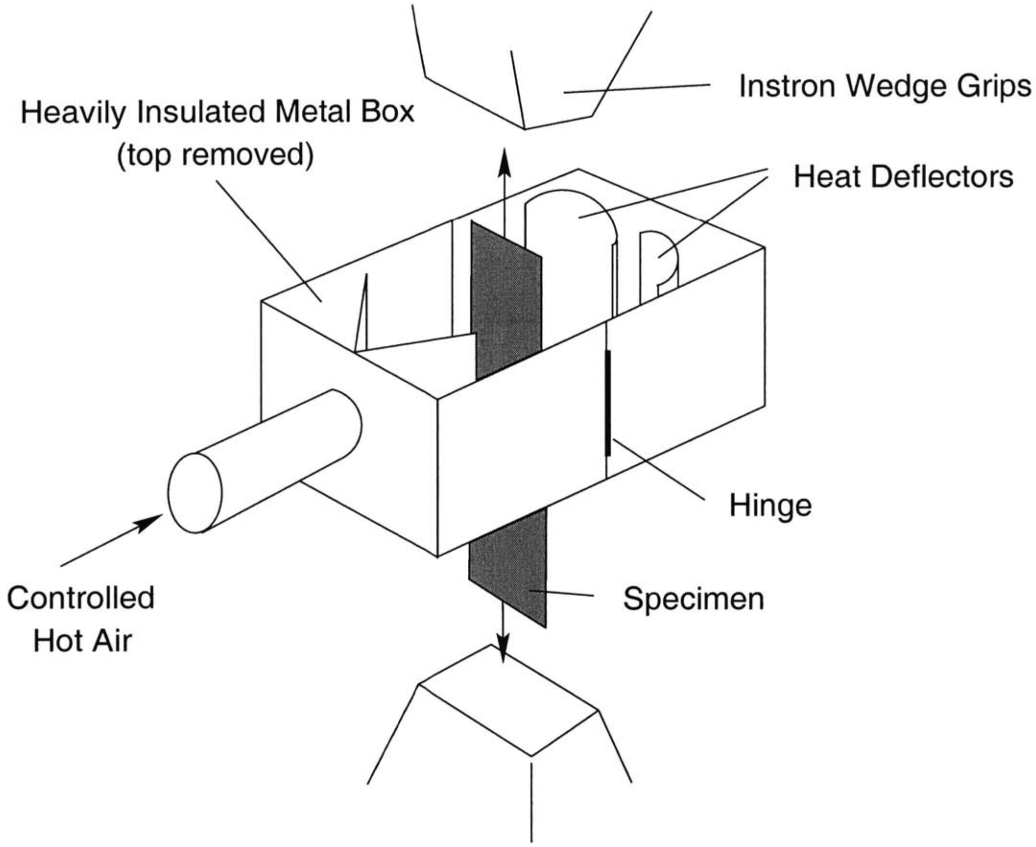

Figure 3-5: Schematic of temperature cabinet

controlled using an Omega 5002K temperature controller. A K-type thermocouple was used to determine the temperature for input into the controller and was attached directly to the facesheet of the specimen. The location of the thermocouple was dependent on the desired test temperature as discussed below. A wiring schematic for the controller is shown in Figure 3-7. During initial tests, the leads and switches in the controller tended to corrode and break down during long duration experiments. A solid state relay (SSR) was then inserted in the system to reduce the electrical load carried by the Omega controller. After it was installed, a majority of the electrical load from the heat gun was routed through the solid state relay, reducing the load on the controller.

A verification procedure was conducted on the temperature cabinet and controller set-up to ensure that the temperature was constant over the test section of the specimen. The temperature variation from top to bottom was ±3° C for the 177° C experiments, ±5° C for the 93° C experiments and ±10° C for -18° C experiments. The details and full results of the procedure are described in Appendix A.

3.2.4 Damage observation

Questar™ microscope

Non-destructive measurement of the delamination and crack growth was carried out with a Questar™ long-working distance microscope model QM 100 MK III. The long focal length of the Questar™ allowed observation of the cracks without removing the specimen from the test machine. A picture showing the Questar™ microscope is shown in Figure 3-8.

The microscope stage is equipped with digital encoders which provides the position in the three translational axes with an accuracy of 0.005 mm. The position of the crack root and tip were recorded after each set of cycles with the load held at the midpoint value of the fatigue cycle.

Dye penetrant

The presence of the titanium facesheets made non-destructive evaluation (NDE) of the specimens difficult because X-ray techniques could not be easily utilized. NDE of the specimens

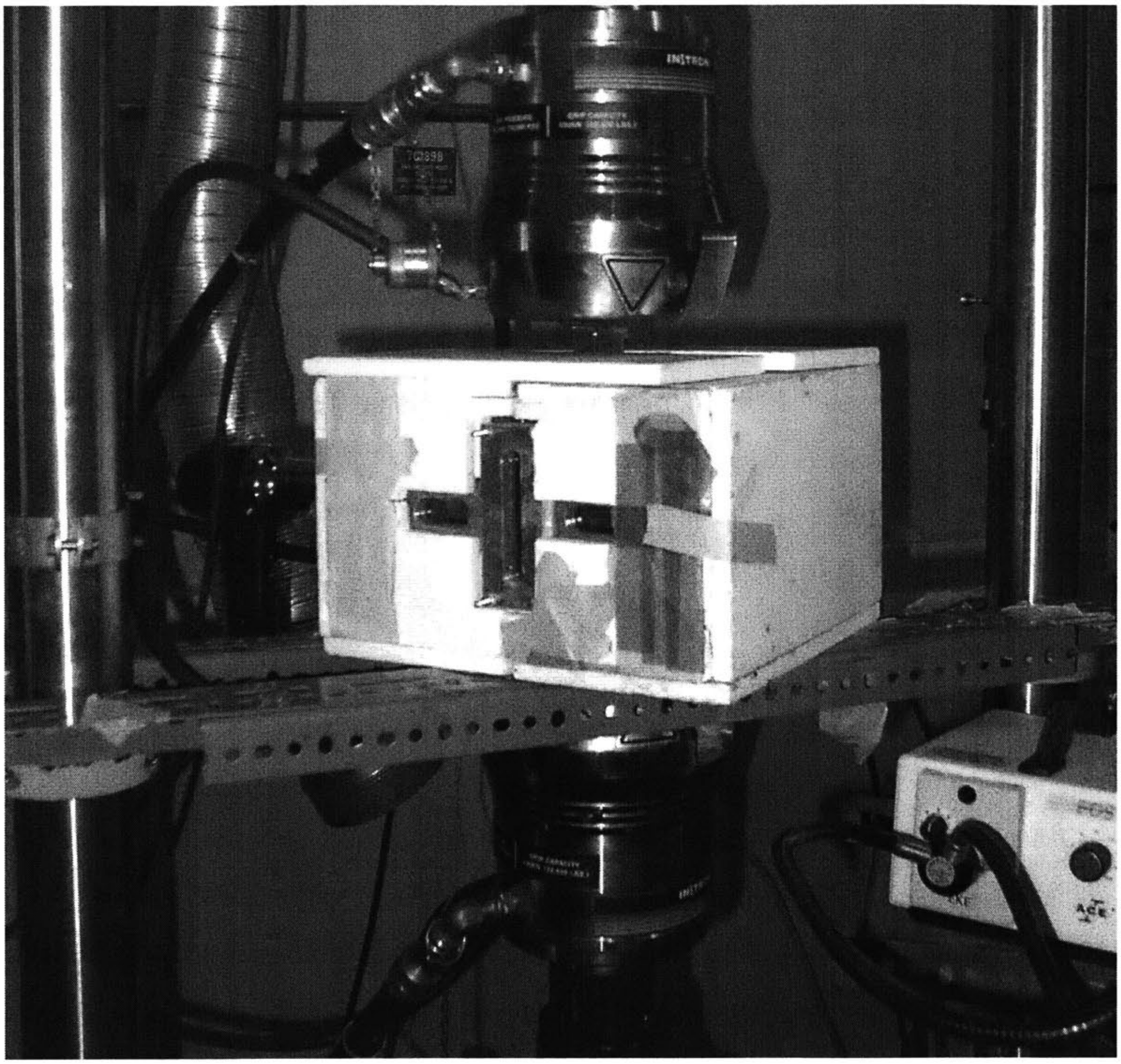

Figure 3-6: Cabinet set-up in load frame

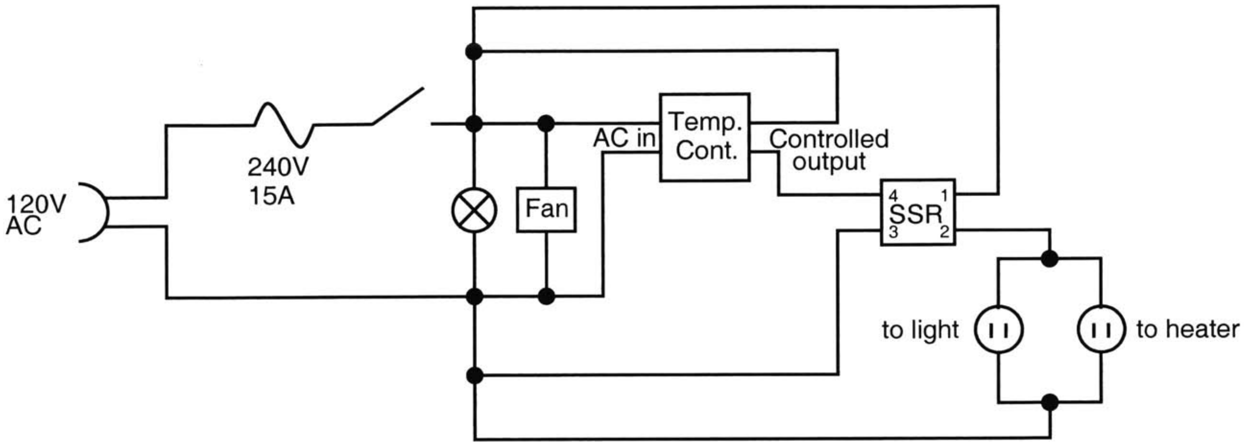

Figure 3-7: Wiring schematic for the temperature control system

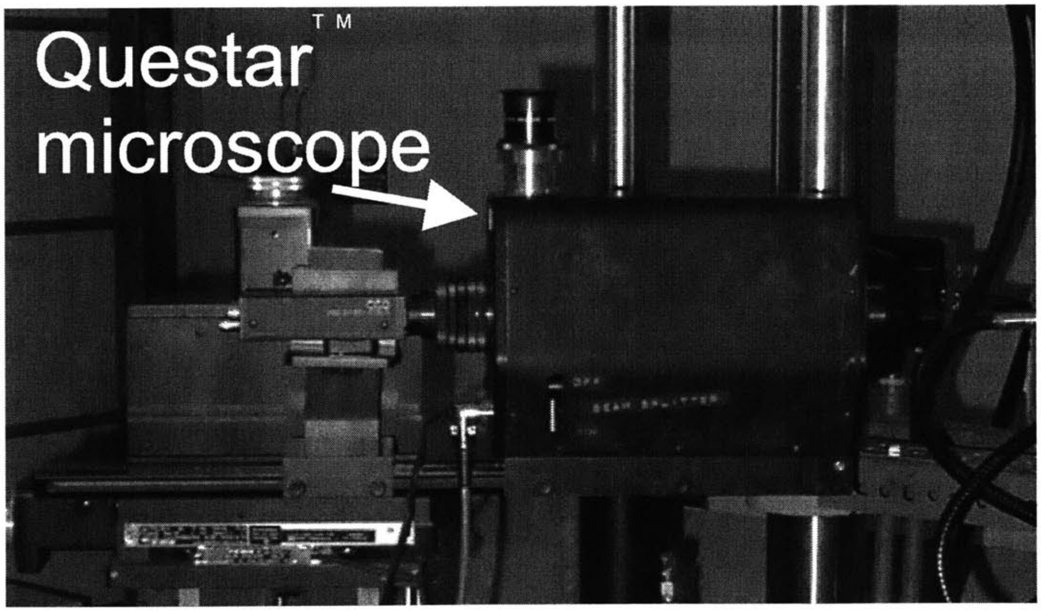

Figure 3-8: Questar™ microscope

was done primarily using the Questar™ microscope as described. However, this only revealed the edge view of the specimen. A destructive method of identifying the extent of the delamination was developed using a dye penetrant to determine the delamination shape profile.

The dye penetrant method employed two agents, a dye and a developer, to indicate the delaminated area. The dye is MagnaFlux Spotcheck™ SKL-SP Penetrant and the developer is MagnaFlux Spotcheck™ SKD-S2 Developer. Firstly, the dye is sprayed liberally on the face and the edges of the specimen and allowed to seep into the delaminated region. After allowing it to dry, the developer is lightly sprayed over the specimen and allowed to soak into the delaminated region. The developer acts as a drying agent to remove any excess dye. Once it has dried, the facesheet is carefully removed. The two step process leaves an outline where the leading edge of the delamination is located. In some cases, two outlines are visible, one from the dye and one from the developer. The dye outline, which is the furthest from the seam/crack, is taken to be the delamination front. Initially, the developer was not applied and the dye did not dry completely and would smear after the facesheet was removed, thus obscuring the delamination front. The delamination profiles observed using the die-penetrant method were similar to the profiles observed using the x-ray procedure discussed subsequently.

X-Radiography

Another method to evaluate the specimens non-destructively was x-radiography. Di-iodobutane (DiB) was used as a tracer agent to indicate the damaged areas in the x-radiographs. For seam specimens and specimens without through-thickness notches, DiB was applied to the edges and the seams of the specimen using a cotton swab while the specimen was held at the mid-point load of the fatigue cycle. For specimens with through-thickness notches, another method was employed to introduce the DiB into the damaged regions. Cellophane tape was placed over the notch on either side of the specimen, creating a reservoir. At a load lower than the mid-point value, DiB was injected into the reservoir and the load was increased to the mid-point value, which drew the DiB held in the reservoir into the damaged regions.

This procedure was repeated for specimens with small reservoirs to ensure that the DiB was drawn into the entire damaged region.

After introducing the DiB into the specimen, it was placed into the Scanray Torrex™ 150D X-ray inspection device in the TELAC laboratory. The specimen was placed onto Polaroid™ instant film in the x-ray machine and exposed for a fixed time interval at 3 mA and 70 kV, depending on the ISO value of the film. The DiB blocks the radiation in the coated areas, which shows up as darker areas on the developed film. Polaroid HC-51 provided the most satisfactory results for the x-radiographs.

Some difficulties were encountered using the x-ray technique due to the presence of the titanium facesheets. The x-ray technique worked well for seam specimens because the facesheets tended to pull away from the composite core, which allowed a sufficient amount of DiB to seep into the specimen, which provided a good contrast on the film. By scanning the images into a computer, and using software to adjust the brightness and exposure of the image, the delamination was clearly visible. However, in some cases, especially for notched specimens with short cracks, it was not possible to obtain a good contrast between the damaged and undamaged areas, even after enhancing the image with software.

Chapter 4

Facesheet Delamination

Previous research on TiGr 2-6-2 laminates indicated that facesheet delamination was a key damage mode for laminate stiffness degradation [3]. In addition, it was shown that the stiffness degradation rate was significantly higher at 177° C compared to room temperature (21° C) as discussed in Section 2.3.2. The seam experiments presented in this chapter provide an independent evaluation for delamination growth mode which is applied in the damage growth models presented in later chapters of this thesis. This chapter presents the results from the seam specimen delamination experiments for four different temperatures for the base laminate. Experiments were also conducted on the $[Ti/0/90/\pm30]_s$ alternate laminate. An analysis comparing the different delamination patterns evident between the two laminates was conducted.

4.1 Experimental Results

4.1.1 Overview of seam specimen experiments

For these experiments, a horizontal seam was manufactured in one of the titanium facesheets. A schematic of the specimen is shown in Figure 4-1 for the base laminate, $[Ti/0/90/0_2]_s$. The dimensions of the specimens were 304.8 mm long by 38.1 mm wide. The seam provided an initiation point for delamination growth such that it could be easily monitored and recorded using the Questar microscope.

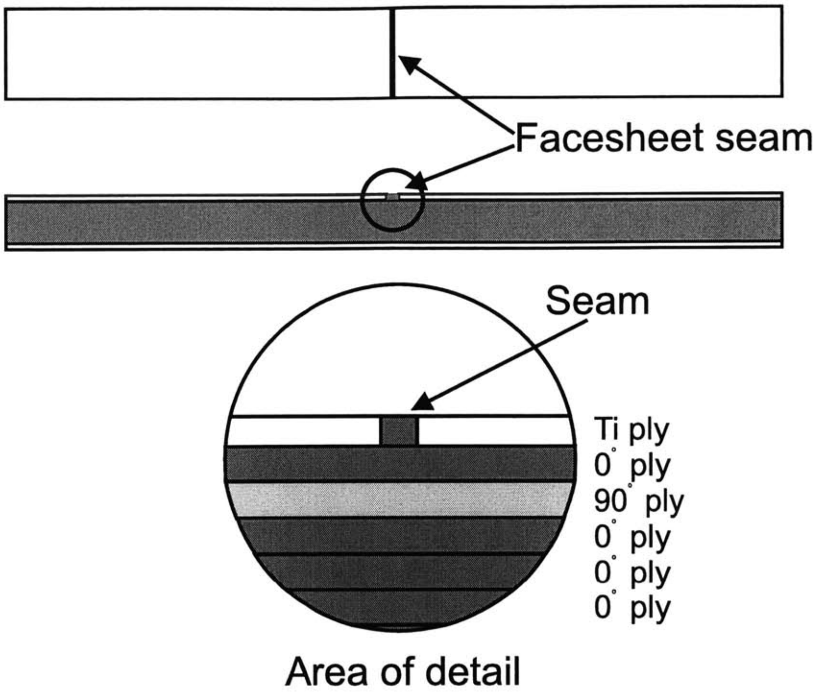

Figure 4-1: Schematic of a seam specimen for a $[\mathrm{Ti}/0/90/0_2]_s$ laminate

Once the end tabs and the thermocouple had been attached to the specimen, it was placed into the test machine by aligning the specimen vertically and gripping with the top grip. The Questar was aligned and focused onto the edge of the specimen and centered on the seam. At that point, the bottom of the specimen was gripped and the specimen was loaded to the midpoint of the load cycle. The temperature box was closed and the temperature was heated/cooled to the appropriate temperature.

The experiments were conducted in load control with an applied minimum to maximum load ratio (R-ratio) of 0.1. The cyclic frequency was 10 Hz for a majority of the experiments. In some cases, with higher maximum loads, the frequency of the experiment was reduced to between 6-8 Hz due to the limitations of the servo-hydraulic load frame. For lower maximum loads, a frequency of 15 Hz was applied. For the elevated and low temperature experiments, the effects of cyclic heating at the higher frequencies should be minimal because the temperature was controlled via a thermocouple mounted on the surface of the specimen. At room temperature, the higher frequencies may cause heating near the crack tip, however these effects were not considered in this analysis. Future work could be performed to consider these effects and determine if the power law relationship between delamination growth rate and the applied strain energy release rate is affected by cyclic frequency. The specimens were tested for a number of cycles resulting in approximately 0.3-0.5 mm of delamination growth and then the cycling was interrupted so that the delamination length could be measured using the Questar microscope. Approximately 5-8 measurements were taken for a given applied stress level. This generally gave a clear indication of the crack growth rate. In order to minimize the number of specimens that were necessary, each specimen was used to measure the crack growth rate for multiple stress levels. For each stress level, the delamination was typically grown 1-3 mm. It was assumed that the damage growth profile was independent of the load and the damage length. For the first experiment on a new specimen, the crack growth data was not recorded until after a visible delamination had initiated. Because the value of interest for these experiments was the delamination growth *rate* and not the total number of cycles to initiation or failure, the number of cycles to initiation of the delamination growth was not considered in the analysis.

Based on experimental observations made in this work, it was assumed that the delamination grew uniformly away from the seam and that the stress level did not affect the delamination profile. Destructive evaluation of the specimens using dye penetrant revealed that the delamination propagated further at the edges than in the center of the specimen as shown in Figure 4-2. The shape is approximately the same for the different temperatures and was not considered in modeling the delamination growth. The relevant measurement for these specimens was the rate of growth of the seams and if the delamination profile has a constant shape, the rate of growth is the same for the edges and center. The loading axis in Figure 4-2 is vertical.

4.1.2 Quasi-static experiments

In addition to the fatigue experiments, one specimen of the base laminate configuration ($[\mathrm{Ti}/0/90/0_2]_s$) and one alternate laminate ($[\mathrm{Ti}/0/90/\pm 30]_s$)were loaded quasi-statically to obtain a baseline value for the facesheet delamination resistance at room temperature. The specimens were loaded in position control with a ramp rate of approximately 1.25 mm/minute.

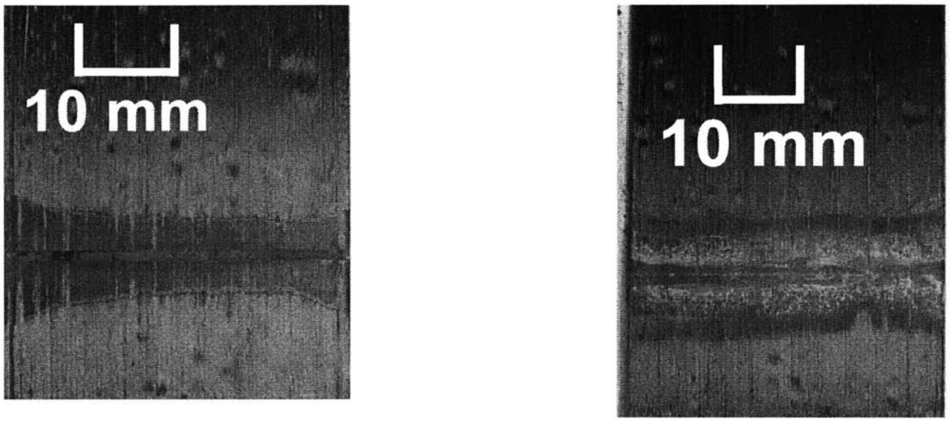

(a) 21° C

(b) 93° C

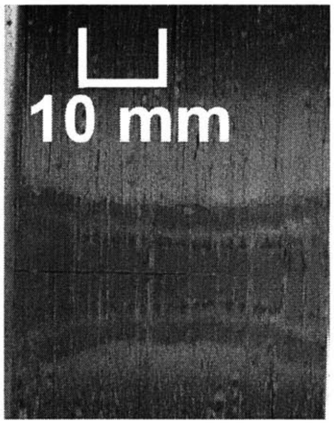

(c) 177° C

Figure 4-2: Destructively-evaluated seam specimen showing delamination profile (plan view)

The loading was paused periodically during the ramp to make damage observations using the Questar™ microscope. In addition, strain gauges were mounted to the surface of the facesheet in order to monitor the delamination as it propagated. When the facesheet delaminates under the strain gauge location, the strain reading is altered. Three strain gauges were mounted along the seam to monitor the delamination. One strain gauge was along the vertical centerline and the other two were mounted on either edge, approximately 3.2 mm away from the edge. Two strain gauges were mounted along the vertical centerline approximately 64 mm above the seam, with one on the front and one on the back, to monitor the far-field strain. A schematic of the gauge placement is shown in Figure 4-3. The $[Ti/0/90/\pm 30]_s$ specimen was tested first and the strain gauges along the seam were placed 9.5 mm above the seam. The gauges near the seam showed no variation from the far-field values before ultimate failure, leaving optical measurements as the lone indicator of delamination initiation. The gauges on the $[Ti/0/90/0_2]_s$ were placed closer to the seam to see if the delamination could be detected.

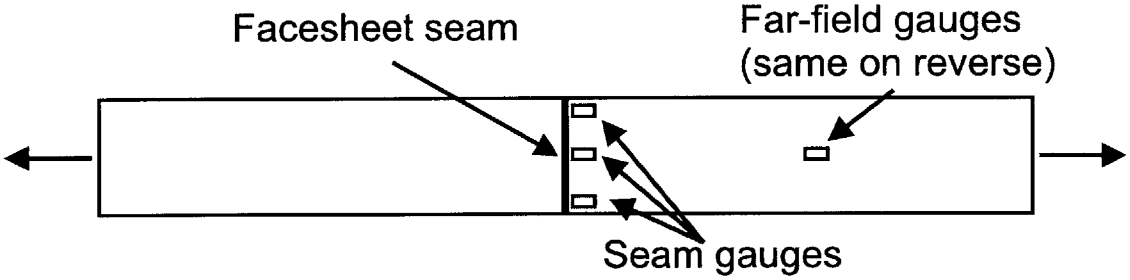

Figure 4-3: A schematic of the strain gauge placement for the static experiments

Initial delamination, observed non-destructively using the Questar™ microscope, occurred at approximately 670 MPa for both the base configuration and for the alternate laminate. This corresponds to a strain energy release rate of approximately 263 J/m^2 and 460 J/m^2, respectively. The strain energy release rate was calculated using the strip method discussed in Section 2.2.1. The strain gauge readings for the base laminate experiment were consistent with the initiation level observed visually using the Questar™ microscope. At a load of 419 MPa, an optical reading was performed, which indicated no delamination. The next visual observation at 670 MPa indicated that delamination had initiated. One of the edge gauges deviated from the slope of the far-field gauges at approximately 500 MPa, indicating that the delamination had initiated during that interval.

4.1.3 Results for base laminate (TiGr 2-6-2)

The data from the experiments was recorded in the form of delamination length as a function of cycles for different stress levels. Micrographs were taken of the damaged areas using an optical microscope. Figure 4-4 shows the titanium foil pulling away from the composite core in the area around the seam. It is important to note that as in previous work [103] some fibers and matrix material remained adhered to the foil after delamination. This indicates that the failure occurs in the polymer matrix and not at the interface between the titanium facesheet and the composite core.

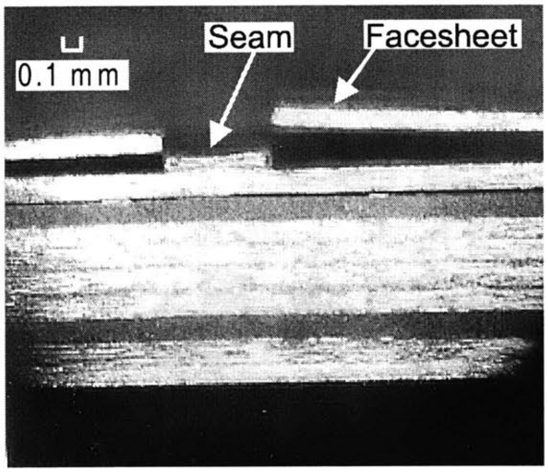

Figure 4-4: Edge view of delaminated seam specimen for $[\mathrm{Ti}/0/90/0_2]_s$ laminate

A plot of delamination length vs. cycles is shown in Figure 4-5 for a maximum far-field stress level of 419 MPa. This far-field stress level results in a facesheet stress of 406 MPa, which is approximately 37% of the monolithic titanium yield stress. The plot shows results for both a room temperature experiment as well as a 177° C experiment. A linear regression was performed for each set of data to determine the average delamination growth rate, $\frac{dD}{dN}$. The strain energy for the laminate is calculated using the steady state calculation discussed in Section 2.2.1 (i.e. the "cut-and-paste" method).

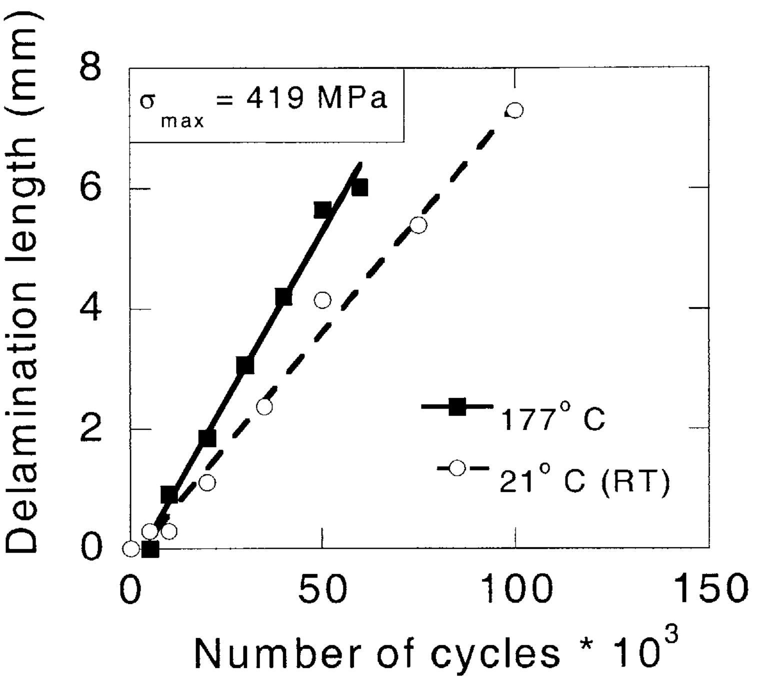

Figure 4-5: Delamination length vs. number of cycles for two temperatures (R=0.1)

For each experiment, a plot similar to Figure 4-5 was created. After conducting a linear regression on the data, the results for the experiments were compiled into a plot of delamination growth rate, $\frac{dD}{dN}$ vs. applied strain energy release rate, ΔG, as shown in Figure 4-6. The average R^2 value of the linear regressions was 0.95 with a standard deviation of 0.07. The plot includes data taken at -18° C, 21° C (room temperature), 93° C, and 177° C.

A power law regression was conducted on the results shown in Figure 4-6 to determine an expression for delamination growth rate as a function of applied strain energy release rate similar to Paris' Law for cracks growing in a monolithic material. The general form of the power law function is:

$$\frac{dD}{dN} = A\left(\Delta G\right)^m \tag{4.1}$$

where:

$\frac{dD}{dN}$ = delamination growth rate

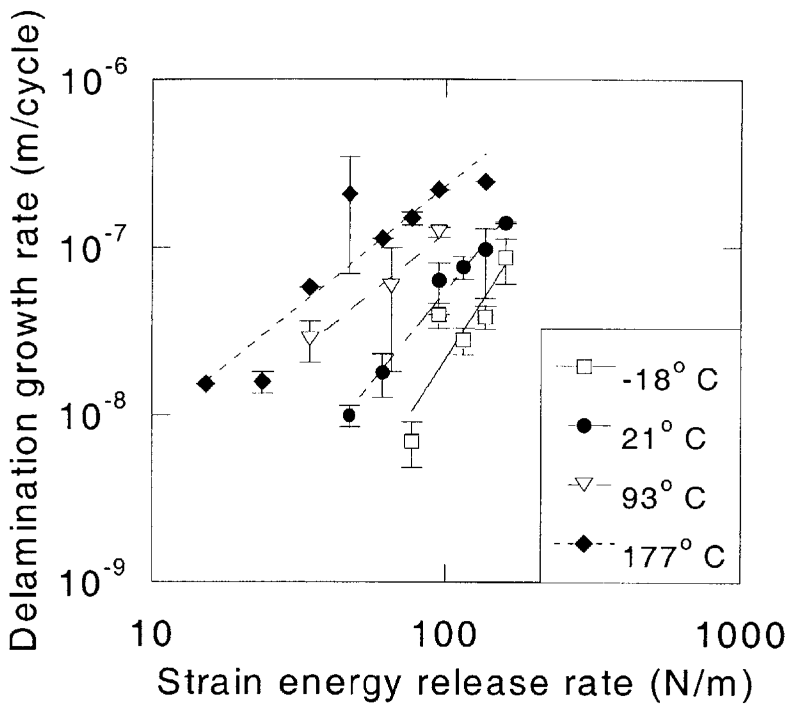

Figure 4-6: Delamination growth rate vs. applied cyclic strain energy release rate for four temperatures

ΔG = strain energy release rate

A, m = curve fit parameters

The values for A and m from the power law regression are tabulated in Table 4.1 along with the curve fit correlation coefficient, R^2. For the power law equation, the units for $\frac{dD}{dN}$are m/cycle and the units for ΔG are J/m^2.

Table 4.1: Fatigue delamination growth law parameters for four temperatures

Temperature (° C)	A (m/cycle)	m	R^2
-18	$6.39 \cdot 10^{-14}$	2.76	0.81
21	$2.71 \cdot 10^{-12}$	2.15	0.98
93	$1.91 \cdot 10^{-10}$	1.40	0.97
177	$3.32 \cdot 10^{-10}$	1.42	0.68

The data points shown in Figure 4-6 represent an average of the data points recorded at each stress level. The error bars represent the bounds of the data included in the averaged value. Because the seam was centrally located on the test specimen, the delamination grew in either direction away from the seam, producing two sets of data for each experiment. In some cases one of the delamination tips was obscured from view, and only one data point was available from that experiment. There did not appear to be any bias for delamination growth between the upper tip and the lower tip.

In order to investigate the physical mechanisms causing the temperature dependence of the delamination growth rate, a scanning electron microscope (SEM) was used to view the fracture surfaces of the delaminated portions of the facesheet. A small section of the facesheet from the delaminated region of specimens tested at three different temperatures, -18° C, 21° C, and 177° C, was mounted and coated with a thin layer of gold for viewing in the SEM. In addition, a section of the facesheet from a specimen that delaminated under quasi-static loading was mounted and coated. The surfaces of representative regions were photographed at several magnification factors for both the fatigue specimens and the quasi-static specimen.

Figure 4-7 shows the micro-graphs for the quasi-static delamination experiment. At a low magnification, Figure 4-7(a), it is clear that two distinct regions exist, one in which a significant amount of the thermoplastic matrix and carbon fibers have remained adhered to the titanium and a smoother region where the adherent PMC material is sparse and/or not present. Figure 4-7(b) shows the smooth region at a higher magnification factor, clearly showing regions where the matrix and fibers are no longer adhered to the facesheet. Figures 4-7(c) and 4-7(d) show regions where a significant amount of material remains adhered to the titanium at two magnification factors. The hackled regions that are labeled are typical of Mode II dominated fracture behavior.

The difference between the quasi-static delamination and fatigue delamination is obvious by looking at the SEM photographs of the fatigue surfaces in Figure 4-8. The fatigue specimens do not show any indication of the hackled regions visible in the static case. In addition, there is a significant difference between the -18° C case (Figures 4-8(a) and 4-8(b)), the 21° C case (Figures 4-8(c) and 4-8(d)), and the 177° C case (Figures 4-8(e) and 4-8(f)). The difference is most evident in Figure 4-8(f), which shows the 177° C fracture surface at a high magnification factor. Tiny ridges are evident on the surface which are probably an

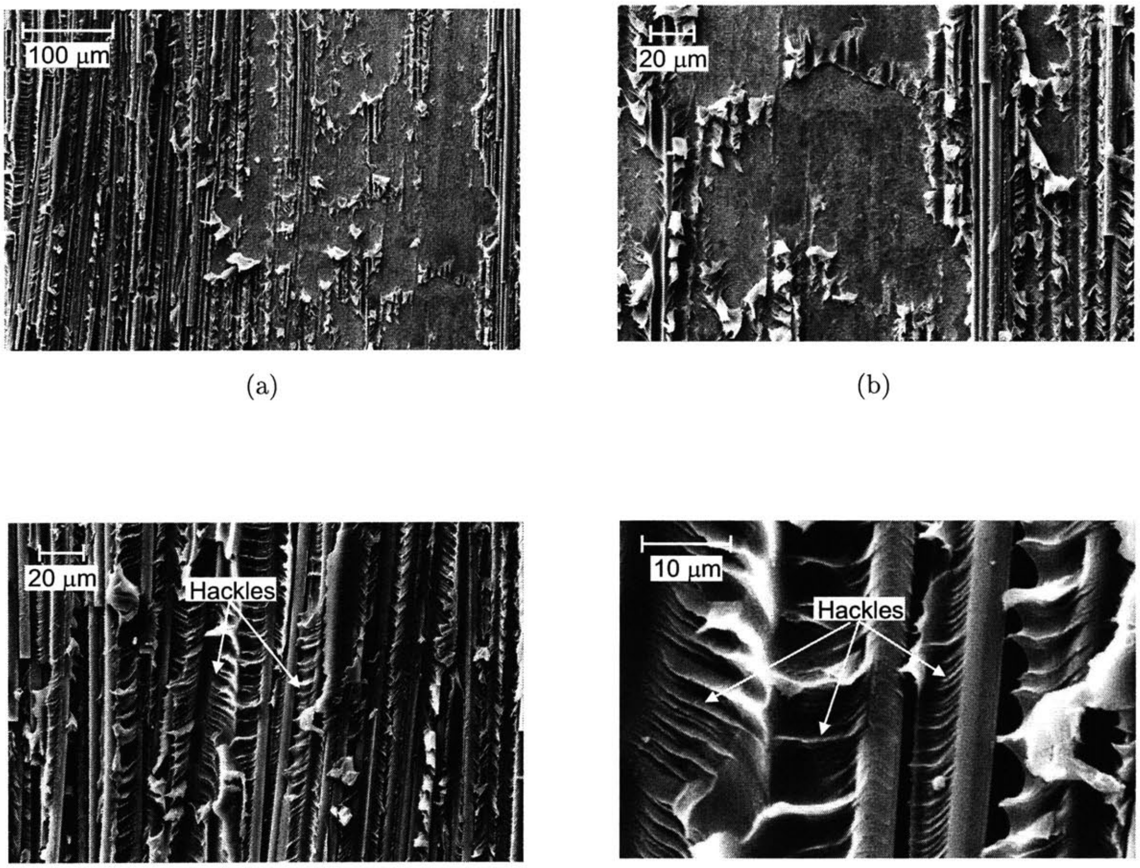

(a)

(b)

(c)

(d)

Figure 4-7: SEM micrographs of a statically delaminated specimen at multiple magnification factors (vertical loading axis) indication of increased plastic deformation during the fatigue delamination growth.

4.1.4 Results for alternate laminates

In addition to the experiments conducted on $[\mathrm{Ti}/0/90/0_2]_s$, experiments were conducted on TiGr laminates with a lay-up of $[\mathrm{Ti}/0/90/\pm30]_s$. However, when the fatigue loading was applied, delamination did not grow consistently from the seam. After the initial delamination from the seam, edge delaminations formed at the free edges between the interior composite plies. The edge delaminations were likely caused by free edge stresses due to the elastic mismatch between the plies. Figure 4-9 shows an edge view of a delaminated specimen. In addition to the seam delamination, both the 90°/30° and the +30°/-30° interfaces have delaminated. This precluded the measurement of delamination growth rates for this set of laminates.

4.2 Discussion

4.2.1 Delamination Modeling

In order to understand better the difference between the behavior of the TiGr 2-6-2 seam laminate and the laminate with ± 30° plies, the strain energy release rate of the two damage modes were compared for the $[\mathrm{Ti}/0/90/\pm\theta]_s$ family of laminates. A schematic of the seam damage is shown in Figure 4-10 and a schematic of the edge delamination is shown in Figure 4-11.

For the damage cases considered in this work, the loading was unidirectional, therefore an approximation was made by assuming that the strain energy release rate, G, at a given load, P, can be determined by calculating the rate of change of compliance with respect to delamination length, $\frac{dC}{dD}$:

$$G = \frac{P^2}{2W}\frac{dC}{dD} \tag{4.2}$$

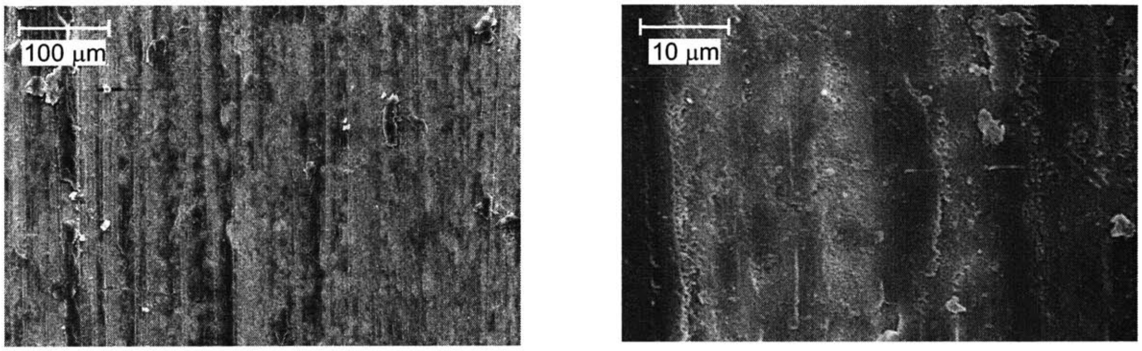

(a) -18° C

(b) -18° C

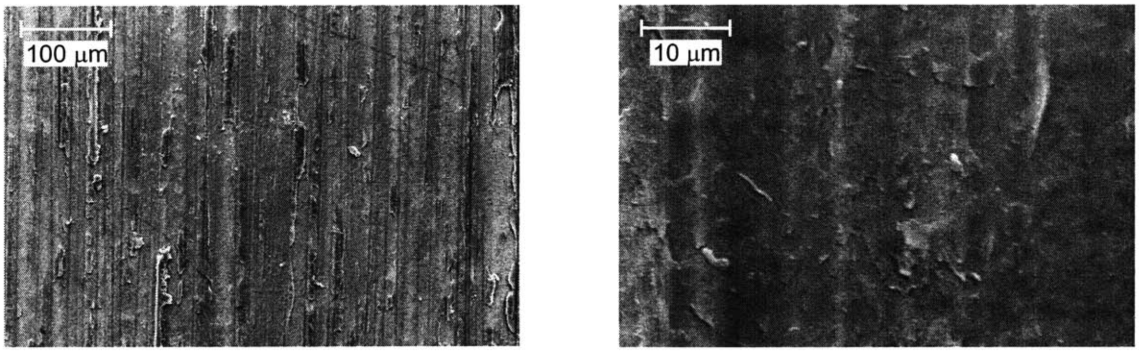

(c) 21° C

(d) 21° C

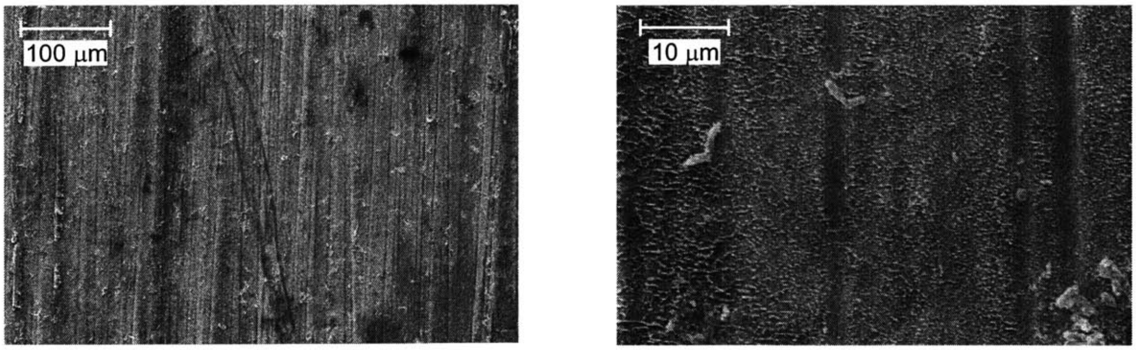

(e) 177° C

(f) 177° C

Figure 4-8: SEM micrographs of fatigue delamination surfaces at three different test temperatures (vertical loading axis)

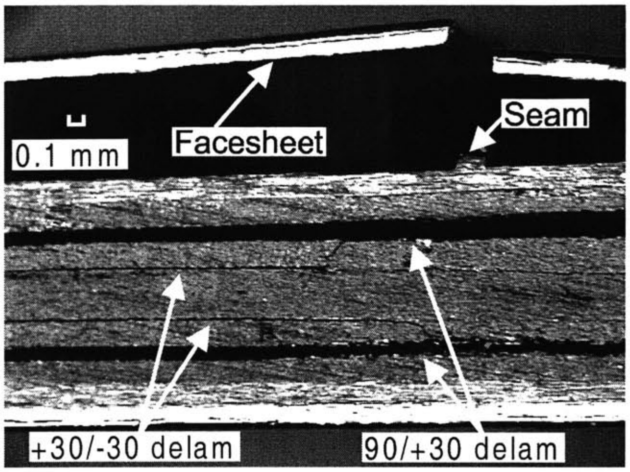

Figure 4-9: Edge view of a delaminated seam specimen for $[\mathrm{Ti}/0/90/\pm 30]_s$ laminate

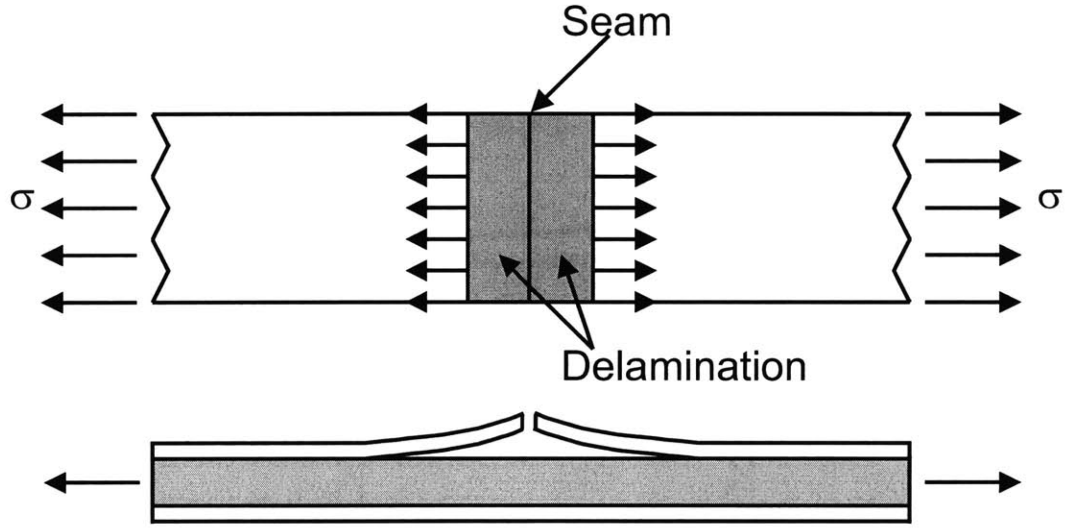

Figure 4-10: Schematic of seam delamination

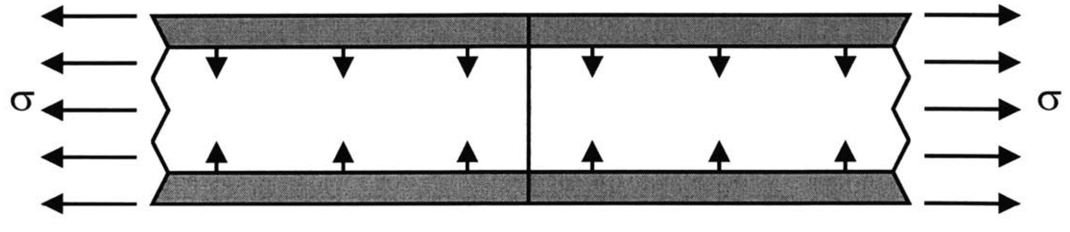

Figure 4-11: Schematic of edge delamination

The compliance of the specimen is determined by assuming the damaged section and the undamaged section act as springs in series as shown in Figure 4-12 for a half specimen with a width, W. The stiffness, i.e. inverse compliance, of each spring is described by:

$$K_i = \frac{A_i E_i}{L_i} \tag{4.3}$$

where:

E_i = Young's modulus for the segment

A_i =cross-sectional area for the segment

L = segment length

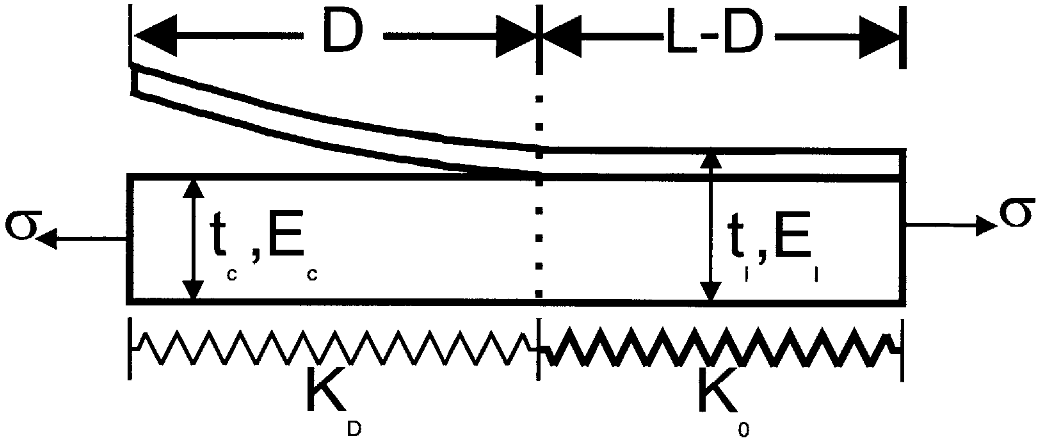

Figure 4-12: Schematic of spring model

The total specimen compliance is defined by:

$$C_{tot} = \frac{1}{K_{tot}} = \frac{1}{K_0} + \frac{1}{K_D} \tag{4.4a}$$

$$C_{tot} = \frac{L-D}{Wt_l E_l} + \frac{D}{Wt_c E_c} \tag{4.4b}$$

Taking the derivative of Equation 4.4b with respect to the delamination length, D:

$$\frac{dC}{dD} = \frac{-1}{Wt_lE_l} + \frac{1}{Wt_cE_c} \tag{4.5}$$

Equation 4.5 can be inserted into Equation 4.2 to calculate the strain energy release rate. In non-dimensional form, the strain energy release rate is:

$$\frac{GE_l}{\sigma^2 t_l} = \frac{1}{2}\left(\frac{t_lE_l}{t_cE_c}\right)\left(1 - \frac{t_cE_c}{t_lE_l}\right) \tag{4.6}$$

where:

E_l, E_c = Young's modulus for full laminate and composite core with one facesheet (calculated using Classical Laminated Plate Theory)

t_l, t_c = thickness for full laminate and composite core

σ = applied stress

G = strain energy release rate

It is important to note that using this formulation, the strain energy release rate is independent of the delamination length. In addition, the analysis conducted for these experiments make no assumptions about the mode-mixture of the configuration and the strain energy presented is the total for all modes. An approximation for the mode-mixture for seam delaminations is made using the analysis of Hutchinson and Suo [108] for an interface crack between two elastic layers which shows the mode-mixture angle, ψ, to be 55°, where ψ is defined as:

$$\psi = \arctan\left(\frac{K_{II}}{K_I}\right) \tag{4.7}$$

In the analysis, it is assumed that the second Dundurs parameter, β was equal to 0 where the Dundurs parameters are defined as:

$$\alpha = \frac{\frac{E_{Ti}}{1-\nu_{Ti}{}^2} - \frac{E_{core}}{1-\nu_{core}{}^2}}{\frac{E_{Ti}}{1-\nu_{Ti}{}^2} + \frac{E_{core}}{1-\nu_{core}{}^2}} \tag{4.8a}$$

$$\beta = \frac{1}{2}\frac{\mu_{core}(1-2\nu_{Ti}) - \mu_{Ti}(1-2\nu_{core})}{\mu_{core}(1-\nu_{Ti}) + \mu_{Ti}(1-\nu_{core})} \tag{4.8b}$$

The strain energy release rate for the edge delamination was calculated based on analysis by O'Brien [28]:

$$\frac{GE_l}{\sigma^2 t_l} = \frac{1}{2}\left(1 - \frac{E^*}{E_l}\right) \tag{4.9}$$

The variables are the same as listed above for Equation 4.6, except for E^*, which is an effective modulus calculated using the rule of mixtures on the sub-plies created by the delaminated interface. Further details are available in the reference by O'Brien [109]. As before, the strain energy release rate for a steady state delamination is independent of the delamination length, which is valid for delaminations extending several ply thicknesses.

The above analysis was applied to the $[\mathrm{Ti}/0/90/\pm\theta]_s$ family of laminates. The strain energy release rate was calculated for the growth of seam delaminations and for edge delaminations for each of the four interfaces within the laminate (Ti/0°, 0°/90°, $90°/+\theta$, and $+\theta/-\theta$). Figure 4-13 shows the results of the calculations for θ=0° through θ=90°. For this analysis, a higher strain energy release rate at a certain interface indicates a greater propensity for delamination growth at that interface, assuming that the delamination had initiated. In the case where θ=0° (i.e. TiGr 2-6-2) the strain energy release rate for the seam delamination and for the 90°/0° interface are similar in value. However, at θ=30°, the edge delaminations at the $90°/+\theta$ interface, and at the $+\theta/-\theta$ interface have significantly higher value of strain energy release rate than the seam delamination. This is in agreement with the experimental observations which showed that edge delamination becomes a dominant damage mode, which prevents accurate measurement of the seam delamination growth.

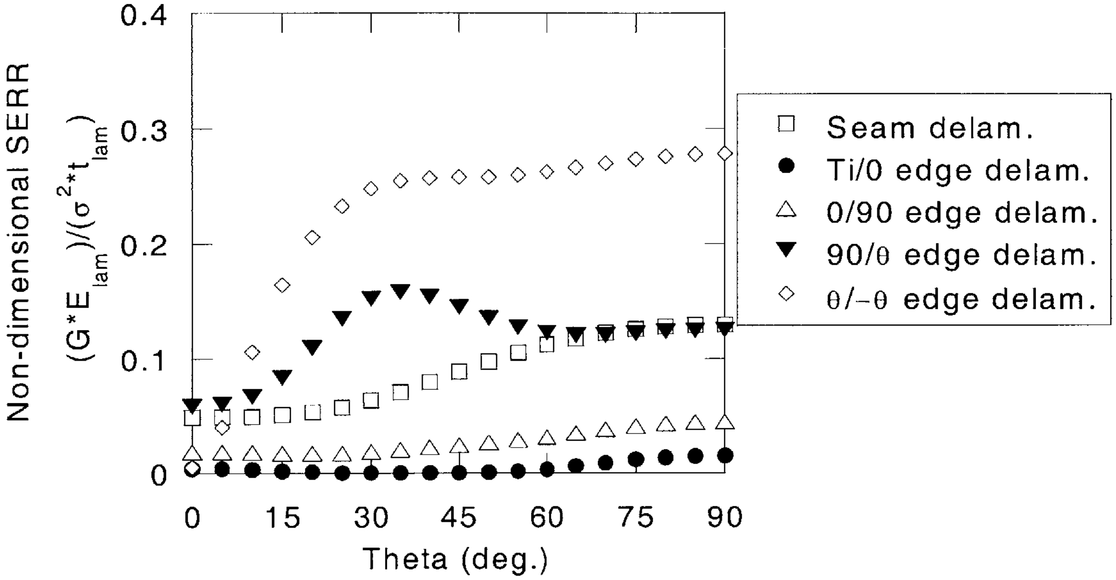

Figure 4-13: Non-dimensional strain energy release rate by interface for the $[\mathrm{Ti}/0/90/\pm\theta]_s$ family of laminates

A similar analysis was conducted on a laminate containing the same plies, but with a stacking sequence of $[\mathrm{Ti}/+\theta/90/-\theta/0]_s$. The results are shown in Figure 4-14. The in-plane properties of the two laminates are the same, but by changing the stacking sequence, the delamination growth behavior is changed. Most notably, the maximum value for the normalized strain energy release rate for the critical interface is lower in the $[\mathrm{Ti}/+\theta/90/-\theta/0]_s$ laminates than in the $[\mathrm{Ti}/0/90/\pm\theta]_s$ family of laminates.

While it appears that edge delamination is a critical damage mode for TiGr laminates with angle plies, it is not any more significant in TiGr laminates than in non-hybrid composites. Figure 4-15 shows the strain energy release rate for the $[0/\pm\theta/90]_s$ family of laminates consisting only of IM7/PIXA-M polymer matrix composites with no titanium facesheets. The overall values of strain energy release rate are of the same order in this family as in the previous results for hybrid laminates. This indicates that edge delamination as a critical damage mode is not unique to hybrid laminates. Furthermore, this study focused on coupon-level experiments. In larger structures, such as an airframe, the proportion of struc-

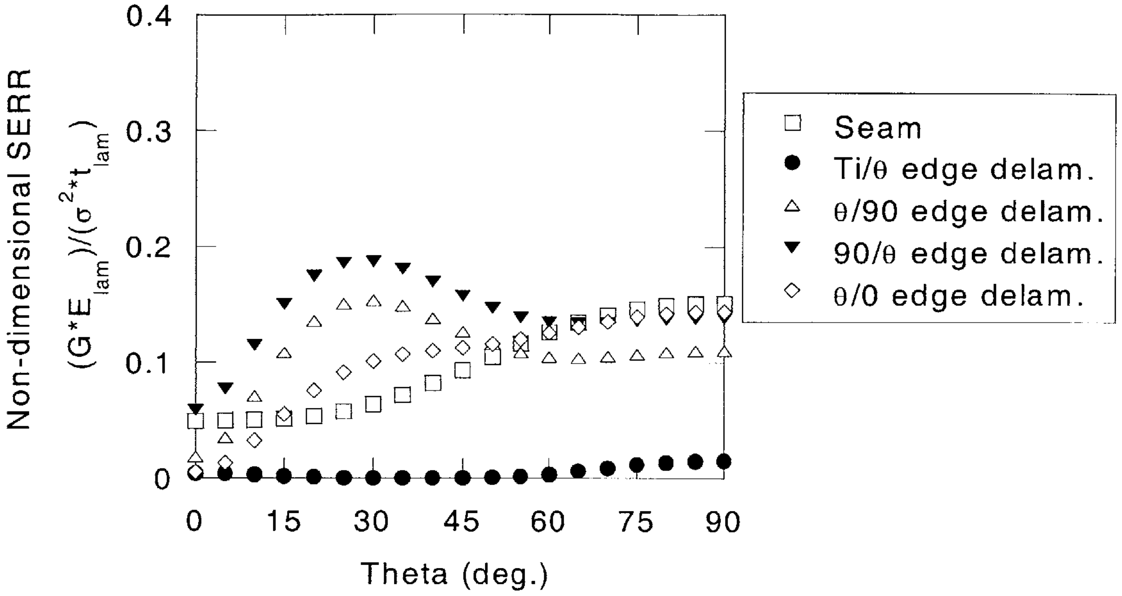

Figure 4-14: Non-dimensional strain energy release rate by interface for the $[\mathrm{Ti}/+\theta/90/-\theta/0]_s$ family of laminates

ture affected by free edge stress will be much lower. However, seam delamination is a damage mode unique to hybrid laminates that will have a greater significance in larger structures and thus needs to be considered in structural designs using TiGr laminates.

4.2.2 Fractography

The hackles observed in the quasi-static fracture surfaces (Figure 4-7) are consistent with a Mode II-dominated loading. The high toughness, and tendency for fibers and matrix to remain adhered to the titanium are indicative of a good bond between the metal and the PMC. The increased evidence of the matrix ductility in the fatigue surfaces (Figure 4-8) at elevated temperatures suggests that the mechanism underlying the temperature sensitivity of the delamination growth rate is the temperature-dependence of the plastic behavior of the matrix material.

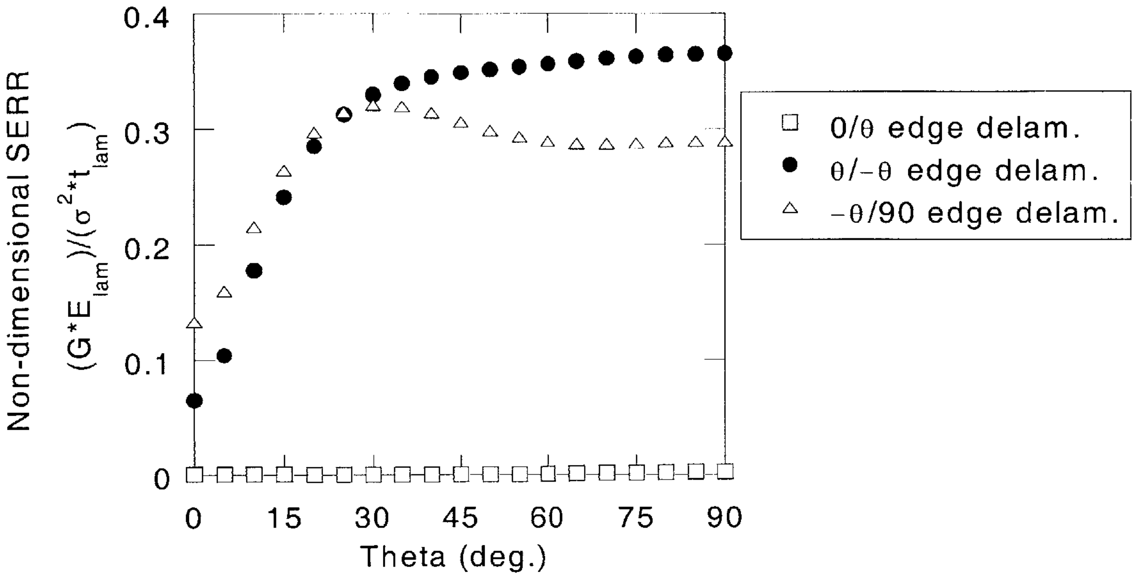

Figure 4-15: Non-dimensional strain energy release rate by interface for $[0/\pm\theta/90]_s$ family of laminates

4.2.3 Effects of Temperature

In order to model the increased delamination growth rate at elevated temperatures, an Arrhenius-type relationship was applied to the experimental results. Arrhenius relationships are often used to describe the temperature dependence of physical/chemical reactions of materials. Equation 4.1 for delamination growth rate might then be expressed by:

$$\frac{dD}{dN} = B\exp^{\left(\frac{-Q}{RT}\right)}(\Delta G)^m \tag{4.10}$$

where:

$\frac{dD}{dN}$ = delamination growth rate

B,m=curve fit constants

Q=activation energy

R=universal gas constant

T=temperature

ΔG = applied cyclic strain energy release rate

The experimental results are shown in Figure 4-16 for four values of applied strain energy release rate. The R^2 values for the regression lines shown in Figure 4-16 are greater than 0.97 in all cases. The model provides a reasonable description of the shift in growth rate as a function of temperature. The calculated value of the "activation energy" ranges from 12 kJ/mole to 17 kJ/mole. No evidence was found for a physical or chemical reaction, typically associated with Arrhenius behavior, with this range of activation energy. The results are a phenomenological fit to the experimental results and provide no insight into the physical processes governing the delamination growth. However, the relationship described in Equation 4.10 provides a convenient form in which to express the temperature-dependence of delamination growth and is applied in the models presented in Chapter 5. The benefit of having an analytic relationship between delamination growth rate and temperature is the ability to model and predict material behavior without having to conduct a large number of experiments.

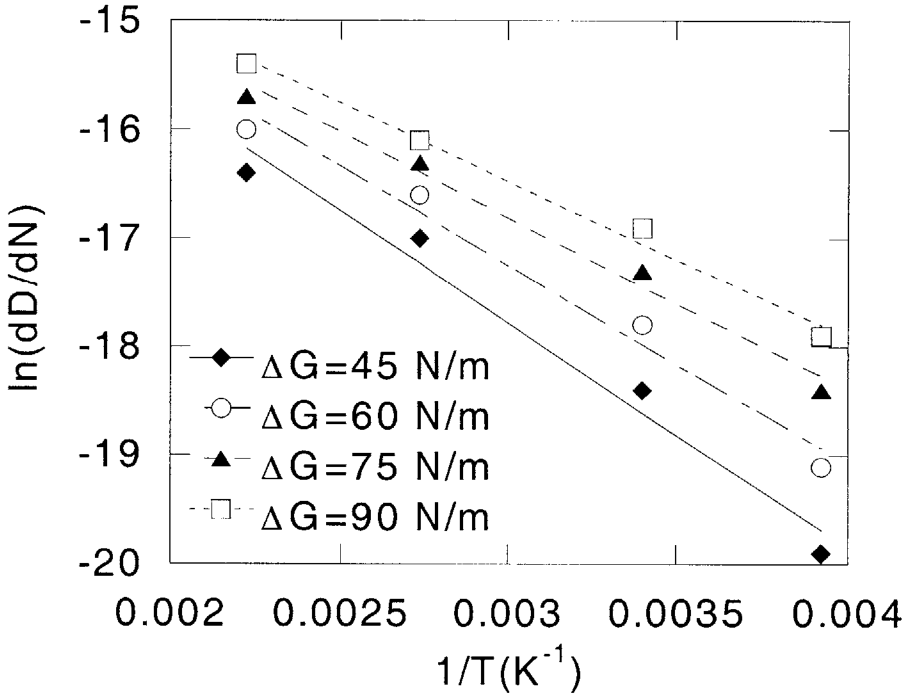

Figure 4-16: Application of an Arrhenius relationship to the delamination growth behavior from facesheet seams

4.3 Summary of Facesheet Delamination Studies

The goal of this chapter was to investigate the behavior of TiGr specimens with facesheet seams under fatigue loading. Tests on the base lay-up revealed that the delamination growth rate obeyed a power law function of the applied cyclic strain energy release rate at -18° C, 20° C, 93° C, and at 177° C. Increasing the test temperature results in a significant increase in delamination growth rate for a given applied strain energy release rate. In addition, an Arrhenius-type relationship was found to provide a reasonable description of the dependence of delamination growth rate on test temperature.

Experiments on an alternate TiGr lay-up containing ±30° plies were conducted to obtain similar data for facesheet delamination growth rates. However, edge delamination of the interior ply groups was the dominant mode in these experiments. Analysis of the two damage types indicated that the edge delamination had a higher strain energy release rate than the seam delamination and therefore it would be the dominant damage mode. However it is important to note that while edge delaminations may be important in coupon-level testing, larger structural configurations would be less likely to have free edges. In addition, the value of the strain energy release rate for the observed damage modes for TiGr laminates is similar to that of non-hybrid composite laminates.

The results of the experimental and analytic work performed using TiGr seam specimens provides valuable insight for future applications using TiGr laminates. The insight gained into the behavior of laminates in the presence of facesheet discontinuities, which will be necessary in any large-scale application of TiGr, will provide valuable information for design engineers using TiGr laminates. The observations about the damage mode and the relationship between the applied strain energy release rate and the delamination growth rate are inputs into the mechanism-based combined damage growth model presented in the next chapter.

Chapter 5

Crack Propagation in Titanium Facesheets

The purpose of this chapter is to develop a model that can predict the propagation of the coupled facesheet crack and delamination observed in TiGr laminates. The model is calibrated using observations and data from experiments previously conducted on the individual damage modes. Two approaches are used to calculate the effective stress intensity factor at the crack tip and, hence, the crack growth rate; a two-dimensional bridged crack model based on those developed for similar problems and a three-dimensional finite element model using the virtual crack closure technique. The modeling procedure for each type of model is outlined and the predictions from the bridged-crack model are compared to those from the 3D VCCT model for the specific configuration of a $[\mathrm{Ti}/0/90/0_2]_s$ laminate. The discrepancies of the two models are discussed and studies are conducted to determine the cause of the discrepancies. A strip model is also developed to determine the shape and size of the delamination growing in the wake of the facesheet crack. The results from the models are compared to experimental results in Chapter 6.

5.1 Overview of damage modes

A schematic of the damage modes to be modeled is shown in Figure 5-1. The crack is assumed to extend completely through-the-thickness of the titanium facesheet and the delamination exists between the facesheet and the top polymer matrix composite (PMC) ply. The damage is also assumed to be symmetric through-the-thickness of the laminate for all configurations and about the appropriate centerline for center cracked specimens and double edge notch specimens. Figure 5-1(b) shows the starter notch, or pre-crack in the specimen. The starter notch is cut through all the plies of the laminate and is an unbridged region of the crack and the initiation location for the crack. The assumed planar shape of the delamination is discussed subsequently during the discussion of the individual models.

The significance of two damage modes growing in parallel is that although the titanium facesheet is cracked, the underlying composite plies remain intact and act to shield the crack tip from the full effects of the applied load. Therefore, the crack in the titanium does not propagate at the same rate as it would in a similarly loaded monolithic sheet of titanium. Experimental evidence shows that for TiGr, the crack growth rate initially decreases as the crack propagates and approaches a constant crack growth rate for longer cracks. In addition, the crack in the facesheet provides a visual indication of the presence of damage during routine inspections.

5.2 Bridged crack model

5.2.1 Model overview and assumptions

A two-dimensional bridged crack model is developed using a mechanism-based approach, which implies that the model is based upon the physical and/or chemical damage/degradation mechanisms, similar to those discussed in References [90, 91, 96]. By modeling the physical damage mechanisms, observed through experiments, it is hoped that the model will have a predictive capability without relying on numerous and more complex experiments. However, some experiments are necessary to validate the modeling assumptions for parameters such as the delamination profile and the simultaneous growth of the two damage modes near the

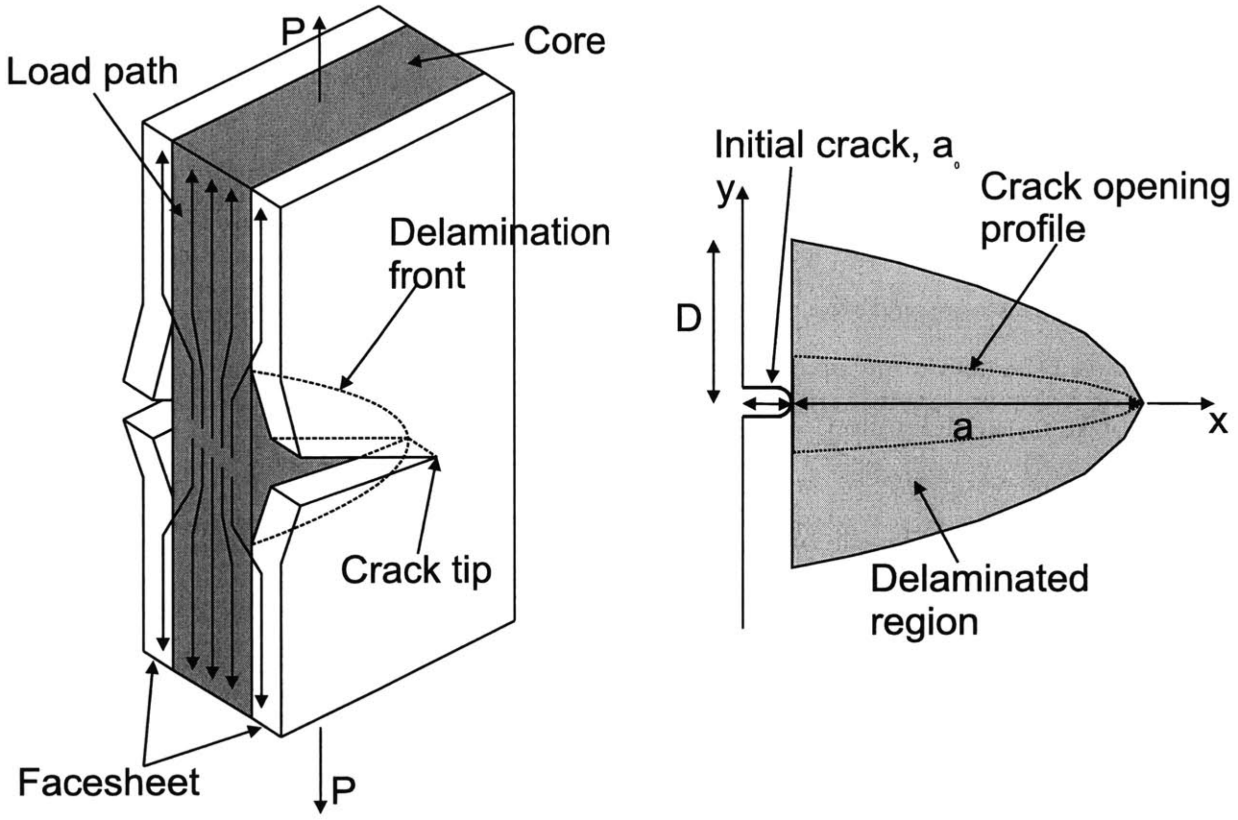

(a) 3D view of damage modes (b) Plan view of damage modes

Figure 5-1: Schematic of facesheet crack and delamination crack tip. Note that, although the model is described as being two-dimensional, some three-dimensionality exists in the model since the composite core and the facesheet are modeled as separate layers.

The model for the coupled growth of a facesheet crack and delamination utilizes models and experimental data obtained for the individual damage modes to determine the physical parameters governing the combined damage growth. The stress state interaction due to the two damage modes is captured via a finite element model. A potential benefit of using the models and the experimental observations of the individual damage modes as inputs for the coupled damage growth model is the ability to develop an understanding of the factors controlling the interaction of the two damage modes.

In order to keep the model simple enough to be useful in a material development or an accelerated testing program, a number of assumptions are made in calculating the crack growth. Firstly, it is assumed that the delamination profile maintains a self-similar shape, i.e. as the crack and the delamination propagate, the profile of the delamination remains the same and the growth of the delamination can be described by the growth at the root of the crack. Based on previous work [90, 96], an elliptical profile is chosen as the delamination profile. By choosing an elliptical profile, the bridging stresses in the wake of the crack are approximately constant along the length of the crack, thus making the calculation of the effective stress intensity factor more efficient. The ratio of delamination length to crack length, $\frac{D}{a}$, which is also the ratio of the elliptical axes, is allowed to vary in the bridged-crack model. Although the two damage modes are coupled, with the amount of coupling determined by the finite element model, they are allowed to propagate independently according to the physical growth laws determined using the experiments on the individual damage modes.

The two main parameters controlling the fatigue damage growth within each load cycle are the effective range of the stress intensity factor at the crack tip in the facesheet, ΔK_{eff}, and the range of the strain energy release rate for the delamination, ΔG. The effective stress intensity factor is controlled by the applied load and the bridging stresses along the crack front. The strain energy release rate is a function of the rate of change of compliance with respect to the area of delamination. Both parameters are calculated with the aid of the finite element procedure as described.

In the calculations of the bridging stresses and the strain energy release rate, the effects of thermally-induced residual stresses are ignored. The residual stresses are constant for each ply and are independent of the applied stress. Therefore, the effects of the thermal stresses cancel out in the calculation of the controlling fatigue fracture mechanics parameters, ΔG and ΔK_{eff}. However, the residual stresses will alter the effective R-ratio. The effects of R-ratio on the crack growth rate are discussed in more detail in Chapter 6.

5.2.2 Finite element model

The purpose of the finite element model is to provide a relationship between the physical damage mechanisms, i.e. the facesheet crack and the delamination, and the fracture mechanics parameters that control the growth of delamination. All finite element models for this research were conducted using the commercially available software, ABAQUS$^{\text{TM}}$ [110]. By executing the finite element model for a range of crack lengths and delamination lengths, while keeping the delamination profile constant, analytic expressions are determined relating the ratio of the delamination size to the bridged crack length with the fracture mechanics parameters. The analytic expressions can then be applied to calculate the bridging tractions and strain energy release rate for the current damage state without executing the full finite element model for each iteration of the crack growth model.

The model consists of two layers of two-dimensional, linear-elastic, eight-noded plane-stress continuum elements, one layer representing the titanium facesheet and the other layer representing the composite core. Both layers have the same mesh and node location. The base laminate for the models is TiGr 2-6-2 ($[\text{Ti}/0/90/0_2]_s$). The material properties for the constituent materials and for the composite materials, as determined by Classical Laminated Plate Theory (CLPT), are listed in Table 3.1. The symmetry of the specimen and the assumed symmetry of the damage modes allows for the use of a one-quarter finite element model for the single edge notch tension specimens (SENT). A schematic of the boundary conditions for SENT specimens is shown in Figure 5-2. Along the cracked edge, x-symmetric boundary conditions are applied to the composite layer and to the uncracked portion of the facesheet. A single node on the cracked centerline half way between the crack tip and the free edge of the specimen is constrained in the y-direction to eliminate rigid body modes during the analysis. The SENT boundary conditions are similar to those applied in [111].

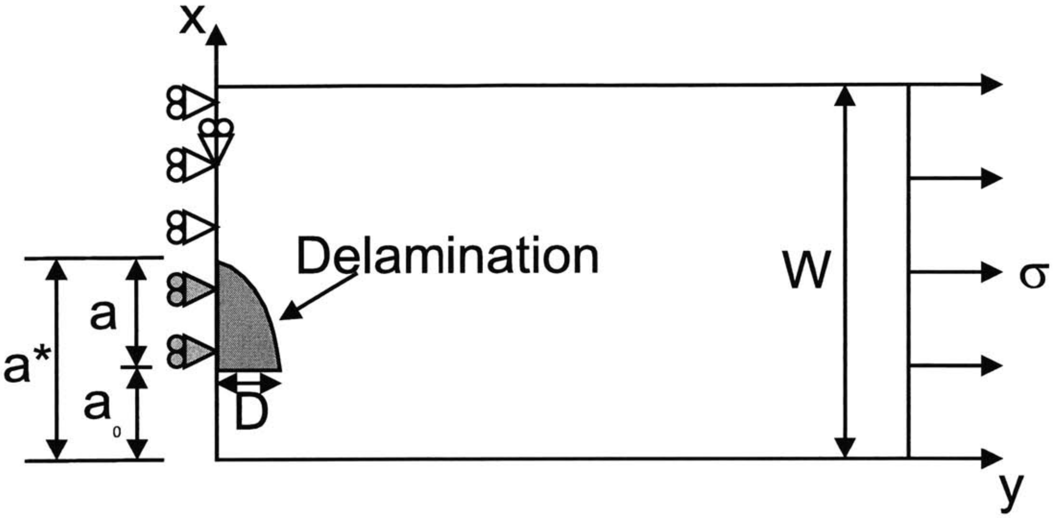

Figure 5-2: Finite element boundary conditions for the single edge notch tension model

A simple rectangular mesh is applied with 100 evenly distributed elements in the width direction and 50 evenly distributed elements in the length direction. The element size and mesh density is constant for all crack length and delamination profiles used in the bridged-crack model. A mesh refinement study was conducted and is discussed subsequently. In the undelaminated region, the nodes of the two layers are tied together using a multi-point constraint. In order to avoid distorting the elements, the delamination boundary is not modeled exactly. However, this was found not to affect the solutions obtained because of the global energy methods used to calculate the bridging tractions and the strain energy release rate.

Bridging force calculation

The bridging forces in the model are a critical component in the calculation of ΔK_{eff} and are calculated using the finite element model described in the previous section. The bridging forces in the finite element model are the reaction forces from the boundary conditions applied to the composite core in the cracked region. These boundary conditions are shown as shaded in Figure 5-2. Since it is assumed that the delamination profile is elliptical, the reaction forces in the cracked region are approximately constant along the length of the crack as discussed in Reference [82]. Although the bridging force distribution is slightly non-constant near the crack tip and near the crack root in the finite element model output, the distribution is constant for most of the length and is considered constant for the purposes of the bridged-crack model.

The total bridging force is calculated by summing the reaction forces along the crack front and is normalized by the far-field applied load. The normalized bridging force is plotted as a function of crack length and a linear regression is performed to obtain the best fit line. A typical plot of normalized bridging force as a function of crack length is shown in Figure 5-3 for $\frac{D}{a}$=1. Similar curves are determined for other values of $\frac{D}{a}$. Typically the R^2 value for the curve fits was 0.99 or higher. The slope of the curve fits are then plotted as a function of $\frac{D}{a}$ as shown in Figure 5-4 and an analytic expression, is determined for each laminate configuration:

$$\frac{d\left(P_{br}/P_{appl}\right)}{da} = A_1 + B_1\left(1 - \exp^{-C_1\frac{D}{a}}\right) \tag{5.1}$$

where:

P_{br} = total bridging forced

P_{appl} = applied load

a = crack length

A_1, B_1, C_1 = constants

The values of A_1, B_1, C_1 depend on the particular choice of the geometry and will be shown later. For the plot shown in Figure 5-4 the R^2 value is 0.999.

Strain energy release rate calculation

The strain energy release rate is assumed to be the key parameter determining the delamination growth behavior. The strain energy release rate for the facesheet delamination is obtained using a global compliance method discussed in Section 2.2.1. Neglecting the effects

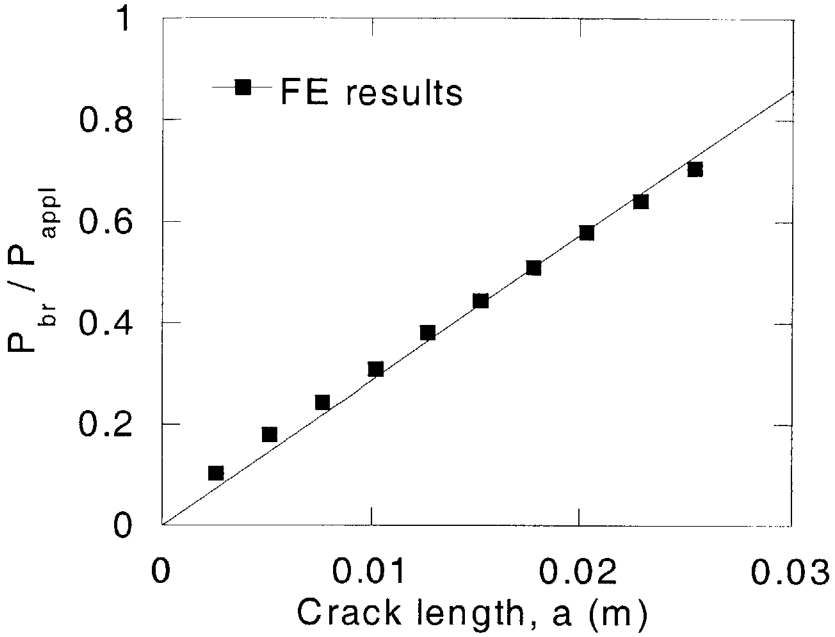

Figure 5-3: Normalized bridging force as a function of crack length for $\frac{D}{a}$=1

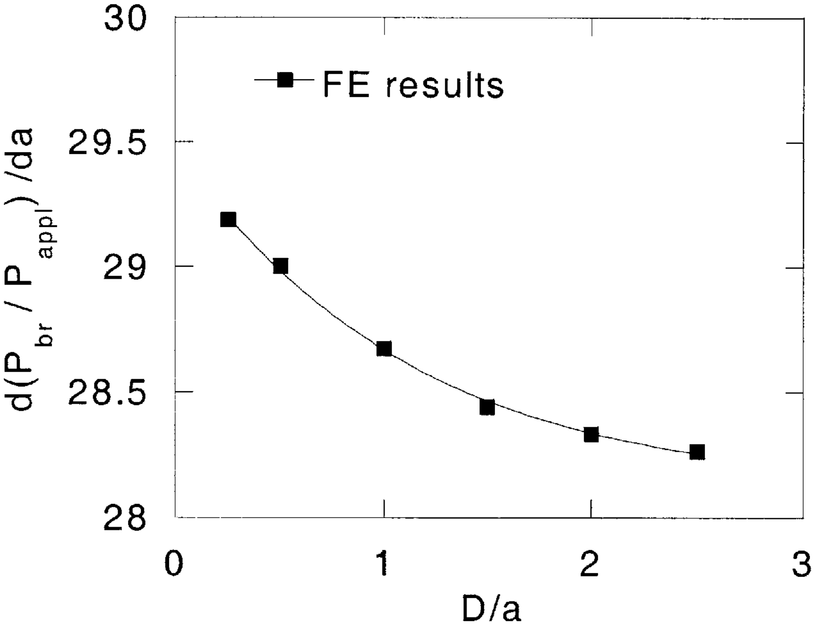

Figure 5-4: Normalized bridging force slope as a function of $\frac{D}{a}$

of thermal stresses, the general form for the strain energy release rate as a function of the rate of change of compliance, originally given as Equation 2.12, is:

$$G = \frac{1}{2} P^2 \frac{dC}{dA} \tag{5.2}$$

Due to the symmetry assumptions in the finite element model used to calculate the rate of change of compliance, it is necessary to apply a scaling factor to $\frac{dC}{dA}$. For example, if the specimen is modeled in the finite element procedure with half the actual length, the deflection due to the same applied load, P, is half that of the original specimen. The scaling factor for single edge notch specimens is 0.25 and can be calculated using:

$$\frac{dC}{dA} = \left(\frac{dC}{dA}\right)_{FEM} * \left(\frac{t_{FEM}}{t}\right)\left(\frac{L}{L_{FEM}}\right)\left(\frac{A_{FEM}}{A}\right) \tag{5.3}$$

where t is the thickness, L is the length, and A is the delamination area. The subscript FEM refers to the dimension of the finite element model. For example, if the thickness of the finite element model is one-half that of the actual specimen, the first term, $\frac{t_{FEM}}{t}$, in the scaling factor is one-half. The second term, $\frac{L}{L_{FEM}}$ is 2 because the finite element procedure only models half the length of the full model. The third term, $\frac{A_{FEM}}{A}$, which refers to the delamination area, is 0.25 for the single edge notch tension specimens because the finite element model only represents one quarter of the delamination area in the actual specimen.

A relationship between $\frac{dC}{dA}$ and $\frac{D}{a}$ is determined using a similar procedure to the one described previously for the bridging tractions. The compliance for a particular crack length and $\frac{D}{a}$ ratio is calculated by dividing the deflection at a far-field node, i.e. away from the crack and the delamination, by the total applied load. The compliance is plotted as a function of delamination area and a linear regression is performed to give the rate of change of compliance, $\frac{dC}{dA}$, for different values of $\frac{D}{a}$. A typical plot of compliance vs. area is shown in Figure 5-5. The R^2 values for the regression lines shown in Figure 5-5 are all greater than 0.99. It is important to note that the area calculated is only that of the delamination and does not include the area of crack surface created in the facesheet. This is appropriate because the delamination area is much larger than that of the facesheet crack. For a 17 mm crack, not including the starter notch, with a $\frac{D}{a}$ ratio of 1, the delamination area is 908 mm^2 and the crack area is 2.1 mm^2. A typical plot of $\frac{dC}{dA}$ vs. $\frac{D}{a}$ is shown in Figure 5-6. The R^2 values for the regression curve shown in Figure 5-6 is greater than 0.999. The rate of change of compliance is plotted as a function of $\frac{D}{a}$ and a regression of the same form as that in Equation 5.1 is performed giving an analytic relationship between $\frac{dC}{dA}$ and $\frac{D}{a}$ which can be used in the crack growth simulation.

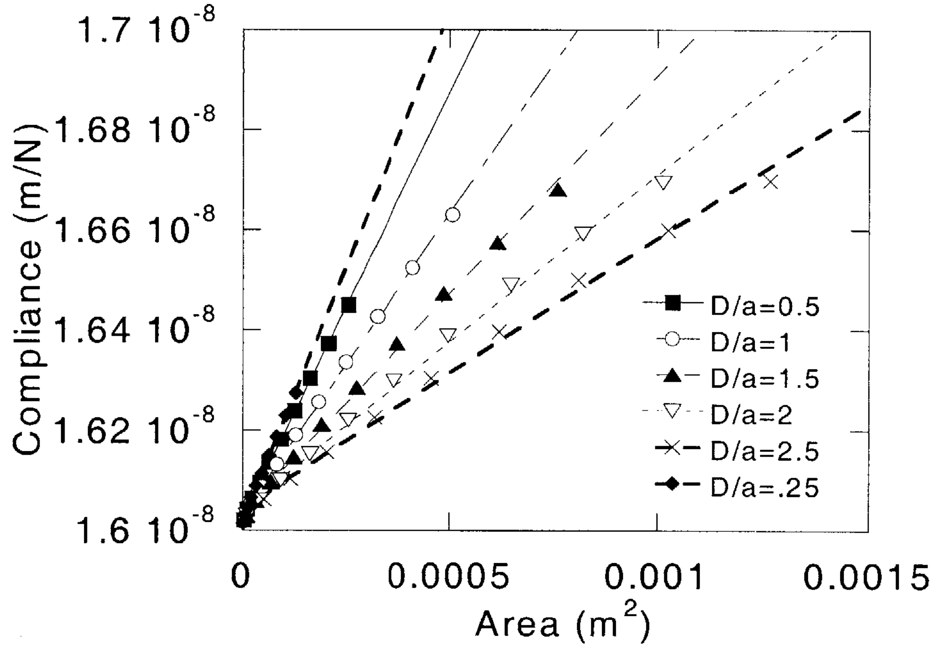

Figure 5-5: Compliance vs. area plot from finite element results for $[Ti/0/90/0_2]_s$ laminate.

Verification and mesh refinement

A mesh refinement study was conducted for both the length and the width directions to determine the correct size of the mesh. The study was conducted on single-edge notched tension (SENT) TiGr specimens with a width of 38.1 mm and a half-length of 76.2 mm. Successively finer mesh densities were implemented independently for the length and the width directions. Three successively finer mesh densities were tried in the x-direction, 25, 50, and 100 elements, holding the number of elements along the y-direction at 50-elements.

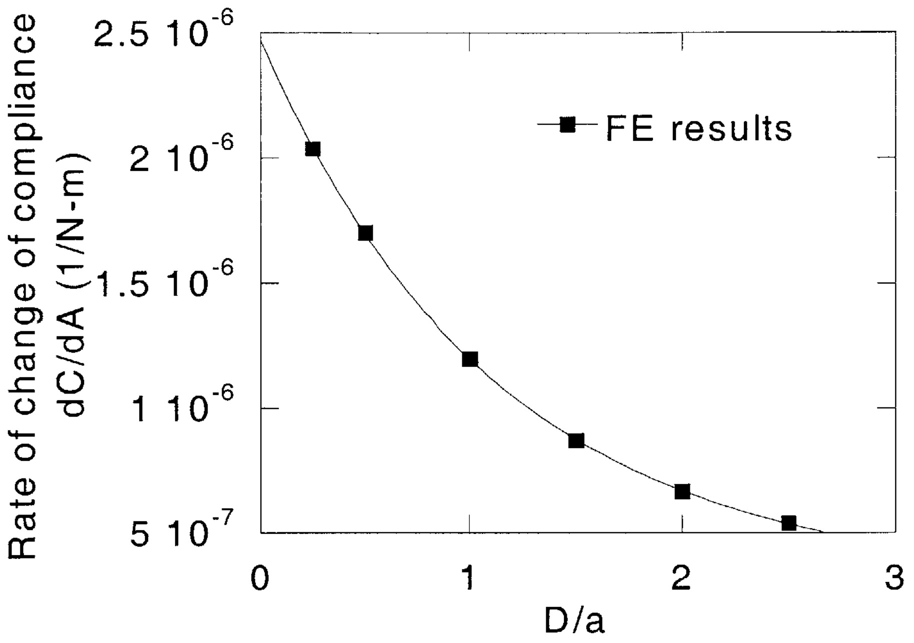

Figure 5-6: Rate of change of compliance as function of $\frac{D}{a}$

The difference between the 50-element run and the 100-element run for both the bridging force slope and the rate of change of compliance is less than 0.35% for all values of $\frac{D}{a}$ recorded. A similar study was conducted in the y-direction, i.e. along the crack front, with 25, 50, 100, and 150 elements while holding the number of elements along the x-direction at 50 elements. The difference between the 100-element run and the 150-element run was less than 0.2% for all values of $\frac{D}{a}$ recorded. The mesh size for the bridged crack model was 50 elements along the x-direction and 100 elements along the y-direction.

5.2.3 Model execution

The results of the finite element analysis are applied, along with the experimental results on the individual damage modes, using an iterative code to determine the fatigue crack growth behavior. This section provides an overview of the steps in the iterative code. The two principal steps in the procedure are the calculation of the crack growth rate in the facesheet and the delamination growth rate between the facesheet and the core. Once these two values are calculated, they are applied for a block of cycles, N, and the crack and the delamination are extended accordingly and the procedure is repeated. Numerical inputs from the finite element model and from the previous experiments [112] are given for the specific case of a $[\mathrm{Ti}/0/90/0_2]_s$ laminate in a single-edge notch configuration, with a width, W, of 38.1 mm, a length, L, of 152.4 mm, and a through-thickness starter notch, a_0, of 2 mm.

For a given value of the crack length, a, and the delamination length, D, the growth rate of the delamination, $\frac{dD}{dN}$, is calculated by determining the strain energy release rate from the FEM results and inserting the value into the power-law relationship relating the fatigue delamination growth rate to the applied strain energy release, ΔG, determined experimentally [112]. It is implicitly assumed that the Paris regime for fatigue crack growth holds. The relationship from the FEM procedure relating $\frac{D}{a}$ to the rate of change of compliance, in units of 1/N-m, for the specific example described above and shown in Figure 5-6 is:

$$\frac{dC}{dA} = 2.72 \cdot 10^{-6} + 2.38 \cdot 10^{-6} \left(1 - \exp^{-0.89\frac{D}{a}}\right) \tag{5.4}$$

Equation 5.4 is inserted into Equation 5.2 to determine the value of the strain energy release rate, G. The form of the power-law relationship relating fatigue delamination growth rate to the applied strain energy release rate is:

$$\frac{dD}{dN} = B\left(\Delta G\right)^m \tag{5.5}$$

The values for the constants B and m for different test temperatures are given in Table 4.1. The units for ΔG in Equation 5.5 are N/m and the units for $\frac{dD}{dN}$ are m/cycle.

Referring to Figure 5-1(b), the value of D, the delamination length, is taken to be the value at the root of the delamination. It is assumed that the shape of the delamination remains constant, i.e. elliptical, and that the growth of the delaminated region can be described by the growth at the root. Although the shape of the delamination remains elliptical, the aspect ratio of the ellipse, i.e. $\frac{D}{a}$, is allowed to vary as the damage propagates. Experimental observations show that in the base laminate, no delamination growth is evident in the "shadow" of the starter notch, i.e. the strip of material from the free edge to the tip of the initial through-thickness notch, parallel to the loading axis.

The effective stress intensity factor range involves two components, the applied stress intensity factor, ΔK_{appl}, and the stress intensity factor due to the bridging, ΔK_{br}. Since it is assumed that the material behaves linearly elastic, the two parameters can be combined using superposition as shown below, which is the same as Equation 2.22.

$$\Delta K_{eff} = \Delta K_{appl} + \Delta K_{br} \tag{5.6}$$

The applied stress intensity factor is calculated using the relationship from Tada [74] for a single edge notch tension specimen with a finite width:

$$K_{appl} = \sigma_{Ti}\sqrt{\pi a^*}\, F\left(\frac{a^*}{W}\right) \tag{5.7}$$

$$F\left(\frac{a^*}{W}\right) = \frac{\sqrt{\frac{2W}{\pi a^*}\tan\frac{\pi a^*}{2W}}}{\cos\frac{\pi a^*}{2W}}\left(0.752 + 2.02\left(\frac{a^*}{W}\right) + 0.37\left(1 - \sin\frac{\pi a^*}{2W}\right)^3\right) \tag{5.8}$$

where:

K_{appl} = applied stress intensity factor in the titanium facesheet

σ_{Ti} = stress in titanium layer determined by CLPT

a^* = a_0+a =total crack length (including the sum of the initial notch, a_0, and the bridged crack length, a)

W = specimen width

The other component of the effective stress intensity factor is a result of the composite plies bridging the facesheet crack. The total bridging force is determined from the results of the finite element procedure. For the specific example outlined above, the relationship between $\frac{D}{a}$ and the normalized bridging force slope, in units of m^{-1}, is:

$$\frac{d(P_{br}/P_{appl})}{da} = 29.5 + 1.37\left(1 - \exp^{-0.90\frac{D}{a}}\right) \tag{5.9}$$

Using Equation 5.9, the slope of the normalized bridging force vs. crack length relationship can be determined for the current value of $\frac{D}{a}$. Given the current crack length, the normalized bridging force is calculated and multiplied by the total applied force to obtain the total bridging force. Because it was assumed that the bridging forces were constant along the entire length of the crack, the bridging tractions can be calculated by dividing the total bridging force by the crack length.

The contribution of the bridging traction to the effective stress intensity factor is calculated using a formula from Tada [74] for a point load acting on the crack face. Because the bridging force is assumed to be constant along the entire length of the crack, the value of the point load is the total bridging force divided by the bridged crack length. The relationship for the point load is integrated numerically using the trapezoidal method along the crack face from the starter notch, a_0, to the tip, a^*. A schematic of the configuration is shown in Figure 5-7 for the single edge notch configuration and is calculated using the following set of equations:

$$K_{br} = \int_{a_0}^{a^*} \frac{2\overline{P}}{\sqrt{\pi a^*}} F\left(\frac{a}{W}\right) C_{ba}\, dx \tag{5.10}$$

$$\overline{P} = \frac{P_{br}}{t_{lam}\left(a^* - a_0\right)} \tag{5.11}$$

$$\begin{aligned} F\left(\frac{a}{W}\right) &= 3.52\frac{\left(1-\frac{x}{a^*}\right)}{\left(1-\frac{a^*}{W}\right)^{\frac{3}{2}}} - \frac{4.35-5.28\frac{x}{a^*}}{\left(1-\frac{a^*}{W}\right)^{\frac{1}{2}}} + \\ & \left[\frac{1.3-0.3\left(\frac{x}{a^*}\right)^{\frac{3}{2}}}{\sqrt{1-\left(\frac{x}{a^*}\right)^2}} + 0.83 - 1.76\frac{x}{a^*}\right]\left[1-\frac{a^*}{W}\left(1-\frac{x}{a^*}\right)\right] \end{aligned} \tag{5.12}$$

$$C_{ba} = \frac{1}{3}\left[\frac{5}{\left(1+\frac{D}{a}\right)} - \frac{2}{\left(1+\frac{D}{a}\right)^2}\right] \tag{5.13}$$

where:

K_{br} = stress intensity factor due to bridging

P_{br} = total bridging load

t_{lam} = laminate thickness

x = distance from the specimen edge to the point load (see Figure 5-7)

W = specimen width

The loads considered in calculating the bridging stress intensity factor are only those carried in the facesheet, as determined by CLPT. The term C_{ba} is an additional correction term which is necessary for the configuration shown in Figure 5-7 to be applied to the modeled configuration of a facesheet crack with a delamination in the wake. Due to the presence of the delamination, the bridging tractions do not act directly on the crack flanks, as described in the Tada solution. In reality, the tractions act at the delamination front between the facesheet and the core. The correction term, shown in Equation 5.13 is derived from Tada [74] and is described in [82]. Note that for each cycle, ΔK_{br} involves the total bridging load range, ΔP_{br}.

Once the effective stress intensity factor is calculated, the fatigue crack growth rate can be calculated using experimental results from monolithic titanium. The monolithic experiments were conducted by Boeing [106] for Ti 15-3 and the results are shown in Figure 5-8. The power-law relationship between fatigue crack growth rate at ambient conditions, in units of

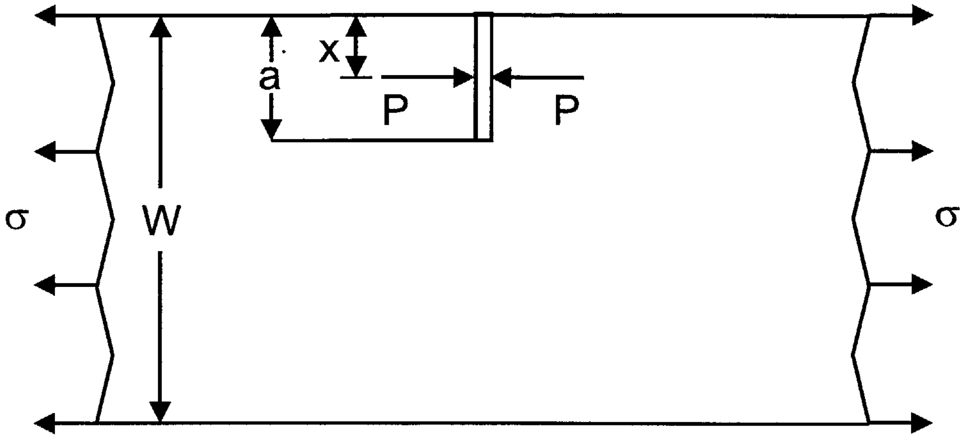

Figure 5-7: Schematic for the calculation of stress intensity factor due to a point load acting on the crack face

m/cycle, and stress intensity factor, in units of MPa$\sqrt{\text{m}}$, is:

$$\frac{da}{dN} = 8.66 \cdot 10^{-11} \left(\Delta K_{eff}\right)^{2.66} \tag{5.14}$$

Once the growth rates for the delamination and the facesheet growth are determined, they are multiplied by N to obtain the extension for the iteration, where N represents a block of cycles. As long as N was less than approximately 0.5% of the total expected life cycles, the results of the simulation were not affected significantly. The delamination and the crack are extended by the calculated amount and the procedure is repeated for the new values of the crack and delamination lengths. The results of the bridged-crack model are discussed in the next section in comparison to the 3D finite element model results.

5.2.4 Influence of model inputs

The model presented in this section is dependent on the input from the individual damage mode experiments. A study was conducted to determine the influence of the model inputs. The Paris Law constants from the monolithic facesheet crack growth experiments, c and m with a subscript 1, and the delamination growth experiments, c and m with a subscript 2,

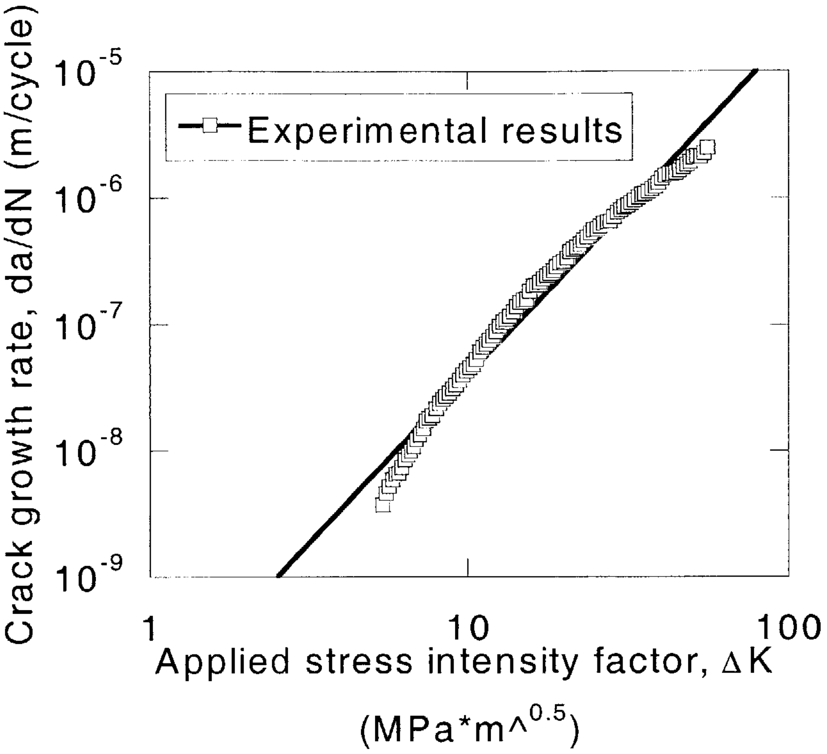

Figure 5-8: Experimental crack growth results for monolithic Ti 15-3 sheet [106]

were systematically altered by ±10% to determine the effect on the model results. Figures 5-9(a) and 5-9(b) show the results from the study. The model results are represented as continuous curves in Figures 5-9(a) and 5-9(b). However, the curves are constructed by connecting a series of individual data points determined during the execution of the model.

Changing the leading coefficients, c_1 and c_2, did not alter the model results significantly. However, changing the exponents m_1 and m_2 did alter the results, suggesting that the key parameter to capture in the individual damage mode experiments is the power law exponent. This percentage difference from the baseline model is shown in Tables 5.1 and 5.2 for a few values of the applied stress intensity factor in the titanium facesheet.

5.3 Three-dimensional modeling

To validate the results from the bridged-crack model, a three-dimensional finite element model was constructed to determine the stress intensity factor at the crack tip for facesheet cracks in TiGr laminates. By comparing the stress intensity factor at the crack tip for dif-

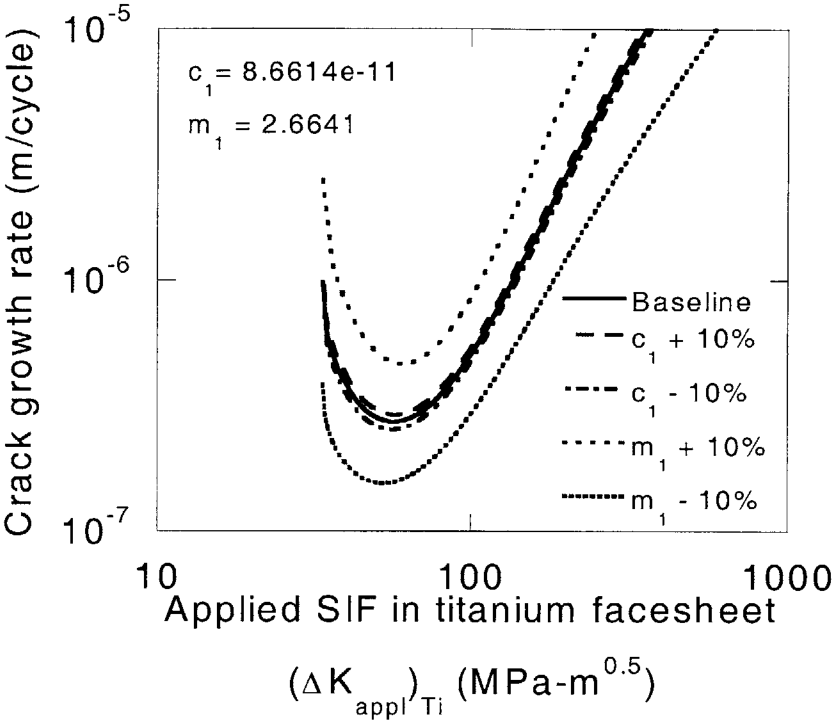

(a) Influence of Paris' law constants for facesheet crack growth

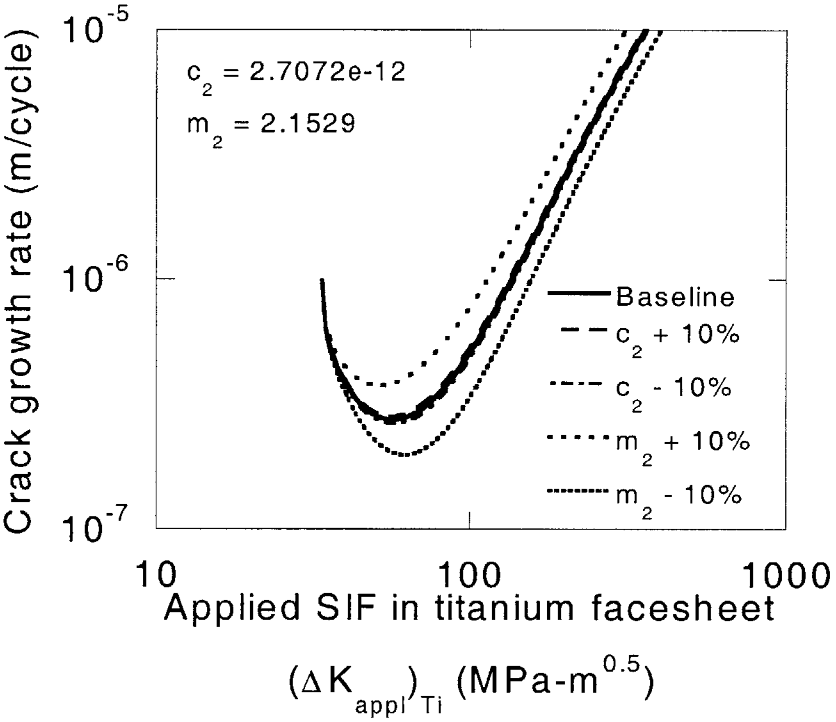

(b) Influence of Paris' law constants for delamination growth

Figure 5-9: Parametric study on influence of model inputs

Table 5.1: Influence of Paris law constants for facesheet crack growth

Applied SIF	% change from baseline			
(MPa-m$^{0.5}$)	c_1+10%	c_1-10%	m_1+10%	m_1-10%
33.3	10	-10	154	-61
56.5	6.7	-6.9	72	-43
100	6	-6.8	68	-42
200	7.3	-9.4	108	-53

Table 5.2: Influence of Paris law constants for delamination growth

Applied SIF	% change from baseline			
(MPa-m^{0}.5)	c_2+10%	c_2-10%	m_2+10%	m_2-10%
33.3	0	0	0	0
56.5	3.1	-3.3	40	-26
100	4.2	-4.4	53	-33
200	1.2	-3.3	42	-28

ferent material properties and damage configurations, the regions of validity for the bridged-crack model can be determined.

5.3.1 Model setup

In order to minimize the execution time and memory requirements for the model, a hierarchical approach is used for the 3D modeling. A global model, with a relatively course mesh, is constructed for the entire specimen from 8-noded solid elements. The model was executed using the commercial finite element code, ABAQUS™ [110]. The specimen modeled has a total width of 38.1 mm and a half length of 76.2 mm. There were 60 elements uniformly distributed in the width direction. Along the length direction, there were 60 elements uniformly distributed along the 38.1 mm nearest the crack and 30 uniformly distributed elements for the remaining 38.1 mm. Each ply in the global model is modeled with a single element through the thickness. Since the configuration is symmetric, only half of the length and half of the thickness are modeled with the symmetry boundary conditions applied along the midline and the mid-plane of the model. The delamination is modeled in a manner similar to the bridged-crack model where coincident nodes are created along the delaminated surface and tied together in undelaminated regions. For the 3D cases, the delamination-to-crack ratio is assumed to be constant with a value of one ($\frac{D}{a}$=1), which is consistent with the experimental observations presented in Chapter 6. In addition, the delamination profile was assumed to be triangular, as opposed to elliptical in the bridged-crack model, which is also more consistent with the experimental evidence shown in Chapter 6. The effects of these two assumptions are discussed later. The facesheet crack is modeled by eliminating the symmetric boundary condition in the cracked region. A constant stress is applied at the end of the specimen.

The second step of the hierarchical model is the development of the local model. A local model is constructed around the crack tip using eight-noded solid elements as in the global model. The model has 50 elements along the crack path and 25 elements perpendicular to the crack path. Each element, except for those surrounding the crack tip which are discussed below, is 0.0254 mm square on the faces of the specimen. This is equivalent to 20% of the ply thickness of the titanium ply in the base laminate. The local model covers the space of two elements along the crack direction and one element along the length direction of the global model, with the crack tip located at the centerline of the local model. The nodes on either side of the crack tip are shifted to the quarter point, to capture the singular stresses near the crack tip more accurately. Through the thickness, the model consists of ten elements for the titanium facesheet ply, ten elements for the first composite ply, and one element for the other composite plies. The facesheet and the first composite ply have a high density through the thickness because they have the largest influence on the stress intensity factor, and hence the crack growth rate. The boundary conditions for the local model are determined from the displacement results of the global model. Verification of the mesh density and the hierarchical procedure is discussed subsequently.

5.3.2 Virtual crack closure technique

The results from the local model are used to determine the stress intensity factor at the crack tip using the virtual crack closure technique (VCCT) [113]. The VCCT uses nodal forces for the node ahead of the crack tip and the nodal displacements for the node behind the crack tip to calculate the strain energy release rate. For each layer of elements through the thickness of the facesheet plies, the forces and displacements of the appropriate nodes are determined from the finite element model. A 2D schematic of the VCCT procedure is shown in Figure 5-10. Using the VCCT the strain energy release rate, G, is determined using:

$$G_{VCCT} = \frac{1}{r\,t}\left(u_x \cdot F_x\right) \tag{5.15}$$

where:

u_x = displacement one node behind the crack tip

F_x = nodal force one node ahead of the crack tip

r = element width along crack path

t = element thickness

Since it is assumed that the problem is linear elastic and essentially plane stress in nature, the stress intensity factor (SIF) is related to the strain energy release rate and the facesheet modulus, E_{Ti}, using:

$$K = \sqrt{E_{Ti}\, G_{VCCT}} \tag{5.16}$$

A typical result from the 3D FEM for a given crack length, is shown in Figure 5-11 with the normalized stress intensity factor, K, plotted as a function of the normalized location through the facesheet thickness $(\frac{z}{t_{Ti}})$ where t_{Ti} is the facesheet thickness, z is the coordinate through the thickness of the facesheet with $z = 0$ at the outer surface and $z = t_{Ti}$ at the interface with the PMC core. The stress intensity factor is normalized by the applied far-field stress *in the facesheet*, σ_{Ti}, multiplied by the square root of the facesheet thickness $(\sigma_{Ti}\sqrt{t_{Ti}})$. The normalization was performed to easily compare the results for laminates with different facesheet properties. Note that as with the bridged-crack model, a scaling factor needs to be applied to the FEM results to calculate the actual value of the strain energy release rate,

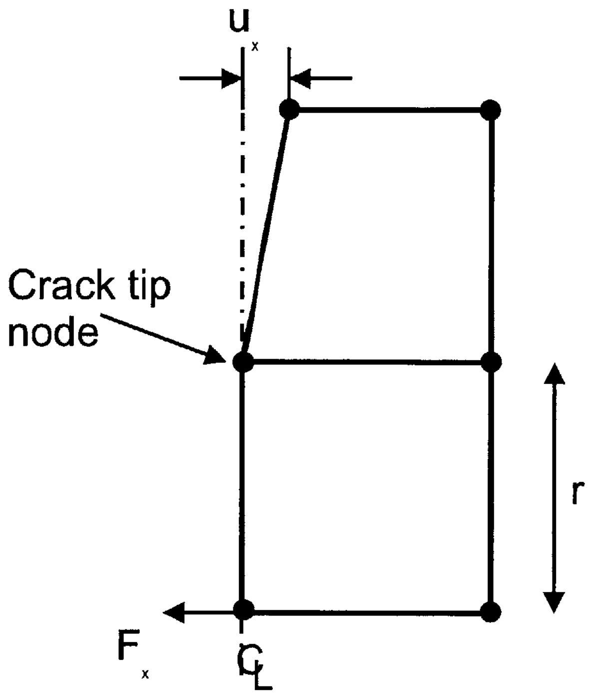

Figure 5-10: Schematic of virtual crack closure technique

which for the symmetry conditions discussed previously is two.

Mesh refinement

To check the mesh refinement and the validity of the two-step hierarchical model a three-step procedure was implemented for comparison. An additional model is constructed with dimensions between those of the global model and the local model for a select case. The boundary conditions for the mid-level mesh are derived from the results of the global model and the boundary conditions for the local model are then derived from the results of the mid-level model. The mesh for the mid-level model spans 4 elements of the global model on either side of the crack tip in the width direction and 4 elements of the global model in the length directions, with an element size of 0.1 mm. Through the thickness, the number of elements is the same as the local model described previously. The elements in the local model span 12.5 elements in the width direction and 6.25 elements in the length direction from the mid-level model. A second three-step model is conducted with the in-plane elements in the local model reduced in size by half. For the case with a total crack length, a^*, of 19 mm, the

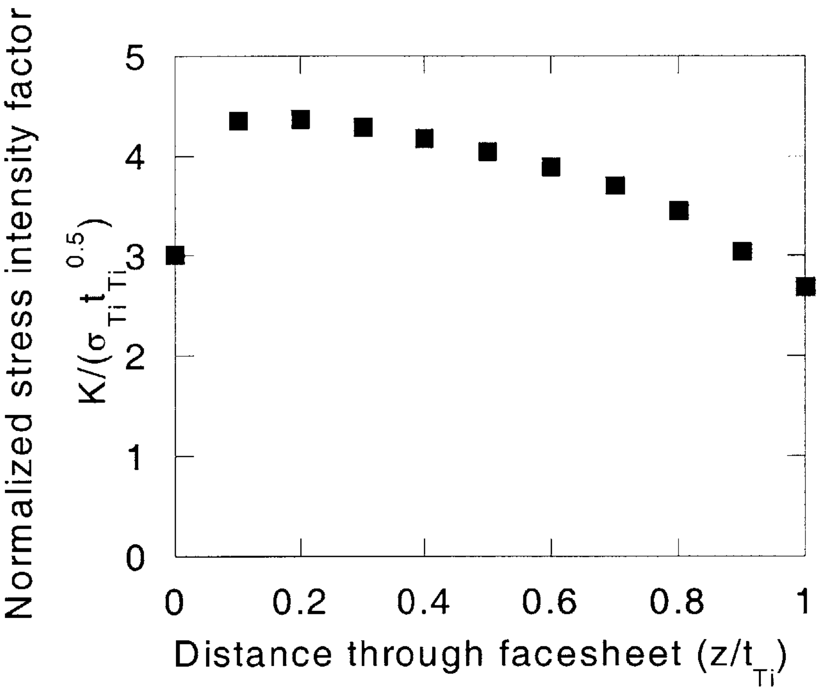

Figure 5-11: Profile of stress intensity factor through thickness from 3D VCCT model for $[Ti/0/90/0_2]_s$ laminate with a 19 mm crack, $\frac{D}{a} = 1$. (The interface with the PMC is at $\frac{z}{t_{Ti}}$=1 and the free surface of the facesheet is at $\frac{z}{t_{Ti}}$=0)

comparison between the two-step and the three-step models is shown in Figure 5-12. The element size in the local model for both the two-step and coarse three-step model results is 0.0254 mm and the element size for the more refined three-step model is 0.0127 mm. The difference between the average stress-intensity factor through the thickness for the three-step model with the smaller elements and the two-step model is less than 1%. Therefore, the two-step hierarchy is valid and is used for this analysis

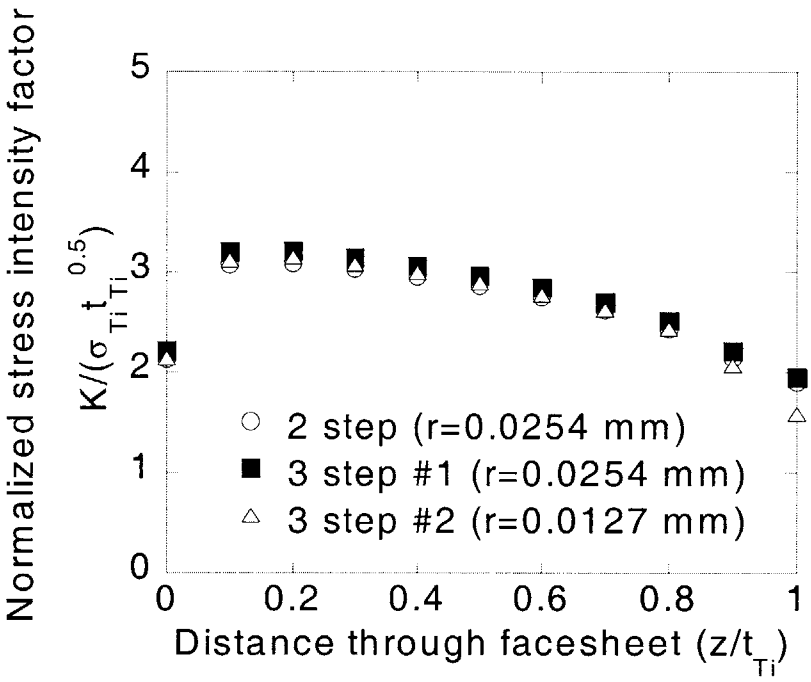

Figure 5-12: Stress intensity factor comparison between two-step and three-step hierarchical 3D model

Crack tip plasticity

To determine if plasticity at the crack tip affects the crack growth behavior, a plastic analysis was conducted on the three-dimensional model. A simple model was applied with a bilinear stress-stress strain curve with the break point at the yield stress of the monolithic titanium (1100 MPa). The elastic modulus of the facesheet modulus in the plastic region is estimated to be one-fifth of the elastic modulus. The estimation was made based on a stress-strain curve for Ti 15-3 [104]. The model was executed at a total applied load of 419

MPa. Initially, the model was executed without including the thermally-induced residual stresses, and indicated not plastic deformation occurred. In a second run of the model, the thermally induced residual stresses were included for room temperature conditions. Figure 5-13 shows the equivalent plastic strain (PEEQ) for the local model on the top surface of the facesheet, as determined from the finite element model. The top surface represents the largest extent of plasticity because the surface at the interface with the composite core is heavily constrained by the core. The effective stress intensity factor for the surface layer of elements is approximately 13.8 MPa$\sqrt{m}$. The different bands in Figure 5-13 indicate different levels of plastic strain in the facesheet. The total plastic zone extends approximately two elements, 0.05 mm) or 40% of the facesheet thickness, ahead of the crack tip.

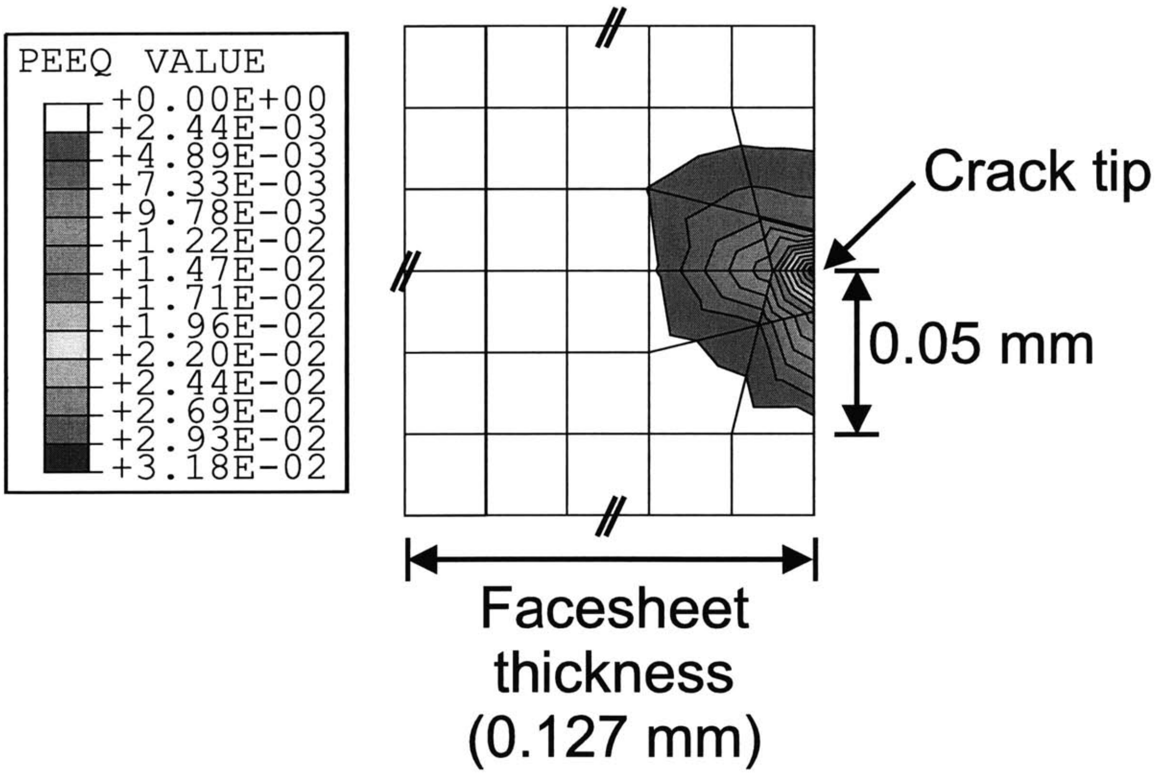

Figure 5-13: Finite element results showing equivalent plastic strain (PEEQ) on the facesheet surface with a crack length, a^*, of 19 mm and a total applied stress of 419 MPa

In addition to the finite element model, the size of the plastic zone was estimated using the Irwin plastic zone approximation for plane stress:

$$r_p = \frac{1}{\pi}\left(\frac{K_{eff}}{\sigma_y}\right)^2 \tag{5.17}$$

where:

r_p = plastic zone size

K_{eff} = effective stress intensity factor at the crack tip
(≈13.8 MPa$\sqrt{m}$ for the conditions and location through the thickness
shown in Figure 5-13)

σ_y = facesheet yield stress (≈1100 MPa for Ti 15-3 [106])

The plastic zone size calculated using Equation 5.17 is 0.05 mm. This is comparable to the values from the finite element model shown in Figure 5-13. Their is some concern in the use of stress intensity factors to describe the crack growth. To determine if the stress intensity field is a valid parameter, the computed stress levels ahead of the crack tip were compared to the asymptotic elastic approximation given by:

$$\sigma_{11} = \frac{K}{\sqrt{2\pi r}} \tag{5.18}$$

where:

σ_{11} = stress parallel to the loading axis

K_I = stress intensity factor at the crack tip as determined from the finite element model
(≈13.8 MPa$\sqrt{m}$ for the conditions and location through the thickness
shown in Figure 5-13)

r = distance ahead of the crack tip

The results of the comparison are shown in Figure 5-14. The asymptotic elastic solution underestimates the finite element solution by less than 10% in a region 0.07 mm ahead of the crack tip. This is approximately the maximum domain of K-dominance [114] and is larger than the plastic zone size. Assuming that the grain size is sufficiently small, the material in this region can be considered homogeneous, and therefore the stress intensity factor in the Paris Law relationship is valid for describing the fatigue crack growth for this configuration.

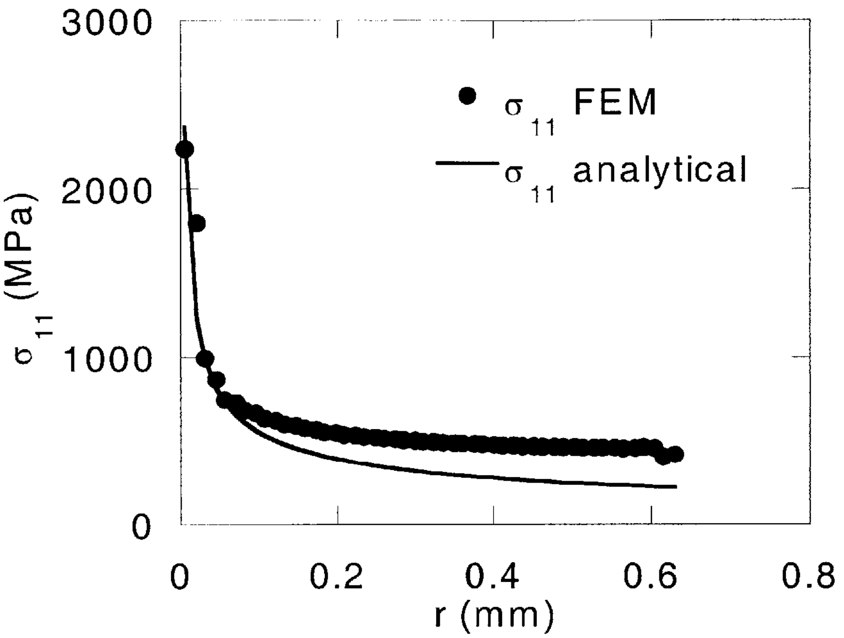

Figure 5-14: Comparison between the stresses predicted by the approximate analytic solution and the the stresses predicted using the finite element model in order to determine the region of K-dominance

Another way to look at the validity of the Paris Law is to compare the plastic zone size to the facesheet thickness. The data in Figure 5-8, which was used to determine the power law expression in Equation 5.14, was generated from experiments on monolithic Ti 15-3 with a thickness of 1.3 mm. The maximum value of K in Figure 5-8 is 57 MPa$\sqrt{m}$ (R=0.1, ΔK=51 MPa$\sqrt{m}$). The maximum value is used in calculating the plastic zone size in order to be consistent with the values used in the finite element analysis shown above. Assuming that the maximum value for stress intensity factor shown in Figure 5-8 defines the upper limit for the applicability of the Paris' Law relationship and applying Equation 5.17, K=57 MPa$\sqrt{m}$ corresponds to a plastic zone size of 0.85 mm or 67% of the thickness of the facesheet. Relative to the facesheet thickness, this is similar in size to the plastic zone in TiGr facesheets for the example shown above, indicating that the Paris Law relationship is valid for TiGr facesheets with similar effective stress intensity factors. The crack length used in the above example for TiGr laminates is in the steady-state growth regime where the crack growth rate is approximately constant, as will be shown in Chapter 6. For shorter cracks within the influence region of the initial notch, the effective stress intensity factor is higher and therefore the plastic zone is larger. In these regions, the use of the Paris relationship will begin to break down. However, the length of the influence region is small compared to the specimen width for the examples considered here. Therefore, the errors in calculating the crack growth behavior should be small.

Another factor that may influence the size of the plastic zone is temperature. For Ti-β21S, which is a similar allow to Ti 15-3, the yield stress is 25% lower at 204° C compared to the room temperature (24° C) value [115]. Assuming that temperature affects the yield stress of Ti-15-3 in a similar manner, the yield stress is reduced by approximately 20% at a temperature of 177° C. However, the thermally-induced residual stresses in the facesheet will be lower at elevated temperatures.

5.4 Comparison of model results

The purpose of constructing the 3D model is to validate the results of the bridged-crack model. When comparing the bridged-crack model results to the 3D results, the 3D stress intensity factor is taken as the average value calculated from the distribution of the stress intensity factor through the thickness. Figure 5-15 shows the comparison for the base $[\mathrm{Ti}/0/90/0_2]_s$ laminate, with a fixed $\frac{D}{a}$ ratio of 1. Both the bridged-crack model and the VCCT model are executed for discrete values of the crack length. While the results from the bridged-crack model initially decrease and then increase as the crack length increases, the results from the 3D model initially decrease and then level off at a constant value of stress intensity factor. This indicates that the bridged-crack model is not accurately describing the effective stress intensity factor, and hence the crack growth rate, for this configuration. This section attempts to determine the source of the discrepancy between the bridged-crack model and the three-dimensional VCCT model.

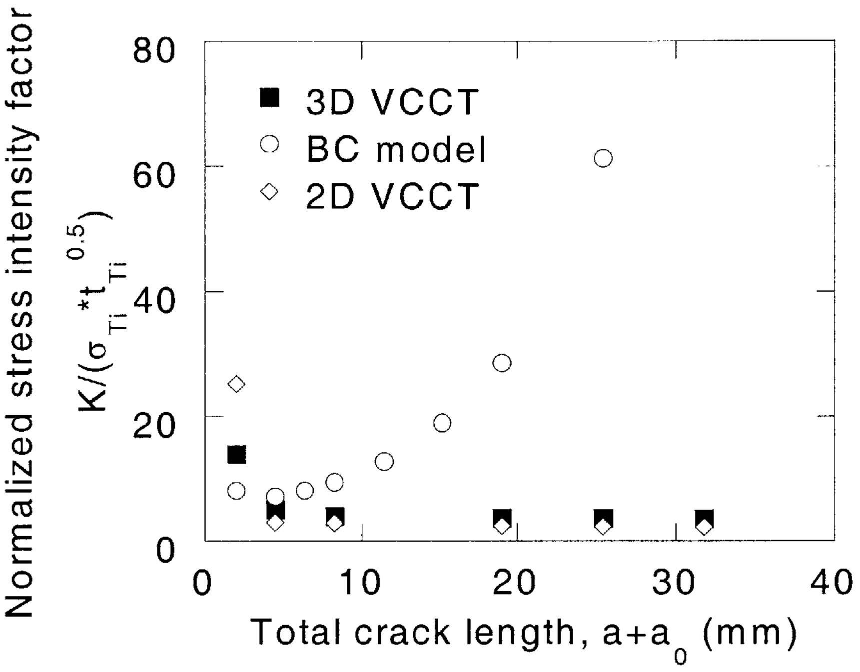

Figure 5-15: Comparison of bridged-crack(BC) model and 3D VCCT model for $[Ti/0/90/0_2]_s$ laminate

5.4.1 Application of VCCT to 2D model

The bridged-crack model assumes that the stress intensity factor does not vary with thickness. The 3D model shows some variation, as indicated in Figure 5-11, which is most significant near the free surface and the interface with the composite core where the variation from the mean value of the stress intensity factor is approximately 28%. In addition, the bridged-crack model is inherently two-dimensional and through-thickness stresses and strains are not included in the analysis. To evaluate the effect of these variables, a 2D finite element model using the virtual crack closure technique was used to calculate the stress intensity factor. The same hierarchical procedure was applied as in the three-dimensional VCCT model. The elements for the 2D VCCT model were 4-noded, plane stress elements configured in two layers, one representing the core and one representing the facesheet. As in the previous models, the delamination was represented by tying the nodes of the two layers together in the undelaminated regions. The 2D global and local models use the same in-plane element dimensions as the corresponding 3D model, with the boundary conditions for the local model determined from the results of the global model. Because the nodes of the layers were co-located in the 2D VCCT model, the boundary conditions for the local model were applied manually in the input file using displacement boundary conditions.

The results in Figure 5-16 show that the trend in the stress intensity factor predicted by the 2D VCCT model is the same as that of the 3D model, i.e. the stress intensity factor initially decreases and then approaches a constant value as the crack length increases. However, the magnitude of the stress intensity factors predicted using the 2D VCCT model are consistently 60% of the average stress intensity factor predicted using the 3D VCCT model, except for short cracks near the initial notch. The fact that the 2D and 3D VCCT analyses produce similar trends indicate that the dimensionality of the model is of lesser importance and other factors are causing the discrepancies observed between trends predicted using the bridged-crack model and the trends predicted using the virtual crack closure model. The comparisons presented in this research are conducted using results from the 3D VCCT model.

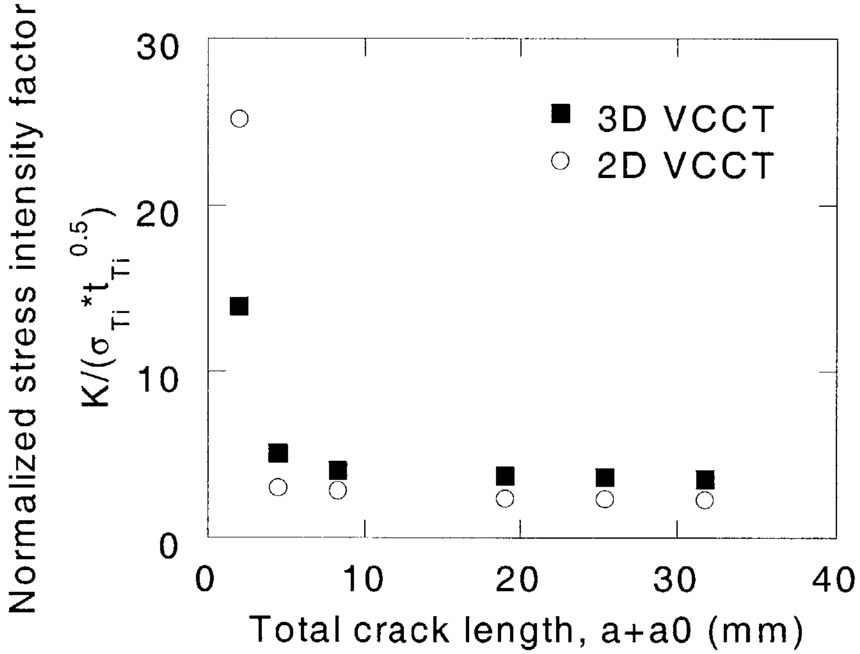

Figure 5-16: Comparison of 2D VCCT model and 3D VCCT model for $[Ti/0/90/0_2]_s$ laminate

5.4.2 Effect of delamination and bridging stresses near the crack tip

In order to understand the viability and usefulness of the bridged-crack model for TiGr and for similar composites, it is important to determine under what conditions the bridged-crack model is valid. The results presented thus far indicate that the bridged-crack model is not valid for predicting facesheet crack growth in TiGr laminates. One area that may not be captured well by the bridged-crack model is the full effect of the delamination and the bridging forces near the crack tip. The global nature of the bridged-crack model requires that the details of the delamination and the bridging forces near the crack tip are not explicitly modeled. The delamination profile is assumed to be constant and "smooth" over the crack length and the bridging forces are assumed to be constant over the entire crack length.

Delamination

Figure 5-17 compares the crack growth rate from the bridged-crack model for an elliptical and a triangular delamination shape, showing no significant difference between the predictions for the two cases. Figure 5-18 compares the same two situations using the 3D model, which indicates a significant effect of changing the delamination shape. In addition, the 3D results for a triangular delamination with $\frac{D}{a} = 0.5$ and $\frac{D}{a} = 2$ are also included.

From the results of the bridged-crack model, it is evident that the global parameters are not greatly influenced by the delamination shape. However, the results of the 3D model indicate that the delamination shape has a significant effect on the stress intensity factor at the crack tip and hence, the crack growth rate. This is emphasized further by plotting the crack opening displacement profiles near the crack tip from the 3D finite element results. Figure 5-19 plots the half-crack opening displacement from the local 3D model for the delamination profiles shown in Figure 5-18, with $\frac{x}{a} = 1$ located at the crack tip and $\frac{x}{a} = 0$ at the free edge. The results shown in Figure 5-19 indicate that the local delamination shape around the crack tip has a large effect on the crack opening displacement and, hence, the stress intensity factor at the crack tip, an effect not captured by the bridged-crack model.

To verify the dependence on local delamination profile, a 3D model was constructed with

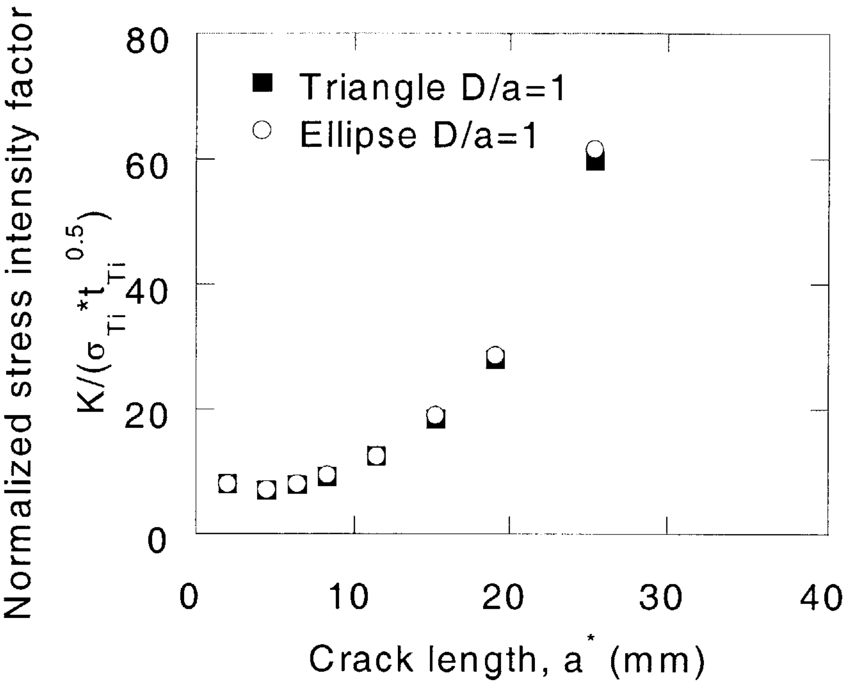

Figure 5-17: Effect of delamination shape on bridged-crack model results

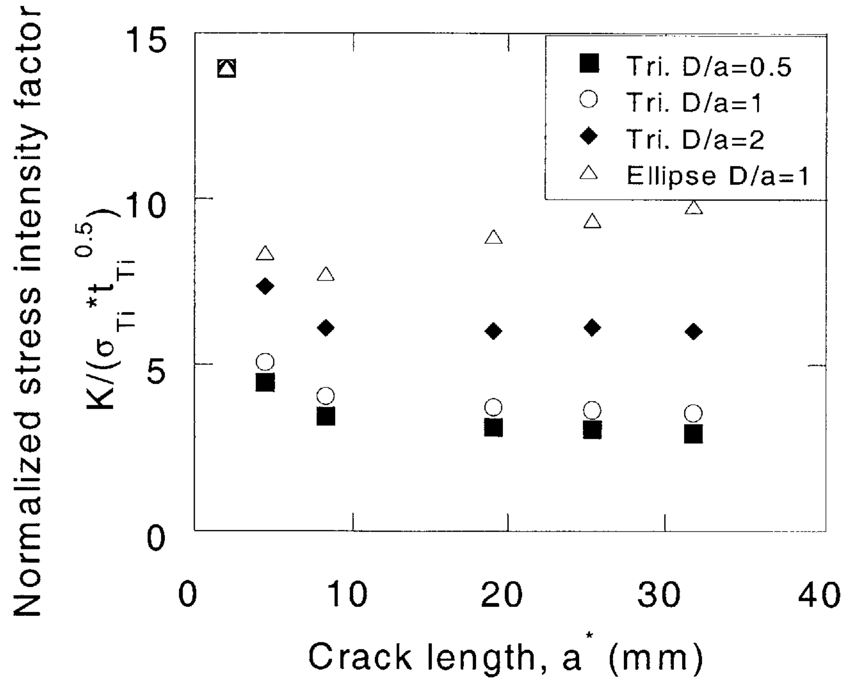

Figure 5-18: Effect of delamination shape on 3D VCCT model results

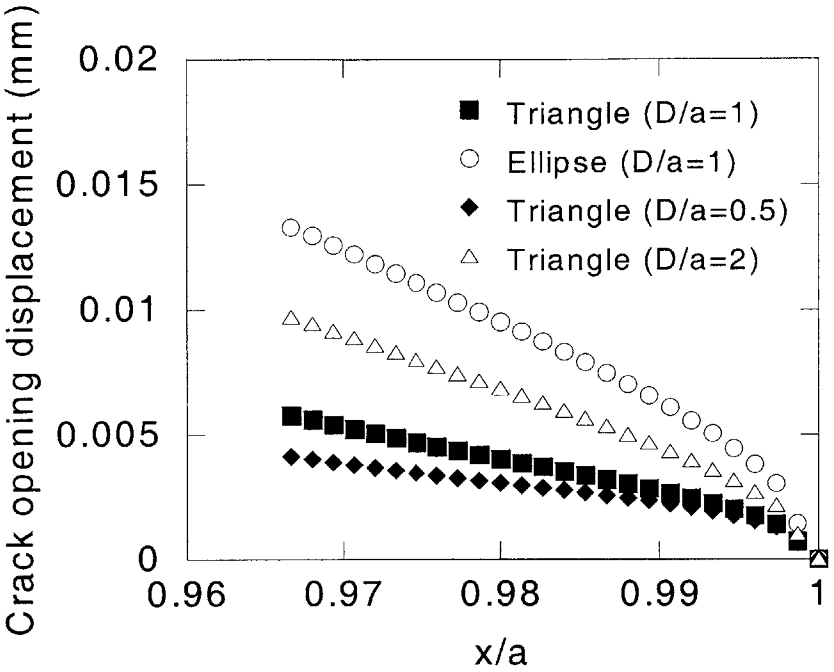

Figure 5-19: Crack opening displacement profiles near the crack tip as computed from the 3D FE model

a bi-linear delamination profile. Near the crack tip, the ratio of delamination length to crack length is equal to 1. At a distance 3.18 mm behind the crack tip, i.e. five elements in the global model, the $\frac{D}{a}$ ratio is changed to 2. A schematic of the bi-linear delamination profile is shown in Figure 5-20. A comparison of the local half crack opening displacements for the bi-linear case and the cases with a triangular delamination with $\frac{D}{a}$ ratios of 1 and 2 is shown in Figure 5-21. The bi-linear case and the triangular cases with $\frac{D}{a}$ equal to 1 are nearly identical along the crack front, further confirming that the delamination shape near the crack tip is a critical parameter

Effect of bridging tractions near the crack tip

The bridged-crack model assumes an elliptical delamination profile with a constant bridging traction over the length of the crack. This section studies the effects of the bridging tractions near the crack tip to determine if small changes in the bridging tractions near the crack tip will affect the results of the bridged-crack model. Equation 5.12 contains terms that increase rapidly close to the crack tip ($x \to a^*$). Therefore, it is likely that small deviations

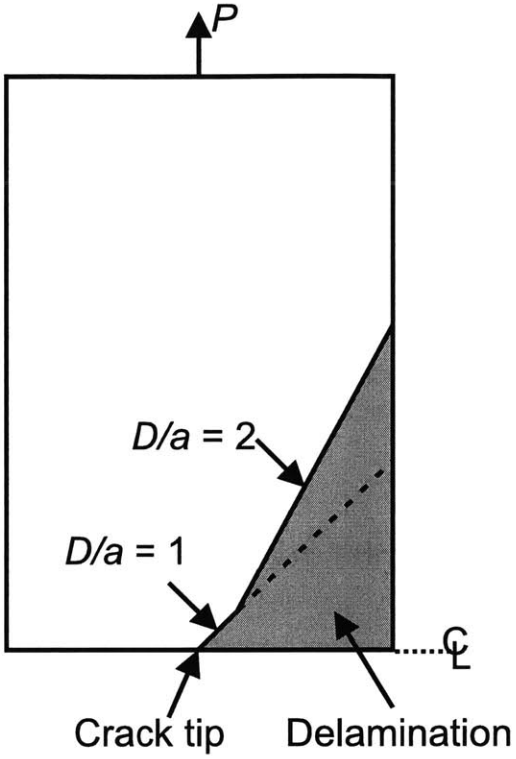

Figure 5-20: A schematic of the bi-linear delamination profile

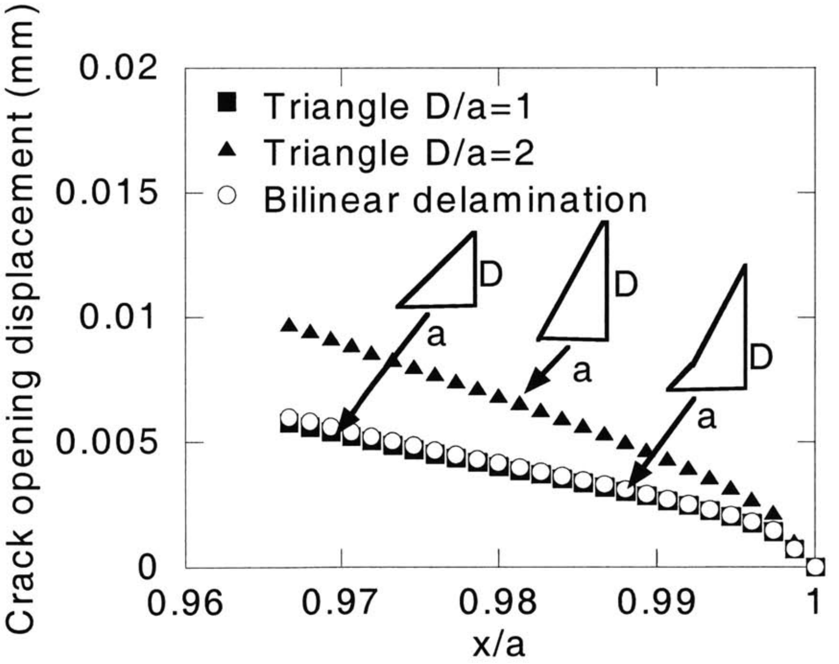

Figure 5-21: Comparison of crack opening displacement for bi-linear delamination profile from 3D FE model

in approximating the bridging tractions near the crack tip will be amplified.

Figure 5-22 presents the results of the bridged-crack model with altered bridging tractions near the crack tip. The bridging tractions were changed by ±10% and ±50% for the 5% of the crack length closest to the tip. The large variation in the results shown in Figure 5-22 indicates that the model is very sensitive to the magnitude of the bridging tractions near the crack tip. Figure 5-23 shows the results of changing the bridging load by +10% over four different percentages of the crack length close to the crack tip. The results indicate that most of the effect occurs within the 1% of the crack length closest to the tip. Coupled with the result showing the effect of the delamination on the crack opening displacement near the crack tip, these results indicate that the stress intensity factor at the crack tip is strongly affected by the behavior of the delamination shape and/or the bridging tractions near the crack tip. The bridged-crack model may not accurately capture the details near the crack tip and therefore is not reliable for capturing the crack growth behavior in TiGr laminates

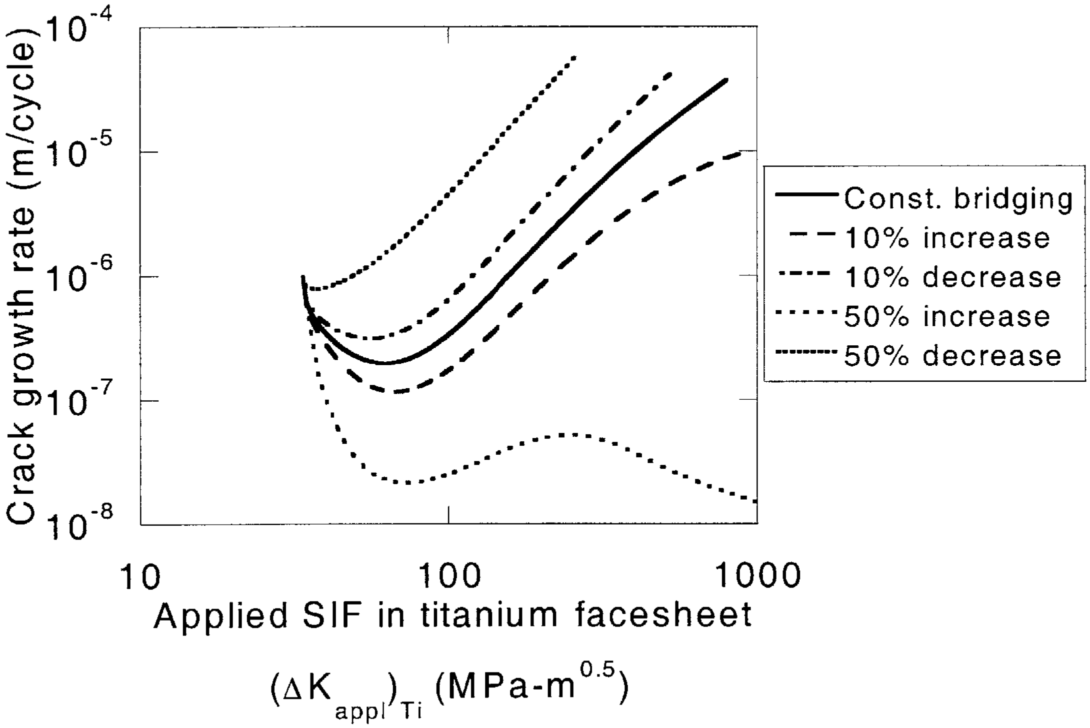

Figure 5-22: Effect of changing the amplitude of the bridging traction over the 5% of the crack closest to the crack tip using the bridged-crack model

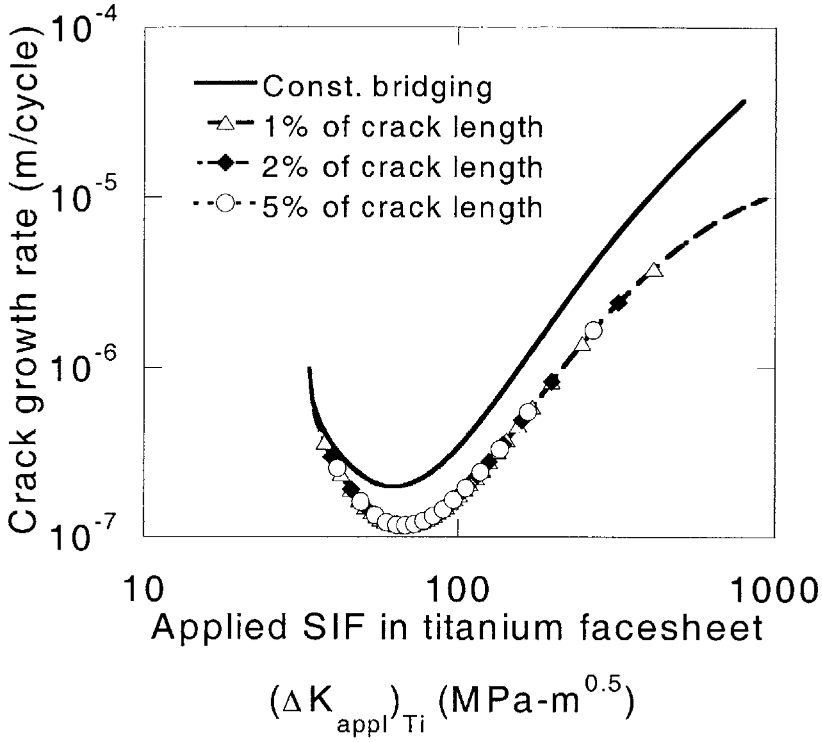

Figure 5-23: Effect of changing the amplitude of the bridging traction by 10% for different percentages of the total crack length using the bridged-crack model

5.4.3 Crack tip extension

The constant fatigue growth rate of cracks in constrained layers is not unique to hybrid laminates. Similar behavior is observed in transverse ply cracking of laminates containing off-axis plies, often called tunneling cracks, as discussed in Section 2.2.2. A variational model [58] developed by Nairn is applied here to calculate the strain energy release rate for a tunneling crack growing in the facesheet of a TiGr laminate 2.16.

Nairn's model considers two cases, one where the cracked transverse plies are interior plies and one where the cracked transverse plies are the outermost plies in the laminate. The latter case has similarities to the facesheet crack propagation in TiGr laminates. Potentially, the tunneling crack model could be applied to calculate the crack growth rate in the TiGr facesheets. However, the tunneling model does not consider the delamination effects in the wake of the crack. To determine the effect of the delamination on the crack tip behavior, the 3D model was modified so that the crack extends ahead of the delamination front by a distance, a_t as shown in Figure 5-24. In theory, as the crack extends well beyond the delamination, the effects of the delamination become less important and the crack behavior approaches that of a tunneling crack as determined by Nairn's analysis.

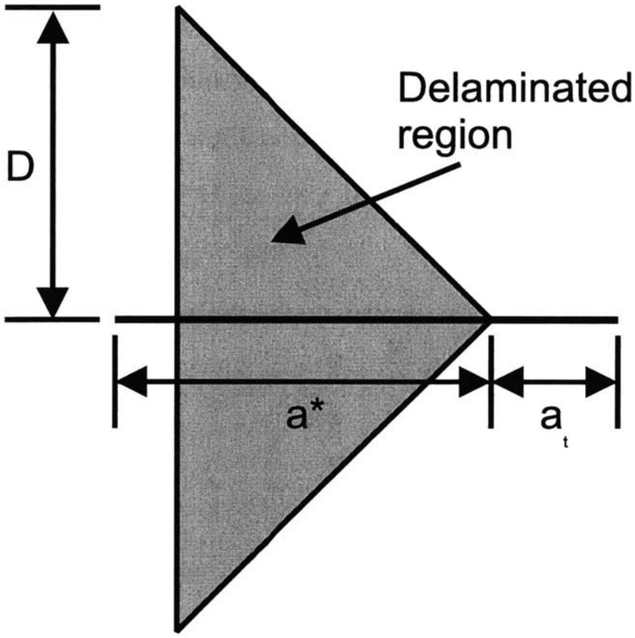

Figure 5-24: Schematic of crack extension

Figure 5-25 shows the extended crack results for five different values of a_t. The length of a_t is expressed in terms of a factor times the facesheet thickness, t. For example, a length of $2t$ indicates that the value of a_t is twice the thickness of the laminate. The results for a 19 mm crack with no delamination in the wake are also included. As the undelaminated portion of the crack extends, it approaches the value for no delamination, as expected. In addition, the approximate stress intensity factor calculated using Nairn's analysis is shown as a constant because it does not vary through the thickness. The value from Nairn's result is in the same range as the 3D FEM results and may provide a simple approximation for the stress intensity factor at the crack tip for facesheet cracks. If this is consistent for other laminates, the tunneling mode may provide a simple model which can be used to predict crack growth rate. However, since the tunneling model ignores the influence of the delamination near the crack tip, the model must be used cautiously. At worst, the tunneling model is a lower bound for the steady-state crack growth rate because it represents the limiting case of no delamination in the crack wake, which corresponds to the highest bridging tractions and the lowest crack growth rate. If the delamination extent near the crack tip is negligible, which would be the case if the crack extends ahead of the delamination front (Figure 5-24), then the tunneling model would provide a reasonable prediction for the crack growth rate. In all cases, the predictions should be compared to experimental results to verify the accuracy of the prediction. This comparison is conducted for TiGr in Chapter 6.

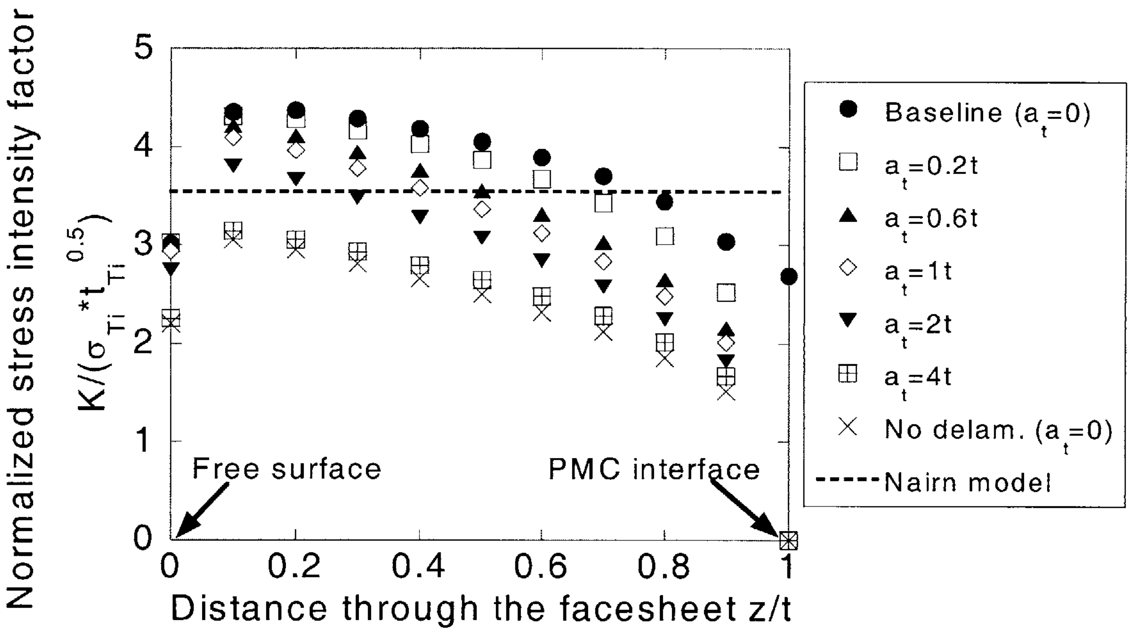

Figure 5-25: Results of extending the crack beyond the delamination front using 3D FE model and a comparison to a tunneling crack model for a total crack length, a^*, of 19 mm and an applied far-field stress of 419 MPa

5.4.4 Effect of relative facesheet stiffness and thickness

One of the main physical differences between TiGr laminates and its predecessors, ARALL, CARALL, and GLARE is that the titanium plies in TiGr laminates are relatively thin and more compliant compared to the PMC core. Therefore, it is hypothesized that a bridged-crack approach may be more appropriate in cases where the stiffness and/or thickness of the facesheet is large than the core. Figure 5-26 shows the normalized stress intensity factor as a function of crack length for a range of facesheet stiffness values. The calculations were conducted with the same composite core as the base laminate, with the Young's modulus of the facesheet being systematically increased and/or decreased. The Poisson's ratio for the facesheet material is kept the same as for monolithic Ti 15-3 for the purposes of this analysis. Therefore, the shear modulus is scaled by the same factor as the Young's modulus. The results show that for a very stiff facesheet ply, relative to the core, the trends for the 3D model are similar to that of the bridged-crack model. The results of the two models are compared in Figure 5-27.

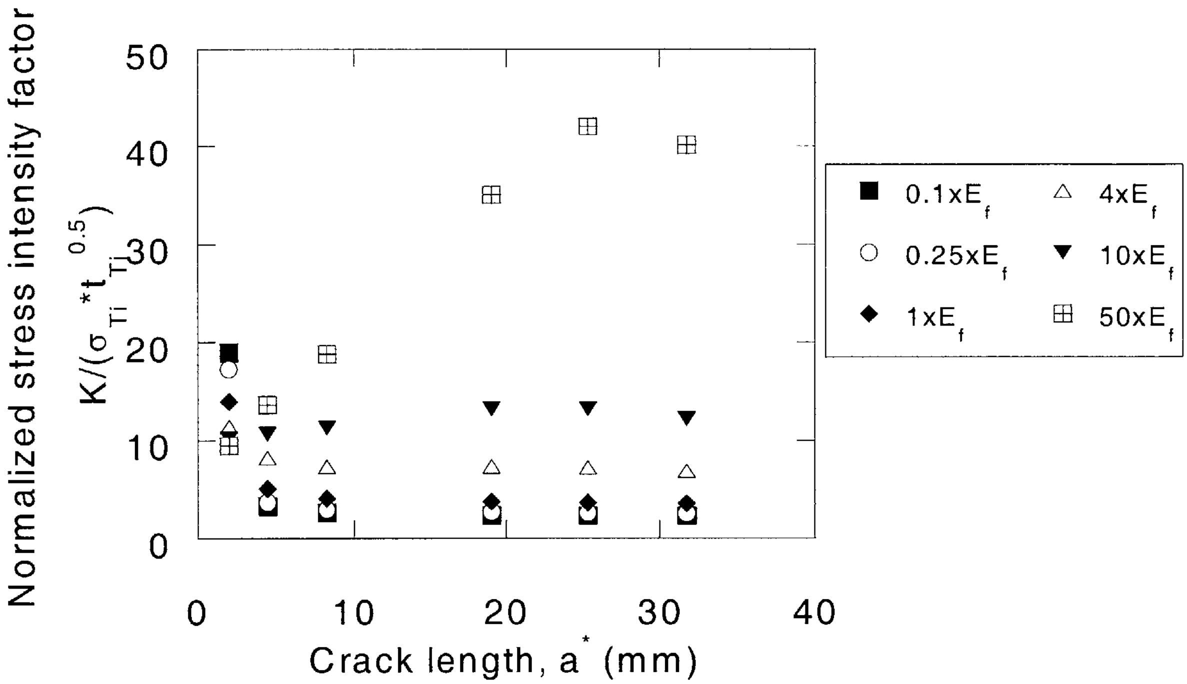

Figure 5-26: Effect of relative facesheet stiffness on 3D FE model results

In addition to altering the stiffness, a study was conducted on the effect of relative facesheet thickness. The stress intensity factor at the crack tip was compared for models with the thickness four times smaller than the baseline value of 0.127 mm and four times larger than the baseline value. Figure 5-28 shows that altering the thickness does not effect the predicted crack growth trends significantly, except for short cracks that are influenced by the initial notch. The values of the crack tip stress intensity factor is altered for each value of the thickness, but the overall trend is not altered.

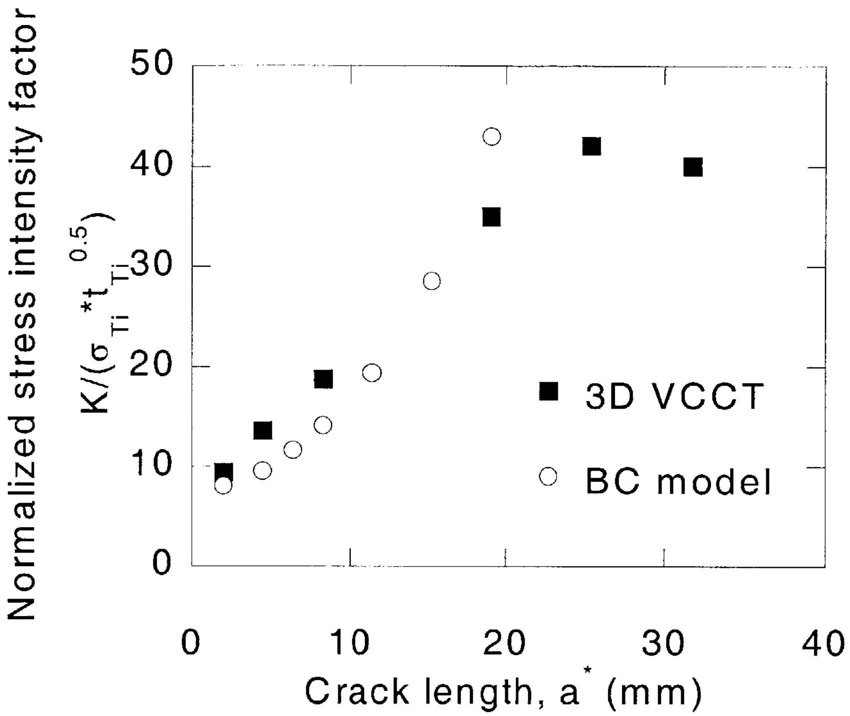

Figure 5-27: Comparison of bridged-crack model and 3D VCCT model for a facesheet ply 50 times stiffer than Ti 15-3

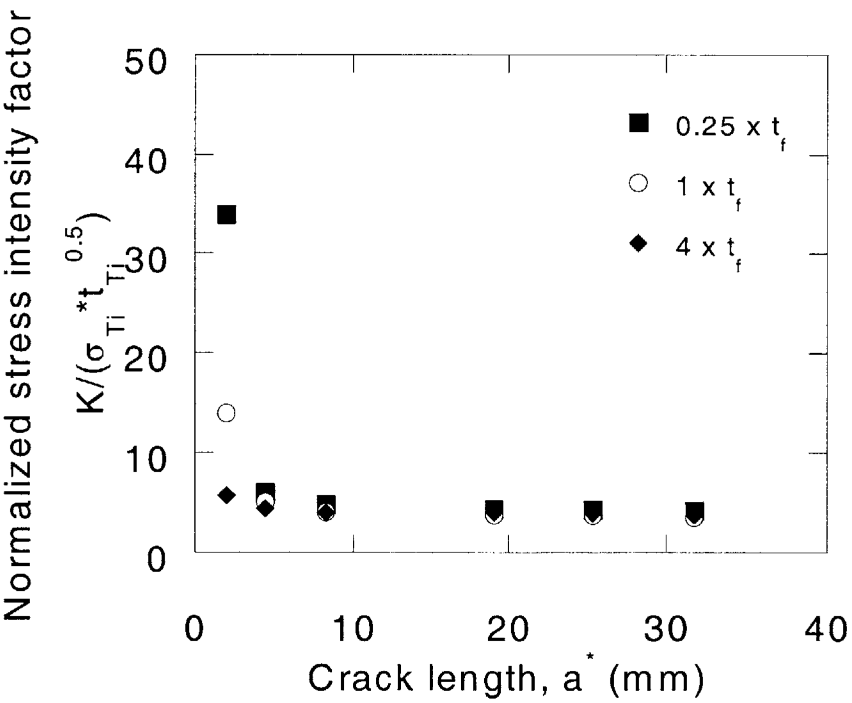

Figure 5-28: Effect of relative facesheet thickness on 3D VCCT model results

5.4.5 Comparison to previous work

Previous researchers have successfully applied a bridged-crack approach to model the crack growth behavior in other fiber metal laminates such as ARALL, CARALL and GLARE [90, 91, 96, 99]. Because the specimens studied in [96] were similar in size and configuration to the TiGr samples studied in this thesis, the results from the bridged-crack model developed in this research are compared to the experimental results from [96] to determine if the bridged-crack model described above captures the trends present in the previous experimental data. The inputs for the bridged-crack model, as reported in [96], are shown in Table 5.3. With the exception of the material properties, the models were executed using the same procedures as described in Sections 5.2 and 5.3. The specimen configuration was single edge notch tension with an initial through-thickness notch 2 mm in length.

Table 5.3: CARALL properties input into the present bridged-crack model

Specimen width	30 mm
Specimen length	100 mm
Facesheet modulus (Longitudinal)	71 GPa
Facesheet thickness	1 mm
Core modulus	109 GPa
Core thickness	0.28 mm
Facesheet crack power law relationship (AL 2024-T3) ($\frac{da}{dN}$ has units of $\frac{m}{cycle}$)	$\frac{da}{dN} = 4.3 \cdot 10^{-11}(\Delta K)^{3.3}$
Facesheet delamination power law relationship ($\frac{dD}{dN}$ has units of $\frac{m}{cycle}$)	$\frac{dD}{dN} = 1.74 \cdot 10^{-12}(\Delta G)^{2.17}$

Figure 5-29 compares the results from the present bridged-crack model to experimental results for CARALL laminates [96] indicating that the bridged-crack model captures the experimental trends reported for that material. Model results presented in [96] for a similar bridged-crack model also correlate to the experimental results. In order to perform the comparison, a small inconsistency had to be addressed. The tuning factor is a result of a discrepancy in [96] between the stated starter notch length and that indicated by the experimental results. The experimental procedures described in [96] indicate that the initial notch size was 2 mm in length, while the presented data clearly assumes an initial notch of 6 mm. Therefore, in the present work the model was executed using a 2 mm configuration and a shift factor was applied to the model results such that they could be easily compared to the experimental results. The agreement between the bridged-crack model developed here and the experimental results, along with the model results shown in [96] suggest that the bridged-crack model described in Section 5.2 was implemented correctly.

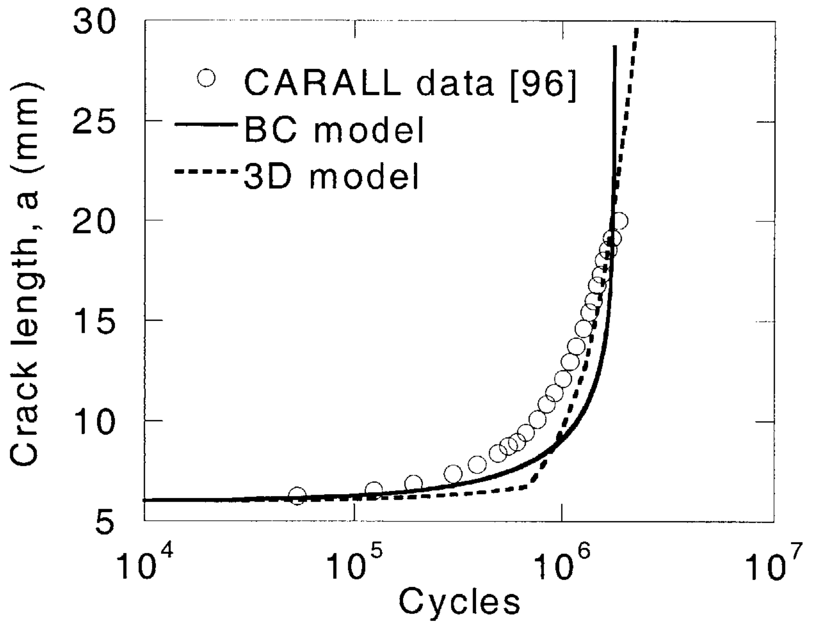

Figure 5-29: Comparison of bridged-crack model to previous research on CARALL laminate [96]

Figure 5-30 shows the normalized stress intensity factor as a function of crack length from the three-dimensional VCCT model conducted for CARALL laminates. The prediction for 3D model shown in Figure 5-29 was calculated by applying the results shown in Figure 5-30. The results shown in Figure 5-29 indicate that the VCCT model, with the same tuning factor as the bridged-crack model, also accurately captures the crack growth behavior for this laminate.

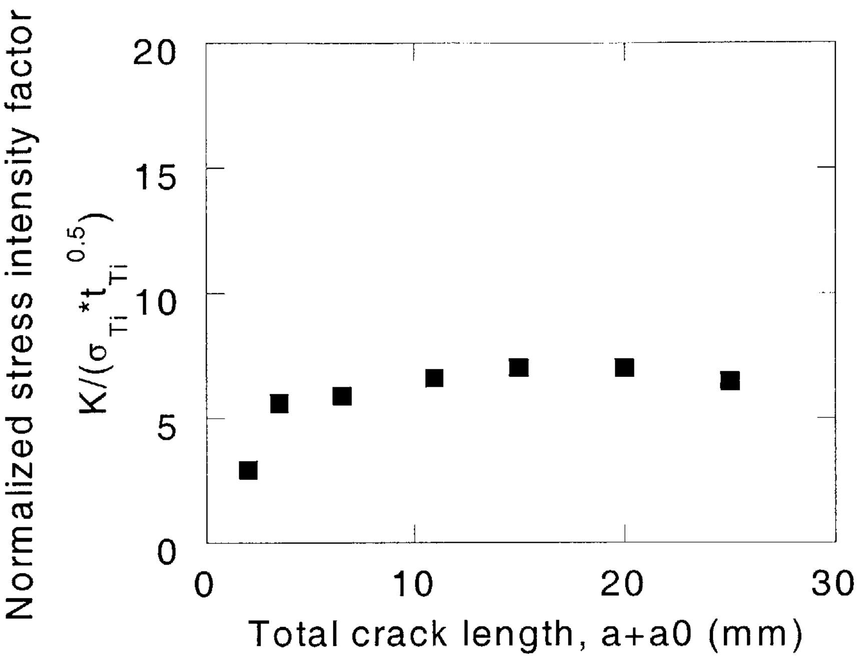

Figure 5-30: Results of 3D VCCT model applied to CARALL laminates [96]

5.5 Delamination shape model

One of the initial goals of this research was to develop a simple analytical model that could be applied as a comparative design tool for TiGr structures. The initial two-dimensional bridged-crack model is relatively easy to use and it provides a means to predict the combined material response for facesheet cracking and delamination. However, it does not capture the long-term behavior of the fatigue crack growth for the prospective laminates. The fatigue crack growth rate is approximately constant for long cracks and the tunneling model by Nairn provides a reasonable estimate for this steady-state crack growth rate in the facesheet. However, Nairn's model does not apply to the growth of the delamination. Since stiffness reduction can be a critical failure criterion for applications, predicting the extent of the underlying delamination in the crack wake is desirable. In order to achieve this, a simple model has been devised that predicts the delamination angle using the applied load and the lay-up as inputs. The model assumes that the delamination profile is triangular. This is shown experimentally in Chapter 6. In addition, triangular delaminations are one of two possible second order profiles (the other is circular) which can propagate incrementally in a self-similar manner. If an elliptical profile propagates incrementally the same distance along the entire crack front, which is a desirable assumption because it allows the delamination growth to be characterized by the growth at the root, the shape becomes a higher order polynomial and is no longer an ellipse. Further studies should be conducted to determine the local strain energy release rate along the delamination front in order to predict the exact delamination propagation pattern.

5.5.1 Derivation of model

The first step in the model is to determine the two-dimensional stress state in the laminate. For TiGr specimens with a uniaxial applied load per unit width, p, a biaxial stress state exists on a ply-by-ply level. The magnitude of the transverse stresses can be determined by applying strain compatibility in the transverse and longitudinal layers. The subscripts f and c refer to the facesheet and the composite core, respectively, and the subscripts 1 and 2 refer to the loading and the transverse directions, respectively.

The reciprocity relationship states:

$$\frac{\nu_{12f}}{E_{1f}} = \frac{\nu_{21f}}{E_{2f}} \tag{5.19a}$$

$$\frac{\nu_{12c}}{E_{1c}} = \frac{\nu_{21c}}{E_{2c}} \tag{5.19b}$$

For compatibility in the loading direction:

$$\epsilon_{1f} = \epsilon_{1c} \tag{5.20}$$

Applying the stress-strain relationships, Equation 5.20 becomes:

$$\frac{\sigma_{1f}}{E_{1f}} - \frac{\nu_{12f}}{E_{2f}}\sigma_{2f} = \frac{\sigma_{1c}}{E_{1c}} - \frac{\nu_{12c}}{E_{2c}}\sigma_{2c} \tag{5.21}$$

Similarly in the transverse direction the compatibility relationship states:

$$\epsilon_{2f} = \epsilon_{2c} \tag{5.22}$$

Applying the stress-strain relationships and Equations 5.19a and 5.19b:

$$-\frac{\nu_{12f}}{E_{1f}}\sigma_{1f} + \frac{\sigma_{2f}}{E_{2f}} = -\frac{\nu_{12c}}{E_{1c}}\sigma_{1c} + \frac{\sigma_{2c}}{E_{2c}} \tag{5.23}$$

In addition to compatibility, equilibrium must also be satisfied for both the loading and the transverse directions:

$$\sigma_{1f}t_f + \sigma_{1c}t_c = p \tag{5.24a}$$

$$\sigma_{2f}t_f + \sigma_{2c}t_c = 0 \tag{5.24b}$$

With Equations 5.21, 5.23, 5.24a, and 5.24b, the four unknown stresses, σ_{1f}, σ_{2f}, σ_{1c}, σ_{2c}, can be determined:

$$\sigma_{1f} = \frac{p}{Z}\left[\nu_{12f}\,\nu_{12c} - \frac{E_{1f}}{E_{2f}} - \frac{E_{1f}\,t_f}{E_{2c}\,t_c} + \frac{E_{1f}\,t_f\,{\nu_{12c}}^2}{E_{1c}\,t_c}\right] \tag{5.25a}$$

$$\sigma_{2f} = \frac{p}{Z}\left[\nu_{12c} - \nu_{12f}\right] \tag{5.25b}$$

$$\sigma_{1c} = \frac{p}{Z}\left[\nu_{12f}\,\nu_{12c}\frac{t_f}{t_c} - \frac{E_{1c}}{E_{2f}} - \frac{t_f\,E_{1c}}{t_c\,E_{2c}} + \frac{{\nu_{12f}}^2 E_{1c}}{E_{1f}}\right] \tag{5.25c}$$

$$\sigma_{2c} = \frac{p}{Z}\left[\frac{t_f \nu_{12f}}{t_c} - \frac{t_f \nu_{12c}}{t_c}\right] \tag{5.25d}$$

where:

$$Z = -\frac{E_{1c}\,t_c}{E_{2f}} - \frac{E_{1c}\,t_f}{E_{2c}} + \frac{E_{1c}\,t_c\,{\nu_{12f}}^2}{E_{1f}} - \frac{E_{1f}\,t_f}{E_{2f}} - \frac{E_{1f}\,{t_f}^2}{E_{2c}\,t_c} + \frac{E_{1f}\,{t_f}^2 {\nu_{12c}}^2}{E_{1c}\,t_c} + 2\,\nu_{12f}\,\nu_{12c}\,t_f \tag{5.26}$$

For an arbitrary delamination angle, θ, the strain energy release rate normal to the delamination front can be determined using a strip model. To determine the strain energy release rate, the strain energy is determined in a strip of material of length da ahead of the delamination front and from a strip of material length da behind the delamination front. The difference between the two calculated energies is the energy available to propagate the delamination normal to the delamination front. A schematic of the strip method is shown in Figure 5-31.

5.5.2 Model predictions

To apply the strip method to a laminate with a facesheet crack and an arbitrary delamination angle, θ, a strip of material orthogonal to the delamination front is "cut out" far away from the free edge and from the crack tip as shown in Figure 5-31(a). The method will not be applicable near the crack tip and near the free edge because of the stress singularities at those locations. The triangular delamination profile is based on experimental evidence presented in Chapter 6 of this work. Both the stresses and the material properties for the laminate

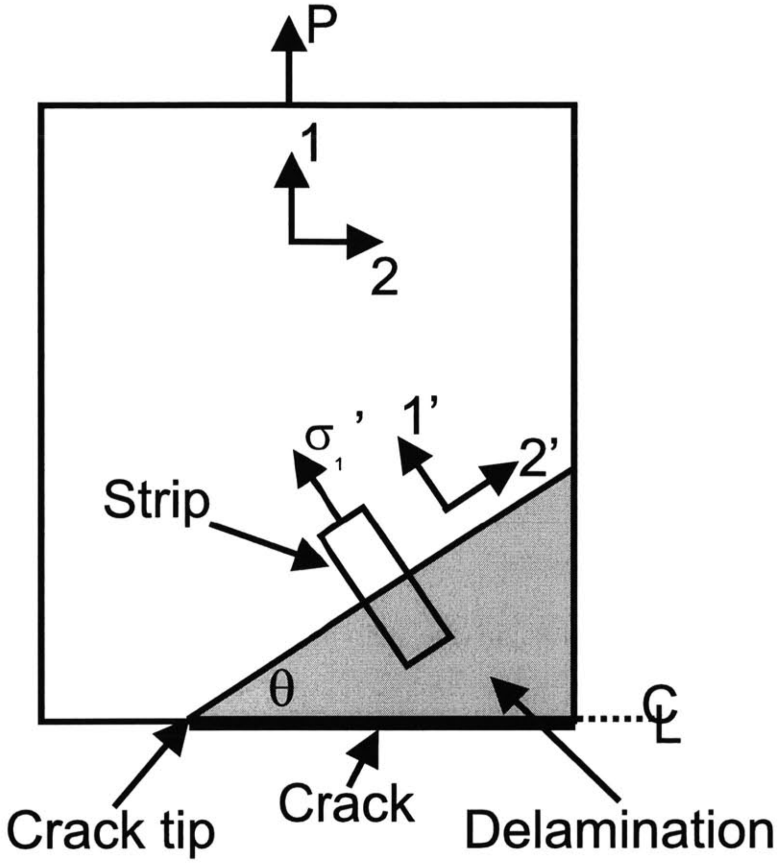

(a) Schematic of strip model, top view

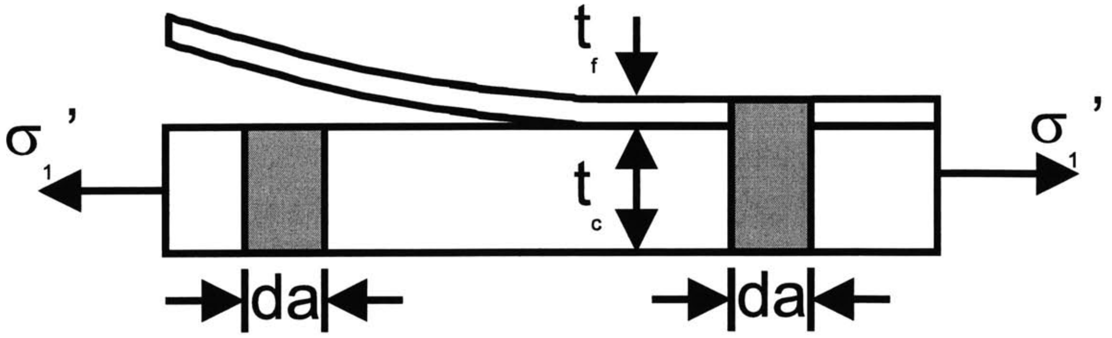

(b) Side view of cut-out in strip model

Figure 5-31: Schematic of facesheet crack and delamination need to be rotated by θ to apply the strip model. The material properties are rotated using classical laminated plate theory and the stresses are rotated using Mohr's circle:

$$\sigma_1{}' = \frac{\sigma_1 + \sigma_2}{2} + \frac{\sigma_1 - \sigma_2}{2}\cos(2\theta) + \sigma_{12}\sin(2\theta) \tag{5.27a}$$

$$\sigma_2{}' = \frac{\sigma_1 + \sigma_2}{2} - \frac{\sigma_1 - \sigma_2}{2}\cos(2\theta) - \sigma_{12}\sin(2\theta) \tag{5.27b}$$

$$\sigma_{12}{}' = -\frac{\sigma_1 - \sigma_2}{2}\sin(2\theta) + \sigma_{12}\cos(2\theta) \tag{5.27c}$$

To predict the delamination angle, the strip model will be applied to find the angle giving the maximum value of strain energy release rate. The strip model method for calculating the strain energy release rate makes no distinction between the different modes of delamination. However, the Mode III component can be separated out from the Mode I and II component [46] and it is assumed to be small for the purpose of this analysis [116]. The value for the total Mode I and Mode II strain energy release rate is calculated with:

$$G(\theta) = \frac{\sigma_{cd}^2(\theta)t_c}{2E_c(\theta)} - \left[\frac{\sigma_c(\theta)t_c}{2E_c(\theta)} + \frac{\sigma_f(\theta)t_f}{2E_f(\theta)}\right] \tag{5.28}$$

where:

G = total Mode I and Mode II strain energy release rate

σ_{cd}= stress in the composite core for the delaminated region

σ_c, σ_f = stresses in the core and the facesheet, respectively, in the undelaminated region

t_c, t_f = core and the facesheet thickness'

E_c, E_f = core and the facesheet moduli.

Note: All values are with respect to the rotated system

Figure 5-32 shows the Mode I and Mode II components of delamination plotted as a function of delamination angle, θ, for an applied load per unit width of 100 kN/m. The maximum value for strain energy release rate occurs at an angle of approximately 30°. When calculating the stiffness reduction of a component as a crack propagates, this value can be used in conjunction with the constant crack growth rate models shown above to calculate the stiffness reduction due to delamination. Experimental verification of this model will be presented in Chapter 6.

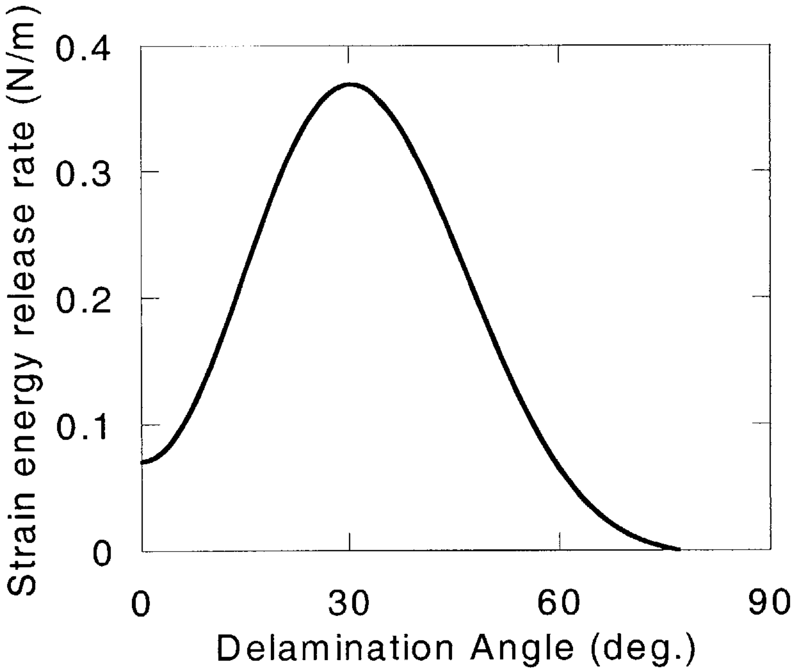

Figure 5-32: Combined strain energy release rate (Mode I + Mode II) as a function of delamination angle for an applied load per unit width of 100 kN/m

5.6 Modeling conclusions

Some important conclusions can be drawn from the modeling procedures described above. Most significantly, the bridged-crack model that has been successfully applied previously to hybrid laminates, as as well as other damage growth problems in composite laminates, is not effective at estimating the crack tip stress intensity factor and consequently the fatigue crack growth behavior in TiGr laminates. A three-dimensional finite element model using the virtual crack closure technique developed for TiGr laminates predicts a constant crack growth rate for the facesheet cracks whereas the bridged-crack model predicts an accelerating crack growth. The main reason for the discrepancy between the bridged-crack model and the three-dimensional finite element model is that the bridged-crack model does not accurately capture the details near the crack tip. A three-dimensional model showed that the delamination slope near the crack tip significantly affects the behavior of the facesheet near the crack tip whereas the global nature of the bridged-crack model does not capture this effect. In addition, it was also shown that the magnitude of the bridging stresses near the crack tip has a large influence on the crack growth prediction for the bridged-crack model. The global nature of the bridged-crack model may not accurately capture the details of the bridging tractions near the crack tip. Potentially, the 3D finite element model could be used to capture the general profile of the bridging tractions, which could be used to improve the performance of the bridged-crack model.

A two-dimensional model using the virtual crack closure technique (VCCT) predicts the same steady-state trend as the 3D VCCT model. However, the magnitude of the stress intensity factor is underpredicted using the 2D VCCT model. This type of model may be implemented to compare different configurations, but the magnitude of the stress intensity factor predicted using the 2D VCCT model should be verified with a full three-dimensional model or with experimental results. The success of the 2D VCCT model in predicting the trends of the stress intensity factor indicates that the problems with the bridged-crack model, which is also two-dimensional in nature, are not a result of through-thickness effects.

In addition to the finite element model and the bridged-crack model, a constrained layer crack tunneling model was applied to the facesheet crack growth in TiGr laminates. Inherently, the tunneling model predicts a constant stress intensity factor, independent of the crack length. The value of the stress intensity factor predicted with the tunneling model is of the same order as that predicted by the three-dimensional finite element model. However, because the tunneling model does not consider the delamination behavior, the results should be used with caution and compared to experimental data for verification. The tunneling model is compared to experimental results for three different TiGr laminates in Chapter 6.

A two-dimensional strip model was derived to approximate the delamination angle between the facesheet and the core. Thus far, it has not been possible to model the propagation of the delamination using mechanism-based techniques. The strip model provides an estimate of the final angle for the delamination, with respect to the crack, but does not predict the delamination growth. The VCCT models discussed above were executed using experimental observations to approximate the shape and size of the delamination. Further modeling should be conducted to determine the growth behavior of the delamination, especially in the vicinity of the crack tip.

Chapter 6

Facesheet Crack Growth Experiments and Comparison to Models

In Chapter 5, a bridged-crack model, a 2D and a 3D finite element model were constructed for the coupled damage growth of a facesheet crack and delamination in Titanium-Graphite hybrid laminates (TiGr). In this chapter, experimental results are presented which measure the facesheet crack growth rate then these results are compared to the model predictions. Three different lay-ups were tested at different fatigue load levels. One of the laminates, $[\mathrm{Ti}/0/90/0_2]_s$, was tested at an elevated temperature to determine the thermal effects on the crack growth. Observations of the damage modes were performed using destructive and non-destructive techniques to verify the assumptions that went into the models and to validate their predictive capability.

6.1 Single edge notch crack growth experiments

6.1.1 Test equipment and procedures

The test specimens were 152 mm x 38 mm rectangular coupons for the room temperature experiments and 305 mm x 38 mm specimens for the elevated temperature experiments. The difference in specimen length for the elevated temperature experiments is due to the size requirements for the thermal chamber. The specimen lay-up for the base laminate was

$[\mathrm{Ti}/0/90/0_2]_s$, also known as TiGr 2-6-2. This is a high-strength lay-up with potential use on fuselage crown panels. The two alternate lay-ups that were tested were $[\mathrm{Ti}/90/0/90_2]_s$, which is a 90° rotation of the base laminate, and $[\mathrm{Ti}/0/90/\pm30]_s$, which incorporates off-axis plies. These laminates were only tested at room temperature. Material properties for the constituent materials and for the laminates are given in Table 3.1. The constituent properties were supplied by The Boeing Company [106] and the laminate properties were calculated using Classical Laminated Plate Theory (CLPT). All of the specimens had a 2 mm long notch in the edge of the specimen located along the centerline of the specimen. The notch was cut using a 0.64 mm diameter diamond grit end mill mounted in a Dremel™ tool mounted on the table of a milling machine with digital position encoders as described in Chapter 3.

The fatigue tests were carried out using a servo-hydraulic load frame with a sinusoidal waveform under load control. Damage observation was performed using a Questar™ long distance microscope system. The stage for the microscope was equipped with digital position encoders along all three axes, which allowed for measurement of the crack length without removing the specimen from the load frame. The fatigue cycling was interrupted and the load was held at the mid-point of the fatigue cycle in order to measure the crack length. Although the cracks did not propagate along a perfect horizontal line, only the lateral distance was recorded and the small vertical component was ignored. The specimens tested at elevated temperatures were mounted within the temperature cabinet described in Chapter 3. One thermocouple, offset by approximately 32 mm below the crack, was used to control the temperature.

The delamination profile was tracked with a x-radiography. The specimen was injected with a di-iodobutane solution and removed from the load frame to be x-rayed in a Scanrray Torrex 150D x-ray device. In addition, post-mortem analysis of the delamination profile was conducted by spraying the laminate with die penetrant and allowing it to flow into the damaged regions. The evaluation procedures are discussed in more detail in Chapter 3.

6.1.2 Experimental results for base laminate and comparison to model predictions

Experimental data for the fatigue crack growth rate as a function of applied stress intensity factor in the facesheet for the base laminate, $[\mathrm{Ti}/0/90/0_2]_s$, is shown in Figure 1 for three applied stress levels, σ_{max}=314 MPa, σ_{max}=419 MPa, and σ_{max}=524 MPa. The load levels correspond to stress levels in the facesheet plies that are 28%, 37%, and 46% of the monolithic titanium yield stress. The far-field stress level in the facesheet, determined using Classical Laminated Plate Theory (CLPT), was 97% of the total applied far-field stress level.

The experimental results show that as the crack extends, i.e. for increasing values of stress intensity factor, the crack growth rate approaches a constant value. This is consistent with the 3D modeling results discussed in Chapter 5. The results from the 3D FE model for a fixed delamination to crack ratio, $\frac{D}{a}$, of 1 are also shown in Figure 6-1. The values from the 3D FE model were calculated for six discrete values of the crack length. For clarity, the discrete values are represented with straight lines connecting the individual data points. Because the 3D model produced a non-uniform stress intensity factor through-the-thickness of the facesheet, the value of the stress intensity factor from the 3D model was calculated by averaging the results through the thickness. The crack growth rate was derived from the stress intensity factor range determined from the finite element results using the Paris' Law relationship for Ti 15-3 shown in Equation 5.14. The predictions from the 3D VCCT model show a very good correlation with the experimental results. The results of the 3D VCCT model shown in Figure 6-1 have no additional tuning or adjustment. For comparison, the power law curve fit, derived from the experimental results shown in Figure 5-8, for monolithic titanium 15-3-3-3 is also shown in Figure 6-1. For the monolithic material, the crack growth rate increases as the crack extends, as opposed to the initially decreasing and then steady-state behavior predicted and observed for TiGr laminates.

Figure 6-2 compares the experimental results on the base laminate at all three stress levels to the crack growth rates calculated using Nairn's tunneling crack model [58] discussed in Chapter 5. The tunneling model provides a reasonable estimate for the crack growth rate once the crack has extended beyond the influence of the starter notch. However, the tunneling

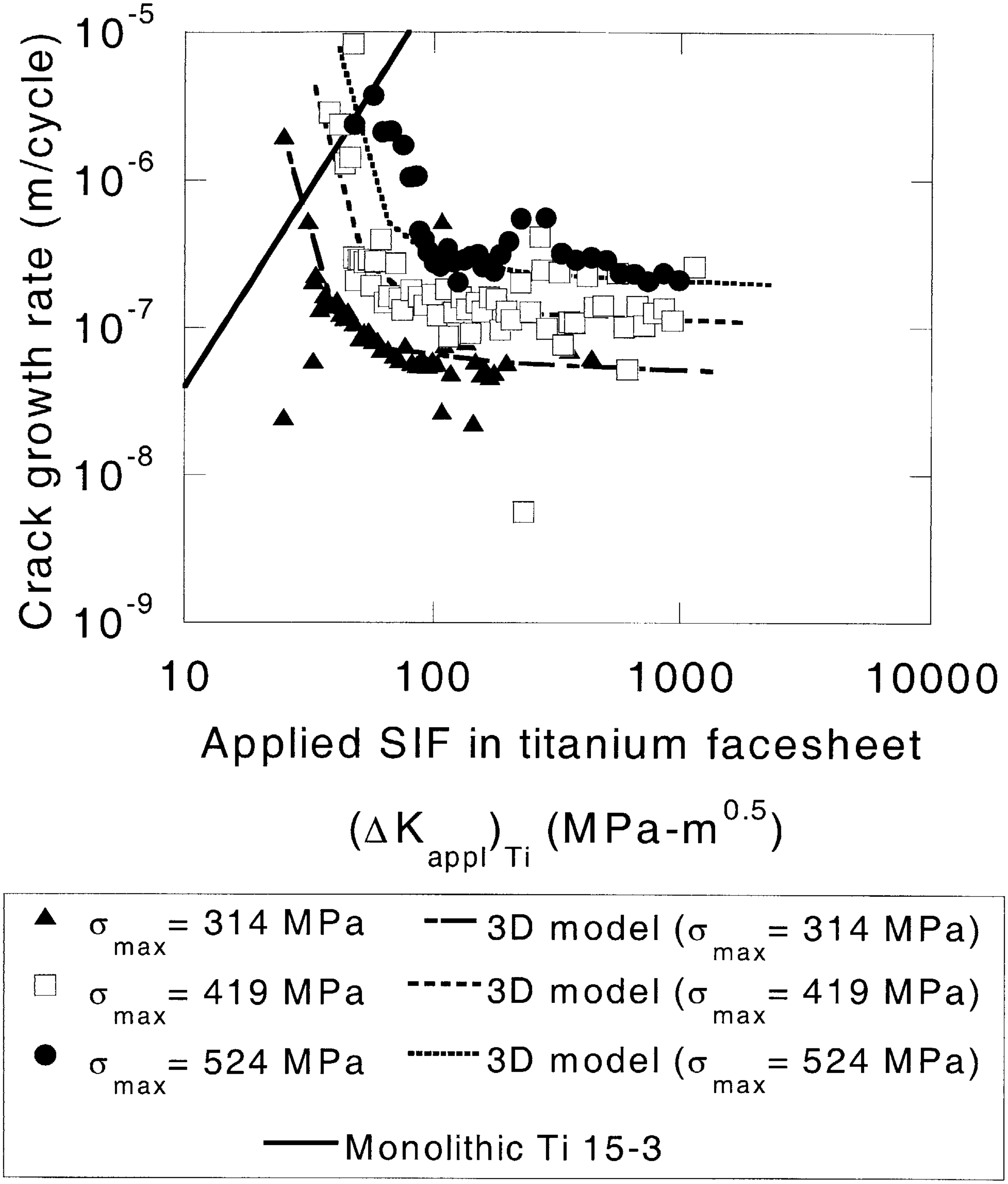

Figure 6-1: Experimental fatigue crack growth behavior of $[Ti/0/90/0_2]_s$ laminate compared to 3D VCCT model results

model does not account for the initial decrease in crack growth rate for short cracks.

6.1.3 Damage observation

One of the assumptions of the models developed in Chapter 5 was that the delamination growth was self-similar. In order to investigate the validity of this assumption, destructive evaluation was conducted on the specimens after the completion of the fatigue cycling. Die penetrant was sprayed onto the specimen and allowed to wick into the delaminated areas. Once dried, the facesheet was removed from the core and the furthest delamination was evident from the residue left by the die penetrant. A digital photograph was taken of the global delamination profile. The delamination angle was analyzed using the software program CorelDraw™. To measure the angle, a line was drawn parallel to the crack and a second line was rotated from the parallel until it was tangent with the delamination profile in the photograph. The angle between the two lines was taken as the delamination profile angle. This procedure gives the global delamination angle. The die penetrant procedure for determining the delamination angle did not have the accuracy to determine the angle near the crack tip.

Figure 6-3 illustrates the delamination extent from a number of test specimens with different final crack lengths. The delamination profiles were approximately triangular for a majority of the specimens and the angle with respect to the facesheet crack ranged from 30°to 45°(45°corresponds to $\frac{D}{a}$=1 in the 3D model). There is a trend indicating that the delamination angle remains closer to 45° for shorter cracks and begins to decrease as the crack length extends. Figure 6-4 compares the experimental results for the delamination angle to the value predicted with the strip model in Chapter 5. For short cracks, the model underestimates the delamination angle. For longer cracks, the model is more accurate. In Figure 6-4, the data point for a 37 mm crack, signified with an open triangle, was from a 76.2 mm wide specimen. Another mechanism which may affect the global delamination angle is splitting in the 0° plies. There was evidence of splits in the plies emanating from the notch tip and running parallel to the loading axis. Future experiments should be conducted to determine how the splits influence the global delamination angle.

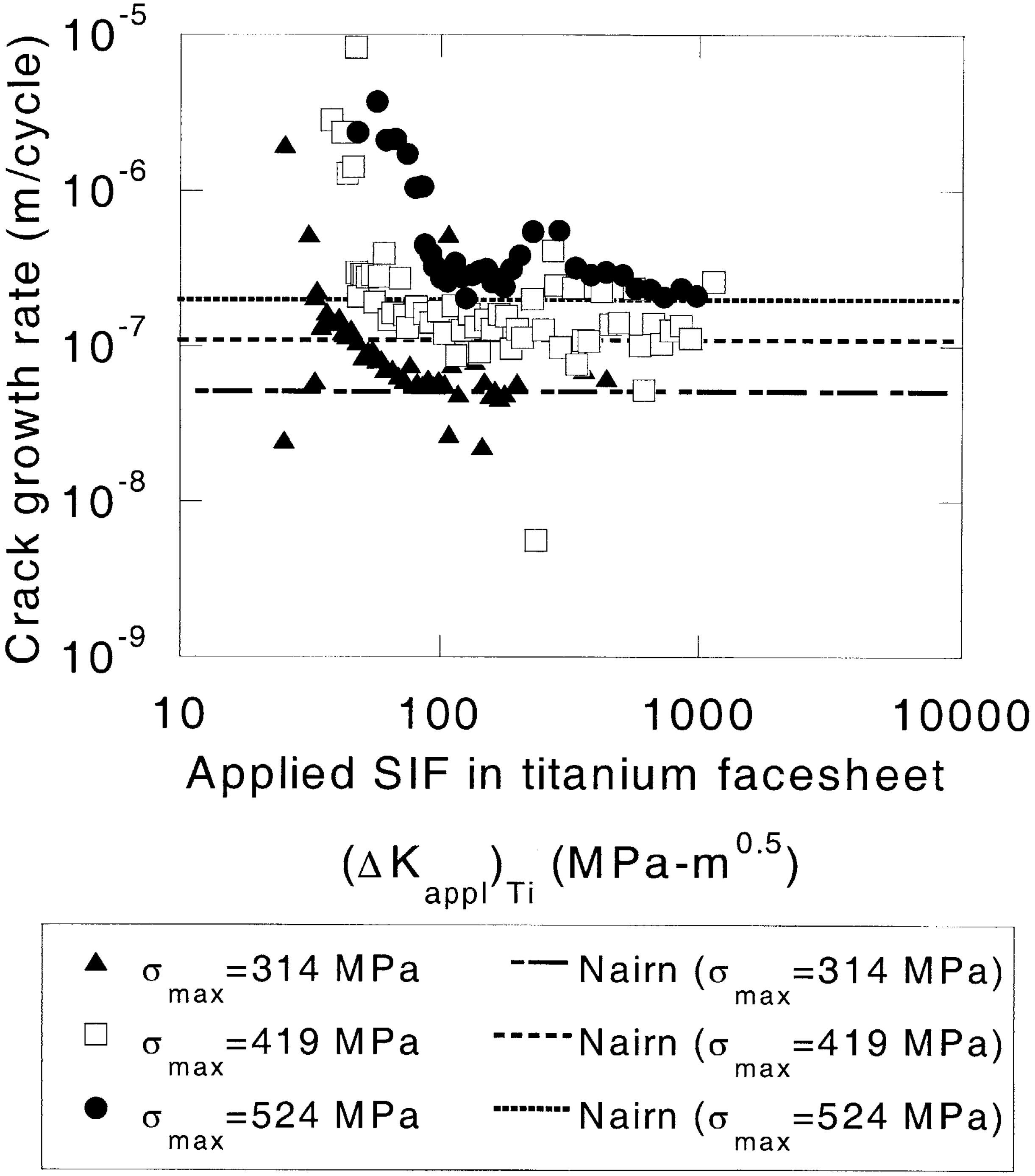

Figure 6-2: Comparison of the experimental fatigue crack growth behavior of $[Ti/0/90/0_2]_s$ laminates to tunneling model

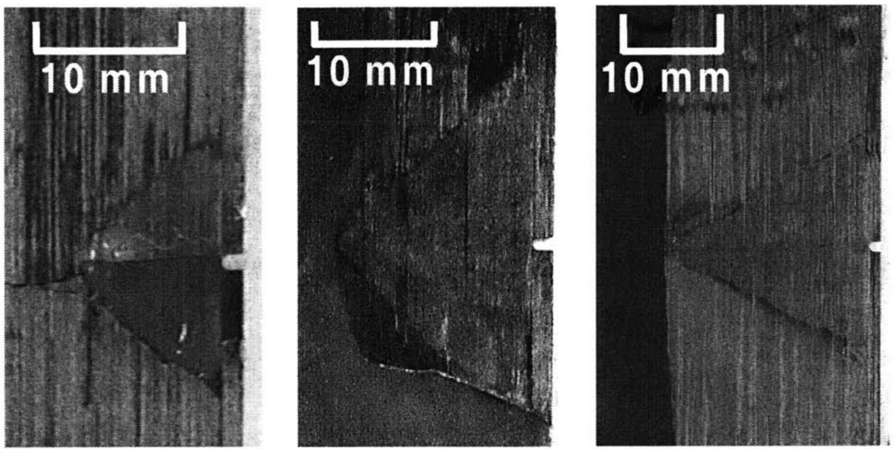

a*≈8.7 mm a*≈19 mm a*≈23 mm

Figure 6-3: Delamination profiles observed using die penetrant method from specimens cycled with σmax=419 MPa and R=0.1

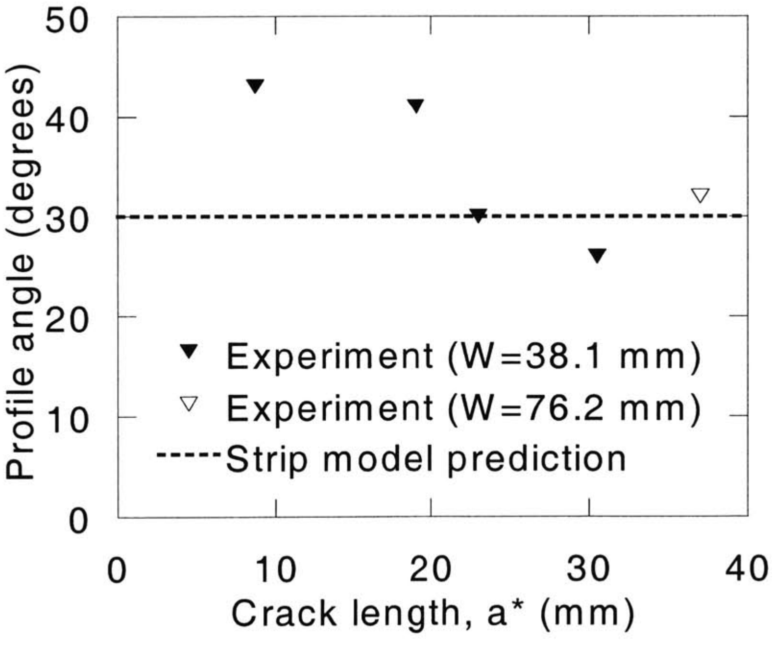

Figure 6-4: Comparison of predicted delamination profile angle to experimental results

One possible explanation for the decreasing angle is that the boundary conditions near the free edge and at the crack tip have an effect on the angle at which the delamination front propagates. Therefore it is not possible to predict the delamination profile for short cracks without understanding the full influence of the boundary conditions, including the free edge effects, the splits which emanate from the notch tip and the local stress field that exists at the crack tip. However, as was stated in Chapter 5, the primary influence on the crack tip stress intensity factor is the delamination slope in the vicinity of the crack tip. The die penetrant method does not provide sufficient detail to characterize the exact delamination shape near the crack tip. Therefore, the changing of the far-field delamination angle will not necessarily change the behavior of the delamination at the crack tip. Further studies need to be conducted to determine the factors that control the delamination growth behavior near the crack tip.

Micrographs were taken of the delamination and crack fracture surface using a scanning electron microscope. The results from the crack tip extension studies in Section 5.4.3 indicate that the stress intensity factor at the crack tip is reduced if the facesheet crack advances ahead of the delamination front. However, no conclusive evidence was found that the facesheet crack growth precedes the delamination. Figure 6-5 shows a micrograph taken of the delaminated region of the titanium facesheet near the crack tip, which shows the delaminated region and the location of the crack tip. Near the tip, it appears as if the triangular portion of the delamination stops short of the crack tip. However, some additional delamination is present between the delamination tip and the crack tip. The results from Chapter 5 showed that the stress intensity behavior near the crack tip was strongly dependent on the local delamination geometry at the crack tip. Therefore, the change of geometry of the delamination front shown in Figure 6-5 could affect the crack growth behavior significantly.

6.1.4 Alternate laminates

Fatigue experiments were also conducted on TiGr laminates with lay-ups of $[\mathrm{Ti}/90/0/90_2]_s$ and $[\mathrm{Ti}/0/90/\pm30]_s$. The experiments were conducted so that the far-field stress level in the facesheet ply matched that of the experiments on the base laminate. The experimen-

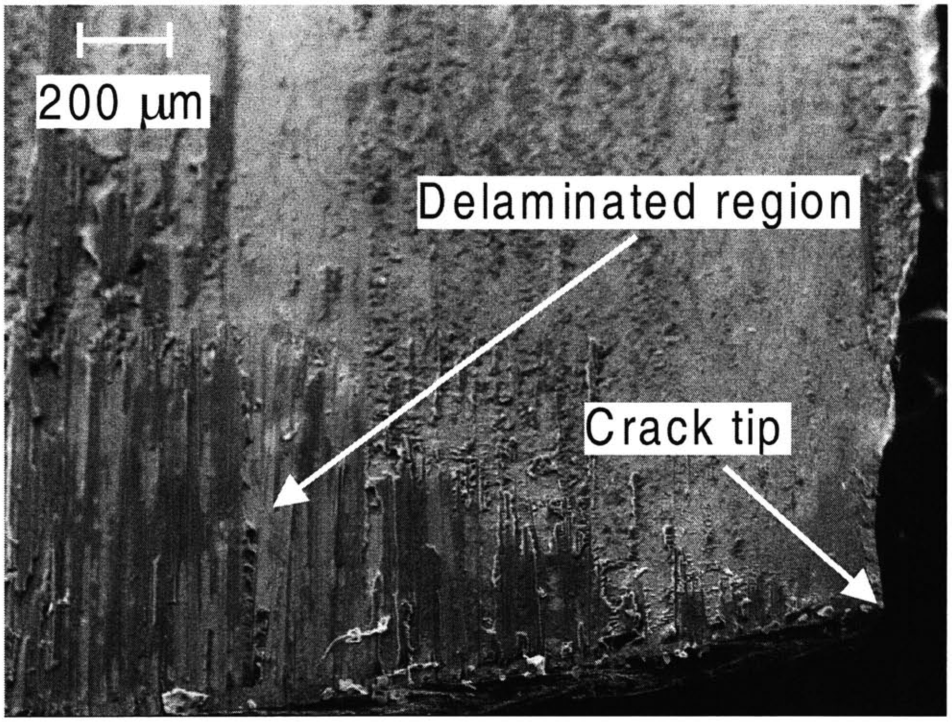

Figure 6-5: Micrograph of delamination shape near the crack tip

tally measured fatigue crack growth rate is plotted as a function of the applied facesheet stress intensity factor for three different applied stress levels in Figures 6-6 and 6.1.4 for the $[Ti/90/0/90_2]_s$ laminate. Figure 6-6 compares the experimental results to the 3D finite element model predictions and Figure 6.1.4 compares the same experimental results to the tunneling crack model by Nairn. The experimental results for the $[Ti/90/0/90_2]_s$ laminate indicate a slightly higher steady-state growth rate as compared to the base $[Ti/0/90/0_2]_s$ laminate. Both the 3D VCCT model and the tunneling model provide reasonable estimates for the crack growth behavior for the $[Ti/90/0/90_2]_s$ laminate, except in the region near the initial notch where the tunneling crack model does not capture the decreasing crack growth rate.

The difference between the experimental results and the model predictions is likely to be a result of the slightly different underlying damage modes evident in the $[Ti/90/0/90_2]_s$ laminates. The damage mode modeled for the base lay-up consisted of a crack in the facesheet with a triangular delamination between the facesheet and the core in the crack wake. In the

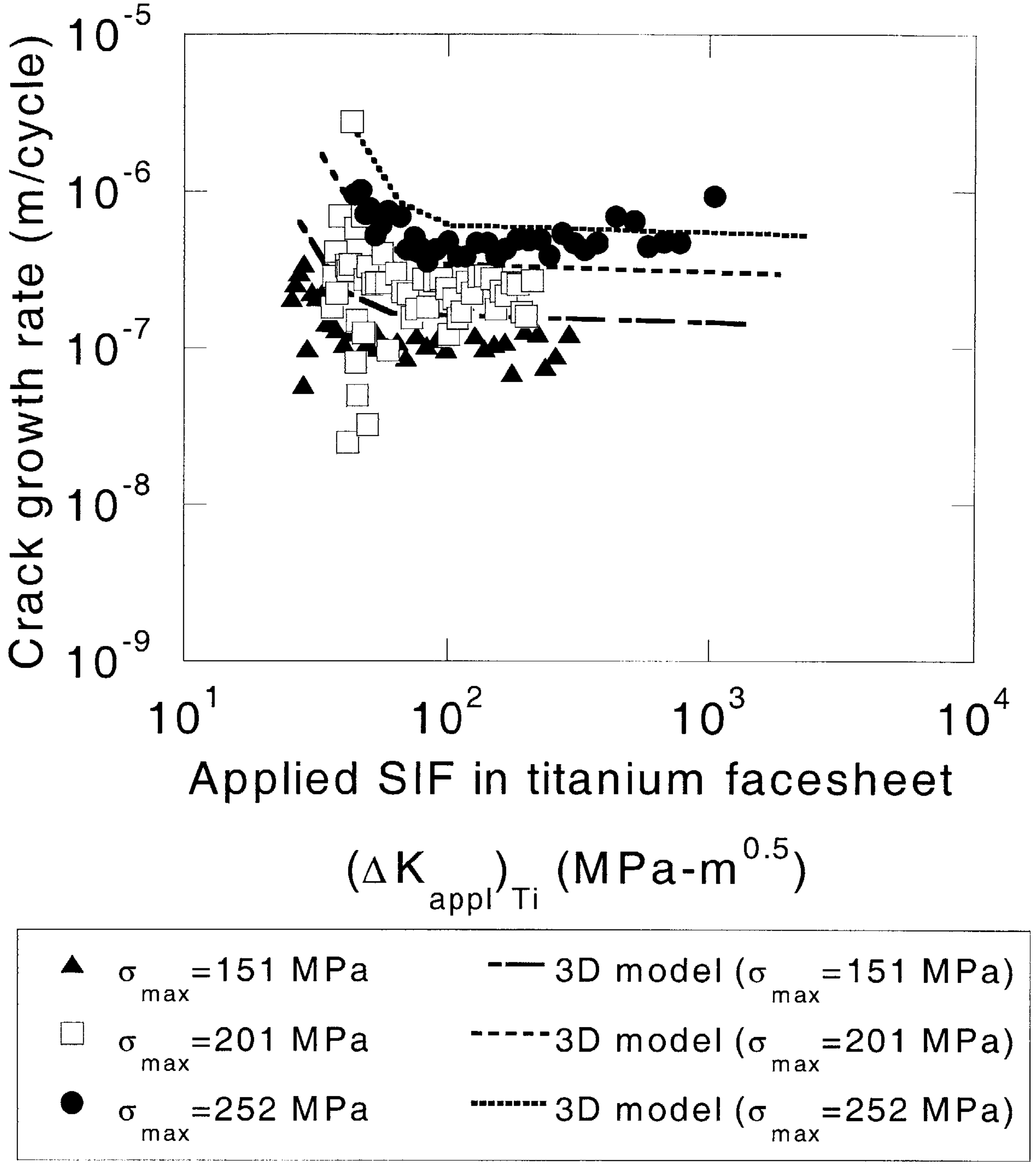

Figure 6-6: Experimental fatigue crack growth rate results compared to 3D VCCT model prediction for $[\mathrm{Ti}/90/0/90_2]_s$ laminates at three different applied far-field stress levels

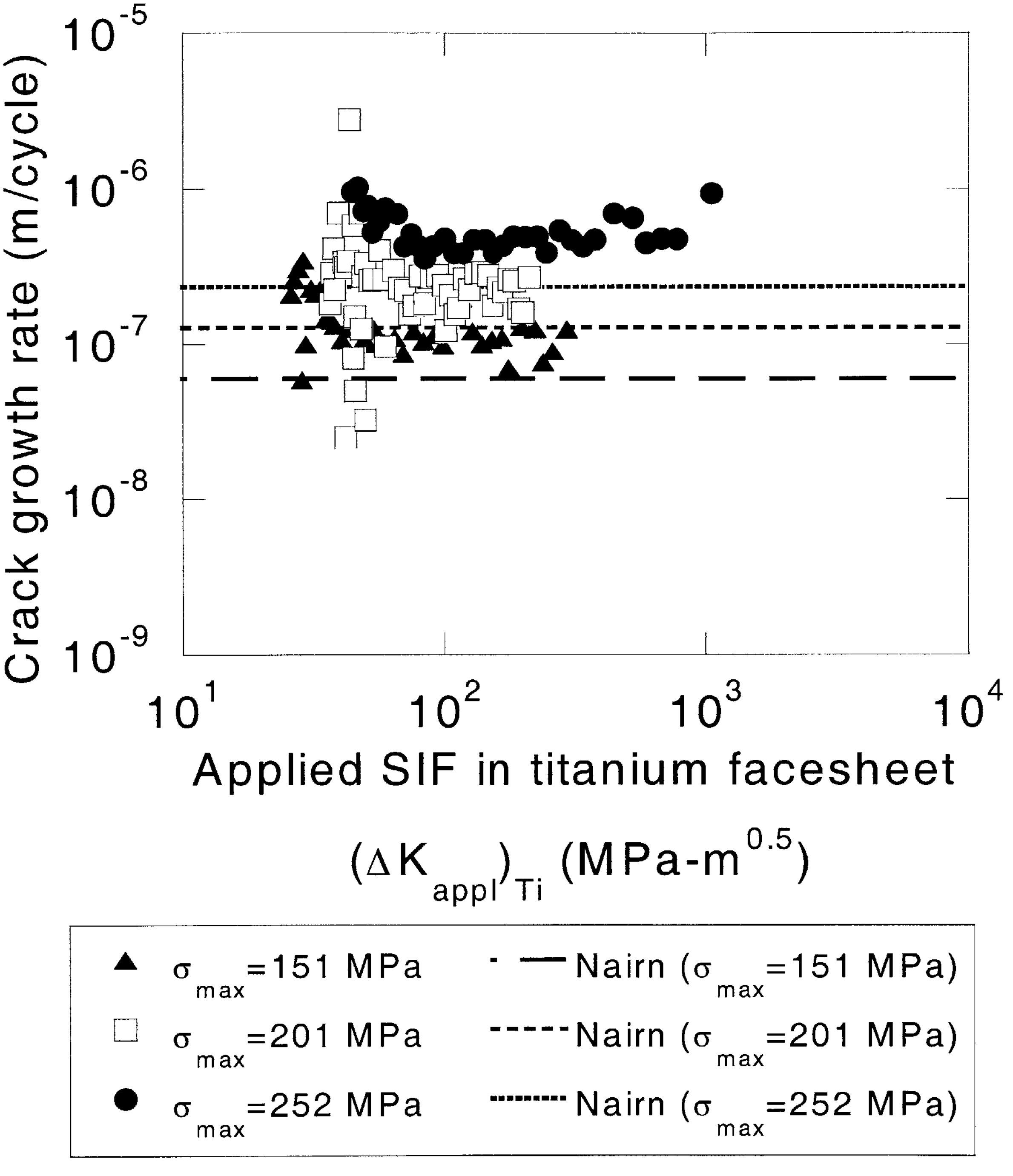

Figure 6-7: Experimental fatigue crack growth rate results compared to tunneling model prediction for $[Ti/90/0/90_2]_s$ laminates at three different applied far-field stress levels

$[\mathrm{Ti}/90/0/90_2]_s$ laminate, x-radiography and microscopy revealed a slightly different damage pattern. Firstly, there were significantly more transverse ply cracks evident from the x-radiographs as shown in Figure 6-8a. In addition, the delamination profile, while still triangular, propagated at a reduced angle with respect to the facesheet crack. The delamination also propagated at the interior 90°/0° interface, as opposed to the interface with the facesheet, as was observed in the base laminate. An edge view of a damaged laminate is shown in Figure 6-8b, which clearly shows the delamination between the 90°/0° interface.

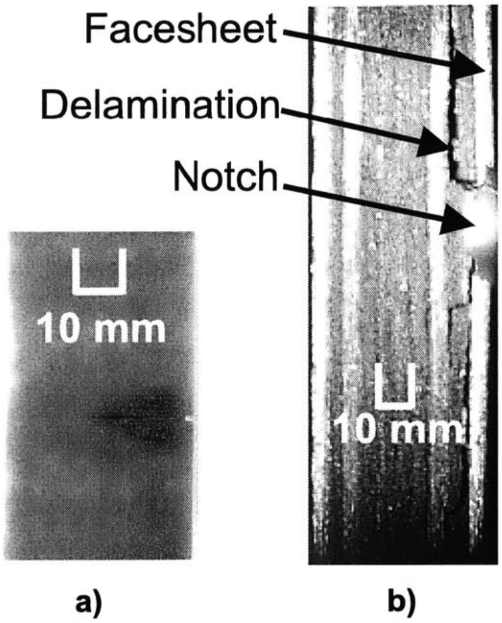

Figure 6-8: Damage modes in $[\mathrm{Ti}/90/0/90_2]_s$ laminates a) plan view x-ray showing delamination profile b) side view showing delaminated plies

Figures 6-9 and 6-10 display crack growth rate measurements from experiments conducted on $[\mathrm{Ti}/0/90/\pm 30]_s$ laminates. Similar to the two laminates discussed above, the $[\mathrm{Ti}/0/90/\pm 30]_s$ laminates have an initially decreasing crack growth rate that becomes constant as the crack extends. For the same applied facesheet stress, the steady-state crack growth rate is slightly lower than that of the base $[\mathrm{Ti}/0/90/0_2]_s$ laminate. The predictions of the 3D VCCT model, Figure 6-9, and of the tunneling crack model, Figure 6-10, are not in as good of agreement with the experimental results compared to the two laminates discussed previously. Although the trends in the model predictions match those of the experiments, the 3D VCCT model predicts a higher steady-state growth rate compared to the experimental results. The tunneling model predicts a lower steady-state growth rate compared to the experimental results.

The underlying damage modes in the $[\mathrm{Ti}/0/90/\pm30]_s$ laminates are noticeably different than those of the base $[\mathrm{Ti}/0/90/0]_s$ laminate. Figure 6-11a shows an x-radiograph from a specimen with ±30° plies, with an indication of edge delamination near the notch root and Figure 6-11b shows the full delamination pattern to be of a different shape than that of the base laminate. Figure 6-11c shows an edge view of the laminate near the notch indicating delamination between the interior plies, as opposed to the facesheet delamination for the base laminate. The above results indicate that the crack growth behavior depends on the laminate stacking sequence.

6.1.5 Effects of Specimen size

In addition to the alternate laminates, specimens were tested with different widths to determine the effect of specimen size on the growth rate. The effect of specimen width is significant when predicting how the coupon level experimental results translate to structural applications. A $[\mathrm{Ti}/0/90/0_2]_s$ specimen with a width of 76.2 mm and a 2 mm initial notch was cycled to compare the effects of width. The applied stress level was 419 MPa, with a load ratio, R, of 0.1, for the laminate, which corresponds to a stress of 406 MPa in the facesheet layers. The result of the experiment is compared to the 38.1 mm specimen at the same applied stress level in Figure 6-12. The wider specimen exhibits approximately the same fatigue behavior as the narrow specimen. Once out of the region influenced by the notch, the crack growth rate reaches a steady state value. Despite the large amount of scatter in the data, the growth rates for both specimens appear to level off at approximately the same value ($1 \cdot 10^{-7}$ m/cycle), within a factor of 2, indicating that the width of the specimen does not affect the long-term growth behavior significantly. The 3D model predictions are virtually identical for both the 38.1 mm specimens and for the 76.2 mm specimens. This is consistent with the conclusion stated in Chapter 5 that the facesheet thickness is the key dimension controlling damage growth.

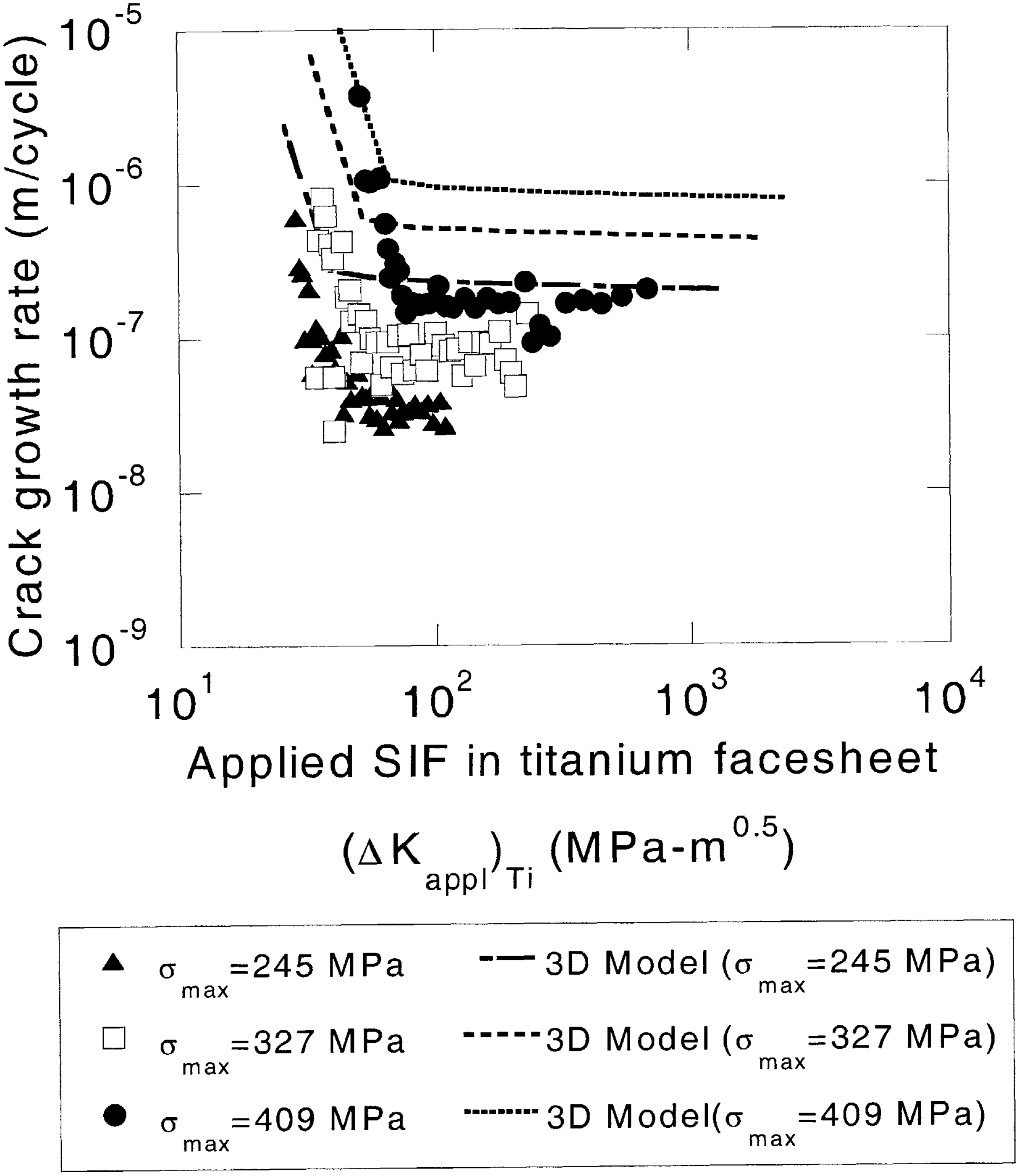

Figure 6-9: Experimental fatigue crack growth rate results compared to 3D VCCT model prediction for $[Ti/0/90/\pm30]_s$ laminates at three different applied far-field stress levels

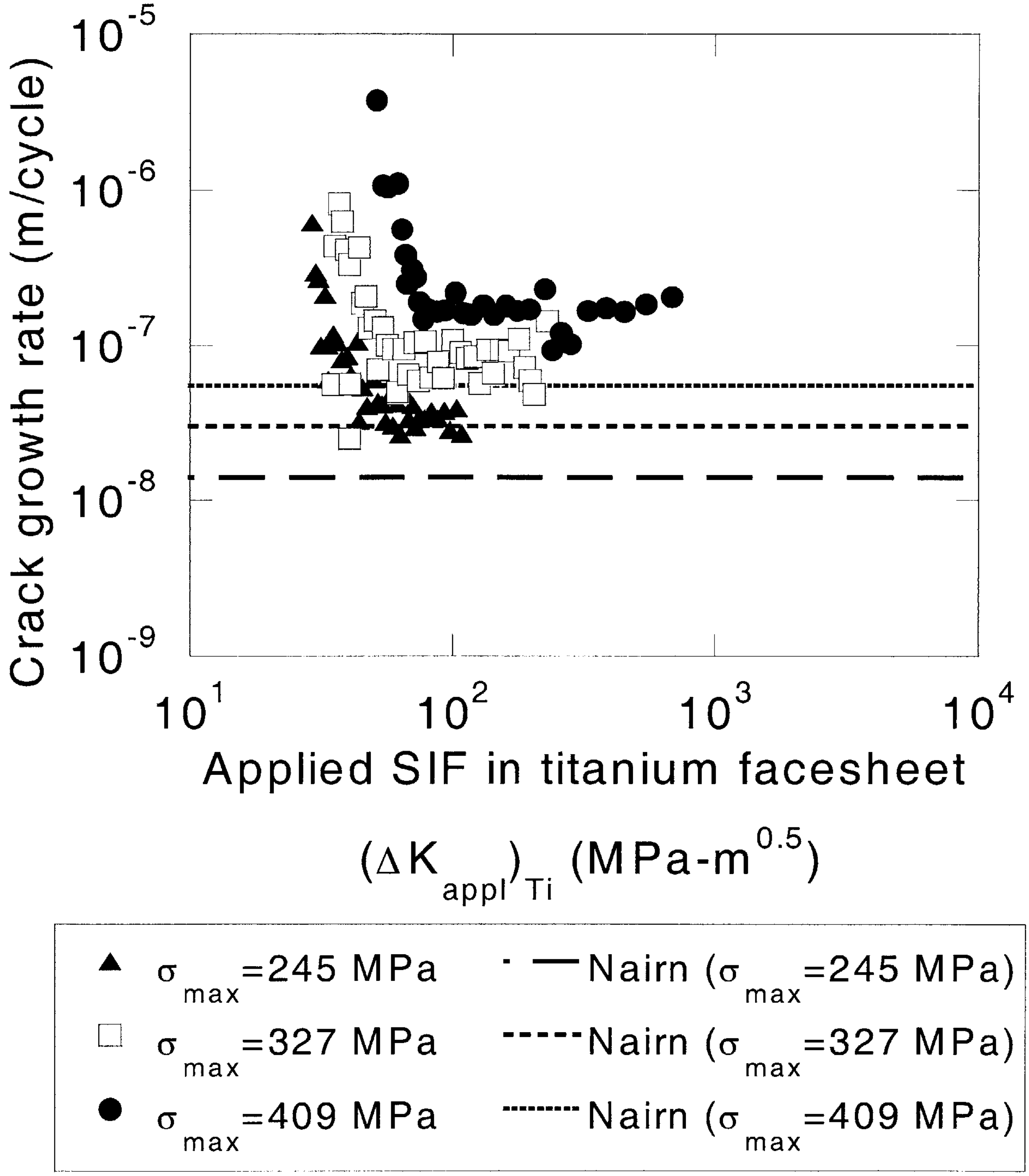

Figure 6-10: Experimental fatigue crack growth rate results compared to tunneling model prediction for $[Ti/0/90/\pm 30]_s$ laminates at three different applied far-field stress levels

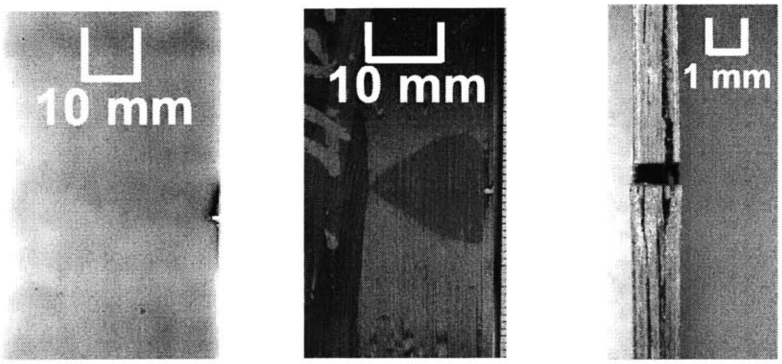

a) b) c)

Figure 6-11: Damage modes in $[\mathrm{Ti}/0/90/\pm30]_s$ laminates a) x-radiograph showing edge delamination b) delamination profile marked by die penetrant c)edge view of interior delamination

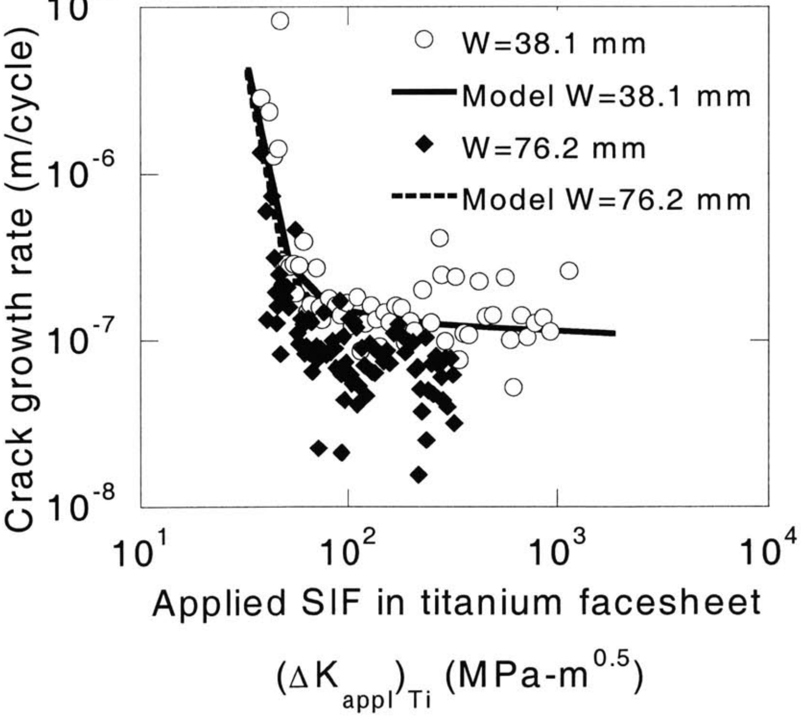

Figure 6-12: Effect of specimen width on fatigue crack growth behavior compared to 3D VCCT model for $[\mathrm{Ti}/0/90/0_2]_s$ laminates

6.2 Effects of temperature

The effect of temperature on damage growth in TiGr is an important issue for design. The experimental results on delamination growth from facesheet seams presented in Chapter 4 indicated that the delamination growth rate increased by an order of magnitude at 177° C compared to room temperature. Research on the titanium alloy Ti-β-21S, which is similar to Ti 15-3, indicated that no significant effect on the crack growth rate behavior, i.e. the Paris Law behavior and the associated constants, occurred for temperatures up to 482° C [115]. Therefore, any change in the crack growth rate at elevated temperatures is likely to be due to a change in the delamination growth behavior or a change in the R-ratio due to the presence of thermally-induced residual stresses. Crack growth experiments were conducted on $[Ti/0/90/0_2]_s$ laminates at room temperature and at 177° C to determine the effect of temperature on crack growth rate. Figure 6-13 compares the room temperature experimental measurements to the elevated temperature measurements. Note that the results shown in Figure 6-13 are for 76.2 mm wide specimens. The three-dimensional VCCT model prediction is also shown for the two cases. The model prediction is the same for both the elevated temperature and for the room temperature because the model does not account for temperature effects.

The experimental results for the base laminate show that the elevated temperature increases the average steady-state crack growth rate by approximately 70%. The average steady-state crack growth rate for each experiment was calculated from all of the data points for total crack lengths, a^*, longer than 4 mm. This distance was chosen arbitrarily as the crack length where the effects of the initial notch, a_0, are diminished and the crack growth has become steady-state. This is a much smaller effect than what was originally expected given the large temperature dependence of delamination growth shown in Chapter 4. Chapter 4 indicated an order of magnitude higher growth rate for the delamination at 177° C compared to room temperature. Figure 6-14 compares the damage state, as shown via x-ray, between a room temperature experiment and an elevated temperature. Globally, the shape of the delamination is approximately the same for both temperatures. However, the x-ray of the elevated temperature specimen (Figure 6-14(b)) appears to have a larger delaminated

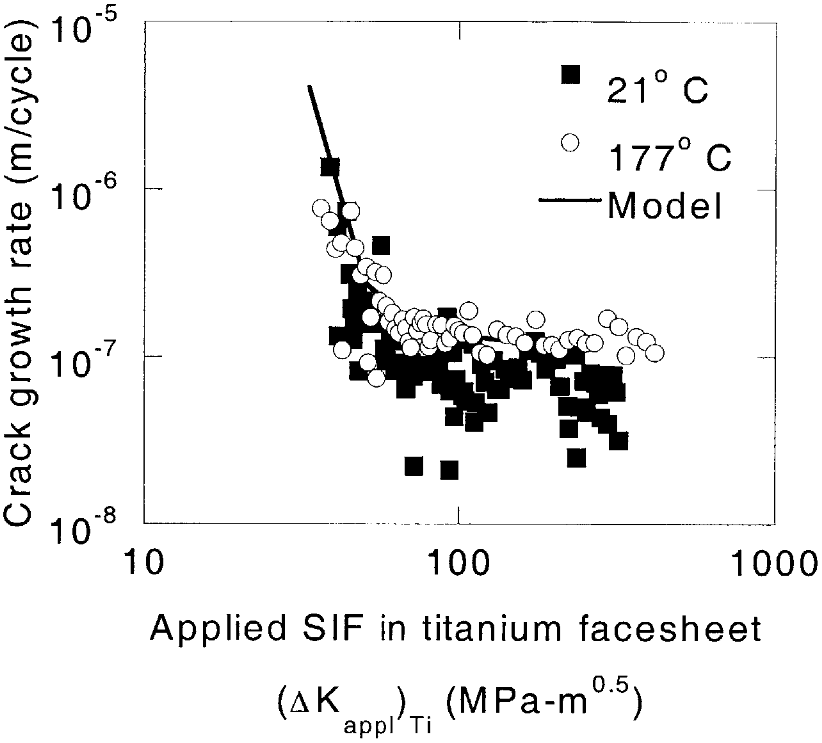

Figure 6-13: Effect of temperature on fatigue crack growth behavior in $[Ti/0/90/0_2]_s$ laminates compared to 3D VCCT model

area near the edge of the specimen. In addition, the delamination in the elevated temperature specimen extends into the region in the shadow of the initial notch, while the room temperature specimen did not indicate evidence of delamination growth in the shadow of the initial notch. Using the NDE techniques available, there was no distinguishable difference in the behavior between the two specimens for the critical region near the crack tip. Future studies should be conducted to determine the effects of temperature on the region near the crack tip.

The presence of thermally-induced residual stresses may account for the small difference between the room temperature crack growth rate and the elevated temperature crack growth rate. The effects of the residual thermal stresses were ignored in the analysis conducted in Chapter 5 because the residual stresses are independent of the applied stress and thus do not affect the value of the stress intensity factor range, ΔK:

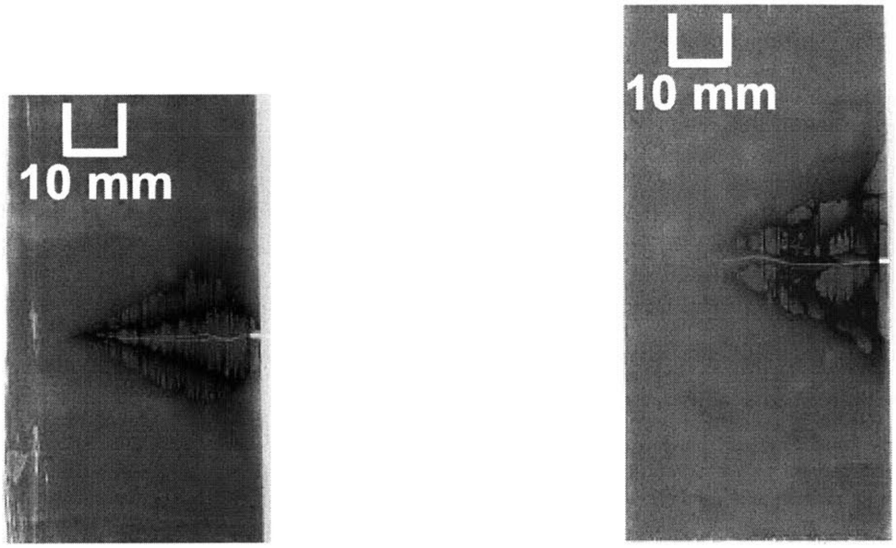

(a) (b)

Figure 6-14: X-radiograph of facesheet crack and delamination in specimens at a) room temperature and b) 177° C

$$\Delta K = K_{max} - K_{min} = (K_{max} + K_{thermal}) - (K_{min} + K_{thermal}) \tag{6.1}$$

However, the residual thermal stresses are significant in the titanium facesheets and while they do not affect ΔK, they change the effective R-ratio in the facesheet ply during fatigue cycling. The stress-free temperature for TiGr laminates is approximately 260° C [106]. For a room temperature experiment, the thermal residual stress in the facesheet ply of the base $[\text{Ti}/0/90/0_2]_s$ laminate, calculated using CLPT, is approximately 159 MPa. With a maximum applied stress in the facesheet ply of 406 MPa (far-field stress = 419 MPa) and an applied R-ratio of 0.1, the effective R-ratio is approximately 0.35. An elevated temperature experiment was conducted such that the effective R-ratio and the applied value of the stress range, $\Delta\sigma$, were matched to that of the room temperature experiments. The residual thermal stress in the facesheet ply at 177° C is 55 MPa. To match the effective R-ratio of 0.35 and the original applied $\Delta\sigma$ of 377 MPa, the experiment was conducted with a maximum stress of 510 MPa and an applied R-ratio of 0.28. Figure 6-15 compares the results of the elevated temperature experiment to that of the baseline room-temperature experiment. The average steady-state crack growth rates for the two experiments are within 27% of each other. This confirms that the difference between the room temperature and the elevated temperature experiments shown in Figure 6-13 is at least partially due to the change in R-ratio due to the thermally induced residual stresses.

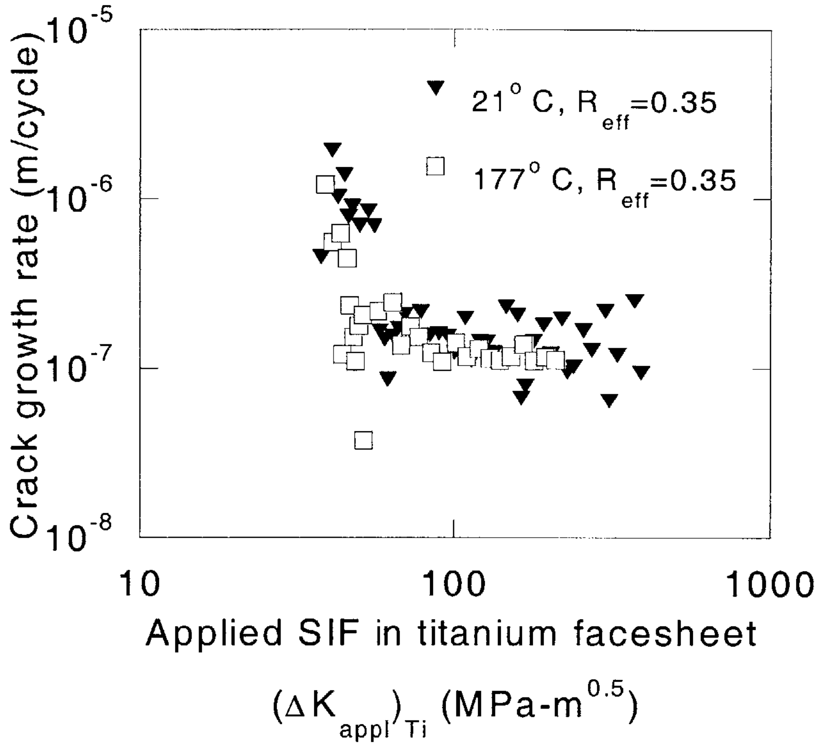

Figure 6-15: Effect of temperature on fatigue crack growth behavior in $[\mathrm{Ti}/0/90/0_2]_s$ laminates with a constant effective R=0.35

This ability to account for the effects of temperature on the facesheet crack growth rate by adjusting the R-ratio based on residual stresses is significant. Elevated temperature fatigue experiments are very expensive and take a considerable amount of time. If the same results can be achieved with room temperature experiments with an adjusted cyclic loading profile, the time and cost savings can be significant. It is important to note that the delamination growth is greatly effected by temperature, as discussed in Chapter 4. Although the effects on the facesheet crack growth can be accounted for by altering the R-ratio, the effects of temperature on the underlying delamination still need to be quantified.

6.3 Crack opening displacement results

To verify that the finite element models were accurately capturing the load transfer mechanism between the intact composite core and the cracked and delaminated titanium facesheet, a comparison was conducted between the predicted crack opening displacement from the 3D finite element model described in Chapter 5 and experimental results obtained from the facesheet crack growth experiments. To obtain the experimental crack opening profile, an acetate replication procedure was used. At a total crack length, a^*, of 16 mm, the cycling was interrupted and a replicate was taken of the crack opening with the specimen held at a constant stress level. To obtain the replicate, a strip of 25 mm wide acetate film was cut to the appropriate length and held against the surface of the specimen in an uncracked region. A small amount of acetone was applied to the side of the acetate tape facing the specimen and the tape was carefully pressed against the specimen surface over the cracked region, including the initial notch. After the acetone had dried, the tape was slowly removed and placed between microscope slides for observation. The replicate was initially inspected for smudges or contamination and if either has occurred, the procedure is repeated until a quality replicate was obtained.

Replicates were taken at each of five different laminate stresses, 0 MPa, 168 MPa, 288 MPa, 419 MPa, and 524 MPa. Each of the replicates was studied under an optical microscope at approximately 200x magnification. The crack opening displacements was recorded along the crack length for each applied stress level. The measurements were performed using the Zeiss™ KS-300 software package. The measurement tools in the software package were calibrated to the output from the microscope. The residual crack opening displacement at 0 MPa was subtracted from the results at the higher stress levels to determine the net crack opening displacement profile as a function of the applied stress. The results are compared to the finite element results in Figure 6-16. The error bar shown in Figure 6-16 is representative for all of the data points shown, with the data point in the centered on the error bar. The magnitude of the error was estimated based on the resolution of the replicate and microscope systems as well as the ability to accurately detect and measure the crack opening displacement. Given the errors associated with the replicate and measurement procedures, there is good agreement between the finite element results and the experimental results, indicating that the 3D finite element model is capturing the load transfer mechanism across the facesheet crack.

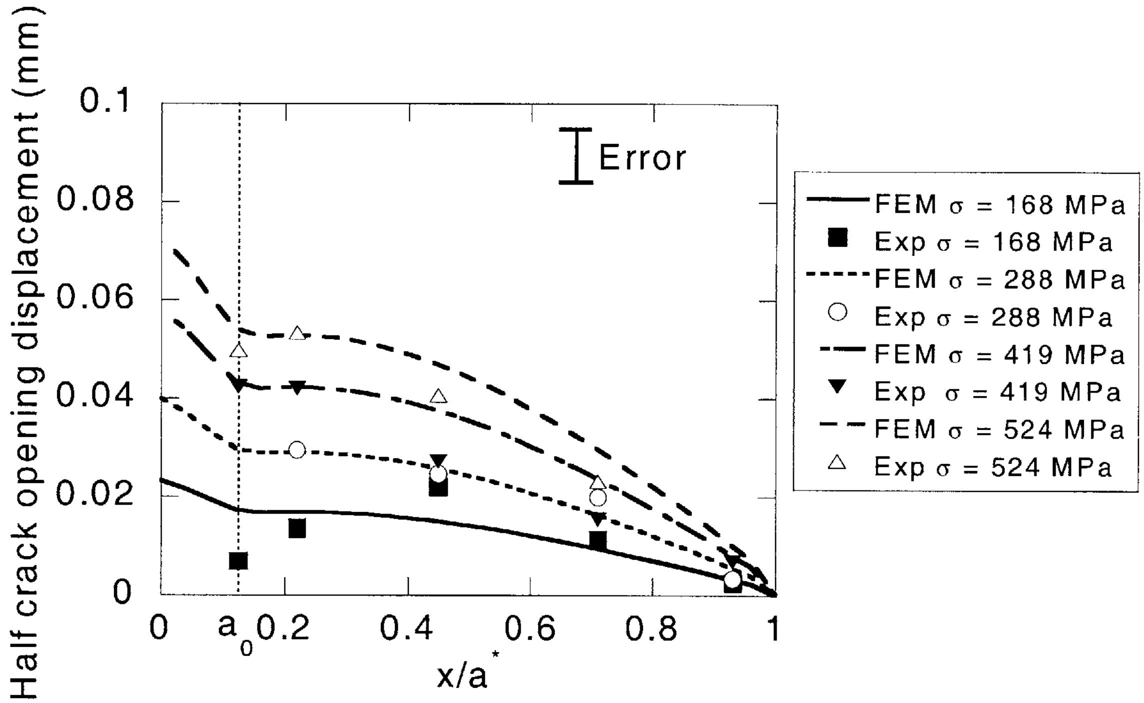

Figure 6-16: Comparison between finite element and experimental crack opening displacement profiles at 4 different applied stress levels ($\frac{x}{a}$=1 is the crack tip)

To emphasize the significance of the crack bridging, Figure 6-17 compares the crack opening displacement for an applied facesheet stress of 406 MPa to the theoretical solution for the crack opening displacement profile in a monolithic titanium sheet with the same applied stress. The large difference between the monolithic case and the TiGr specimen clearly shows the strength of the crack bridging by the underlying PMC plies. The experimental results and the results from the 3D finite element model could potentially be used to find a bridging traction profile to be used in the bridged-crack model.

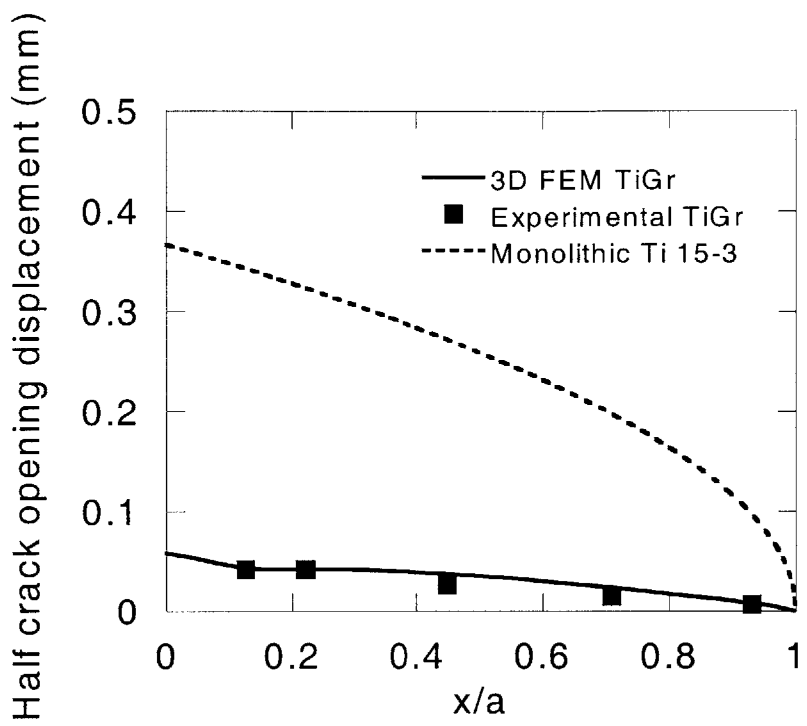

Figure 6-17: Comparison between monolithic titanium and TiGr crack opening displacement profiles for an applied facesheet stress of 406 MPa

6.4 Summary of experimental results and comparison to the modeling

The experimental results for facesheet fatigue crack growth in TiGr laminates exhibit a consistent behavior for three different lay-ups. The crack growth rate initially decreased and after a short crack advance, the growth rate leveled out to a constant value. If the constant fatigue crack growth behavior exhibited by TiGr is a characteristic of the material, the crack growth rate, obtained either from experiments or models, can be utilized to characterize damage growth of a crack discovered during service of a structural component.

The three-dimensional model developed in Chapter 5 of this thesis correlated well to the experimental results for a $[\mathrm{Ti}/0/90/0_2]_s$ laminate at three load levels. Verification that the three-dimensional model captured the load transfer mechanism of the crack bridging phenomenon was achieved by comparing the crack opening displacements from the model and from the experiments. The two-dimensional VCCT model also predicted a constant crack growth behavior. However, the values for the stress intensity factor at the crack tip did not exactly match those predicted with the three-dimensional model.

A steady-state crack tunneling model developed by Nairn also correlated well with experimental results for the $[\mathrm{Ti}/0/90/0_2]_s$ laminate in the steady-state regime of the crack growth. However, the tunneling model under-predicts the steady-state crack growth rate for the two alternate laminates and does not capture the behavior near the initial notch. The tunneling model provides a simple analytic estimation of the steady-state fatigue growth rate that could potentially be used to compare different lay-ups and configurations.

Experimental observations on the delamination angle indicate that the angle is approximately 45° for shorter cracks and decreases to 30° for longer cracks. The strip model presented in Chapter 5 provides an estimate for the delamination profile angle, but is not accurate for short cracks. Thus far, no reliable method to predict delamination growth has been determined. Further studies need to be conducted to understand thoroughly the delamination growth behavior and the effects of 0° ply splits.

Experiments were also conducted on the $[\mathrm{Ti}/0/90/0_2]_s$ laminate at 177° C. The experiments revealed that the elevated temperatures do not affect the fatigue crack growth rate significantly. The thermally induced residual stresses alter the load ratio, R, and likely accounts for a majority of the change in fatigue crack growth rate at elevated temperatures. The ability to account for temperature effects by changing the load profile and conducting the experiments at room temperature can significantly reduce the cost of validating the material performance at elevated temperatures.

Experiments on two alternate TiGr laminates ($[\mathrm{Ti}/90/0/90_2]_s$ and $[\mathrm{Ti}/0/90/\pm 30]_s$) were also conducted. Both laminates showed similar trends in the crack growth rate as the crack length increased, but the magnitude of the steady-state growth rate was different for each laminate. The underlying damage modes were slightly different for the alternate laminates. The difference in the underlying damage modes diminished the ability of the models to capture the crack growth behavior.

Chapter 7

Potential Application and Observations

The work presented in the preceding chapters focused on the mechanics of fatigue damage growth in TiGr laminates. Specifically, the problem of a titanium facesheet crack with a facesheet delamination in the wake of the crack was investigated both using analytic models and experiments. There are two main goals of this chapter that extend the work discussed in the previous chapters. The first section focuses on applying the crack growth rate results from the 3D facesheet crack growth model developed in Chapter 5 to TiGr coupons with open holes. The goal is to use the model to predict the growth of the crack and delamination and determine the stiffness reduction as a function of fatigue cycles due to the propagation of the two damage modes. Previous work [3] identified the stiffness reduction as a key damage metric for TiGr laminates loaded in fatigue. The second section explores the implications of the modeling and experimental results presented in this research for future applications to both TiGr laminates and other composite materials.

7.1 Application of facesheet crack growth models

The preceding chapters described the behavior of facesheet crack growth in TiGr laminates. The goal of this section is to use the results from the models and the experiments to predict the reduction in local stiffness due to the facesheet crack and delamination growth and compare the prediction to the measured stiffness reduction for TiGr laminates with open holes. The application of the model of a different structural configuration will provide insight into how effectively the results can be used in the design process without significant recalibration. The models and analysis discussed in the previous chapters are used to describe the crack growth behavior and the delamination growth behavior necessary to assess the stiffness reduction.

7.1.1 Prediction of stiffness reduction

Previous research [3] indicated that stiffness reduction due to fatigue damage accumulation is the critical failure metric of TiGr laminates with open holes and that most of the stiffness reduction is a result of facesheet delamination. The delamination develops in the wake of the facesheet cracks emanating from the open hole. Once the crack in the facesheet layer reaches the specimen edge, the delamination continues to grow in a manner similar to that of the seam specimens described in Chapter 4.

A simple model has been developed to predict the local stiffness reduction as a function of fatigue cycles. The model consists of two different components, one to capture the growth of the crack and delamination until the crack reaches the specimen edge and the second to capture the growth behavior of the delamination after the crack reaches the specimen edge. In a structural application, the effect of the crack reaching a free edge would be similar to the crack reaching a facesheet seam or multiple cracks linking together.

The prediction of the damage growth before the crack reaches the edge of the specimen will be conducted using the results from Chapters 5 and 6. Some approximations are necessary to apply the predictions from the damage growth models described in the previous chapters to the open hole configuration. Firstly, the delamination profile in the wake of the facesheet crack will be approximated as a rectangle for the calculation of the laminate stiffness. This allows a simple analytic approximation to be made for the stiffness reduction during this phase of the damage growth. The actual shape observed from experiments is triangular. However, the effect of using a rectangle in this case should be minimal because the stiffness change during this phase of the growth is believed to be small compared to that which occurs during the second phase. Using a rectangular delamination, the local stiffness reduction during the first phase of the crack growth is approximately 10% for the specimen configuration in this study. The ratio of delamination length to crack length, $\frac{D}{a}$ will be kept at a constant value of 1 in the model, which is similar to the value used in the 3D VCCT model and observed experimentally.

The crack growth rate applied for the facesheet cracks is derived from the results of the 3D finite element model described in Chapter 5. The 3D model predicted the stress intensity factor for six different crack lengths. For the purposes of the stiffness reduction model, the crack growth rate derived for a specific crack length in the 3D model was applied over a range of crack lengths both higher and lower than the actual crack length used for the model. For example, if the 3D model produced values for the stress intensity factor for crack lengths of 10 mm, 20 mm, and 30 mm, the value obtained for a 20 mm crack would be applied for cracks 15 mm to 25 mm in length in the stiffness reduction model.

Although experimental evidence indicates that a multiple crack and delamination pattern forms around the hole, for simplicity the damage is approximated as a single, centrally-located crack propagating outward toward the specimen edge. A schematic view of the damage approximation is shown in Figure 7-1.

The reduction in local stiffness associated with the damage growth is calculated using springs to represent the damaged and undamaged regions of the laminate. A schematic of the model is shown in Figure 7-2. The gauge length, GL, for the stiffness model is the same as that of the extensometer used for the experimental measurements, 50 mm. In the damaged region, the springs are in parallel and the stiffness of the damaged region, K_D is calculated using:

$$K_d = 2K_{d-lam} + K_{d-core} \tag{7.1a}$$

$$K_{d-lam} = \frac{E_{lam} t_{lam} \left(\frac{W}{2} - a\right)}{2D} \tag{7.1b}$$

$$K_{d-core} = \frac{E_{core} t_{core} 2a}{2D} \tag{7.1c}$$

where:

E_i = Young's modulus of section
W = width of section
t_i = thickness of section
a = crack length
D = delamination length
i = lam, core for the laminate and the composite core, respectively

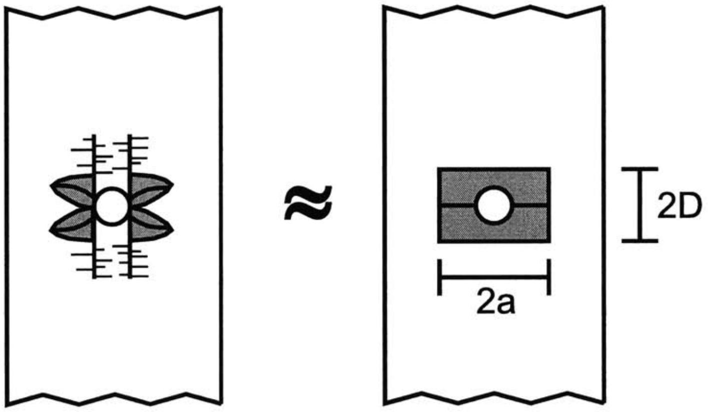

Figure 7-1: Schematic of damage approximation for stiffness reduction model

The local stiffness over the entire gauge length is calculated using:

$$\frac{1}{K_{tot}} = \frac{2}{K_{lam}} + \frac{1}{K_d} \tag{7.2}$$

To be comparable to the experimental results, it is necessary to modify the calculation of the local stiffness shown in Equation 7.2 once the delamination extends beyond the gauge length of the extensometer, GL. When this occurs experimentally, the extensometer remains

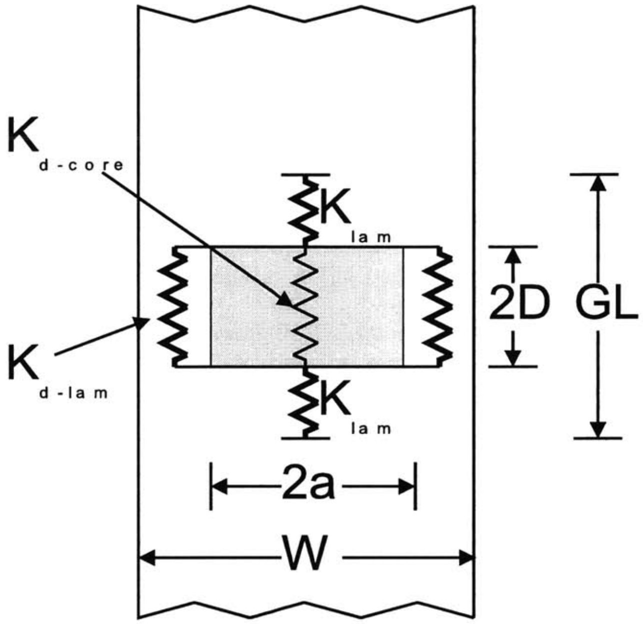

Figure 7-2: Schematic of spring model to calculate stiffness reduction

attached to the delaminated facesheet. The deflection measured with the extensometer for these cases is that of the entire damaged portion of the laminate. Therefore, the stiffness recorded by the extensometer is only representative of the damaged section, i.e. $K_{tot} = K_d$.

Once the crack reaches the edge of the specimen, the continued growth of the delamination will be governed by the results of the seam experiments presented in Chapter 4. The delamination growth rate is related to the applied strain energy release rate using a power-law relationship, as described in Section 4.1.3 and can be altered depending on the test temperature.

All of the experimental work was conducted with an applied R-ratio of -0.2 or +0.1 for the entire laminate. For the R = 0.1 experiments, the stress range, $\Delta\sigma$, used to calculate the crack growth rate is the difference between the maximum and the minimum stresses. For the R = -0.2 experiments, the calculation of the $\Delta\sigma$ is more complex. It is assumed that the facesheet crack closes and does not propagate when the facesheet stress is less than or equal to zero. However, the residual stresses in the facesheet need to be included when calculating the zero stress level in the facesheet, at which point the crack closes. For experiments at

177° C, the residual stress in the facesheet ply is 55 MPa. For the experiments conducted at 177° C, the magnitude of the thermally induced residual stress in the facesheet, $\sigma_{res,Ti}$, is 55 MPa. If the magnitude of the minimum applied stress level, σ_{min}, is less than, $\sigma_{res,Ti}$, the entire applied stress range, $\sigma_{max} + \sigma_{min}$, is used to calculate the stress intensity factor. If the magnitude of the minimum applied stress level is greater than $\sigma_{res,Ti}$ then the stress range is bounded by the maximum applied stress and the residual stress. For example, if R = -0.2 and σ_{max}=100 MPa, the minimum stress is -20 MPa. In this case, the magnitude of the minimum stress is less than the residual stress in the facesheet indicating that the crack never fully closes. Therefore the stress range, $\Delta\sigma$ is 120 MPa. However, if σ_{max}=300 MPa and R=-0.2, the minimum stress is -60 MPa. The magnitude of the minimum stress (60 MPa) is larger than magnitude of the residual stress (55 MPa). In this case, the crack is assumed to be closed for part of the cycle and $\Delta\sigma$ is $\sigma_{max} + \sigma_{res,Ti}$ or 355 MPa. These cases for calculating the stress intensity factor are outlined graphically in Figure 7-3.

The calculation of the strain energy release rate is more straightforward because the delamination growth is mainly in Mode II. Therefore, the entire applied stress range is used to calculate the strain energy release. Figure 7-3 graphically demonstrates the stress ranges used to calculate the various damage growth parameters.

7.1.2 Comparison of local stiffness reduction to experimental results

The experimental results for the local stiffness reduction are taken from Reference [3]. Details of the experiments and the data collection procedures are contained in Reference [3]. Table 7.1 lists the applied load levels and the parameters controlling the crack and delamination growth used as inputs into the compliance model.

Figure 7-4 compares the results of the model to the experimental measurements at four different percentages of the open hole tension (OHT) strength. These experiments were conducted at 177° C at an applied R-ratio of -0.2. The local stiffness reduction predicted with the model has the same profile as the experimental results where the stiffness decreases gradually for a number of cycles and then begins to decrease rapidly. However the "drop-off"

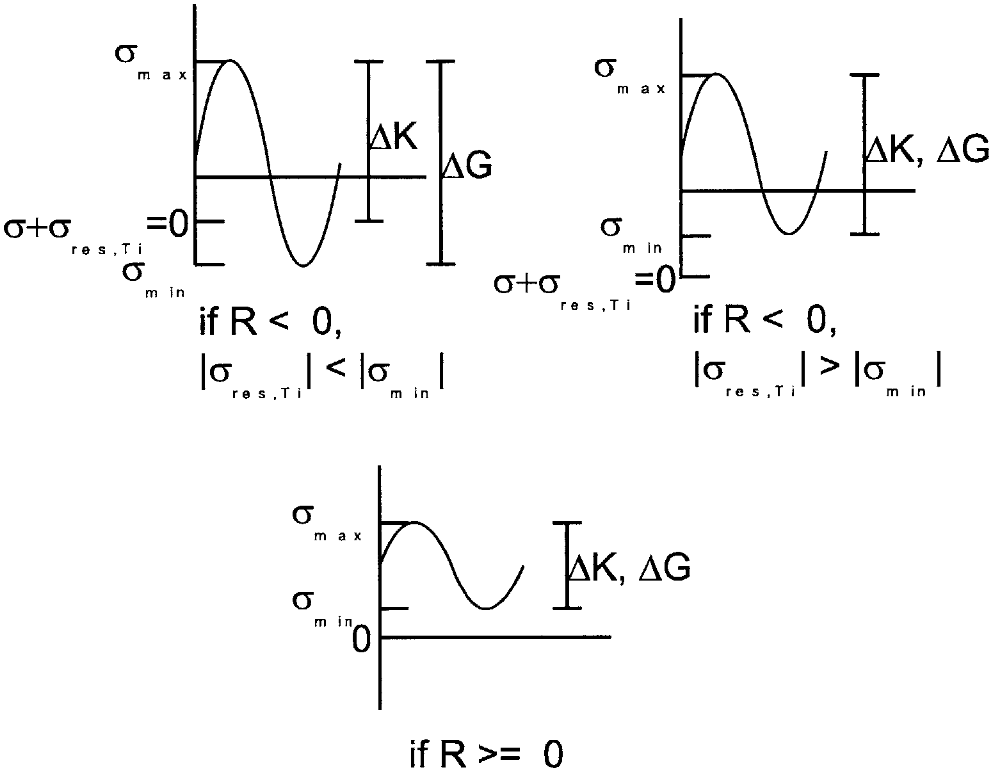

Figure 7-3: Calculation of the stress intensity amplitude and the strain energy release rate amplitude

region, is not the same for the model and the experiments. The model predicts the drop-off to occur at a higher number of cycles than the experiments. For this configuration, the "drop-off" is controlled by the number of cycles required for the facesheet crack to reach the specimen edge, i.e. the first phase of the damage growth. Based on the results shown in Figure 7-4, the prediction for the trends in the stiffness reduction after the crack reaches the specimen edge match the trends in the experimental results for the second phase of growth.

In order to tune the model, the model prediction is adjusted to match the experimental results for one applied stress level (45% OHT). The adjustment factor is a factor of 5. This tuning factor is equivalent to adjusting the number of cycles that the crack requires to reach the specimen edge, or shifting the model prediction. If the model results for the other load levels are tuned by a factor of 5, the predictions are in better agreement with the experimental results as shown in Figure 7-5.

Table 7.1: Inputs for stiffness degradation model

σ_{max} (MPa)	Temperature (° C)	R	Stress range for calculating ΔK_{eff} (MPa)	ΔG (N/m)	dD/dN (m/cycle)
100	177	-0.2	$\sigma_{max} \rightarrow \sigma_{min}$	5.98	$4.21 \cdot 10^{-9}$
300	177	-0.2	$\sigma_{max} \rightarrow \sigma_{res}$	53.8	$9.52 \cdot 10^{-8}$
453	177	-0.2	$\sigma_{max} \rightarrow \sigma_{res}$	121	$3.01 \cdot 10^{-7}$
453	21	-0.2	$\sigma_{max} \rightarrow \sigma_{min}$	121	$8.25 \cdot 10^{-8}$
453	177	0.1	$\sigma_{max} \rightarrow \sigma_{min}$	119	$2.94 \cdot 10^{-7}$
604	177	-0.2	$\sigma_{max} \rightarrow \sigma_{res}$	215	$6.81 \cdot 10^{-7}$

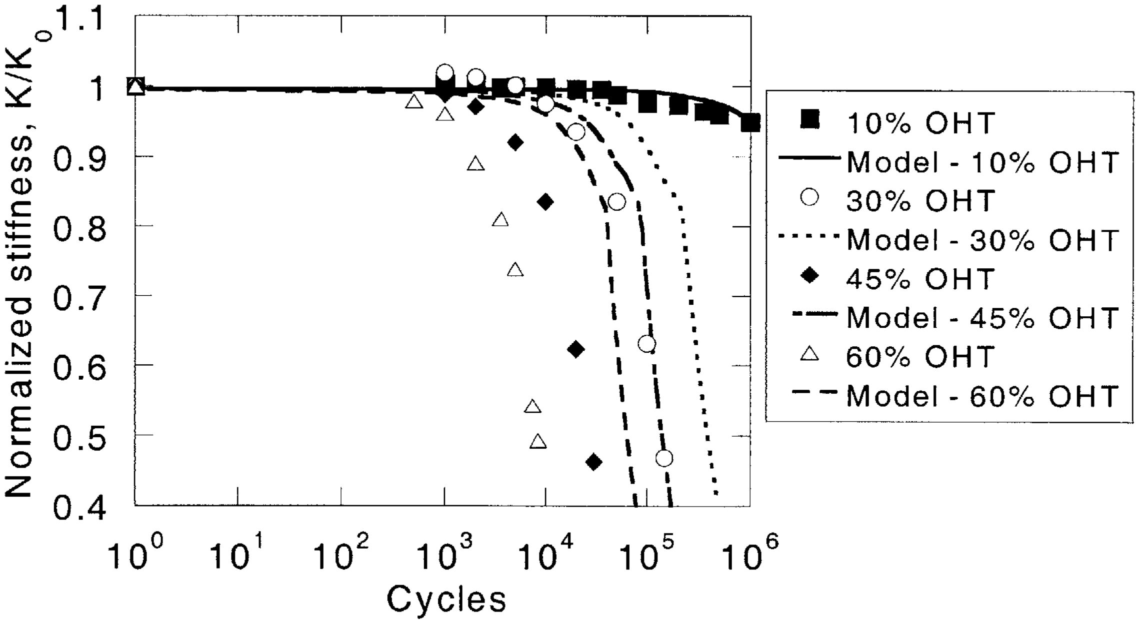

Figure 7-4: Comparison of stiffness reduction predictions to experimental results for multiple applied stress levels tested at 177° C, R=-0.2 as a percentage of the open hole tensions strength (OHT)

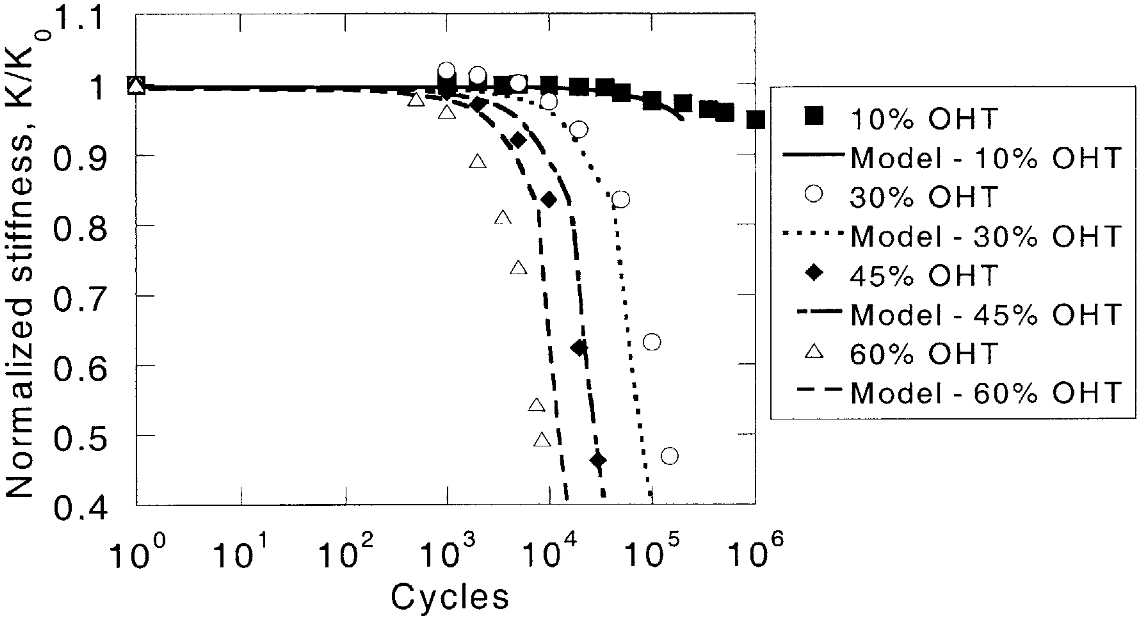

Figure 7-5: Comparison of stiffness reduction predictions to experimental results shown in Figure 7-4 with tuned model

The necessity of the tuning factor may be due to different specimen geometry. The single-edge notch tension models developed in Chapter 5 were used to predict the crack growth rate. The experimental results from [3] are from specimens with centrally located open holes. Since the crack growth for short cracks is influenced by the geometry and size of the hole/notch, the tuning factor is an engineering solution to avoid the complex issues associated with short crack fatigue growth [114]. The size and shape difference between the two configurations may affect the crack growth rate for short cracks and alter the number of cycles required for the crack to grow to the specimen edge.

The tuned model prediction for the specimen tested at an R-ratio of 0.1 is shown in Figure 7-6. Results comparing the local stiffness reduction model at 21° C and at 177° C are shown in Figure 7-7. The model predicts the same stiffness reduction profile for the region before the crack reaches the specimen edge for both temperatures because the facesheet crack growth rate is not dependent on temperature. The difference between the two cases is evident after the crack reaches the edge of the specimen. At that point, the model prediction for the 21° C specimen has a "knee" in the data representing the different delamination growth rate for the lower temperature.

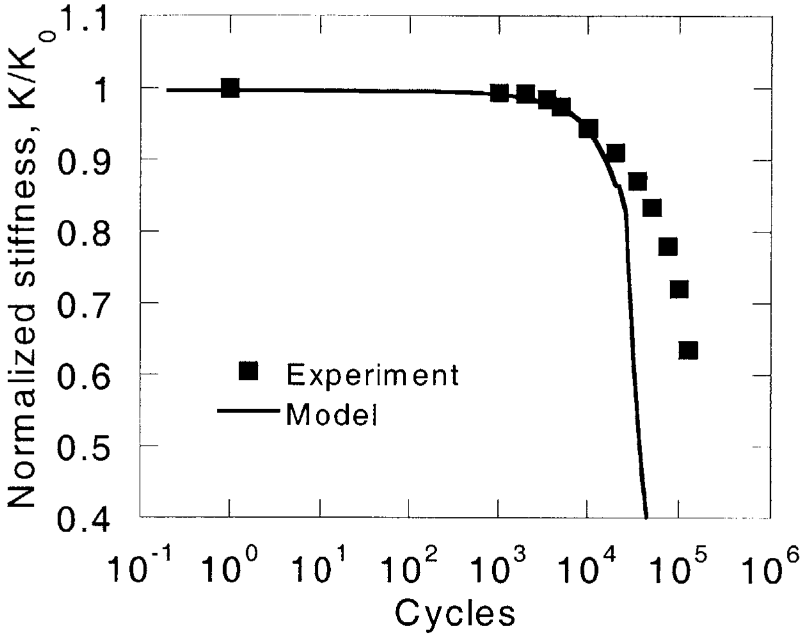

Figure 7-6: Comparison of stiffness reduction predictions to experimental results for an R-ratio of 0.1, $\sigma_{max} = 453\ MPa$, T=177° C

For the laminates tested in Reference [3], specimen failure was defined as the point where the local stiffness, as measured with an extensometer, reached 50% of the initial value. An S-N curve was presented for the failure condition of 50% reduction in local laminate stiffness. Figure 7-8 shows the predictions of the tuned model to the experimental S-N results. The tuned model predictions, presented as five calculated cases connected by straight lines, correlate well with the experimental results.

Although a tuning factor is necessary to match consistently the local stiffness reduction predicted using the model to the experimental results, the model is useful for determining the effects of specimen geometry and applied load. Figure 7-9 compares the model prediction for stiffness reduction for two specimens with different widths, 38.1 mm and 610 mm, and the same length, 914 mm. For the wider specimen, the "drop-off" is delayed. In addition, a larger percentage of stiffness reduction occurs before the crack reaches the specimen edge for the

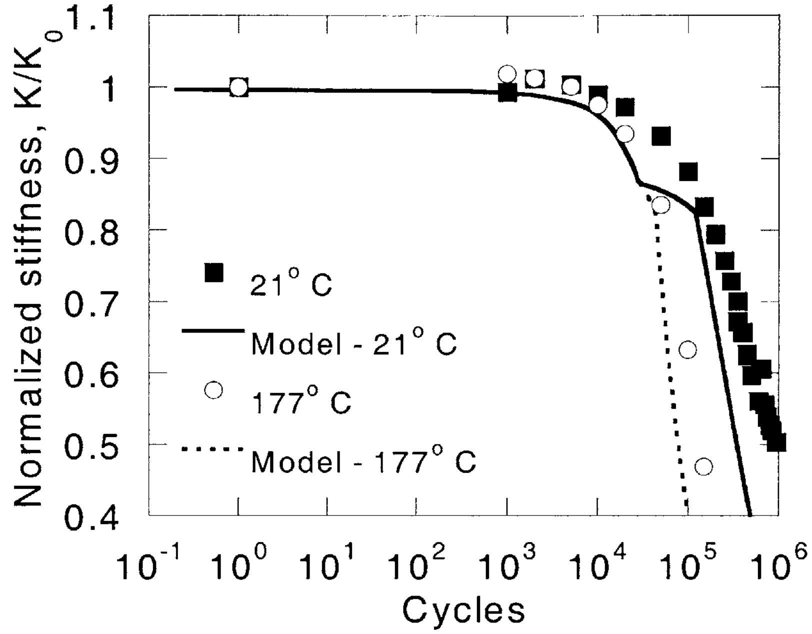

Figure 7-7: Comparison of stiffness reduction predictions to experimental results for 21° C and 177° C, $\sigma_{max} = 300\ MPa$, R=-0.2

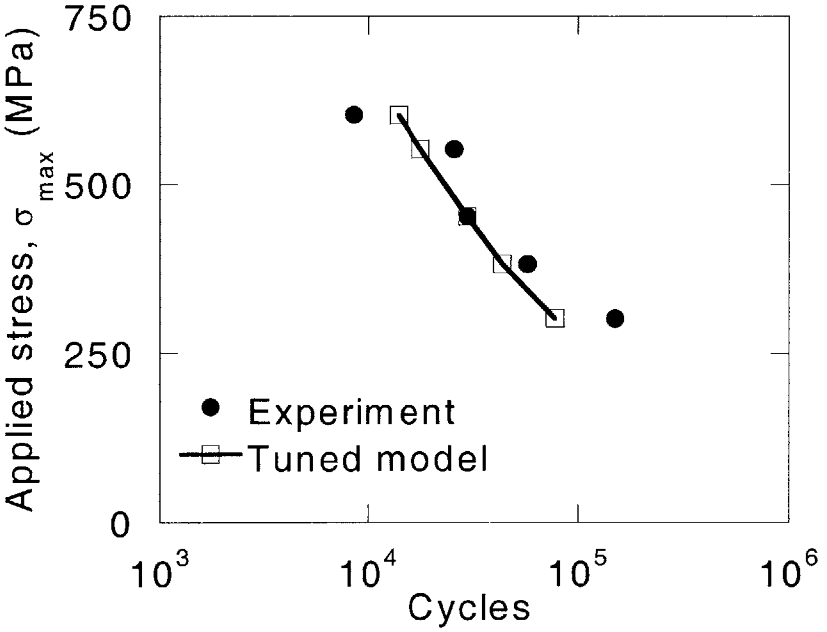

Figure 7-8: Experimental S-N plot for 50% stiffness reduction compared to tuned model results [3]

wider specimen. These results indicate that although the steady state crack growth rates for 610 mm wide specimens is similar to that of the 38.1 mm specimens, as shown in Chapter 6, the stiffness reduction does not necessarily scale in the same manner. In addition, the percentage of stiffness reduction before the crack in the facesheet layer reaches the specimen edge is different for the two configurations. For the wider specimen, the global stiffness is reduced by approximately 50% when the crack reaches the specimen edge as opposed to a 10% reduction in the narrow specimen when the crack reaches the edge. The comparison between the two specimen sizes is one example of how the types of models developed in this work can be useful for predicting the effects of scale for different configurations without a significant number of experiments.

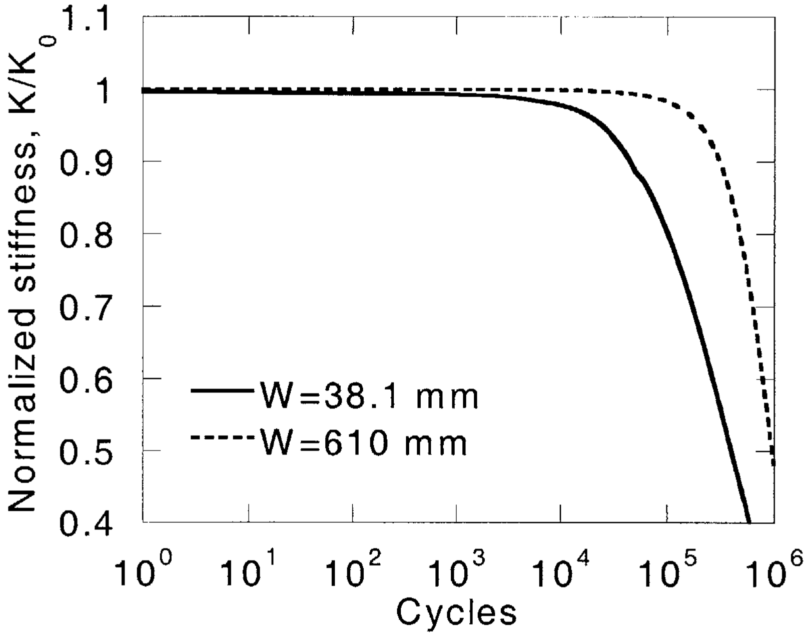

Figure 7-9: Comparison of model results for two specimen widths for $\sigma_{max} = 453 MPa$, R=-0.2

7.2 Observations

This section summarizes the key results from the present research and their implications on future research on TiGr and on modeling of layered composite materials in general. The first section focuses on TiGr laminates and their use in future structural applications. The second section focuses on the application of models to fatigue crack growth in TiGr and other composite laminates.

7.2.1 TiGr laminates

TiGr laminates are a promising candidate for structural applications on future aerospace vehicles such as the High Speed Civil Transport (HSCT). The results from this research indicate that the fatigue crack growth behavior of TiGr is significantly better than that of monolithic titanium and that the composite damage mechanisms are similar to those observed in non-hybrid composites. If the main role of the titanium facesheet is to act as a protective layer for the underlying composite, extensive delamination and cracking of the facesheets will reduce its ability to shield the core from the environment.

The cracks in the facesheet layers are likely to be the first noticeable damage mechanism for TiGr laminates. Therefore, it is significant that the results show that the facesheet crack growth is regular and predictable. The presence of cracks in the facesheets may allow inspection techniques similar to those used currently on aluminum aircraft to be used on TiGr structures. One of the main design concerns with non-hybrid composites is the difficulty of non-destructive damage detection of composite parts in service. The presence of visible damage should aid the inspection of TiGr components. The ability to detect and predict the crack growth behavior would allow accurate damage tolerant design techniques to be applied. For the base laminate studied in this research, i.e. $[\mathrm{Ti}/0/90/0_2]_s$, the most critical underlying damage mode is delamination of the facesheet in the wake of the crack resulting in a reduction in laminate stiffness. However, alternate lay-ups of the composite core may have other key damage modes, such as delamination and transverse ply cracking, that need to be identified and modeled in order to be useful in an aircraft design.

The modeling and results developed for the facesheet crack growth in TiGr laminates with a lay-up of $[\mathrm{Ti}/0/90/0_2]_s$ can be applied for similar damage problems in other TiGr configurations. In Chapter 6, the finite element model was extended to wider TiGr laminates and showed reasonable correlation with the experimental results. The steady-state crack growth behavior, observed both experimentally and analytically for wider specimens, indicates that modeling techniques and the experimental observation of a steady-state crack growth rate can be extended for larger structures. If the use of the models is extended to other laminates or configurations, some experimental analysis should be conducted to verify the underlying damage modes. The three-dimensional finite element model assumes a constant delamination profile based on experimental evidence for this particular TiGr laminate. Experiments on alternate laminates have indicated that the underlying damage modes are slightly different than those observed in the base laminate and further investigation should be conducted to determine how the alternate damage modes affect the crack growth rate.

Additional attention should also be focused on the prediction of delamination growth. A simple model was developed to estimate the approximate angle of the delamination. However, the model does not predict the growth behavior of the delamination. The experiments and models conducted for TiGr specimens with facesheet seams could be used in conjunction with a finite element model to evaluate the strain energy release rate for delamination and to predict the growth at a variety of temperatures. In addition, detailed studies of the delamination growth near the crack tip may provide information on how the delamination affects the crack growth behavior. Environmental issues associated with cracking and facesheet delamination need to be addressed.

7.2.2 The role of models in fatigue of laminated composites

A significant emphasis has been placed on analytic models as a part of this research. The intent of the modeling effort was partially to predict the experimental results in TiGr and partially to evaluate the ability of analytic models to substitute for some experiments in material validation programs. It has been proposed that a significant cost and time savings can be achieved by applying models to the material development process. However, as was made clear in this thesis, the use of models does not come without risk. In Chapter 5, a two-dimensional bridged-crack model was developed for predicting the growth of coupled damage modes in TiGr laminates. Such a model has successfully predicted similar damage modes in similar hybrid laminates. However, a three-dimensional finite element analysis and experimental evidence showed that the two-dimensional bridged-crack damage model was not effective at predicting coupled facesheet crack and delamination growth in TiGr laminates. On the other hand, the three-dimensional model was effective at capturing the experimental crack growth behavior. Nevertheless, models similar to the bridged-crack model developed for TiGr have been applied successfully for other hybrid laminates as well as for other damage mechanisms in composite laminates. Future development of bridged-crack models should be conducted with caution. The work on TiGr indicates that the local details around the crack tip have a significant effect on the damage growth and cannot be ignored. In the future, the use of bridged-crack models will require proof that the local details, or potentially other unknown variables, do not affect the global behavior significantly.

Based on the results presented in this thesis, some comments can be made on how models can be effectively used in the design and validation process of new materials and where in the material design process it makes sense to use modeling as a substitute for experiments. It is suggested that models can be successfully applied for composite materials as a substitute for some, but not all, experiments at certain stages of the design and validation process.

One situation where models may be beneficial is in the comparison between different materials and/or configurations in the early stages of the design process. Simple experiments can be conducted on different materials to identify the critical failure mechanisms. Models can be developed based on the experimental results to identify how key parameters such as size, thickness, and lay-up affect the failure, so that the most important parameters can be identified and tested further. The models can provide key information about a wide range of configurations and material combinations, avoiding extensive and expensive experimental programs on each configuration or material combination. Future experimental programs can be designed to test the critical issues for the best configuration and to validate the models in an optimum sense.

An example of how this type of modeling could be applied for TiGr laminates is as follows. Suppose that the functional requirements specify a critical facesheet crack rate for a specific application. The three-dimensional finite element model for the $[\mathrm{Ti}/0/90/0_2]_s$ laminate, which was based on experimental evidence and observation, could be modified to predict the crack growth behavior for other lay-ups/configurations, assuming that the underlying damage modes are similar. Using the model predictions, certain configurations can be identified for further experimental investigation to determine if they meet the functional requirement for crack growth and if the model assumptions on crack growth behavior and damage state are accurate. This eliminates the need to conduct experiments on many different configurations if the damage modes observed are similar.

Similar to the idea of constructing models for use in the early phases of material validation and design is the concept of environmentally accelerated fatigue testing. If parameters such as temperature or moisture can be used to accelerate fatigue experiments and determine which of the candidate materials are well suited for the application, the number of costly, long-term fatigue experiments can be reduced. A review of the issues associated with accelerated testing can be found in Reference [117]. For TiGr laminates, temperature could potentially be used as an accelerating parameter to study delamination, particularly for facesheet seams, because the behavior for that damage mode is reproducible and the elevated temperature does not alter the damage mode significantly.

In Chapter 6 it was demonstrated for single edge notch tension specimens that the effects of temperature on the facesheet crack growth behavior are primarily due to the change in the R-ratio caused by thermally induced residual stresses. For this particular damage mode, the effects of temperature on the crack growth behavior could be studied without a large number of expensive and time-consuming elevated temperature fatigue experiments. However, the temperature and R-ratio effects on the delamination growth in the wake of the crack have not been verified. Future work should be conducted to determine these effects.

Models can potentially be applied to determine the effects of structural scale when evaluating the applicability of coupon-level experimental results to larger structures. The results in Chapter 6 indicated that wider samples have similar steady-state crack growth rates to the narrow samples. This was confirmed with the 3D finite element model for the wide sample. Potentially, a model that has been developed and validated for coupon-level experiments can be extended to large-scale structures with the same damage patterns. This could reduce the amount of costly experiments necessary to validate full structures.

Chapter 8

Conclusions and Recommendations

Fatigue damage growth has been studied both experimentally and analytically for Titanium-Graphite Laminates. The following conclusions and recommendations are made based on the results of this research.

8.1 Conclusions

One of the objectives of this research was to determine the fatigue damage growth characteristics for TiGr laminates. The following conclusions pertain to the fatigue behavior of TiGr laminates and the implications for use of TiGr in future aerospace structures.

- Facesheet delamination growth from seams was characterized at different temperatures as a function of the applied strain energy release rate. A power law relationship was found between the delamination growth rate and the applied strain energy release rate. Elevated temperatures accelerate facesheet delamination growth significantly. An Arrhenius-type relationship was found to describe the effects of temperature on the delamination growth rate.
- Cracks in the facesheets of TiGr laminates form and propagate with a delamination in the wake of the crack. The crack growth rate, for cracks initiating at through-thickness notches, initially decreases and then reaches a constant steady-state growth rate. The crack growth rate is significantly less than the crack growth rate of monolithic titanium

at an equivalent applied stress due to the bridging effect. Temperature does not appear to affect the steady-state crack growth rate significantly.

- The delamination in the wake of the facesheet crack propagates in a self-similar manner until the crack reaches the specimen edge. At this point, the delamination propagates in a manner similar to the seam specimens.
- Temperature has a relatively small effect on the facesheet crack growth behavior in TiGr laminates. The small effect that was observed is primarily due to the change in R-ratio associated with the thermally-induced residual stresses. Potentially, the effects of temperature on the crack growth behavior could be captured by altering the loading profile, thus reducing the number of elevated temperature experiments necessary to characterize the damage growth behavior. However, temperature has been shown to affect the delamination growth for TiGr laminates and more research needs to be conducted to characterize the effects of temperature on the delamination growth.
- A model of the local stiffness reduction for the configuration in Reference [3] indicates that during the first phase of damage growth, i.e. before the crack reaches the specimen edge, the stiffness is reduced by less than 10%. The majority of the stiffness reduction occurs after the crack reaches the specimen edge.

The other objective of this research was to evaluate the use of analytic models to predict damage growth in composite laminates. The models developed for predicting damage growth in TiGr laminates led to the following conclusions:

- A two-dimensional bridged-crack model, which assumes a constant bridging traction, is not effective for predicting facesheet crack growth in TiGr laminates. Similar models were successfully applied to other laminates, however the bridged crack model does not capture the crack growth behavior for TiGr laminates.
- A three-dimensional model using the Virtual Crack Closure Technique successfully predicts the facesheet crack growth behavior for $[\mathrm{Ti}/0/90/0_2]_s$ TiGr laminates. Using

the same model, a reasonable prediction is also obtained for $[\mathrm{Ti}/90/0/90_2]_s$ TiGr laminates. The predictions for $[\mathrm{Ti}/0/90/\pm30]_s$ TiGr laminates is not as accurate due to the difference in the damage modes in the wake of the crack. A two-dimensional bridged-crack VCCT model predicts the same crack growth trends as the three-dimensional model. However the magnitude of the stress intensity factor does not match that of the three-dimensional model. The mechanistic approach that has been applied in this research allows the models that have been developed to be applied to other layered materials and damage configurations. The specifics of the models, including the material properties and configuration as well as the damage patterns, can be altered in order to predict the behavior in other applications using the modeling framework described in this thesis.

- The discrepancy between the two-dimensional bridged-crack model and three-dimensional virtual crack closure model is due to the inability of the bridged-crack model to capture the behavior near the crack tip. The bridged-crack model is, by design, based on the global behavior of the laminate. Therefore, it does not model the details of the damage near the crack tip. It was shown that the delamination profile near the crack tip significantly affects the crack opening profile and therefore, the stress-intensity factor. In addition, it was shown that small perturbations in the amplitude of the bridging tractions near the crack tip had a significant effect on the results of the bridged-crack model.

- Global, two-dimensional modeling techniques, similar to the bridged-crack model discussed here, have been applied successfully for other damage phenomena in composite materials. However, the results of the modeling for TiGr laminates indicate that care must be used when applying global models to damage growth problems to ensure that they capture all of the relevant details.

- A tunneling crack model provides a reasonable estimate for predicting the steady-state value of the facesheet crack growth rate for the base laminate. However, it is not as accurate for the two alternate laminates that were tested. The difference is likely due to variation in the underlying damage modes for the alternate laminates.

- Using the results from the 3D VCCT model, a model was developed to predict the stiffness reduction as a function of fatigue cycles. The model consistently captures the stiffness reduction from experiments conducted on TiGr samples with open holes with an appropriate tuning factor. The tuning factor accounts for geometric factors and uncertainty in predicting he crack initiation in the procedures and assumptions used for the model.

8.2 Recommendations

The following recommendations for future work on TiGr laminates and on modeling techniques for composite materials were identified based on the results of the present research.

- The three-dimensional model developed for this research correctly predicts the crack growth if a constant delamination profile is assumed based on experimental evidence. Given that the delamination profile near the crack tip was identified as a key parameter affecting the crack growth rate, studies should be conducted to better understand the factors that control the delamination growth both globally and near the crack tip. For the delamination growth away from the crack tip, a three-dimensional finite element model could be constructed to determine the strain energy release rate along the crack front. In the vicinity of the crack tip, a more detailed study could be conducted on the behavior of the stress-singularity that exists for the combined damage mode of a facesheet crack and delamination growth.

- The use of models for damage growth in other composite laminates needs to be validated with experiments to ensure that the model is capturing the important physical parameters, particularly for the critical damage modes.

- The seam delamination behavior of TiGr laminates with off-axis plies should be investigated to determine how closely the delamination growth rate relates to the results for the base laminate presented in this work. In addition, studies on the interlaminar growth behavior of PIXA-M should be investigated. PIXA-M is a thermoplastic-polyimide and is the matrix material used in the composite plies of the TiGr laminates investigated in this research.

- Studies should be conducted to determine how the neighboring plies affect the delamination growth. The results on the $[Ti/90/0/90_2]_s$ laminates indicate that the facesheet crack extends through the outer 90° ply and the delamination will propagate along the $90°/0°$ interface. If plies with other orientations are used, it may affect the coupled damage growth.
- Further studies on the effects of scale for TiGr laminates need to be performed in order to apply the coupon-level experimental data and modeling predictions to larger scale structures.
- Further investigation of the use of temperature as an acceleration factor for durability tests is necessary. The results for TiGr specimens with facesheet seams indicated that temperature could potentially be used as an acceleration parameter for facesheet delamination. However, for coupled damage modes the effects of elevated temperature vary, depending on the damage mode.
- The effects of other environmental conditions such as moisture and oxidation in the presence of cracks and delamination need to be studied for TiGr laminates. Long term exposure to elevated temperatures can degrade the properties of both the facesheet and the core. Some examples of potential areas of concern are creep, oxidation, and corrosion. These issues need to be explored before applying TiGr to future high temperature vehicles.
- An investigation should be conducted on the matrix material to determine the "activation energy" discussed in Section 4.2.3 has a physical basis.
- If TiGr is used on aerospace vehicles such as the High Speed Civil Transport, combined thermo-mechanical experiments should be conducted to evaluate the material behavior

and the response to changes in strain rates.

- Finally, investigation of TiGr for use in aerospace structures should continue. The crack growth behavior observed in TiGr shows a significant improvement over monolithic titanium. In addition, the damage in the facesheet should be more easily detected than in non-hybrid composites. While the presence of the titanium facesheet adds some complexity to the design, the critical damage modes are not altogether different from traditional composites. With continued research into the behavior of TiGr laminates, they should be viable candidates for use on high temperature, durability critical applications. In addition, TiGr or similar variants using alternate composite cores can be applied on subsonic aircraft in fatigue sensitive regions such as the wing skin.

References

[1] Li, E. and W. S. Johnson, "An Investigation into the Fatigue of a Hybrid Titanium Composite Laminate," *Journal of Composites Technology & Research*, Vol. 20, No. 1, 1998, pp. 3–12.

[2] Krishnakumar, S., "Fiber Metal Laminates - The Synthesis of Metals and Composites," *Materials and Manufacturing Processes*, Vol. 9, No. 2, 1994, pp. 295–354.

[3] Burianek, D. A., *Fatigue Damage in Titanium-Graphite Hybrid Laminates*, Master's thesis, Massachusetts Institute of Technology, 1998. TELAC Report 98-1.

[4] Spearing, S. M., "The Durability of Fiber Composites–The Case for Mechanism-Based Models," *Journal of Composites Technology & Research*, Vol. 22, No. 4, 2000, pp. 177–186.

[5] Schaff, J. R. and B. D. Davidson, "Life Prediction Methodology for Composite Structures. Part I–Constant Amplitude and Two-Stress Level Fatigue," *Journal of Composite Materials*, Vol. 31, No. 2, 1997, pp. 128–157.

[6] Talreja, R., "Continuum modelling of damage in ceramic matrix composites," *Mechanics of Materials*, Vol. 12, 1991, pp. 165–180.

[7] Talreja, R., "A synergistic damage mechanics approach to durability of composite material systems," in *Progress in Durability Analysis of Composite Systems* (Cardon, A., H. Fukuda, and K. L. Reifsnider, eds.), 1996, pp. 117–129.

[8] Ye, L., "On Fatigue Damage Accumulation and Material Degradation in Composite Materials," *Composites Science and Technology*, Vol. 36, 1989, pp. 339–350.

[9] Yang, J. N., D. L. Jones, S. H. Yang, and A. Meskini, "A Stiffness Degradation Model for Graphite/Epoxy Laminates," *Journal of Composite Materials*, Vol. 24, 1990, pp. 753–769.

[10] Liu, B. and L. B. Lessard, "Fatigue and Damage-Tolerance Analysis of Composite Laminates: Stiffness Loss, Damage-Modelling, and Life Prediction," *Composites Science and Technology*, Vol. 51, 1994, pp. 43–51.

[11] O'Brien, T. K., M. Rigamonti, and C. Zanotti, "Tension Fatigue Analysis and Life Prediction for Composite Laminates," *International Journal of Fatigue*, Vol. 11, No. 6, 1989, pp. 379–393.

[12] Reifsnider, K. L., "The Critical Element Method: A Modeling Philosophy," *Engineering Fracture Mechanics*, Vol. 25, No. 5/6, 1986, pp. 739–749.

[13] Reifsnider, K. L. and Z. Gao, "A micromechanics model for composites under fatigue loading," *International Journal of Fatigue*, Vol. 13, No. 2, 1991, pp. 149–156.

[14] Reifsnider, K. L., "Micromechanical modelling of polymeric composites," *Polymer*, Vol. 35, No. 23, 1994, pp. 5035–5040.

[15] Reifsnider, K. L., S. Case, and Y. L. Yu, "A micro-kinetic approach to durability analysis: The critical element method," in *Progress in Durability Analysis of Composite Systems* (Cardon, A., H. Fukuda, and K. L. Reifsnider, eds.), 1996, pp. 3–11.

[16] Charewicz, A. and I. M. Daniel, "Damage Mechanisms and Accumulation in Graphite/Epoxy Laminates," in *Composite Materials: Fatigue and Fracture* (Hahn, H. T., ed.), ASTM STP 907, pp. 274–297, American Society for Testing and Materials, 1986.

[17] Reifsnider, K. L., "Durability and Damage Tolerance: Testing, Simulation, and Other Virtual Realities," in *Composite Materials: Testing and Design, Thirteenth Volume* (Hooper, S. J., ed.), ASTM STP 1242, pp. 45–59, American Society for Testing and Materials, 1997.

[18] Flaggs, D. L. and M. H. Kural, "Experimental Determination of the In Situ Transverse Lamina Strength in Graphite/Epoxy Laminates," *Journal of Composite Materials*, Vol. 16, 1982, pp. 103–116.

[19] Vaidya, R., J. Klug, and C. Sun, "Effect of ply thickness on fracture of notched composite laminates," *AIAA Journal*, Vol. 36, No. 1, 1998, pp. 81–88.

[20] Ashby, M. F., "Physical modeling of materials problems," *Materials Science & Technology*, Vol. 8, No. 2, 1992.

[21] Kortschot, M. T., *Damage Mechanics of Carbon Fibre Composites*, Ph.D. thesis, Cambridge University Engineering Department, 1988.

[22] Spearing, S. M., P. W. R. Beaumont, and M. T. Kortschot, "The fatigue damage mechanics of notched carbon fibre/PEEK laminates," *Composites*, Vol. 23, No. 5, September 1992.

[23] Spearing, S. M. and P. W. R. Beaumont, "Towards a Predictive Design Methodology Based on the Physical Modelling of the Fracture of Fiber Composites," *Applied Composite Materials*, Vol. 5, No. 2, 1998, pp. 69–94.

[24] Connell, S. J. and F. W. Zok, "Measurement of the Cyclic Bridging Law in a Titanium Matrix Composite and its APplication to Simulating Crack Growth," *Acta Materialia*, Vol. 45, No. 12, 1997, pp. 5203–5211.

[25] Walls, D. P., G. Bao, and F. Zok, "Mode I Fatigue Cracking in a Fiber Reinforced Metal Matrix Composite," *Acta Metallurgica Et Materialia*, Vol. 41, No. 7, 1994, pp. 2061–2071.

[26] Anderson, T., *Fracture Mechanics: Fundamentals and Applications*, CRC Press, 1995.

[27] Fuchs, H. O. and R. I. Stephens, *Metal Fatigue in Engineering*, John Wiley & Sons, 1980.

[28] O'Brien, T. K., "Characterization of delamination onset and growth in a composite laminate," *ASTM STP 775*, 1982, pp. 140–167.

[29] Zhang, J., C. Soutis, and J. Fan, "Effects of matrix cracking and hygrothermal stresses on the strain energy release rate for edge delamination in composite laminates," *Composites*, Vol. 25, No. 1, 1994, pp. 27–35.

[30] Trethewey, Jr., B. R., J. John W. Gillespie, and L. A. Carlsson, "Mode II Cyclic Delamination Growth," *Journal of Composite Materials*, Vol. 22, May 1988, pp. 459–483.

[31] Lu, X. and D. Liu, "Finite Element Analysis of Strain Energy Release Rate at Delamination Front," *Journal of Reinforced Plastics and Composites*, Vol. 10, 1991, pp. 279–292.

[32] Krüger, R. and M. König, "Prediction of Delamination Growth Under Cyclic Loading," in *Composite Materials: Fatigue and Fracture (Sixth Volume)* (Armanios, E. A., ed.), ASTM STP 1285, pp. 162–178, American Society for Testing and Materials, 1997.

[33] Roeck, G. D. and M. M. A. Wahab, "Strain Energy Release Rate Formulae for 3D Finite Element," *Engineering Fracture Mechanics*, Vol. 50, No. 4, 1995, pp. 569–580.

[34] Dattaguru, B., K. S. Venkatesha, T. S. Ramamurthy, and F. G. Buchholz, "Finite Element Estimates of Strain Energy Release Rate Components at the Tip of an Interface Crack Under Mode I Loading," *Engineering Fracture Mechanics*, Vol. 49, No. 3, 1994, pp. 451–463.

[35] Yang, H. T. Y. and C. C. He, "Three-Dimensional Finite Element Analysis of Free Edge Stresses and Delamination of Composite Laminates," *Journal of Composite Materials*, Vol. 28, No. 15, 1994, pp. 1394–1412.

[36] Davidson, B. D., "Prediction of Energy Release Rate for Edge Delamination Using a Crack Tip Element Approach," in *Composite Materials: Fatigue and Fracture-Fifth Volume* (Martin, R. H., ed.), ASTM STP 1230, pp. 155–175, American Society for Testing and Materials, 1995.

[37] Davidson, B., "Energy Release Rate Determination for Edge Delamination under Combined In-Plane, Bending, and Hygrothermal Loading. Part I-Delamination at a Single Interface," *Journal of Composite Materials*, Vol. 28, No. 11, 1994, pp. 1009–1031.

[38] Davidson, B., "Energy Release Rate Determination for Edge Delamination under Combined In-Plane, Bending, and Hygrothermal Loading. Part II-Two Symmetrically Located Delaminations," *Journal of Composite Materials*, Vol. 28, No. 14, 1994, pp. 1371–1392.

[39] Lee, L. J. and D. W. Tu, "J-Integral for delaminated composite laminates," *Composites science and technology*, Vol. 47, No. 2, 1993, p. 185.

[40] Bhat, N. V., *Delamination Growth In Graphite/Epoxy Composite Laminates Under Tensile Loading*, Ph.D. thesis, Massachusetts Institute of Technology, 1993. TELAC Report 93-10.

[41] Sankar, B. V. and V. S. Rao, "A Plate Finite Element for Modeling Delaminations," *Journal of Reinforced Plastics and Composites*, Vol. 12, 1993.

[42] Sankar, B. V. and V. Sonik, "Pointwise Energy Release Rate in Delaminated Plates," *AIAA Journal*, Vol. 33, No. 7, 1995, pp. 1312–1318.

[43] Sankar, B. V. and O. Park, "Energy Release Rate Calculations for Laminated Beams and Plates," in *Fourteenth Technical Conference on Composite Materials*, 1999.

[44] Charalambides, P. G., "Steady-State Mechanics of Delamination Cracking in Laminated Ceramic-Matrix Composites," *Journal of the American Ceramics Society*, Vol. 74, No. 12, 1991, pp. 3066–3080.

[45] Spearing, S. M., P. W. R. Beaumont, and M. F. Ashby, "Fatigue damage mechanics of composite materials. II: A damage growth model," *Composites Science and Technology*, Vol. 44, 1992, pp. 169–177.

[46] Jensen, H. M., "Mixed Mode Interface Fracture Criteria," *Acta Metallurgica et Materialia*, Vol. 38, No. 12, 1990, pp. 2637–2644.

[47] Yoon, S. H. and C. S. Hong, "Interlaminar Fracture Toughness of Graphite/Epoxy Composite Under Mixed-mode Deformations," *Experimental Mechanics*, September 1990, pp. 234–239.

[48] Donaldson, S. L., "Fracture toughness testing of graphite/epoxy and graphite/PEEK composites," *Composites*, Vol. 16, No. 2, 1985, pp. 103–112.

[49] Garg, A. C., "Delamination-A Damage Mode in Composite Structures," *Engineering Fracture Mechanics*, Vol. 29, No. 5, 1988, pp. 557–584.

[50] Hutchinson, J. W. and Z. Suo, "Mixed Mode Cracking in Layered Materials," *Advances in Applied Mechanics*, Vol. 29, 1992, pp. 63–191.

[51] Pipes, R. B. and N. J. Pagano, "Interlaminar stresses in composite laminates under uniform axial extension," *Journal of Composite Materials*, Vol. 4, 1970, pp. 538–548.

[52] Kassapoglou, C. and P. A. Lagace, "An Efficient Method for the Calculation of Interlaminar Stresses in Composite Materials," *Journal of Applied Mechanics*, Vol. 53, 1986, pp. 744–750.

[53] Saeger, K. J., *An efficient method for the calculation of interlaminar stresses around holes*, Ph.D. thesis, Massachusetts Institute of Technology, 1989.

[54] Brewer, J. C. and P. A. Lagace, "Quadratic Stress Criterion for Initiation of Delamination," *Journal of Composite Materials*, Vol. 22, 1988, pp. 1141–1155.

[55] Laws, N. and G. J. Dvorak, "Progressive Transverse Cracking In Composite Laminates," *Journal of Composite Materials*, Vol. 22, 1988, pp. 900–916.

[56] Boniface, L., S. Ogin, and P. Smith, "Strain energy release rates and the fatigue growth of matrix cracks in model arrays in composite laminates," in *Proceedings of the Royal Society, London*, Vol. 432, 1991, pp. 427–444.

[57] Yang, W. and J. P. Boehler, "Micromechanics Modelling of Anisotropic Damage in Cross-ply Laminates," *International Journal of Solids and Structures*, Vol. 29, No. 10, 1992, pp. 1303–1328.

[58] Nairn, J. A., "The Strain Energy Release rate of Composite Microcracking: A Variational Approach," *Journal of Composite Materials*, Vol. 23, 1989, pp. 1106–1129.

[59] Kashtalyan, M. and C. Soutis, "The Effect of Delaminations Induced by Transverse Cracks and Splits on Stiffness Properties of Composite Laminates," *Composites Part A: Applied Science and Manufacturing*, Vol. 31, 2000, pp. 107–119.

[60] Kashtalyan, M. and C. Soutis, "Stiffness Degradation in Cross-ply Laminates Damaged by Transverse Cracking and Splitting," *Composites Part A: Applied Science and Manufacturing*, Vol. 31, 2000, pp. 335–351.

[61] Salpekar, S. A. and T. K. O'Brien, "Analysis of Matrix Cracking and Local Delamination in $(0/\theta/-\theta)_s$ Graphite Epoxy Laminates Under Tensile Load," *Journal of Composites Technology & Research*, Vol. 15, No. 2, 1993, pp. 95–100.

[62] Salpekar, S. A., "Analysis of Local Delaminations Caused by Angle Ply Matrix Cracks," *Journal of Composite Materials*, Vol. 30, No. 4, 1996, pp. 418–440.

[63] Ogin, S. L., P. A. Smith, and P. W. R. Beaumont, "Matrix Cracking and Stiffness Reduction during the Fatigue of a $(0/90)_s$ GFRP Laminate," *Composites Science and Technology*, Vol. 22, 1985, pp. 23–31.

[64] Curtain, W. A., "Exact Theory of Fibre Fragmentation in a Single Filament Composite," *Journal of Material Science*, Vol. 74, No. 11, 1991, pp. 5239–5235.

[65] Jamison, R. D., "On the Interrelationship Between Fiber Fracture and Ply Cracking in Graphite/Epoxy Laminates," in *Composite Materials: Fatigue and Fracture* (Hahn, H. T., ed.), ASTM STP 907, pp. 252–273, American Society for Testing and Materials, 1986.

[66] Stinchcomb, W. W. and C. E. Bakis, "Fatigue behaviour of composite laminates," in *Fatigue of Composite Materials* (Reifsnider, K. L., ed.), Vol. 4 of *Composite Materials Series*, ch. 4, pp. 105–180, Elsevier, 1991.

[67] Schultheisz, C. R. and A. M. Waas, "Compressive Failure of Composites, Part I: Testing and Micromechanical Theories," *Progress in Aerospace Science*, Vol. 32, No. 1, 1996, pp. 1–42.

[68] Lagace, P. A. and S. C. Nolet, "Effect of Ply Thickness on Longitudinal Splitting and Delamination in Graphite/Epoxy Under Compressive Cyclic Load," in *Composite Materials: Fatigue and Fracture* (Hahn, H. T., ed.), ASTM STP 907, pp. 335–360, American Society for Testing and Materials, 1986.

[69] Spearing, S. M. and P. W. R. Beaumont, "Fatigue damage mechanics of composite materials. III: Prediction of post-fatigue strength," *Composites Science and Technology*, Vol. 44, 1992, pp. 299–307.

[70] Spearing, S. M. and P. W. R. Beaumont, "Fatigue damage mechanics of composite material IV: Prediction of post-fatigue stiffness," *Composites Science and Technology*, Vol. 44, 1992, pp. 309–317.

[71] Kortschot, M. T. and P. W. R. Beaumont, "Damage mechanics of composite materials. II–A Damaged-Based Notched Strength Model," *Composites Science and Technology*, Vol. 39, No. 4, 1990, pp. 303–326.

[72] Kortschot, M. T., P. W. R. Beaumont, and M. F. Ashby, "Damage mechanics of composite materials. III–Prediction of damage growth and notched strength," *Composites Science and Technology*, Vol. 40, No. 2, 1990, pp. 147–165.

[73] Thouless, M., "Bridging and Damage Zones in Crack Growth," *Journal of the American Ceramics Society*, Vol. 71, No. 6, 1988, pp. 408–413.

[74] Tada, H., P. C. Paris, and G. R. Irwin, *The stress analysis of cracks handbook*, Del Research Corporation, 1973.

[75] Toribio, M., *Compressive Response of Notched Composite-Honeycomb Sandwich Panels*, Master's thesis, Massachusetts Institute of Technology, 1999. TELAC Report 99-6.

[76] Soutis, C. and P. Curtis, "A method for predicting the fracture toughness of CFRP laminates failing by fibre microbuckling," *Composites Part A: Applied Science and Manufacturing*, Vol. 31, No. 7, 2000, pp. 733–740.

[77] Marshall, D., B. Cox, and A.G.Evans, "The Mechanics of Matrix Cracking in Brittle-Matrix Fiber Composites," *Acta Metallurgica*, Vol. 33, No. 11, 1985, pp. 2013–2021.

[78] McMeeking, R. and A. Evans, "Matrix Fatigue Cracking in Fiber Composites," *Mechanics of Materials*, Vol. 9, 1990, pp. 217–227.

[79] Bao, G. and R. M. McMeeking, "Fatigue Crack Growth in Fiber-Reinforced Metal-Matrix Composites," *Acta Metallurgica et Materialia*, Vol. 42, No. 7, 1994, pp. 2415–2425.

[80] Bucci, R. J., L. N. Mueller, L. B. Vogelesang, and J. W. Gunnink, "ARALL Laminates," *Aluminum Alloys–Contemporary Research and Applications*, Vol. 31, 1989, pp. 295–322.

[81] Gunnink, J. W., "Design Studies of Primary Aircraft Structures in ARALL Laminates," *Journal of Aircraft*, November 1988, pp. 1023–1032.

[82] Marissen, R., *Fatigue crack growth in ARALL, A hybrid aluminium-aramid composite material:Crack growth mechanisms and quantitative predictions of the crack growth rates*, Ph.D. thesis, Delft University of Technology, 1984.

[83] Guo, Y. J., X. R. Wu, and Z. L. Zhang, "Characterization of delamination growth behaviour of hybrid bonded laminates," *Fatigue & Fracture of Engineering Materials & Structures*, Vol. 20, No. 12, 1997, pp. 1699–1708.

[84] Lin, C. T. and P. W. Kao, "Fatigue Delamination Growth in Carbon Fibre-Reinforced Aluminum Laminates," *Acta Metallurgica*, Vol. 27A, No. 1, 1995, pp. 9–15.

[85] Ritchie, R. O., W. Yu, and R. J. Bucci, "Fatigue Crack Propagation in ARALL Laminates: Measurement of the Effect of Crack-Tip Shielding From Crack Bridging," *Engineering Fracture Mechanics*, Vol. 32, No. 3, 1989, pp. 361–377.

[86] Salivar, G. C. and C. A. Gardini, “The Influence of Stress Ratio and Temperature on the Fatigue Crack Growth Rate Behaviour of ARALL,” *Journal of Composites Technology & Research*, Vol. 15, No. 1, 1993, pp. 46–51.

[87] Li, E., W. S. Johnson, and J. L. Miller, “High Temperature Hybrid Titanium Composite Laminates: An Early Analytical Assessment,” in *The Tenth International Conference on Composite Materials*, 1995.

[88] Yeh, J. R., “Fatigue Crack Growth in Fiber-Metal Laminates,” *International Journal of Solids and Structures*, Vol. 32, No. 14, 1995, pp. 2063–2075.

[89] Toi, Y. and Y. Fujiwara, “Fatigue Characterization of Fiber/Metal Laminates,” in *1st AIAA Aircraft Engineering, Technology, and Operations Congress*, 1995. AIAA-95-3932.

[90] Marissen, R., “Flight Simulation Behaviour of Aramid Reinforced Aluminum Laminates (ARALL),” *Engineering Fracture Mechanics*, Vol. 19, No. 2, 1984, pp. 261–277.

[91] Guo, Y. J. and X. R. Wu, “A Theoretical Model for Predicting Fatigue Crack Growth Rates In Fibre-Reinforced Metal Laminates,” *Fatigue & Fracture of Engineering Materials & Structures*, Vol. 21, 1998, pp. 1133–1145.

[92] Papakyriacou, M., S. E. Stanzl-Tschegg, and J. Schijve, “Fatigue Behaviour of Notched Components of Fiber-Metal Laminates (GLARE),” in *Fatigue Design 1995*, Vol. 1, 1995, pp. 309–320.

[93] Lin, C. T., P. W. Kao, and F. S. Yang, “Fatigue Behaviour in Carbon Fibre-Reinforced Aluminum Laminates,” *Composites*, Vol. 22, No. 2, 1991, pp. 135–141.

[94] Lin, C. T. and P. W. Kao, “Effect of Bridging on the Fatigue Crack Propagation in Carbon Fiber-Reinforced Aluminum Laminates,” *Material Science and Engineering A*, Vol. 190, 1994, pp. 65–73.

[95] Lin, C. T., P. W. Kao, and M. H. R. Jen, “Thermal Residual Strains in Carbon Fibre-Reinforced Aluminum Laminates,” *Composites*, Vol. 25, No. 4, 1994, pp. 303–307.

[96] Lin, C. T. and P. W. Kao, "Delamination Growth and Its Effect on Crack Propagation in Carbon Fiber Reinforced ALuminum Laminates Under Fatigue Loading," *Acta Metallurgica*, Vol. 44, No. 3, 1996, pp. 1181–1188.

[97] Guo, Y. J. and X. R. Wu, "Bridging Stress Distribution in center-cracked fiber reinforced metal laminates: modeling and experiment," *Engineering Fracture Mechanics*, Vol. 63, 1999, pp. 147–163.

[98] Guo, Y. J. and X. R. Wu, "Stress Intensity Factor Equation for Center Cracked Tension (CCT) Specimens of Fiber Reinforced Metal Laminates under Cyclic Loading," *Key Engineering Materials*, Vol. 145–149, 1998, pp. 101–106.

[99] Guo, Y. J. and X. R. Wu, "A phenomenological model for predicting crack growth in fiber-reinforced metal laminates under constant-amplitude loading," *Composites Science and Technology*, Vol. 59, 1999, pp. 1825–1831.

[100] Miller, J. L., D. J. Progar, W. S. Johnson, and T. L. S. Clair, "Preliminary Evaluation of Hybrid Titanium Composite Laminates," technical memorandum, NASA Langley Research Center, April 1994.

[101] Li, E. and W. S. Johnson, "An Evaluation of Hybrid Titanium Composite Laminates for Room Temperature Fatigue," in *The Tenth International Conference on Composite Materials*, 1996.

[102] Li, E., "Residual Strength Study of Fatigued Open-Hole Titanium-Graphite Hybrid Composite Laminates," in *39th AIAA/ASME/ASCE/AHS/ASC Structures, Structural*, 1998.

[103] Burianek, D. A. and S. M. Spearing, "Fatigue Damage in Titanium-Graphite Hybrid Laminates," in *38th AIAA/ASME/ASCE/AHS/ASC Structures, Structural Dynamics, and Materials Conference*, 1998.

[104] Fanning, J. C., "*TIMETAL* 15-3 Property Data," in *Beta Titanium Alloys in the 1990's* (Eylon, D., R. Boyer, and D. Koss, eds.), The Minerals, Metals & Materials Society, 1993.

[105] Hartness, J. T., "The characterization of a thermoplastic polyimide composite," in *Technology Transfer in a Global Community*, Society for the Advancement of Material and Process Engineering, 1996.

[106] Zabora, R., "The Boeing Company," 1996. Personal Communication.

[107] Fisher, J. M., A. N. Palazotto, and R. S. Sandhu, "A Study of Failure Characteristics in Thermoplastic Composite Material at $250°F(121°C)$," *The Journal of Composite Technology and Research*, Vol. 13, 1991, pp. 152–160.

[108] Suo, Z. and J. W. Hutchinson, "Interface Crack Between Two Elastic Layers," *International Journal of Fracture*, Vol. 43, 1990, pp. 1–18.

[109] O'Brien, T. K., I. S. Raju, and D. P. Garber, "Residual Thermal and Moisture Influences on the Strain Energy Release Rate Analysis of Edge Delamination," *Journal of Composites Technology & Research*, Vol. 8, No. 2, 1986, pp. 37–47.

[110] Hibbet, Karlsson, and Sorensen, "ABAQUS." Providence, RI.

[111] Mowbray, D. F., "A Note on the Finite Element Method in Linear Fracture Mechanics," *Engineering Fracture Mechanics*, Vol. 2, 1970, pp. 173–176.

[112] Burianek, D. A. and S. M. Spearing, "Delamination Growth from Facesheet Seams in Cross-ply Titanium-Graphite Hybrid Laminates," *Composites Science and Technology*, Vol. 61, 2001, pp. 261–269.

[113] Rybicki, E. and M. F. Kanninen, "A Finite Element Calculation of Stress Intensity Factors By A Modified Crack Closure Integral," *Engineering Fracture Mechanics*, Vol. 9, 1977, pp. 931–938.

[114] Suresh, S., *Fatigue of Materials*, Cambridge University Press, 1991.

[115] H.Ghonem, Y. Wen, D. Zheng, M. Thompson, and G. Linsey, "Effects of temperature and frequency on fatigue crack growth in Ti-β21S monolithic laminate," *Materials Science and Engineering A*, Vol. 161, 1993, pp. 45–153.

[116] Nilsson, K. F., J. C. Thesken, P. Sindelar, A. E. Giannakopoulos, and B. Storåkers, "A Theoretical and Experimental Investigation of Buckling Induced Delamination Growth," *Journal of the Mechanics and Physics of Solids*, Vol. 41, No. 4, 1993, pp. 749–782.

[117] Gates, T. S. and M. A. Grayson, "On The Use of Accelerated Aging Methods For Screening of High Temperature Polymeric Composite Materials," in *40th AIAA/ASME/ASCE/AHS/ASC Structures, Structural Dynamics, and Materials Conference*, 1999.

Appendix A

In order to verify the performance of the cabinet and the controller system, a trial was run on the test setup for each test temperature. Thermocouples (K-type) were mounted on a TiGr specimen as shown in Figure A-1 for the 177° C experiment and for the 93° C experiment. The front of the specimen was defined to be the side closest to the heat gun. The placement of the thermocouple for the -18° C experiment was the same as that for the 93° C experiment except that the location of the #4 thermocouple and controller thermocouple were reversed. Changing the placement of the control thermocouple between the three test temperatures (the room temperature experiment did not use a control thermocouple) was necessary to obtain accurate measurement of the temperature distributions. The optimal placement was determined through trial and error during the verification trials. During an actual fatigue test of a TiGr specimen, the only thermocouple present was the control thermocouple.

The front of the specimen was defined as the side facing the heat gun input. The assembly was placed in the temperature cabinet and heated to the specified temperature. The thermocouples were connected to a Power Macintosh™ computer via an A/D board and the temperature versus time data was recorded using a program written with the LabView™ software package.

At a test temperature of 177° C the cabinet is controlled to +/- 1° C. Figures A-2, A-3, and A-4 compare three sets of thermocouple pairs along the length of the specimen. The difference between the front reading and the back reading is approximately 2° C at each location. Figure A-5 compares the thermocouple readings of the top (#1) and bottom (#6) thermocouples showing a difference between temperatures of approximately ±3° C. The test

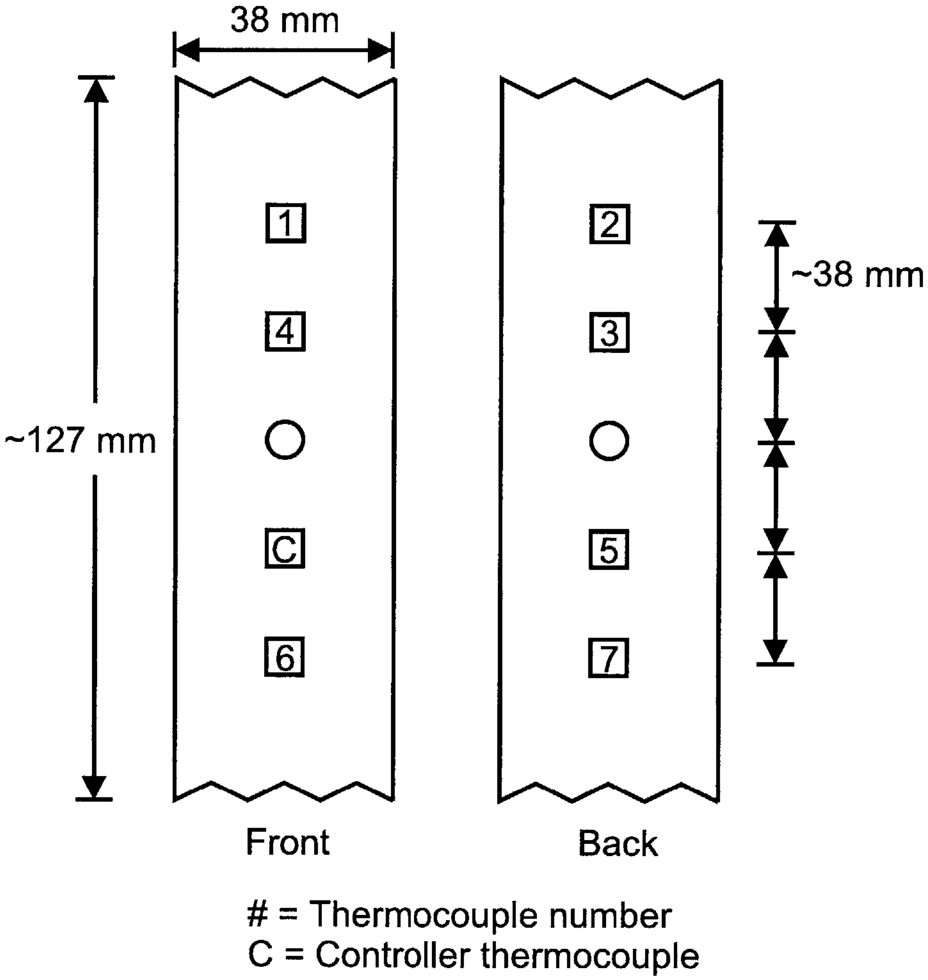

Figure A-1: Placement of thermocouples on 177° C and the 93° C trial specimen at 177° C was conducted to confirm that the results previously obtained and described in [3] for the oven with no windows was still valid with the new design. Therefore, the duration of the test was limited to the time necessary to heat up to the steady state value and ensure that the control and temperature distributions were similar to those obtained previously.

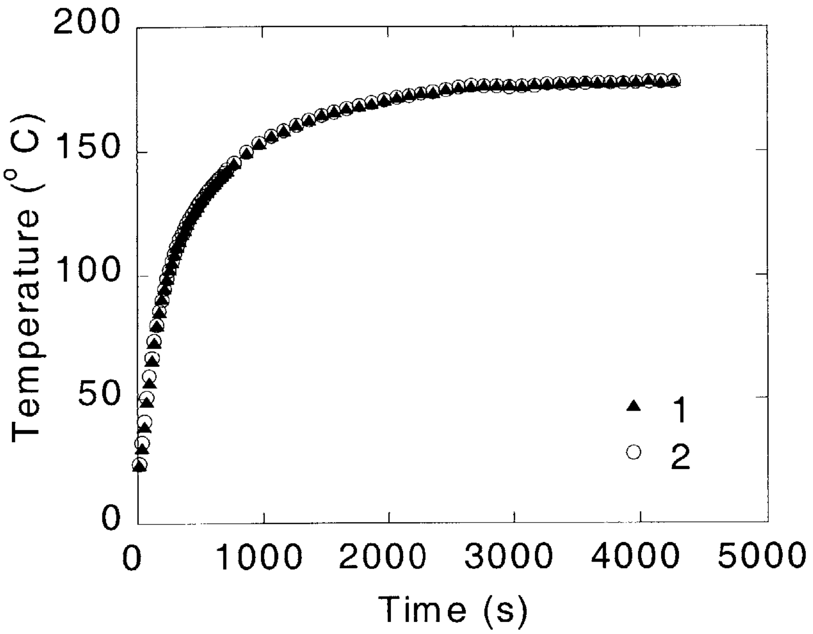

Figure A-2: Comparison between two top thermocouple (#1 and #2) for the 177° C trial

The initial verification experiments at 93° C showed large gradients between the top thermocouples and the bottom thermocouples. As mentioned previously, the location of the control thermocouple was altered to help solve this problem. In addition, a pair of 38.1 mm fans were attached near the top of the box ahead of and behind the specimen. The fans circulated the warmer air at the top of the box with the cooler air at the bottom to produce a more uniform temperature distribution. Figures A-6, A-7, and A-8 compare the front to back readings of three sets of thermocouples along the length of the specimen. Figure A-9 compares the thermocouple readings of the top (#1) and bottom (#6) thermocouples showing a difference between temperatures of approximately 5° C.

The overall temperature oscillates by ±2° C around the test temperature, and the variation from front to back is approximately 2° C. Note that the control temperature was set to 95° C in order to obtain the most uniform distribution between the top and bottom

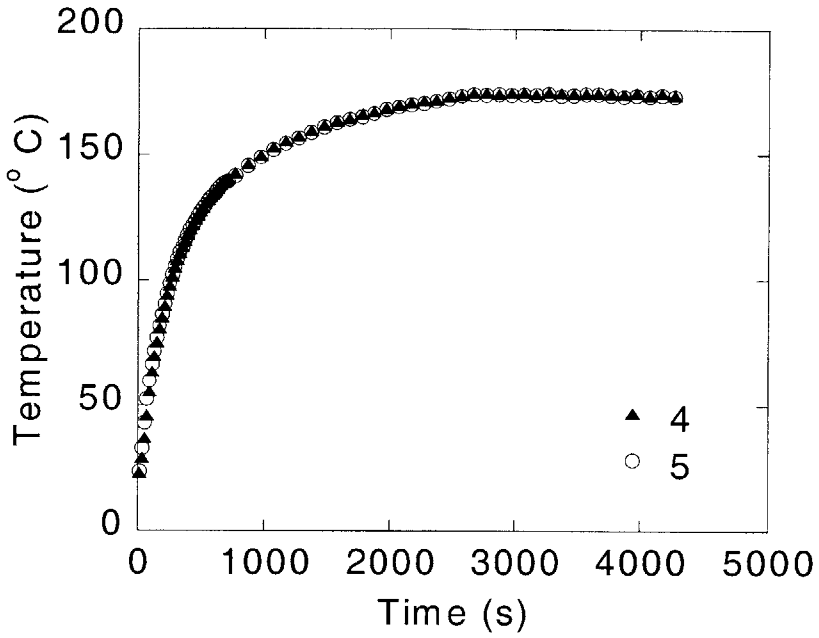

Figure A-3: Comparison between the two middle thermocouples (#4 and #5) for the 177° C trial

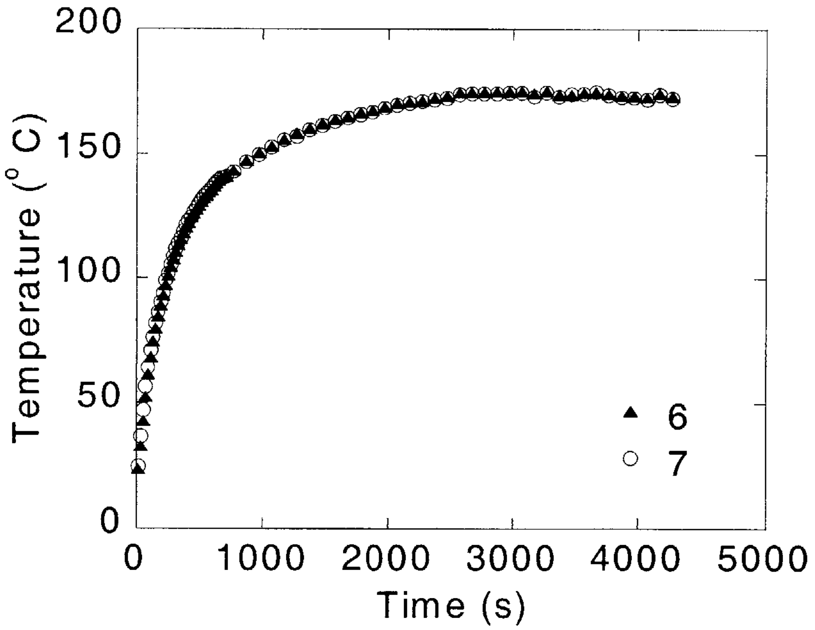

Figure A-4: Comparison between the two bottom thermocouples (#6 and #7) for the 177° C trial

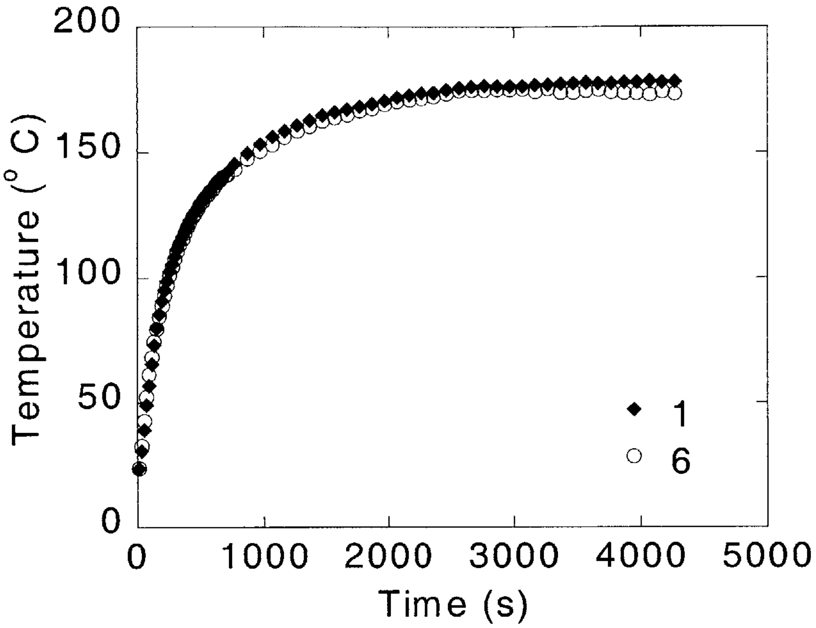

Figure A-5: Comparison between the top and bottom thermocouples (#1 and #6) for the 177° C trial

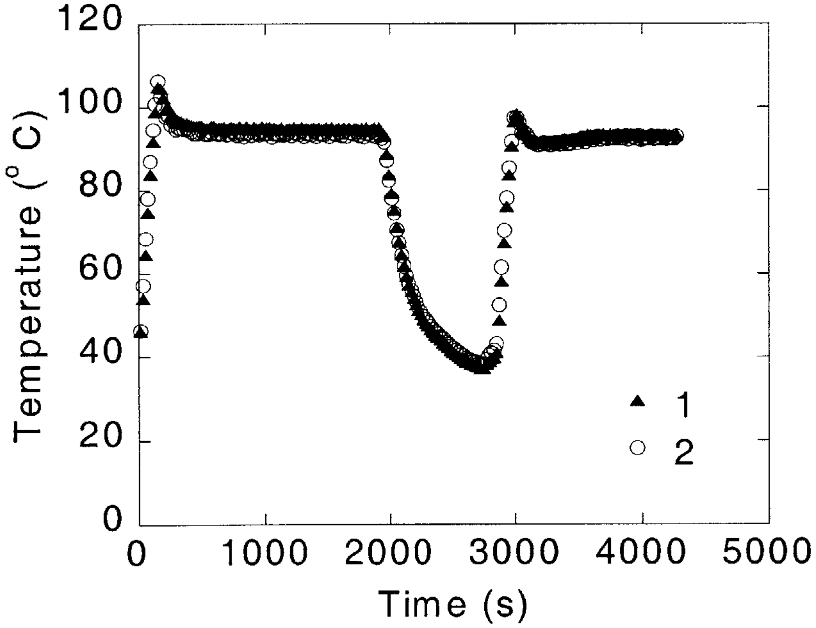

Figure A-6: Comparison between two top thermocouple (#1 and #2) for the 93° C trial

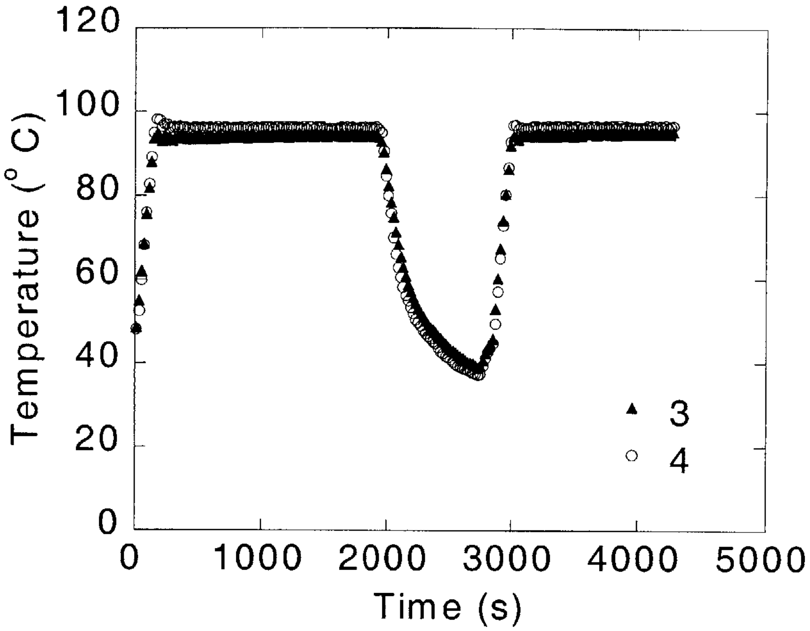

Figure A-7: Comparison between the two middle thermocouples (#3 and #4) for the 93° C trial

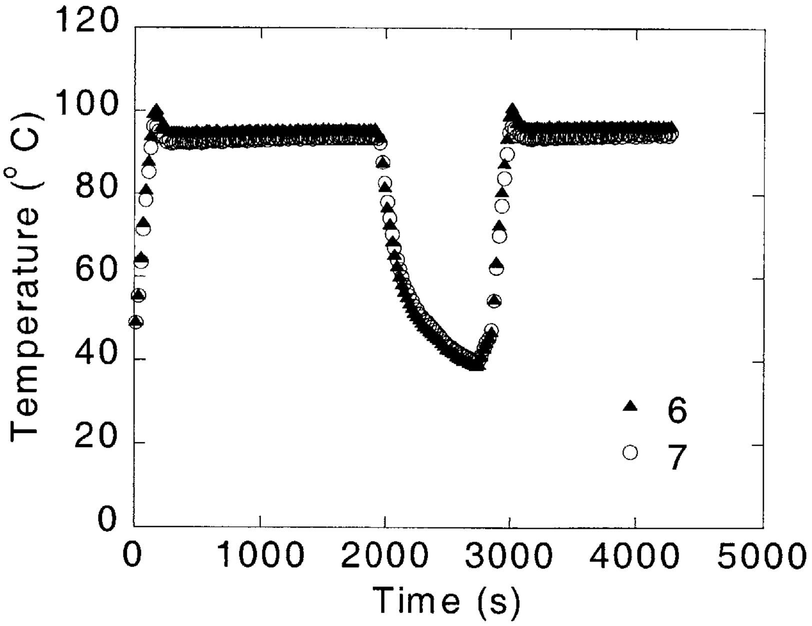

Figure A-8: Comparison between the two bottom thermocouples (#6 and #7) for the 93° C trial

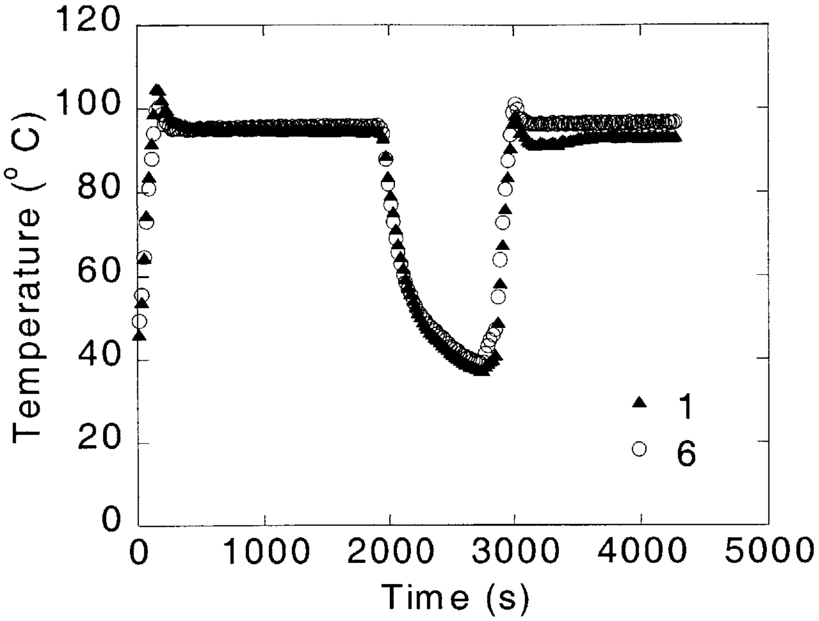

Figure A-9: Comparison between the top and bottom thermocouples (#1 and #6) for the 93° C trial

(around the test temperature of 93° C). The temperature drop evident in the experimental data was due to the box being opened to simulate crack length readings that occur during actual experiments. This identified the time necessary for reheating the box to the test temperature.

The temperature oven was modified slightly to conduct low temperature experiments. A picture of the oven in shown in Figure A-10. Styrofoam inserts approximately half the height of the test chamber were placed inside the oven. Dry ice was used as the cooling agent and was placed on top of the styrofoam inserts. The inserts were necessary because the results of the initial verification trials indicated an unacceptable temperature gradient between the top and the bottom. The inserts raised the level of the dry ice such that it was closer to the warm regions at the top of the box. The thermocouple placement was altered slightly from the previous trials in order to locate the control (monitor) thermocouple closer to the top of the box.

The quantity of dry ice inserted into the box at the beginning of a test run was measured using 5 ounce paper cups. Approximately four full cups of dry ice chunks were spread around the oven to form an even layer at the beginning of the experiment. During a fatigue test,

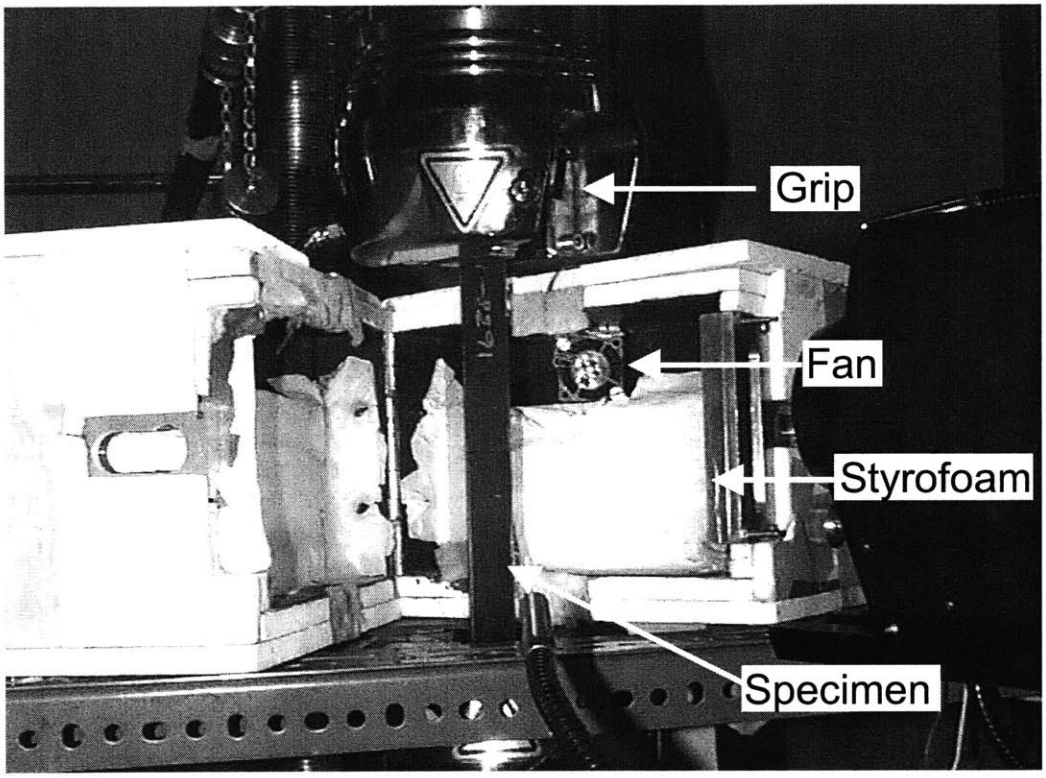

Figure A-10: Picture of oven with styrofoam inserts it was necessary to open the oven to record the delamination length. While the oven was opened, an additional cup of dry ice was spread around the temperature oven. The amount of dry ice to be added while the oven was open and the approximate interval was determined by trial and error.

The cooling fans were directed to blow the cold air sublimating from the dry ice directly onto the specimen. The combination of the inserts raising the level of the dry ice and the cooling fans reduced the temperature gradient between the top of the box and the bottom of the box to a more acceptable level of ±10° C as indicated in Figure A-14. Figures A-11, A-12, and A-13 show the front-back thermocouple pairs as before. The spikes in temperature are due to the box being opened in order to determine the amount of dry ice that would need to be added during a fatigue run and to determine the time necessary to return to the test temperature. This simulates the box being opened in order to record a delamination length measurement.

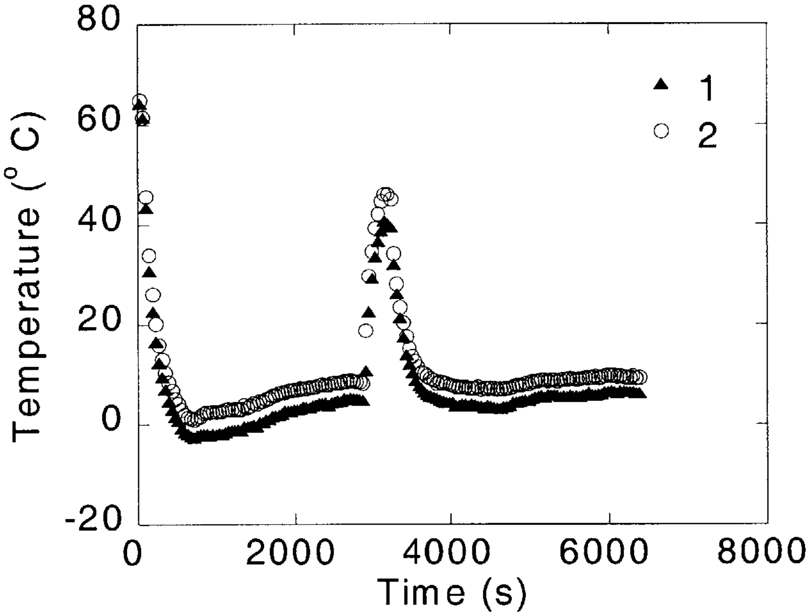

Figure A-11: Comparison between two top thermocouple (#1 and #2) for the -18° C trial

An assumption was made that if the amount of dry ice contained in the box was constant than the temperature would remain constant as well. The assumption was tested during the verification tests where the box was opened and shut at various intervals to simulate the

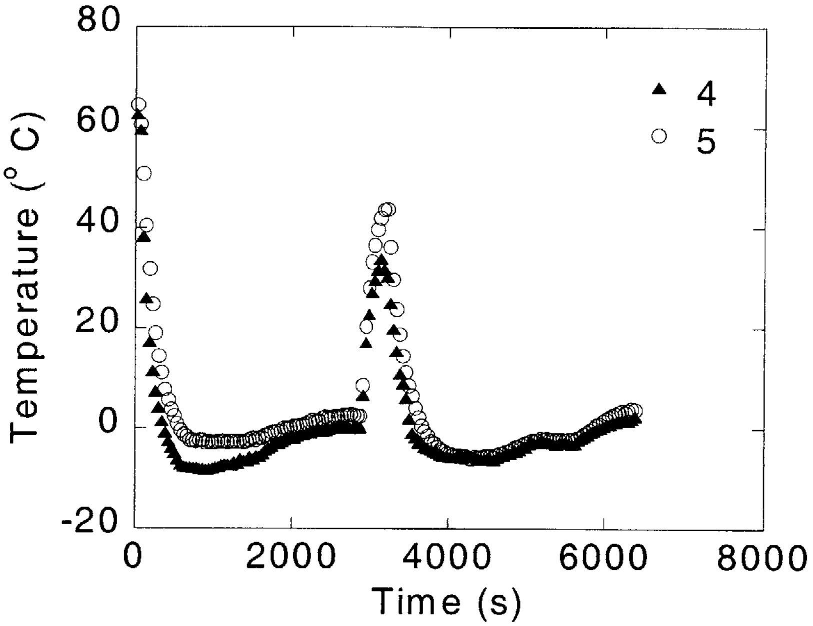

Figure A-12: Comparison between the two middle thermocouples (#4 and #5) for the -18° C trial

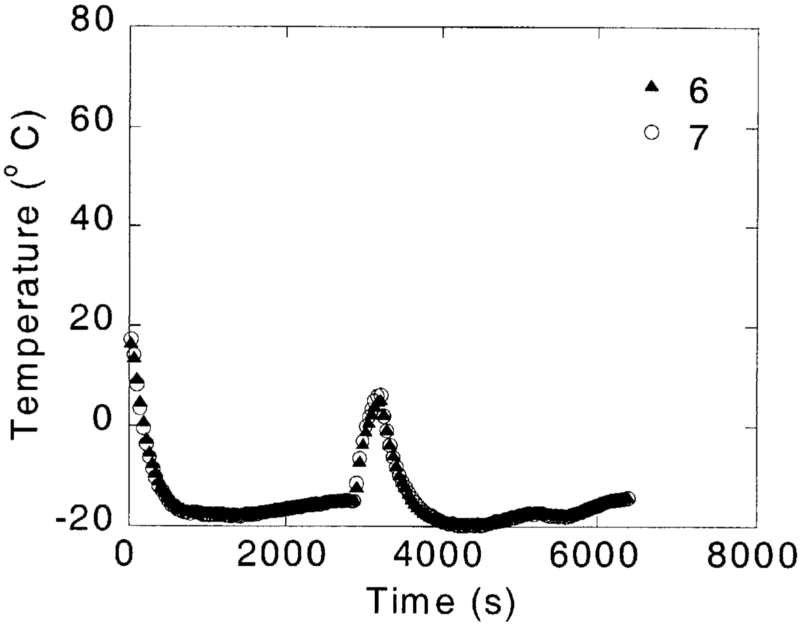

Figure A-13: Comparison between the two bottom thermocouples (#6 and #7) for the -18° C trial

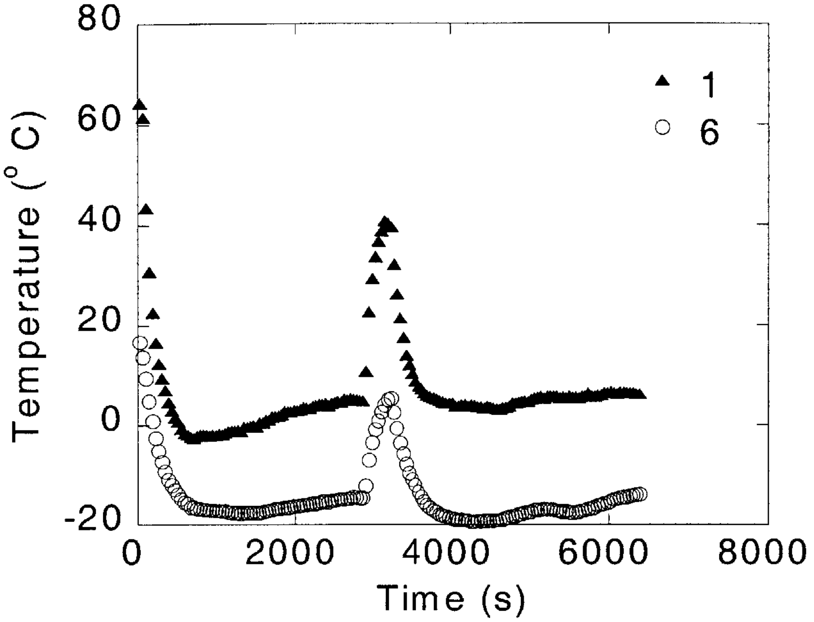

Figure A-14: Comparison between the top and bottom thermocouples (#1 and #6) for the -18° C trial

opening of the box to measure the delamination length. The dry ice that had sublimated was replaced while the box was open. Since the temperature was assumed to be constant, the control thermocouple was not necessary. However, the control thermocouple was still attached to the specimen in every experiment for monitoring purposes.